Spectropolarimetric and imaging properties of Fabry-Pérot etalons.

Applications to solar instrumentation.

Francisco Javier Bailén

Programa de Doctorado en Física y Ciencias del Espacio

Universidad de Granada

UNIVERSIDAD DE GRANADA

Supervised by D. Orozco Suárez and J.C. del Toro Iniesta.

Agradecimientos

Esta tesis no habría sido posible si no fuese por mis padres. Ellos me han educado para ser la persona que soy ahora y han dado todo para que mi vida no dependiese de los caprichos del destino, sino de mis propios méritos y capacidad. Y lo que es más importante, me han otorgado lo mejor que se le puede dar a un hijo, el regalo de la vida. Además de mis padres, hay un número incontable de personas a las que me encantaría agradecerles haberme ayudado a llegar hasta aquí. Desafortunadamente no puedo pararme a nombrarlas a todas, aunque sí que me veo obligado a mencionar a algunas. Me gustaría comenzar por un par de profesores que han marcado enormemente mi vocación. El primero, Manuel Rama, mi profesor de Matemáticas durante la mayor parte de mis años en la educación secundaria. Él me enseñó a disfrutar de la belleza de la naturaleza expresada el lenguaje de los números y vio en mí un potencial que me impulsó a iniciar mi camino en la ciencia. El segundo, ya en mi etapa universitaria, es José Vicente Álvarez, de quien aprendí cómo se hace ciencia y a quien sólo tengo palabras de agradecimiento por sus consejos y su ayuda en el preámbulo de mi carrera profesional.

Gracias también a todos mis compañeros del IAA por haberme abierto las puertas y haber hecho que me sienta como uno más desde el principio. En especial, gracias a Jose Carlos y a David por confiar en mí desde el principio, por ayudarme en todo lo que he necesitado durante estos años, por supervisar con exquisito detalle todo mi trabajo, por darme libertad y autonomía y por dedicarme tantas horas de su tiempo. Esta tesis es tan mía como de ellos. Quisiera expresar también mi gratitud de forma explícita a Olga. Si no fuese por ella dudo que ahora formase parte del IAA y, por tanto, que estuviera escribiendo estas palabras.

En el ámbito de mi vida personal, además de a mis padres, debo mencionar a Isabel, mi compañera de vida y alegrías, mi apoyo para levantarme tras cada caída. Gracias por seguir a mi lado. A Simón y Teresa, probablemente las dos mejores personas que conocí en Madrid. Espero que sigan formando parte de mi vida siempre. Y, por supuesto, qué sería de mí si no fuese por el resto de mi familia y por mis amigos de siempre, de los que disfruto desde mi infancia y adolescencia, los que aún me escuchan, me entienden y me dejan formar parte de sus vidas. Por último, pero no menos importante, quiero agradecer a mi hermana el detalle de diseñar la portada de esta tesis, así como su apoyo y admiración incondicional.

Abstract

The use of Fabry-Pérot etalons as tunable narrow-band filters has consolidated over the last decades in solar instrumentation. However, its performance has been evaluated in most studies only to some extent —e.g., assuming purely monochromatic effects, isotropy, or ideal illumination—. In this work we address the spectral, polarimetric, and imaging features of Fabry-Pérot etalons and their influence in solar spectropolarimeters in both collimated and telecentric configurations with especial considerations on (i) the quasi-monochromatic nature of the observations, (ii) possible birefringent effects appearing in solid etalons, (iii) imperfections on the illumination and (iv) the impact of etalon defects.

This thesis is based on a series of four papers on Fabry-Pérot etalon-based instruments published in *The Astrophysical Journal Supplement Series*. In the first paper we start with a general outlook of the basic characteristics of etalons. We revisit the historical approach followed to evaluate the impact of irregularities and inhomogeneities of etalons on the transmission profile and we generalize the commonly employed expressions for the finesse of the profile to any arbitrary magnitude of the defects in both air-gapped and crystalline etalons. We examine the spectral and imaging response of each setup, collimated or telecentric, including the polychromatic effects caused by the finite bandpass of the filter and possible deviations from ideal illumination. In particular, we pay special attention to pupil apodization effects occurring in telecentric mounts and we focus on the consequences of the asymmetries, shifts and widenings induced on the transmission profile and point-spread functions when the etalon is tilted with respect to the optical axis of the instrument, when considering errors in the alignment of the optical components, or by departures from the ideal paraxial propagation of light through the instrument.

In the second paper, we tackle the polarimetric response of anisotropic etalons filled with a solid material (e.g., $LiNbO_3$). We find that the analytical form for the Mueller matrix of etalons that exhibit an arbitrary birefringence depends only on four spectral coefficients that vary rapidly along the bandpass and show that the polarimetric response can be arranged as the combined Mueller matrices of a retarder and a mirror, properly modulated across the transmission profile. We derive a compact expression for the Mueller matrix of collimated etalons and we present explicit formulae to numerically evaluate the coefficients of the Mueller matrix for the telecentric configuration. We take care of the different orientations of the principal plane of the crystal in the two configurations and we present the explicit

1

dependence of the birefringence induced in uniaxial crystals with the direction of the incident light beam and with the orientation of the optical axis, necessary to evaluate the Mueller matrix. Then, we assess the response of a Z-cut etalon for the telecentric and collimated cases and study the dependence of their PSFs with the polarization of incident light.

In the third paper, we evaluate the spurious plasma velocities and magnetic field signals induced by the effects studied in the previous papers: pupil apodization arising in telecentric setups, asymmetries on the pupil apodization in imperfect telecentric mounts, and the birefringent effects that appear in the two mounts when a uniaxial etalon is employed. For this purpose, we simulate a spectropolarimeter in configurations similar to the ones of PHI (Solanki et al., 2020) and IMaX (Martínez Pillet et al., 2011) and we compare the line-of-sight plasma velocities and magnetic signals with the ones obtained when assuming an ideal behavior. We take care of the etalon location within the optical train and we distinguish between two important cases: when the etalon is placed after the polarimeter (occuring in dual-beam instruments) and when it is located before the analyzer. We also evaluate the possible contamination between orthogonal channels in dual-beam instruments. We show that birefringence has a minimal impact on the measured Stokes vector compared to the typical artificial signals expected by pupil apodization.

In the fourth paper, we find an analytical formula that describes the transmitted electric field in telecentric mounts, in excellent agreement with the numerical solution of the electric field equation. We use such an expression to infer both the transmission profile and the transmitted wavefront and we derive expressions for the analytical derivatives of the electric field in order to carry out sensitivity analyses of these parameters. In particular, we obtain explicit expressions for the wavefront degradation produced by errors across the footprint of the incident beam and we discuss their maximum allowed magnitude to achieve diffraction-limited performance. We focus on the dependence of the wavefront error with the f-number, with the reflectivity and with the spectral resolution, taking care of the integrated response of the instrument across the transmission profile. We discuss the intrinsic errors on the optical phase introduced by the finite f-number of the incident beam and we compare qualitatively the performance of telecentric mounts with the one expected in collimated setups attending to considerations related to the size, quality, and cost of the etalon and of the instrument itself. Finally, we propose a method to analytically evaluate the Mueller matrix of telecentric etalons adapting the formulation derived for the isotropic case.

Resumen

El uso de etalones Fabry-Pérot como filtros sintonizables de banda estrecha se ha consolidado a lo largo de las últimas decadas en instrumentación solar. Sin embargo, en la mayoría de estudios realizados hasta ahora se ha evaluado su comportamiento sólo hasta cierto punto —por ejemplo, suponiendo efectos puramente monocromáticos, isotropía o iluminación ideal—. En este trabajo abordamos las características espectrales, polarimétricas y de calidad de imagen de los etalones Fabry-Pérot, así como su influencia en espectropolarímetros solares en la configuración colimada y en la telecéntrica, prestando una atención especial a (i) la naturaleza cuasi-monocromática de las observaciones, (ii) los posibles efectos birrefringentes que aparecen en etalones sólidos, (iii) las imperfecciones en la iluminación y (iv) el impacto de los defectos del etalón.

Esta tesis está formada por una compilación de cuatro artículos sobre instrumentos basados en etalones Fabry-Pérot que hemos publicado en *The Astrophysical Journal Supplement Series*. En nuestro primer artículo comenzamos con una revisión general de las características de los etalones. Repasamos el enfoque histórico seguido para evaluar el impacto de las irregularidades e inhomogeneidades de los etalones en el perfil de transmisión y generalizamos las expresiones empleadas comúnmente para la fineza del perfil con el fin de incluir defectos de magnitud arbitraria en etalones tanto cristalinos como de aire. Examinamos su respuesta espectral y la calidad de imagen esperada para cada configuración, colimada o telecéntrica, incluyendo los efectos policromáticos provocados por el ancho de banda finito del filtro y las posibles desviaciones de iluminación ideal. En concreto, nos centramos en los efectos de apodización de pupila que ocurren en las monturas telecéntricas y en las consecuencias de las asimetrías, desplazamientos y ensanchamientos inducidos en el perfil de transmisión y en la PSF cuando el etalón está girado respecto al eje óptico del instrumento, cuando se tienen en cuenta errores en el alineamiento de los componentes ópticos, o por desviaciones de la propagación paraxial ideal de la luz a lo largo del instrumento.

En el segundo artículo, abordamos la respuesta polarimétrica de etalones sólidos uniáxicos (como el $LiNbO_3$). Demostramos que la matriz de Mueller en estos etalones depende sólo de cuatro coeficientes espectrales que cambian rápidamente a lo largo del perfil de transmisión y que la respuesta polarimétrica puede formularse como la combinación de las matrices de Mueller de un retardador y de un espejo, correctamente moduladas a lo largo del perfil de transmisión. También deducimos una expresión compacta para

la matriz de Mueller de etalones colimado, presentamos fórmulas explícitas para evaluar numéricamente sus coeficientes para la configuración telecéntrica, incluimos el efecto de tener diferentes orientaciones del plano principal del cristal en cada configuración y formulamos la dependencia explícita de la birrefringencia inducida en cristales uniáxicos con la dirección de la luz incidente y con la orientación del eje óptico. Por último, evaluamos la respuesta de un etalon con corte en Z para los casos colimado y telecéntrico y estudiamos la dependencia de su PSF con la polarización de la luz incidente.

En el tercer artículo, evaluamos las señales espurias de las velocidades del plasma y del campo magnético debidas a los efectos estudiados en los artículos anteriores: la apodización de pupila que surge en monturas telecéntricas, las asimetrías en la apodización de pupila que aparecen cuando hay imperfecciones en la iluminación de etalones telecéntricos y los efectos birrefringentes que aparecen en las dos configuraciones cuando se usa un etalón uniáxico. Para este fin simulamos un espectropolarímetro en configuraciones similares a las de PHI (Solanki et al., 2020) e IMaX (Martínez Pillet et al., 2011) y comparamos las velocidades y campos magnéticos del plasma a lo largo del campo de visión con los obtenidos cuando se supone un comportamiento ideal. Para ello, tenemos en cuenta la localización del etalón dentro del tren óptico y distinguimos entre dos casos importantes: cuando se coloca detrás del polarímetro (como ocurre en instrumentos de doble haz) y cuando se sitúa antes del analizador. Evaluamos también la posible contaminación entre canales ortogonales que aparece en instrumentos de doble haz y mostramos que la birrefringencia tiene un impacto mínimo en la medida del vector de Stokes en comparación con las señales artificiales esperadas por la apodización de pupila.

En el cuarto artículo, presentamos una fórmula analítica que describe el campo eléctrico transmitido en la configuración telecéntrica que ajusta de manera excelente con los resultados obtenidos tras resolver de forma numérica la ecuación del campo eléctrico. Usamos esta expresión para inferir tanto el perfil de transmisión como el frente de onda transmitido y mostramos las derivadas analíticas del campo eléctrico con el fin de realizar análisis de sensibilidad de estos parámetros. En concreto, obtenemos expresiones para la degradación de frente de onda producida por errores a lo largo de la huella del haz incidente y discutimos su magnitud máxima permitida para alcanzar el límite de difracción. Para ello, evaluamos la dependencia del error del frente de onda con el número f, con la reflectividad y con la resolución espectral monocromáticamente y tras integrar a lo largo de todo el perfil de transmisión. Discutimos los errores intrínsecos en la fase óptica introducidos por el número f finito del haz incidente y comparamos de forma cualitativa el comportamiento de las monturas telecéntricas con la esperada

en instrumentos colimados atendiendo a consideraciones relacionadas con el tamaño, la calidad y el coste del etalón y del propio instrumento. Por último, proponemos un método para evaluar analíticamente la matriz de Mueller de etalones telecéntricos adaptando la formulación derivada para el caso isótropo.

Contents

Introduction

Mapping the solar magnetic field with high spatial and spectral resolution in combination with a large polarimetric sensitivity is of paramount importance to get an insight on some of the fundamental questions that remain unanswered in solar physics, like the origin of the solar dynamo mechanisms responsible for its structure and periodic cycles, the way different layers of the solar atmosphere are connected, or how the heating of the cromosphere and corona is produced. The observation of the magnitude, orientation, structure, and evolution the solar magnetic field is carried out with magnetographs. Solar magnetism cannot be measured *in situ*, though. Instead, magnetographs shall be regarded as imaging spectropolarimeters, that is, instruments that image the solar surface in linear combinations of the Stokes parameters along one or several spectral lines that are sensitive to magnetic fields.[1] The spectropolarimetric properties of the measured light provide information of the magnetic field vector and line-of-sight (LoS) plasma velocities, which can be inferred later through sophisticated inversions of the radiative transfer equation (e.g., Del Toro Iniesta & Ruiz Cobo, 2016).

Modern magnetographs aim at providing for maps of the magnetic field with sub-arcsec angular resolutions in order to resolve structures on the solar surface as small as ~ 10 km while sensing faint magnetic signals of about ~ 1 G in times scales shorter than the ones necessary for the magnetic field structures to change considerably. In particular, fast diffraction-limited observations with a temporal resolution of $1-10$ s, challenging polarimetric sensitivities of $\sim 10^{-3}$ and resolving powers of $\sim 10^5$ or better are typically requested (e.g., Martínez Pillet et al., 2011). Hence, such instruments must demonstrate not only an excellent performance in terms of image quality, but they must provide also observations with signal-to-noise ratios higher than 10^3 while achieving an accurate and rapid scanning of the spectral lines of interest.

The wavelength tuning has been performed historically either with slit-based spectrographs or through narrow-band tunable filters.[2] Examples of the former technology are the Tenerife Infrared Polarimeter at the VTT

---

[1]The Stokes formalism provides the most general description of polarized light. Unlike the Jones formalism, it serves also to represent the polarization state of polychromatic (real) light, which is polarized only to some degree. Its use is widely accepted in the field of solar physics and it will be followed in this thesis. A detailed description on the formulation, physical interpretation and mathematical properties of the Stokes formalism can be found in Del Toro Iniesta (2003).

[2]We refer the reader to Iglesias & Feller (2019) for an exhaustive review on the differences between slit-based spectrographs and narrow-band filtergraphs, as well as on the state of the art and future perspectives of the technologies employed in solar instrumentation.

(Martínez Pillet et al., 1999), the Diffraction-Limited Spectropolarimeter and SPINOR at the NSO Dunn Solar Telescope (Tritschler et al., 2007; Socas-Navarro et al., 2006), the Hinode Spectropolarimeter SP (Lites et al., 2001), or the multiline polarimetric mode of THEMIS (Molodij & Rayrole, 2003). Their main advantage over most bidimensional imaging filtergraphs is that they capture a full unidimensional spectrum of light with a large resolving power $(150,000 - 250,000)$, and they do so in a single exposure. In exchange, they sacrifice spatial information, since they do not image the whole the solar scene in a shot, but they need to scan the other dimension to get an image of the solar surface (Figure 1.1, right). Unfortunately, the time-consuming scanning of the solar surface with such an accurate wavelength sampling limits the study of fast solar events with reasonable fields of view and the highest optical quality.

Meanwhile, magnetographs based on tunable filters enable an accurate and rapid imaging of the solar scene, but only at some selected (discrete) wavelengths along a spectral line (Figure 1.1, left) and typically with lower resolving powers than slit-based spectrographs $(\sim 50,000 - 150,000)$.[3] One of the most important advantages of their rapid imaging capabilities is that post-facto image reconstructions and adaptive optics techniques are easier to implement, thus allowing the study of fast events with the highest optical quality. The most powerful techniques used nowadays in solar filtergraphs are possibly Phase Diversity (Gonsalves, 1982; Paxman et al., 1992), Speckle interferometry (von der Lühe, 1993), and (Multi-Object) Multi-Frame Blind Deconvolution (van Noort et al., 2005). These methods provide precise information of the wavefront error introduced by the instrument and allow for realistic (diffraction-limited) reconstructions with minimal artifacts. On the other side, image restoration techniques in grating-based spectrographs have proven to be difficult to implement due to the shortage of detailed spatial information in every single exposure. Different solutions to overcome this issue are still in development and need farther investigation (e.g., Quintero Noda et al., 2015), although some novel studies have shown that achieving (near) diffraction-limited restorations is possible when a complementary *slit-jaw* camera is used to measure the degradation of the wavefront on the slit of the spectrograph through conventional image reconstruction techniques (van Noort, 2017).

Another advantage of tunable filters is that they can be used together with dual-beam polarimetric techniques (e.g., Martínez Pillet et al., 2011;

---

[3]There are some important exceptions to this rule. Initially, filtergraphs equipped with Fabry-Pérots tended to pursue resolving powers as high as $300,000$ (at least theoretically), but now the trend has been reverted and more recent instruments operate at much lower spectral resolutions (see Table 1.1).
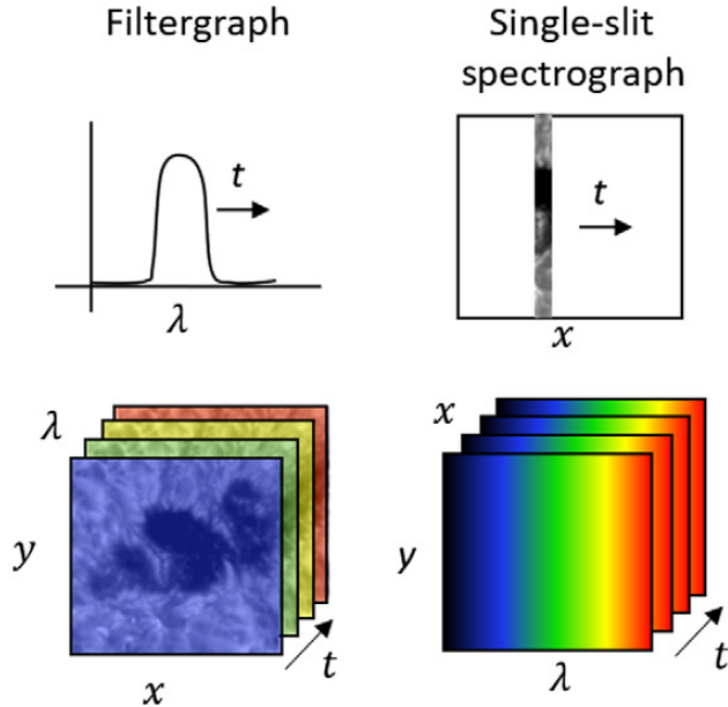
Figure 1.1: Schematic layout of the working principle of a narrow-band filtergraph (left) and of a slit-based spectrograph (right). The two spatial dimensions of the solar scene (x and y) are captured simultaneously in the former, while the wavelength dimension (λ) is scanned sequentially in a time interval t. In the latter, an spectrum over one dimension (y) is obtained in each frame, while the scanning is carried out through the other dimension (x). Figure adapted from Iglesias & Feller (2019) with permission. Licensed under CC BY 4.0.

Scharmer et al., 2008). Dual-beam polarimetry consists in splitting the orthogonal polarization components of incident light with a polarizing beam splitter and focusing each one in a different detector (or in different parts of a single detector). Observing simultaneously two perpendicular states of polarization makes it possible to reduce induced cross-talks between different Stokes parameters that appear as a result of differential motions between pairs consecutive images appearing due to jitter or seeing effects (Collados, 1999).[4] To employ dual-beam polarimetry, the narrow-band filter only needs to be placed before the polarimetric analyzer (beam splitter).

---

[4]Polarimetry is based on differential imaging techniques of the modulated observed object. Therefore, differences between consecutive images are translated into polarimetric signals. If such differences are originated by a shift of one image with respect to

Among the tunable filters, Fabry-Pérot etalons are the most common choice in solar post-focus instruments (Iglesias & Feller, 2019). Some examples are the Italian Panoramic Monochromator (IPM) at THEMIS (Bonaccini et al., 1989, and references therein), the TESOS spectrometer at the VTT (Kentischer et al., 1998), the Interferometric Bidimensional Spectrometer (IBIS) at the Dunn Solar Telescope of the Sacramento Peak Observatory (Cavallini, 1998), the CRisp Imaging SpectroPolarimeter instrument (CRISP) at the Swedish 1-m Solar Telescope (Scharmer et al., 2008), the Imaging Magnetograph eXperiment (IMaX) instrument (Martínez Pillet et al., 2011) aboard the Sunrise balloon observatory (Barthol et al., 2011), the GFPI at GREGOR (Puschmann et al., 2013), the PHI instrument (Solanki et al., 2020) on board the Solar Orbiter mission (Müller et al., 2020) and the future Visible Tunable Filter (VTF) (Schmidt et al., 2016) at DKIST (Rimmele et al., 2020). Some of the basic features of the mentioned etalon-based instruments are displayed in Table 1.1. Their success in solar instrumentation comes from their easiness of both use and interpretation of the measured data (unlike, for instance, Michelson interferometers), as well as for their high spectral resolution. They also show transmissions close to 100 % and are almost insensitive to the polarization of the incident light in most cases (Doerr et al., 2008), contrary to Lyot filters.

1.1 General properties of etalons as tunable imaging monochromators

Fabry-Pérot interferometers are basically resonant optical cavities made of two plane-parallel, high-reflecting surfaces that are slightly spaced — hundreds of micrometers or a few millimeters, normally—. The high reflectivity of the plates causes multiple back and forth reflections across the cavity for each incident ray. Individual rays, then, split and interfere coherently among themselves. The difference of optical path among two consecutive reflections is such that it causes resonances on the transmission under some conditions. The higher the reflectivity of the surfaces, the more the number of interfering rays and the narrower the spectral transmission peaks at which the constructive interferences occur. The conditions of resonance are periodic and depend on the wavelength, refractive index, width of the cavity and on the refracted angle of the incident rays. A change on

the other, then the inferred Stokes vector will be corrupted by an artificial contamination among different Stokes components. Such a displacement can be originated as a consequence of the atmospheric *seeing* and/or of mechanical vibrations of the telescope (*jitter*) that induce instabilities on the image position.

Table 1.1: Main characteristics of some solar etalon-based instruments. From lef to right: the name of the instrument, the configuration employed (collimated or telecentric), its resolving power ($\mathcal{R}$), the number of etalons included, their diameter (in mm), whether the instrument employs dual-beam techniques or not, and the corresponding f-number at the etalon location if telecentric.

Instrument	Conf.	$\mathcal{R}$	# of FPs	Diam.	Dual beam	$f\#$
IPM	Tele	$> 250,000$	1	50	No	192
TESOS	Tele	$\sim 300,000$	3	50	No	125/265
IBIS	Coll	$> 200,000$	2	50	No	-
CRISP	Tele	$\sim 100,000$	2	75	Yes	150
IMaX	Coll	$\sim 80,000$	1(2)	60(25)	Yes	-
GFPI	Coll	$\sim 100,000$	2	70	Yes	-
PHI	Tele	$\sim 60,000$	1	~ 50	No	56/63
VTF	Tele	$\sim 100,000$	1-2	250	No	200

the width, index of refraction or the incident direction, can be employed to tune the peaks, although only variations on the two former parameters are usually preferred to use the etalon as an spectrometer. In fact, the relative shift of the transmission peak wavelength is simply given by the relative change on the refractive index, n', and/or on the thickness, h. Since the relative change in wavelength necessary to scan a spectral line is typically less than 0.01%, a highly stable control of the width and refractive index is crucial for an accurate wavelength sampling. Changes on the direction of the incident light must be minimized too, since the transmission resonances suffer from a displacement to shorter (bluer) wavelengths that increases in a roughly parabolic fashion with the incidence angle (Figure 1.2).

The spectral resolution of the Fabry-Pérot also varies with the etalon parameters and with the incidence angle, but in a much lesser extent. More important is the widening of the transmission profile that arises when the etalon plates and/or cavity suffer from imperfections (*defects*). Defects are originated from inhomogeneities in the refractive index (or in the coating) and from variations on the flatness and parallelism of the etalon plates, both of which displace the transmission profile locally. The average result of having individual shifts that vary from point to point across the etalon aperture is a broadening of the transmission profile bandpass that diminishes the resolving power of the filter. The phase of the transmitted electric field is also affected by defects. Errors in the phase reduce the optical quality of
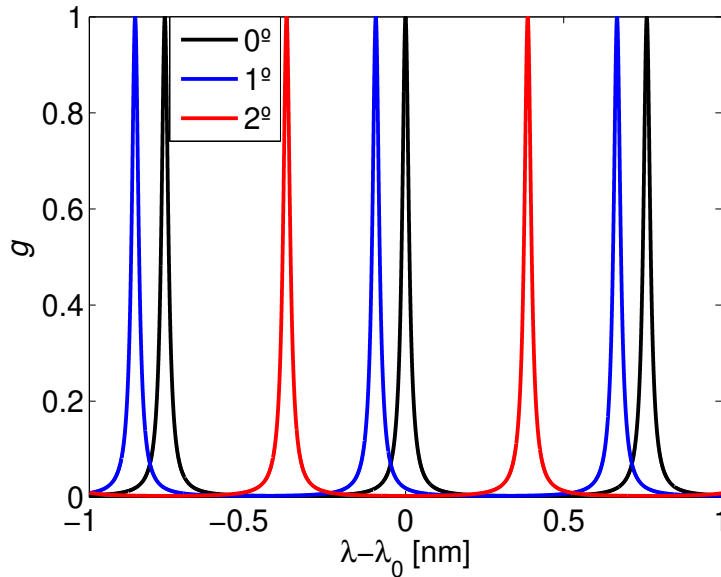
Figure 1.2: Example of the periodic spectral transmission profile, g, typical of a Fabry-Pérot in a narrow window of ± 1 nm about the central wavelength at which the etalon is tuned for on-axis illumination, λ_0. Profiles at incidences with respect to the normal of $0°$ (black), $1°$ (blue) and $2°$ (red) are displayed. Note that the resonances are shifted in a non-linear (almost quadratic) way with the incidence angle. Figure extracted from Bailén et al. (2019a). © AAS. Reproduced with permission.

the transmitted wavefront. Contrary to other filters, the large number of reflections of the wavefront that take place within the optical cavity of the etalon cause an over amplification of the degradation that increases rapidly with the reflectivity and that must be limited to achieve diffraction-limited quality (e.g., Kentischer et al., 1998; Scharmer, 2006).

Errors can be divided in two main categories: large-scale and small-scale defects. The former usually increase with the size of the etalon aperture and appear during the manufacturing process or or simply because of stress tensions caused by the coatings, by the force gravity or by the mechanical pressures (Greco et al., 2019). These errors are usually dominated by a radial (parabolic) departure of the thickness from the center to the edges —*spherical* or *parabolic defect*— or by a linear change in the thickness from one edge to the other along a given direction —*parallelism defect*— (Reardon & Cavallini, 2008). Meanwhile, small-scale defects are basically polishing errors of high frequency that are approximately randomly distributed following a Gaussian density distribution. A layout of the geome-
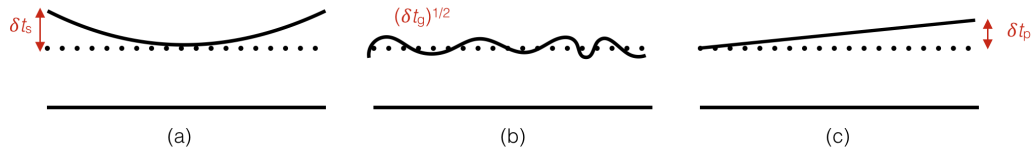
Figure 1.3: Layout of the geometry of the etalon plates when affected by the three most typical defects. From left to right: spherical/parabolic defect with a maximum departure δt_s, Gaussian defect with a root-mean-square deviation across the aperture $(\delta t_g)^{1/2}$, and parallelism defect with an edge-to-edge divergence of δt_p.

tries of the three mentioned defects is displayed in Figure 1.3. Although departures from ideal collimated illumination are not caused by geometric defects, they also broaden the resonances and shift them towards the blue when compared to collimated illumination (e.g., Sloggett, 1984; Atherton et al., 1981). Hence, they are usually treated as another defect —the *aperture defect*—.

1.1.1   Use of etalons as filtergraphs

For Fabry-Pérots to work as tunable filters, isolation of only one resonance order of the transmission profile is mandatory. Otherwise unwanted light from the secondary orders will contaminate the signal and will degrade the spectral purity of the filter. Narrow-band dichroic (interferential) filters with bandpasses comparable to the spectral distance between different peaks of the transmission profile of the etalon (the *free spectral range*) are commonly employed for that purpose. Usually, they are placed prior to the etalon, thus receiving the name of *pre-filters*. The free spectral range (FSR) of the etalon depends quadratically on the wavelength and is inversely proportional to its refractive index and cavity width, but is usually of the order of several Angström. Commercial off-the-shelf dichroic filters are typically broader and custom-made solutions are, hence, normally needed. Pre-filters with good optical quality, high transmission and with such a low bandpass are difficult to manufacture and expensive, though. In addition, even custom-made filters do not offer an absolute out-of-band rejection, since their profile diverges from an ideal rectangular function. Instead, their profile typically resembles that of an imperfect bell-shaped curve with extended wings that let pass some residual light ($\sim 1\,\%$ or more, typically) from the neighboring resonance orders of the etalon (Figure 1.4). Such a spectral contamination is called (spectral) *stray light* or *parasitic*
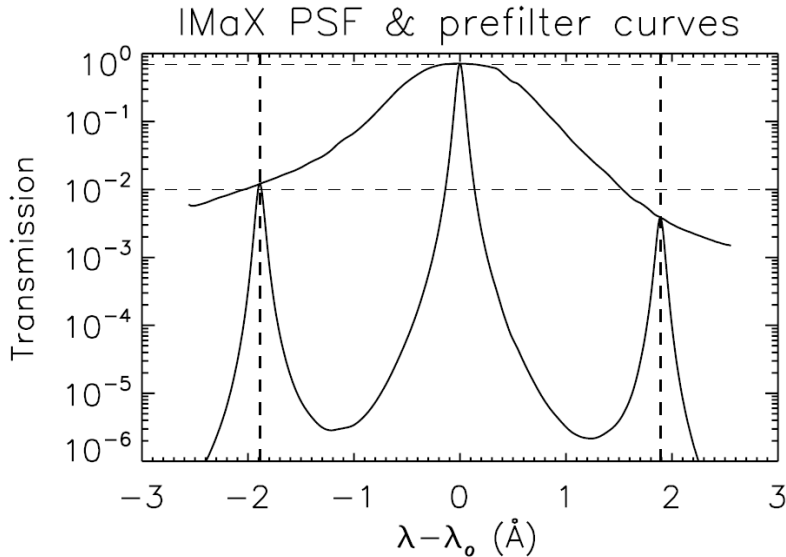
IMaX PSF & prefilter curves

Figure 1.4: Transmission curve (in log scale) of IMaX after including the etalon profile and the measured curve of the pre-filter. The wavelength range covers the main transmission resonance of the etalon at $\lambda_0 = 525.02$ nm and its two closest orders separated roughly ± 1.9 Å and whose peaks are about $1\,\%$ of the maximum transmission. Figure extracted from Martínez Pillet et al. (2011) with permission. Licensed under CC BY 4.0

light and can be minimized by enlarging the FSR or by using two or more etalons with different FSRs. The former is the simplest solution and can be achieved by reducing the cavity spacing, but there are manufacturing, economic and even mechanical constraints that prevent it from being arbitrarily small. Furthermore, reducing the cavity broadens the resolution in an inversely proportional way. A better approach consists in using two or three etalons with a careful choice of their cavities to suppress effectively secondary lobes on the transmission profile (Figure 1.5).

The first instruments that probably used a system of several etalons successfully were IBIS and TESOS with two and three Fabry-Pérots, respectively.[5] The dual-tandem configuration has proven to be the most popular option, though (e.g., IBIS, CRISP, GFPI, and VTF in a future upgrade). The use of several etalons improves not only the FSR, but also the spectral resolution. In fact, if two identical Fabry-Pérots are placed within the optical path, the resolving power is improved up to a factor $\sqrt{2}$, although

---

[5]TESOS initially employed a tandem of two etalons, but it was later upgraded to a three etalon system to reduce even more the spectral parasitic light (Tritschler et al., 2002).
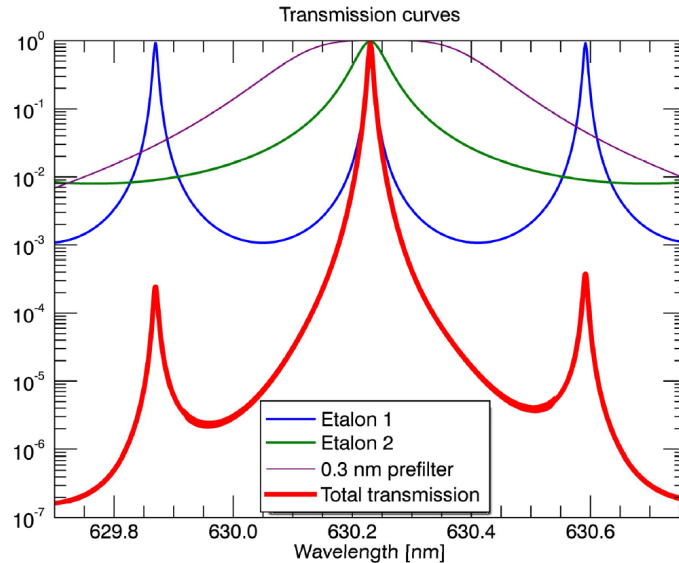
Figure 1.5: Simulated transmission curves of the possible dual-etalon configuration of the VTF instrument. The individual transmission profiles corresponding to a 0.3 nm pre-filter (magenta), the high-finesse etalon (blue), the low-finesse etalon (green) and to the final system (red) are displayed. Note that the relative intensity of the secondary lobes of the total transmission profile are reduced below $0.5 \cdot 10^{-3}$ with respect to the maximum transmission. Courtesy of Schmidt et al. (2016). Reproduced with permission.

the FSR is unaffected (Álvarez-Herrero et al., 2006). An alternative arrangement to improve the resolution while keeping the same FSR consists in forcing the optical beam to go through the etalon twice (*double-pass configuration*). This solution was adopted for IMaX, in which the Fabry-Pérot is followed by a system of two folding mirrors that allow light to pass twice through different subapertures (Figure 1.6).

Since Fabry-Pérots are made of highly reflecting plane-parallel plates, the space between two etalons acts also as a resonant cavity in which multiple internal reflections take place, thus producing a secondary image that is overlapped to the main signal if they are aligned. The spurious image is usually referred as a *ghost image* and contaminates the measured signal, too. There are several ways to get rid of it.

First, the cavities of each etalon can be chosen to reduce to the minimum the amount of ghost signal, but this solution has an impact also on the spectral parasitic light. A rigorous discussion on the best choice of the
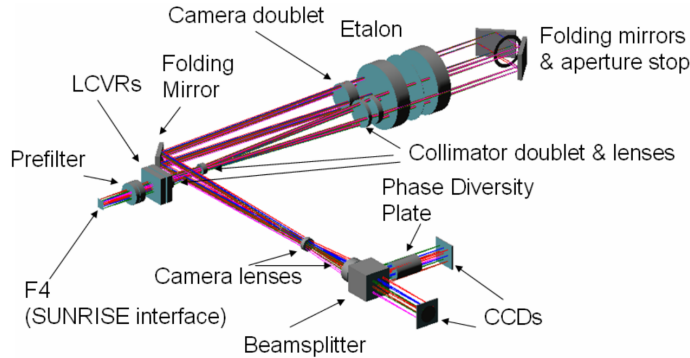
Figure 1.6: Optical layout of the double-pass configuration of IMaX. Light focused by the telescope at F4 passes through the pre-filter and illuminates the modulator of the polarimeter, made of a couple of liquid crystal variable retarders (LCVRs). Light is collimated, then, through one of the subapertures of the etalon by a relay of several lenses. Two folding mirrors reflect the light back and illuminate again the etalon through the second subaperture. A doublet of lenses and a third folding mirror re-direct the light through a camera lens and a beam splitter, which provide images of the two orthogonal polarization components on two different CCDs. Figure extracted from Martínez Pillet et al. (2011) with permission. Licensed under CC BY 4.0.

cavity ratios of the two etalons that reduce both ghost and stray-light contamination can be found in Kentischer et al. (1998), Cavallini (2006), and in Scharmer (2006). The optimum ratio have been found to be either ~ 0.3 or ~ 0.6, although the precise value depends on each particular instrument. Nevertheless, even if the ghost signals are minimized by an accurate choice of the cavity ratio, the spurious signals can be prohibitively large to achieve stringent polarimetric sensitivities of 10^{-3} (Scharmer, 2006). A very effective way to reduce ghost signals farther consists in placing a low-transmission pre-filter between the two etalons. Then, their intensity is reduced by a factor T_{pf}^2, where T_{pf} is the maximum transmission of the filter (e.g., Scharmer, 2006). This solution was implemented in IBIS, whose pre-filter reached a maximum transmission of only $T_{\mathrm{pf}} \simeq 30\,\%$. Nowadays, interferential filters with much higher transmittances ($\sim 80\,\%$) can be manufactured. Deteriorating intentionally the flux of photons to deal with ghost images increases the observation time needed to accomplish the same signal-to-noise ratio, thus limiting the observation of fast events. For this reason, the prospects of this approach in the next generation of instruments are

unclear. A more effective way of dealing with this problem is probably the one employed in CRISP and (before its upgrade to a triple-etalon system) in TESOS, in which one of the two etalons is tilted with respect to the other.[6] That way, instead of reducing the ghost signal, it is moved directly out the instrument detector. Obviously, other problems arise when adopting this solution, as it will be explained later.

1.1.2 Two configurations: general

Historically, there have been two ways to illuminate the etalon in solar instruments: collimated (e.g., Bendling et al, 1992; Martínez Pillet et al., 2011) and telecentric (e.g. Kentischer et al., 1998; Solanki et al., 2020). The most adequate choice of the configuration has been subject to debate for decades and it continues today, since the performance of each one is inevitably limited in distinct ways. Extensive analyses on the influence on the spectral and imaging properties of both setups can be found in Beckers (1998), von der Lühe & Kentischer (2000), Kentischer et al. (1998), Cavallini (1998), Cavallini (2006), Scharmer (2006), and Righini et al. (2010).

The collimated configuration is characterized for having the Fabry-Pérot overlapped to the pupil (or one of its images) and illuminated with a parallel beam of rays with various incident directions, each one corresponding to different points of the object field (Figure 1.7, left). Examples of instruments that opted for this arrangement are IBIS, IMaX, and GFPI. Placing the etalon on a pupil image has the advantage of maintaining always the same area illuminated. In other words, the *footprint* of the incident beam does not change across the field of view (FoV). In return, the variation of incidence angles on the etalon over the FoV shifts the transmission profile peak across the image plane. The main consequence is a field-dependent sampling of the observed spectral line: at the edges of the image the interferometer is tuned to shorter wavelengths of the spectrum than at the center. Fortunately, the displacement on the transmission profile can be calibrated easily as long as it is kept smaller or comparable to the spectral sampling interval of the instrument (e.g., Cavallini, 2006). In addition, since the etalon is at the pupil and the footprint of the incident beam does not change across the FoV, large local errors and aesthetic defects like dust are smoothed out when averaging across the aperture. The optical quality of

---

[6]After the modification of TESOS from a dual-etalon system to a triple-etalon configuration in 2000, the relative tilt of the Fabry-Pérots was suppressed. Instead, the three etalons were aligned accurately to overlap the ghost images and a pre-filter between the first and second etalon was included, followed by and additional blocking filter between the second and third etalon, to reduce their intensity in a similar manner as in IBIS.
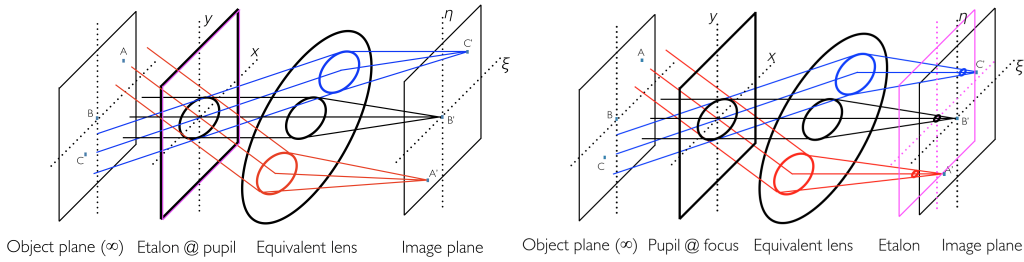
Figure 1.7: Schematic view of the collimated configuration (left) and the telecentric one (right). Figure extracted from Bailén et al. (2019a). © AAS. Reproduced with permission.

the interferometer is preserved constant across the image, too. In exchange, individual plate errors and inhomogeneities across the whole clear aperture of the cavity have an impact on the transmitted wavefront over the whole FoV.

In the telecentric configuration, the etalon is located at an intermediate image plane of the instrument and the entrance pupil (or one of its images) is placed at its object focal plane (Figure 1.7, right). This way, the chief ray —which, by definition, passes through the enter of the entrance pupil— comes out parallel to the optical axis no matter the incident direction. In consequence, the etalon is illuminated uniformly across its aperture when observing an homogeneous object and no shifts of the spectral transmission occur across the FoV (ideally). Another important feature of this setup is that the footprint of the incident beam on the etalon is much smaller than in the collimated case —typically ~ 1mm (e.g., Cavallini, 2006)— but the illuminated area of the etalon changes across the FoV. Small individual defects on the etalon with millimiter sizes are, then, projected onto the final image plane and change the point-spread-function (PSF) and the transmission profile point to point. In return, the impact of errors on the wavefront is minimized as long as the footprint is kept small enough, since large-scale defects have no influence across the footprint. IPM, TESOS, CRISP, PHI and VTF benefit from this arrangement.

The finite aperture of the incident cone of rays imposes a limit on the maximum spectral resolution of the transmission profile even if the etalon were free of defects, though (e.g. Atherton et al., 1981). Illuminating each point of the etalon with rays that come from the pupil with different angles means also that, for a given monochromatic wavelength, the pupil is "seen" by the Fabry-Pérot as if it were inhomogeneously illuminated (Beckers, 1998). The effect is commonly referred to as *pupil apodization* and varies rapidly along the bandpass of the etalon (Figure 1.8). The apodization of
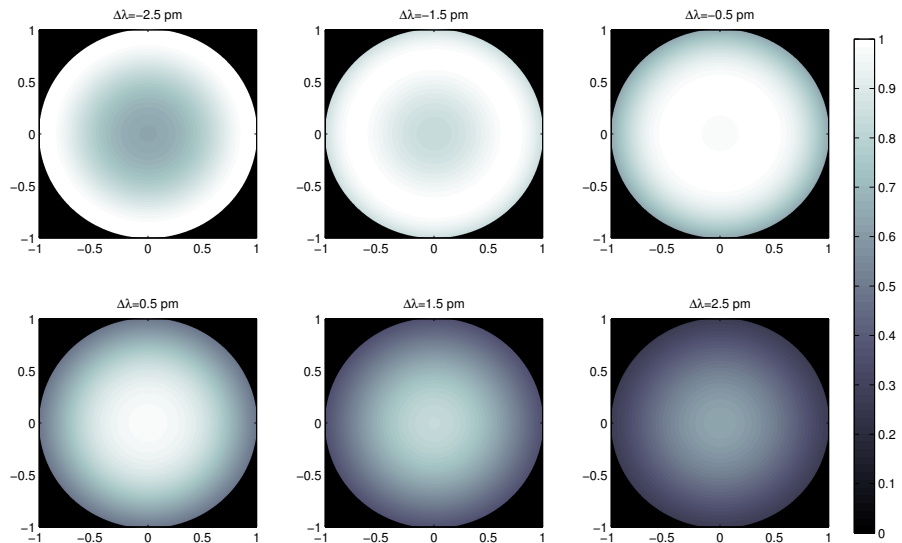
Figure 1.8: Simulated pupil apodization corresponding to an $f/150$ telecentric etalon with a 4 pm resolution at different monochromatic wavelengths from its wavelength peak (617.3 nm): $-2.5, -1.5, -0.5, 0.5, 1.5,$ and 2.5 pm.

the pupil changes the monochromatic PSF in an asymmetric way across the transmission profile of the etalon . The asymmetry over the spectral profile caused by the different illumination of the pupil brings about undesired signals when measuring the spectrum of the Stokes vector that can exceed the polarimetric sensitivity requirements of the instrument (e.g. Beckers, 1998; Kentischer et al., 1998; von der Lühe & Kentischer, 2000; Scharmer, 2006). Pupil apodization is very dependent on the f-number of the incident beam and on the resolution of the instrument, since the thinner the spectral bandpass of the etalon and the larger the incidence angles, the more important is the change of intensity at a monochromatic wavelength across the pupil. Pupil apodization can be minimized, then, by using crystalline etalons (which reduce the refracted angle of the rays), by sacrificing resolving power or by illuminating the etalon with very large f-numbers. The latter is the solution most commonly adopted. Unfortunately, the size of the instrument and of the etalon itself increase linearly with the f-number of the incident beam. Hence, apertures limited to $f/100 - f/200$ are commonly employed to achieve a compromise between the magnitude of the spurious signals and the size and cost of the instrument (Table 1.1).

1.1.3 Degradation of the PSF and spectral profile

Perturbations in the PSF and in the spectral profile have an impact not only on both the image quality and the spectral resolution of the instrument, but also on the measured spectrum of the polarization state of light. Since the spectral dependence of the Stokes vector codify physical properties of the solar atmosphere, such a contamination is directly transferred to the quantities inferred from it. Regarding the above-mentioned pupil apodization effects, the first work to address consequences of the spectral dependence of the PSF across the bandpass of the etalon characteristic of telecentric etalons was the one by Beckers (1998). He showed that the PSF width decreases at wavelengths towards the blue of the transmission peak at the expense of transferring the energy to its wings, whereas towards the red part of the passband the opposite is true: the core of the PSF gets broader while the lobes are reduced to conserve the total energy enclosed by the PSF (Figure 1.9). According to his numerical estimations, the contamination introduced by such an asymmetric spectral response could be as high as 30 ms^{-1} in regions with no real Doppler shifts. Such signals are impossible to correct fully with post-processing techniques of the measured data and led him to conclude that collimated setups should be used in magnetographs that aim to the highest performance. Although the quantitative predictions of Beckers (1998) on the spectral behavior of the PSF in a telecentric mode were correct, he did not consider fluctuations on the phase of the transmitted electric field (*phase errors*), but only the changes in the module of the electromagnetic field originated by pupil apodization. Phase errors were included later by von der Lühe & Kentischer (2000), who showed that they foster the transfer of energy between the central part of the PSF to its lobes. Phase fluctuations evaluated at the strictly monochromatic wavelength of the maximum of the transmission profile exhibit a parabolic trend with the radial coordinate of the pupil. Therefore, a refocus of the final image plane in the way described by Scharmer (2006) can be carried out to correct them, at least to some extent, since their radial dependence is not necessarily that simple at other wavelengths across the transmission profile.

Etalon defects and imperfections from ideal telecentrism deteriorate the optical performance of telecentric etalons even more. On the one hand, local errors on the thickness and/or the cavity homogeneity with sizes comparable to the footprint of the incident beam invalidate the use of a PSF from a strict point of view, since the response of the etalon is expected be field dependent then. The same occurs with the spectral transmission, thus losing this mount one of its main (ideal) advantages over the collimated
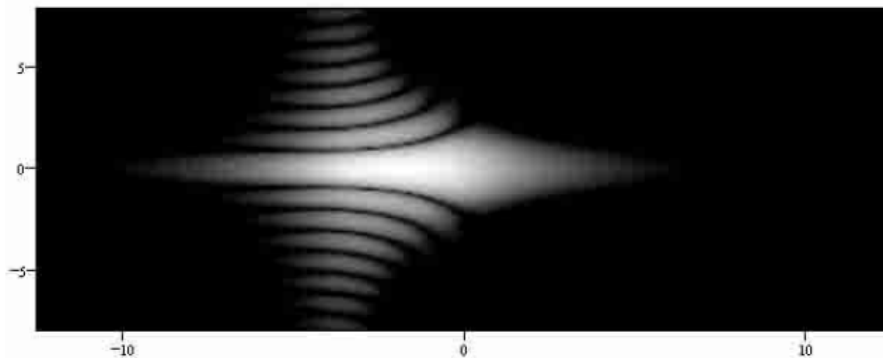
Figure 1.9: Cross section in logarithmic scale of the modeled PSF of the telecentric TESOS $f/128$ mode across a spectral band of ± 15 pm around the peak of the transmission profile (at 500 nm), illustrating the spectral behavior of the PSF across the transmission profile predicted by Beckers (1998). Credit: von der Lühe & Kentischer (2000), reproduced with permission © ESO.

mode: the preservation of the same spectral response across the FoV. The field-dependent variations of the PSF and bandpass of the etalon can be smoothed out by defocusing the Fabry-Pérot, which necessarily increases the footprint of the incident beams and averages local errors over a larger area. In return, the impact of defects on the wavefront will increase. On the other hand, errors on the telecentrism provoke a relative tilt among the incident chief ray and the normal of the etalon plates that vary over the FoV. The imperfection can arise because of departures from first-order optical properties (paraxiality) or from deviations of the optical elements from their nominal position, both occurring in real instruments. The loss of the axial symmetry on the pupil apodization by the off-axis incidence of the chief ray on the etalon induces field-dependent asymmetries, broadenings and shifts on both the PSF and the transmission profile that cannot be compensated by refocusing the etalon.

Deviations on the incidence of the chief ray from normal illumination of the etalon plates also occurs when tilting the Fabry-Pérot to move ghost images out from the image sensor of the instrument, with an equivalent impact on the PSF and transmission profile, but constant across the FoV in this case.[7] Since pupil apodization effects are strengthened with increasing

---

[7]We name indifferently "imperfect telecentrism" throughout this thesis to any loss of radial symmetry on the illumination of a telecentric etalon arising from either a tilt of the Fabry-Pérot or by deviations of the chief ray over the FoV from normal illumination, since the consequences of both are the same in the PSF and in the spectral profiles.

resolving powers, the tilt should be kept as close as possible to the limiting value that ensures that the ghost image is moved away from the detector. Moreover, in dual-etalon instruments the Fabry-Pérots are preferred to have different spectral resolutions to apply the tilt to the one with lowest resolution (Scharmer, 2006). Still, asymmetries in the PSF and in the spectral profile cannot be eliminated completely as long as one etalon is tilted. Besides, in systems with multiple etalons, a field-dependent detuning of the transmission profiles is produced by the local differences in their individual cavity maps. The detuning adds another contribution to the total shift and the asymmetry of the final transmission profile that changes locally. The former can be corrected through flat-fielding procedures during the data processing pipeline, but calibration of point-to-point asymmetries requires more sophisticated reduction methods (e.g., de la Cruz Rodríguez et al., 2015).

In collimated instruments, cavity errors and inhomogeneities are smoothed out across the clear aperture of the etalon and the wavelength-dependent artifacts on the PSF do not appear at all. Unfortunately, wavefront errors caused by plate defects are expected to be amplified more than in the telecentric case, in general. The reason for this is that the footprint of the incident beam is much larger and encompasses not only small-scale defects, but also large-scale errors, whose magnitude might be comparable or even larger (e.g. Schmidt et al., 2016). Besides, the response varies across the FoV because of the different incidence angles on the etalon, like in the (real) telecentric configuration, although in this case the spatial shape of the monochromatic PSF is preserved and the loss of invariance comes only from a shift of the transmission profile towards the borders of the image.

The presence of asymmetric defects of large scale due, for instance, to local stresses caused by the piezo electric actuators used to control the etalon width, is responsible also for an asymmetrization of the transmission profile when a system of multiple etalons is used, since the final transmission profile is no longer given by the product of the individual spectral profiles, but by the average of the product of the local individual transmissions (Reardon & Cavallini, 2008). Even more important is probably the differential shift among the individual transmissions of the etalons when one of them is tilted to suppress ghost images (Cavallini, 2006; Scharmer, 2006). The relative spectral detuning arises from the difference in incidence angles on each etalon and produces a field-dependent asymmetry on the transmission profile and a shift similar to the one occurring in a tandem of telecentric etalons because of local changes on the optical cavity map. The difference being that in this case the dependence with the field can be modeled in a known way. Instead of tilting one etalon, the aforementioned solution

of placing a pre-filter with low transmission among etalons proposed by Cavallini (2006) can be applied to reduce the inner-etalon ghost signal intensity without detuning the etalons. However, apart from deteriorating the flux of photons, introducing the pre-filter between the two etalons in a collimated beam has an additional problem: it must be of the same size of the etalons ($\gtrsim 50$ mm). Such large interference filters are difficult to manufacture with reasonable optical qualities of $\sim \lambda/20$ or better to achieve diffraction limit performance of the instrument. The maximum of its transmission profile would also shift differently across the FoV with respect to those of the etalons because of the unavoidable difference in the indices of refraction, which cause a distinct response with the incidence angle. The impact of such a displacement on the transmission profile induces, again, field-dependent asymmetries and shifts of the total transmission. To minimize the relative variation of the the profiles over the FoV, a *pupil adapter* (e.g., Greco & Cavallini, 2013) should be employed to reimage the pupil on the pre-filter with different size, thus changing the maximum incidence on the pre-filter according to the Lagrange invariant to produce a similar wavelength shift. The trade off for using an adapter is that it adds more optical elements, with the consequent impact on the optical quality and, especially, on the size of the instrument.

Among the mentioned drawbacks of the collimated mode, the most critical to tip the scales in favor of the telecentric configuration is probably the over amplification of plate defects and inhomogeneities of the cavity due to the multiple reflections of the wavefront. A quantitative assessment on this topic was studied first by Ramsay (1969) and then by von der Lühe & Kentischer (2000), both considering strictly monochromatic incident collimated beams. Later, Scharmer (2006) included the effects of integrating over the whole spectral bandpass of the etalon and found that the polychromatic nature of the observations relaxes the amplification of errors approximately to a half. Still, the results of von der Lühe & Kentischer (2000) and Scharmer (2006) are pessimistic about the use of a collimated configuration and suggest the use of the telecentric solution to achieve diffraction-limited performance, contrary to Beckers (1998).

The predictions of Scharmer (2006) seem too hopeless to us, since his conclusions are based on considering highly-reflective etalons that suffer from (incorrigible) microroughness thickness deviations with a root mean square (RMS) value of 2 nm, while etalons with errors in the range of $0.5-1$ nm (including large-scale defects) are feasible to manufacture nowadays, at least for etalons of modest sizes of the order of 50 mm (e.g., Álvarez-Herrero et al., 2006; Greco et al., 2019). Furthermore, part of the wavefront deformation can be compensated for by refocusing the etalon, especially the
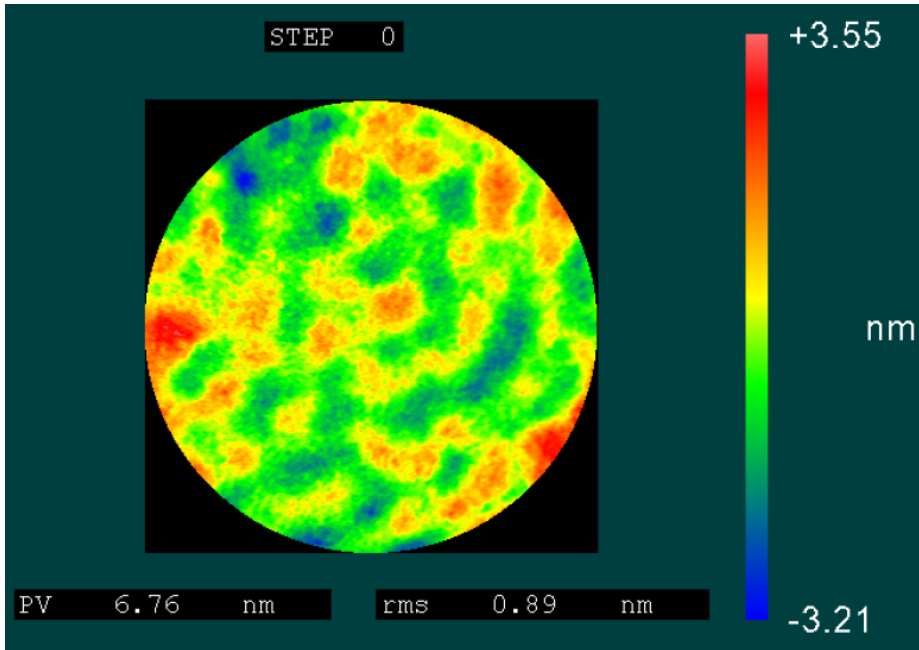
Figure 1.10: Cavity error map measured for an ICOS ET50 model etalon (50 mm diameter) after correction of the parallelism defect through the individual control of piezo-electric actuators. The resulting RMS of the cavity errors is about 0.9 nm, including both small-scale and the remaining uncorrected large-scale defects. Credit: Greco et al. (2019), reproduced with permission © ESO.

commonly dominant parabolic defect contribution. Departures from parallelism can be addressed, too. In fact, an effective method to correct dynamically the loss of parallelism in servo-controlled etalons has been presented recently Greco et al. (2019). Figure 1.10) shows an example of the cavity error map measured by Greco et al. (2019) after applying their tilt correction technique to a real 50 mm etalon etalon. The residual large-scale and small-scale contributions are only ~ 0.6 nm and ~ 0.7 nm, respectively, summing a total of ~ 0.9 nm RMS error.

Excluding the parabolic and parallelism defect, residual errors of the order of ~ 0.5 nm or so —four times smaller than the ones modeled by Scharmer (2006)— seem, then, feasible to achieve (e.g., Reardon & Cavallini, 2008; Greco et al., 2019). Novel manufacturing techniques can minimize microroughness defects even more, although at the expense of increasing dramatically their cost. Such is the case of the large mm VTF etalon, whose microroughness plate errors are smaller than 0.4 nm RMS across its large 250 mm aperture (Sigwarth et al., 2016). Of course, other more com-

plex large-scale variations of the geometry apart from the parabolic and parallelism defect are usually present and have not been corrected so far (Reardon & Cavallini, 2008; Greco et al., 2019). Sometimes their magnitude is similar or larger than the one of microroughness errors, which could prevent the optical performance of the etalon to reach the diffraction limit, but we believe that, in general, it should not be stated that collimated etalons are not suited for diffraction-limit applications. Instead, it is crucial to explore whether tight requirements on the small-scale and the contributions of large-scale defects that are impossible to correct can be accomplished by the manufacturer or not. It is also mandatory to characterize in detail the cavity map of defects once supplied by the manufacturer, since cavity geometries can vary substantially even among similar etalons produced by the same company (Greco et al., 2019).

1.2   Crystalline etalons

Typically, etalons are controlled by piezo-electric (servo-controlled) actuators that accurately adjust the width of the cavity for tuning purposes (e.g., Kentischer et al., 1998; Puschmann et al., 2006; Scharmer et al., 2008). However, there is an alternative form to change the cavity of the Fabry-Pérot: crystalline etalons can be tuned by applying an electric field only. Such etalons are filled with a crystal that lacks a center of symmetry (*non-centrosymmetric*) and exhibits therefore linear (Pockels) electro-optical and piezoelectric properties that allow for a change of both the refractive index and the cavity width in the presence of a differential voltage between the cavity plates. The main advantages of crystalline etalons is that (1) they prevent from vibrations of the etalon caused by the mechanical actuators and (2) their weight is low, both features being very appreciated in space applications.[8] Currently, $LiNbO_3$ is the material *par excellence* in space instrumentation (Martínez Pillet et al., 2011; Solanki et al., 2020). Other crystals, such as MgF_2 have been employed in space etalons too, but only combined with piezo-electric actuators (Gary et al., 2006). An additional asset of these etalons is that they have a refractive index that is usually much larger than that of air ($\sim$ 2.3 in $LiNbO_3$), thus reducing the refracted angle within the cavity and therefore the shift of the transmission profile across the FoV characteristic the collimated configuration and pupil apodization effects in case the etalon is mounted on a telecentric setup (e.g.

---

[8]Michelson interferometers have also been employed successfully in space-born applications (Scherrer et al., 1995, 2012), but they present other drawbacks mentioned in Section 1.1.

Debi Prasad & Gosain, 2002). Solid etalons provide also more stability on the degree of parallelism between the reflecting plates during the spectral scanning compared to servo-controlled etalons (e.g., Greco et al., 2019).

One of their most important problems is probably that the tuning speed of the etalons is slow compared to that of piezo stabilized Fabry-Pérots. For instance, LiNbO$_3$ etalons reach maximum tuning speeds of the order of 0.5 Ås^{-1} (Martínez Pillet et al., 2011), whereas servo-controlled Fabry-Pérots are about one to three orders of magnitude faster. They also need very high voltages —of the order of a few thousand volts— to scan a whole spectral line and they are very sensitive to small variations of the temperature, so they must be controlled thermally.[9] When used in balloon-borne instruments they shall be pressurized too, in order to avoid electrical arc discharges originated by the dielectric breakdown of the surrounding air, occurring at millibar pressures (Martínez Pillet et al., 2011).

The majority of noncentrosymmetric crystals are anisotropic, with the important exceptions of the materials that belong to the cubic system, such as GaAs, which are isotropic. In fact, crystals belonging to the trigonal, tetragonal and hexagonal systems (e.g., LiNbO$_3$) are uniaxial —i.e., they have a preferred direction along which electromagnetic waves propagate as if they were in an ordinary isotropic medium—, whereas those categorized within the orthorombic, monoclinic or triclinic system are biaxial. As anisotropic materials, they can change the polarization state of light. In other words, they are *birefringent*. Crystals with a unique optical axis oriented orthogonally with respect to the etalon plates are preferred, since birefringent effects can be minimized simply by illuminating them with beams as close to the normal of the reflecting plates as possible (Martínez Pillet et al., 2011; Solanki et al., 2020). Etalons with such an orientation of the optical axis are said to have a *Z*-cut configuration, as opposed to the *Y*-cut arrangement, in which the optical axis is parallel to the plates (e.g., Netterfield et al., 1997).

1.2.1   Anisotropy as a source of artificial signals

Even when the *Z*-cut configuration is chosen to avoid birefringent effects, etalons are illuminated by either converging (telecentric) light or with collimated light with incidence angles that vary over the FoV. Cross-talks among different Stokes parameters that can corrupt the measurement of

---

[9]The voltage and temperature tuning constants of LiNbO$_3$ are ~ 0.3 mÅ V^{-1} and ~ 40 mÅ K^{-1}, whereas the maximum voltage and tuning speeds limits recommended by the manufacturer for IMaX and PHI etalons are ± 3 kV and 1.5 kVs^{-1}, respectively (Martínez Pillet et al., 2011; Solanki et al., 2020).
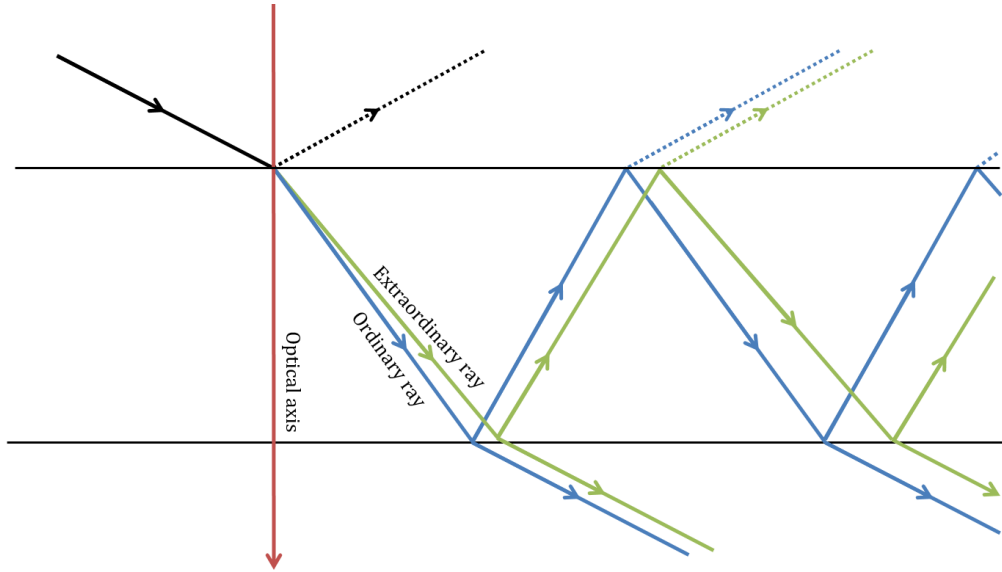
Figure 1.11: Scheme of the propagation for an off-normal ray in a Z-cut etalon. The ray is split into two orthogonal components: the ordinary and the extraordinary rays. Each one travels along different directions and at a different speeds. The difference in optical paths traversed by the two components produce a retardance in the optical phase between both rays that is responsible for a change on the polarization state of the transmitted light. Figure adapted from Bailén et al. (2019b). © AAS. Reproduced with permission.

the polarization state of light are, then, expected (Figure 1.11). When considering local defects of the etalon, such a contamination is field-dependent even in an ideal telecentric setup. Birefringent effects can also appear even in normal illumination conditions due to the existence of local regions in which the optical axis is misaligned with respect to the Z direction (*local domains*). Such deviations may appear during the manufacturing or from hysteresis processes that can take place when fed with very high voltages. The latter effect has been observed in the spare $LiNbO_3$ etalons of the PHI instrument when voltages of ~ 4 kV or more are applied.

The impact of the anisotropy is different also in each optical configuration: collimated or telecentric. When the collimated configuration is chosen, the direction of the incident beam varies for each point of the observed object field and, with it, the birefringence induced in the etalon. For this reason, its Mueller matrix is expected to change from point to point across

the field.[10] In an ideal telecentric configuration the response of the etalon would be constant along the FoV, but imperfections on the illumination and defects on the crystal or in the plates of the etalon cause a field-dependent polarimetric response of the etalon if this configuration is used, much like in the collimated case. Moreover, deviations from perfect telecentrism, or tilts of the etalon to deal with ghost images, are responsible for an asymmetric spectral performance of the Mueller matrix, similar to the one appearing in the transmission profile of isotropic etalons.

Fortunately, the etalon is always placed either between the modulator and the analyzer of the polarimeter (e.g., IMaX) to allow for the use of dual-beam methods with a single etalon, or right after the polarimeter (e.g., PHI). If the etalon is placed within the polarimeter, the modulation of the incident illumination on the etalon and the presence of a linear polarizer right after the etalon are expected to moderate somehow birefringent effects. Birefringent problems disappear or are minimal when the etalon is situated in the optical path after the polarimeter, but at the cost of eliminating the possibility of benefiting from a dual-beam configuration, unless two identical etalons are used, one for each of the channels of the instrument, with the subsequent increase in cost, weight and difficulty to calibrate, operate and interpret the data retrieved by the instrument. In any case, the polarimetric response of the etalon must be taken into account combined with that of the rest of the instrument in order to minimize its influence or, at least, to calibrate it.

An experimental evaluation of the influence of the birefringent properties of a uniaxial (liquid crystal) Fabry-Péróts on the transmission profile can be found in Vogel & Berroth (2003), while numerical algorithms that model the propagation of electric fields in crystalline etalons is performed in Zhang et al. (2017).[11] Meanwhile, studies on the artificial signals that take place because of the polarimetric properties of the multilayer plate coatings has been carried out numerically by Doerr et al. (2008) and Ejlli et al. (2018). According to Doerr et al. (2008), the largest deviation on the PSF introduced by the birefringence of the coatings is only of the order of 10^{-6}

---

[10]The Mueller matrix of a system represents its (linear) response to the incident polarized light with a given Stokes vector through a 4×4 tensor. For farther information on the Mueller matrix formalism, we refer the reader, for instance, to Del Toro Iniesta (2003).

[11]Fabry-Peróts based on liquid crystals have not been employed in solar instruments yet because of the inherent problems of this technology. In particular, the direction of their optical axis changes when tuned, and with it their birefringent properties. They also suffer from a non negligible absorptivity that reduces considerably the maximum achievable transmission.

for etalons illuminated with typical incidence angles characteristic of solar instruments. The influence of crystalline etalons in spectropolarimeters was carried out by Del Toro Iniesta & Martínez Pillet (2012), who considered the effect of solid etalons by postulating that their Mueller matrix is simply given by the sum of a retarder and a mirror. With this premise, they demonstrated analytically that a spectropolarimeter formed by a set of two nematic LCVRs as modulator, a birefringent Fabry-Pérot as tunable filter and a linear polarizer as analyzer can still reach the maximum polarimetric efficiencies with proper modulations of the pair of LCVRs. However, formal derivations of the Mueller matrix of crystalline etalons that take into account the full nature of the problem are still inexistent, up to our knowledge. Hence, the influence of the birefringent properties of solid Fabry-Pérots in magnetographs can be modeled only to some extent.

Motivation and goals

2.1 Motivation

In our opinion, the influence of etalons in imaging spectropolarimeters needs to be revisited and assessed to its full extent. In particular, we believe that there are still some open questions that need to be addressed:

Impact of defects   There are many different approaches to describe the degradation of the spectral resolution caused by defects (e.g., Chabbal , 1953; Meaburn, 1976; Hill, 1963; Sloggett, 1984; Hernandez, 1988), but most of them are either limited to the case in which the broadening of the spectral profile is very large compared to the ideal case (e.g., the *limiting* finesse of Chabbal , 1953) or they are only valid to air-gapped etalons (e.g., the *aperture* finesse of Atherton et al., 1981). Moreover, the manner different types of defects contribute to the final transmission profile remains controversial. The usual approach consists in adding quadratically the RMS contributions of various types of defects to estimate the *effective* broadening of the profile. However, as explained by Sloggett (1984), this is not strictly correct since the distribution function of the different type of defects is not Gaussian in general — and, hence, they are not statistically uncorrelated—. Instead, he proposed to weight each type of defect with and *ad hoc* factor that depends on its magnitude to permit the quadratic sum of the defects. His method provides consistent results and can be generalized easily to crystalline etalons, but it is ignored in most of the works we have reviewed so far.

Wavefront deformation on telecentric mounts   The formulas relating cavity errors with the wavefront quality found by Ramsay (1969), von der Lühe & Kentischer (2000) and Scharmer (2006) are just valid for collimated etalons. As far as we know, only qualitative estimations have been presented so far on the impact of defects in the wavefront for telecentric mounts (e.g., Righini et al., 2010). Typical footprints of a few millimeters on the etalon plates —comparable or larger than the typical sizes of small-scale defects— are, however, common in the telecentric configuration, and they could have a considerable influence on the wavefront.

Analytic formulation of telecentric etalons   An analytical solution of the electric field equation for telecentric etalons has not been found yet, to our knowledge. The benefits of having access to compact analytical expressions of the transmitted field in such mounts are countless. Some of them are sensitivity analyses, like the ones needed to address the wavefront

deformation mentioned above, or onboard calibrations of space-borne instruments, in which evaluating numerically the electric field point-to-point is a heavy task from a computational perspective that consumes considerable resources and time.

Imperfections in telecentrism While the qualitative impact of having an asymmetric pupil apodization produced by a tilt of the etalon or by departures from ideal telecentric illumination is clear, we miss the existence of quantitative studies on the deformation of the PSF and the transmission profile, since deviations of a few tenths of degree —found in real instruments— could very well induce unacceptable asymmetries and field dependencies in the profiles, especially in instruments with tight spectral resolutions.

Polarimetric response of solid etalons To our knowledge, the only analytical study that takes into account the polarimetric properties of birefringent etalons is the one by Del Toro Iniesta & Martínez Pillet (2012), who assumed the etalon to behave as a combination of a retarder and a mirror. Their model is probably too simple, though, as the etalon response is neither simply that of a retarder followed by a mirror, nor spectrally flat. Instead, the polarimetric properties of birefringent etalons are expected to show very strong dependencies with wavelength. This complicates the calibration of the instrument, since it is not possible to eliminate their influence simply re-adjusting the modulation scheme of the polarimeter.

Effect of pupil apodization The evaluation carried out by Beckers (1998) on the spurious plasma velocities arising in telecentric mounts is merely an estimation based on convolving the PSF with a synthetic Gaussian-like spectral line and subtracting the signals at two different points at its wings. Later works have followed similar approaches (e.g., von der Lühe & Kentischer, 2000), but the full nature of the observations is far more complex, since the spectral and spatial information of the solar scene is correlated and changes point to point. Moreover, since both the imaging and the polarimetric properties of the etalon varies spectrally, the integrated quasi-monochromatic response of the instrument depends on the object itself no matter the chosen setup, collimated or telecentric —i.e., the etalon has an influence on the measured Stokes vector that comes from the correlation among the observed object and its response—. This relation holds for both isotropic and anisotropic etalons and is impossible to calibrate to its full extent with usual flat-fielding methods.

Collimated or telecentric?   The opposite conclusions of different authors regarding the use of collimated or telecentric setups are somehow biased and hamper proper comparisons among the two mounts. For instance, the work of Beckers (1998) advocates for the collimated configuration without evaluating the possible over amplification of the wavefront introduced by cavity errors in collimated setups, whereas von der Lühe & Kentischer (2000) and Scharmer (2006) stand up for the telecentric configuration, but they do not discuss in detail neither the consequences of having an unavoidable different point-to-point response in such mounts nor the possible degradation produced by the small, but finite, footprint of the incident beam on the etalon.

2.2   Goals

The aim of this thesis is to provide both qualitative arguments and quantitative tools to analyze the imaging, spectral and polarimetric performance of etalons in collimated and telecentric configurations, while reviewing and highlighting all the possible benefits and disadvantages studied so far and in here. This work aspires to enrich the understanding of the performance of etalon-based instruments that are nowadays in use, as well as to give farther insight on how to make the difficult decision of choosing which configuration suits the best for each particular application in future instrumentation. With the aim of pursuing these rather ambitious targets, we have divided our specific goals in the following ones:

1. To review and summarize the main results presented by other works so far, emphasizing on the impact of defects. We aim to present a general analytical description on the influence of the various types of defects on the transmission profile taking care of their magnitude and the way they must be added. The found expressions should be compatible with crystalline etalons, too.

2. To tackle quantitatively the impact on both the PSF and the transmission profile of deviations from on-axis illumination of the chief ray in telecentric etalons.

3. To derive an analytical expression of the Mueller matrix of uniaxial etalons valid in general for both collimated and telecentric systems with the purpose of exploring the birefringent effects brought about on the measured spectrum of the Stokes vector, as well as the consequent

spurious signals on the measured maps of the magnetic field and LoS velocities.

4. To accurately assess the artificial signals in the magnetic field and plasma velocities produced by the wavelength dependence of the PSF in telecentric mounts, paying special attention to the loss of symmetry in pupil apodization that results from tilts or deviations of the chief ray direction across the FoV.

5. To derive analytical expressions for the module and phase of the transmitted electric field in telecentric etalons and its derivatives. We pursue to find a general solution valid, at least, for the usual range of apertures employed in solar telescopes.

6. To formulate analytically and evaluate the wavefront deformation produced by defects across the footprint of telecentric etalons through sensitivity analyses of the expressions for the transmitted phase obtained in previous goal.

Methodology

3.1   Evaluation of the spectral and imaging properties of etalons

We begin this thesis with a review of the general properties of etalons, based fundamentally on the description provided by Born & Wolf (1999) and Hecht (1998), summarized in Sects. 2 and 3 of Paper I (Chapter 4). We pay special attention to the treatment of the impact of defects on the spectral profile through a revision of the works of Chabbal (1953), Hill (1963), Meaburn (1976), Atherton et al. (1981), Sloggett (1984), Hernandez (1988), Vaughan (1989), and some of their references therein. We take the general approach of Sloggett (1984), valid for defects showing either a small, intermediate, or large impact on the profile in order to derive expressions for the broadening of the spectral profile produced by the most common defects. The formulation of Sloggett (1984) allows us to extend in a natural way the classical formulae of defects to crystalline etalons. Details can be found in Sect. 4.1 and Appendix A of Paper I.

We follow with a comparison of the collimated and telecentric configurations inspired mainly on the studies of Beckers (1998), von der Lühe & Kentischer (2000), Scharmer (2006), and the notes by our friend and former colleague José Antonio Bonet Navarro. These works focus on the evaluation of the transmitted profile and PSF, with special attention on the properties of the telecentric configuration. We follow their method based on the theory of scalar diffraction to calculate the electric field transmitted at the image plane by a telecentric solid etalon similar to the ones employed in IMaX and PHI. Within this approach, the electric field at the image is simply proportional to the Fourier transform of that at the pupil plane (the Fraunhofer integral), with the Fabry-Pérot working as a pupil mask. In particular, the electric field at the image plane, $\tilde{\mathbf{E}}^{(\mathrm{t})}$, for a monochromatic wavefront impinging normally to the pupil plane, is given by Eq. [48] of Paper I:

$$\tilde{\mathbf{E}}^{(\mathrm{t})}(\xi,\eta) = \frac{1}{\pi R_{\mathrm{pup}}^2} \iint_{\mathrm{pupil}} \mathbf{E}^{(\mathrm{t})}(x,y)\, \mathrm{e}^{-\mathrm{i}k(\alpha x + \beta y)}\, \mathrm{d}x\, \mathrm{d}y, \qquad (3.1)$$

where (x,y) and (ξ,η) are the coordinates of the pupil and of the image plane, respectively; R_{pup} is the pupil radius; $\mathbf{E}^{(\mathrm{t})}$ is the transmitted electric field of the etalon given by Eq. [47] of Paper I; $k \equiv 2\pi\lambda^{-1}$ is the angular wavenumber —with λ being the wavelength of the monochromatic beam impinging the etalon—; and α and β are the cosine directors of the *diffracted* wavefront by the pupil aperture. The transmission profile and the PSF are

derived directly from the electric field by multiplying it by its complex conjugate.

The particular dependence of the electric field $\mathbf{E}^{(t)}$ on the pupil in each configuration is discussed in depth in Sect. 4 of Paper I. For the telecentric mount, even if we assume an ideal etalon, the analytical integration is challenging and only numerical approaches to evaluate the integral have been followed until now, up to our knowledge. We proceed this way in Paper I to obtain the image plane electric field. To facilitate the convergence of the numerical integration, we separate the real and imaginary parts of the integral and we use polar coordinates on the pupil. Due to the circular symmetry of the problem, we also set $\beta = 0$ to facilitate the evaluation the electric field on the image plane expressed as a function of the radial coordinate $\rho \equiv f(\alpha^2 + \beta^2)^{1/2}$, where f is the focal length of the instrument at the image plane of the etalon. The numerical integration is performed employing the Matlab routine "quad2d", which relies on two-dimensional adaptive quadrature integration methods. We adjust the absolute tolerance and the maximum number iterations allowed to 10^{-10} and 10^6, respectively. To test the goodness of the numerical solution, we reproduce some of the results presented in the papers of Beckers (1998), von der Lühe & Kentischer (2000) and Scharmer (2006), especially those related to the wavelength-dependent behavior of the PSF. We have tested also that our solution coincides with that of a collimated configuration in the limit of very large f-numbers ($f\# \gg 1$). We compare the results for moderate f-numbers of a few decades with those predicted analytically from the aperture finesse and spectral shift equations in Sect. 4.2.2 of Paper I.

Imperfections in telecentrism are simulated assuming that the pupil is situated on the lens, for the sake of simplicity. The (monochromatic) propagation of an incident plane wavefront with an induced off-axis direction is then calculated. Since the pupil is overlapped to the lens, the orientation of the wavefront incident on the pupil coincides with the one of the chief ray on the etalon. The effect of such an off-axis incidence is included simply by changing α and β by $\alpha' \equiv \alpha - \alpha_0$ and $\beta' \equiv \beta - \beta_0$ in Eq. [48] of Paper I, where α_0 and β_0 are the cosine directors of the *incident* wavefront (see, e.g., Born & Wolf, 1999). The validity of this approach comes from the fact that either deviations from perfect telecentrism or tilts on the etalon have an impact on the PSF and on the transmission profile only because of the relative misalignment with the chief ray. The position of the pupil is, then, irrelevant to determine the response of the etalon as long as the relative inclination of the light cone focused on the etalon is properly taken into account. More details on the calculations can be found in Sects. 5.2 and 6 of Paper I.

41

An analytical solution of Eq. [48] of Paper I for $\alpha = \beta = 0$, is also found for telecentric etalons. Such a particular case gives the electric field evaluated on the intersection of the optical axis of the instrument with the image plane ($\xi = \eta = 0$), whose absolute square and phase represent the transmission profile and the transmitted wavefront, respectively. To find the analytical solution, we separate again the real and imaginary parts of Eq. [48] of Paper I. Then, we express any incidence angle as a function of the radial coordinates of the pupil, we expand it in a power series and we assume a small angle regime (f-numbers much larger than unity). Following this approximation, we find integrals with closed-form analytical solutions given in terms of known trigonometrical functions. An step-by-step explanation of the followed method can be found in Sects. 2 and 3 of Paper IV (Chapter 7).

3.2 Derivation of the Mueller matrix of birefringent etalons

The Mueller matrix of crystalline etalons is derived by extending the approach of Lites (1991), valid for (Y-cut) waveplates that exhibit very low reflectivity, to the general case of uniaxial crystals with coatings of arbitrary reflectivity and whose axis is oriented in any possible direction. Since the whole procedure is explained extensively throughout Paper II and its appendices, we will only give a brief description of the method in here.

First, the different propagation of the ordinary and extraordinary rays in anisotropic collimated etalons is considered after assuming they are given by Eq. [47] of Paper I, except for an arbitrary relative phase which accounts for the birefringence of the etalon (Sect. 2 of Paper II –Chapter 5–). Then, the transmission of the electric field vector is expressed in the Jones matrix formalism and the Mueller matrix terms are calculated analytically through the relation given in Jefferies et al. (1989) (Sect. 3.1 of Paper II). Since the directions along which the ordinary and extraordinary rays vibrate depend on the principal plane —the one containing the wavefront vector and the optical axis (e.g., Del Toro Iniesta, 2003)—, a rotation of the Mueller matrix is considered to account for the different directions of the incident rays (Sect. 3.2 of Paper II). The dependence of the birefringence of a LiNbO$_3$ etalon with the incidence and optical axis angles is also found following Del Toro Iniesta (2003) and the relations by Born & Wolf (1999) in the way described in Sect. 4.1 and Sect. 4.2 of Paper II.

The Mueller matrix of etalons in telecentric mounts is inferred in a sim-

ilar way. In this case, an effective polarimetric response is obtained after integrating the Jones matrices of individual rays across the radial and azimuthal coordinates of the pupil, the latter being related to the orientation of the principal plane. From the "integrated" Jones matrix, the Mueller matrix is derived in the same way as for the collimated case (Sect. 4.3 of Paper II).

The polarimetric imaging response is also addressed for the two mounts by taking into account diffraction effects. For this purpose, the Fraunhofer integral is solved for the ordinary and extraordinary rays and, then, a "diffracted" Mueller matrix is calculated in a similar manner than before (Sect. 5 of Paper II).

3.3 Assessment on the impact of etalons in solar instruments

We evaluate artificial signals arising from: (1) the wavelength dependence of the PSF on the telecentric configuration, (2) deviations from ideal telecentric illumination, and (3) the birefringence of a $LiNbO_3$ etalon in both setups. We obtain the response of a spectropolarimeter formed by two liquid crystal variable retarders (LCVRs) followed by a linear polarizer and a $LiNbO_3$ Fabry-Pérot as tunable filter, similar to IMaX and PHI. Maps of the spectrum of the four Stokes components centered at the 525.02 nm Fe I line in a region of the solar surface containing a magnetic pore are simulated from magnetohydrodynamics (MHD) simulations (Vögler et al., 2005). The maps of the Stokes vector are modulated artificially following the optimum scheme of IMaX and PHI (Del Toro Iniesta & Martínez Pillet, 2012). Then, the etalon is tuned along the spectral line and its spectral PSF is convolved monochromatically with the modulated object. The "measured" intensity at each wavelength is inferred by integrating the monochromatic convolutions across the transmission profile. Then, the incident Stokes vector is obtained demodulating the measured signal with the optimum demodulation matrix of the polarimeter (Del Toro Iniesta & Martínez Pillet, 2012). The LoS magnetic field and plasma velocities are calculated from the inferred Stokes maps using the center of gravity (CoG) method (Semel, 1967) and are compared with the ones obtained assuming the following ideal scenarios: (1) that the PSF is independent of the wavelength, (2) that there are no relative tilts between the chief ray and the etalon, and (3) that the etalon is isotropic. More details of the method can be found in Sect. 2 of Paper III.

The birefringence effects of the etalon are evaluated placing the Fabry-Pérot before and after the linear polarizer. To take into account the different positions of the etalon, the combined Mueller matrix of the polarimeter and the filter is calculated by multiplication of the individual matrices, as described in Sect. 3 of Paper III. In such a case, the modulation matrix is obtained directly from the final Mueller matrix and the demodulation matrix is calculated by inverting it numerically. The polarimetric efficiencies are calculated in the way explained in Del Toro Iniesta (2003).

Paper I: The isotropic case

On Fabry–Pérot Etalon-based Instruments. I. The Isotropic Case

F. J. Bailén , D. Orozco Suárez , and J. C. del Toro Iniesta
Instituto de Astrofísica de Andalucía (CSIC), Apdo. de Correos 3004, E-18080 Granada, Spain; fbailen@iaa.es, orozco@iaa.es, jti@iaa.es

Abstract

Here we assess the spectral and imaging properties of Fabry–Pérot etalons when located in solar magnetographs. We discuss the chosen configuration (collimated or telecentric) for both ideal and real cases. For the real cases, we focus on the effects caused by the polychromatic illumination of the filter by the irregularities in the optical thickness of the etalon and by deviations from the ideal illumination in both setups. We first review the general properties of Fabry–Pérots and we then address the different sources of degradation of the spectral transmission profile. We review and extend the general treatment of defects followed by different authors. We discuss the differences between the point spread functions (PSFs) of the collimated and telecentric configurations for both monochromatic and (real) quasi-monochromatic illumination of the etalon. The PSF corresponding to collimated mounts is shown to have a better performance, although it varies from point to point due to an apodization of the image inherent to this configuration. This is in contrast to the (perfect) telecentric case, where the PSF remains constant but produces artificial velocities and magnetic field signals because of its strong spectral dependence. We find that the unavoidable presence of imperfections in the telecentrism produces a decrease of flux of photons and a shift, a broadening and a loss of symmetrization of both the spectral and PSF profiles over the field of view, thus compromising their advantages over the collimated configuration. We evaluate these effects for different apertures of the incident beam.

Key words: instrumentation: interferometers – instrumentation: spectrographs – techniques: interferometric

1. Introduction

Fabry–Pérot interferometers (filters or etalons) are extensively employed as tunable monochromators in post-focus astronomical instrumentation. Examples can be found in the Italian Panoramic Monochromator at THEMIS (Bonaccini et al. 1989 and references therein), the TESOS spectrometer at the VTT (Kentischer et al. 1998), the Interferometric BIdimensional Spectrometer at the Dunn Solar Telescope of the Sacramento Peak Observatory (Cavallini 2006), the CRisp Imaging SpectroPolarimeter instrument at the Swedish 1 m Solar Telescope (Scharmer et al. 2008; van Noort & Rouppe van der Voort 2008), the IMaX instrument aboard SUNRISE (Martínez Pillet et al. 2011), the GFPI at GREGOR (Puschmann et al. 2013), and the PHI instrument on board the Solar Orbiter mission (Solanki et al. 2015). Their main advantage over single-slit-based spectrographs is that they allow for fast imaging of the solar scene and for post-facto imaging reconstruction techniques.[1] They are also preferred against other devices, such as Michelson interferometers or Lyot filters, in terms of weight and simplicity. When used in combination with a polarimeter, they enable dual-beam polarimetry, which gets rid of the undesired seeing-induced or *jitter*-induced contamination between Stokes parameters. However, they present both spectroscopic and imaging drawbacks that restrict their performance.

Fabry–Pérot etalons present a spectral transmission profile that is characterized by periodic and narrow resonances at certain wavelengths, whose position and width depend on intrinsic parameters of the etalon, such as its thickness or its refraction index, as well as on the way that the filter is illuminated. In particular, the transmission peaks shift toward the blue when the

incident angle is different from zero, which implies a variation on the transmission at monochromatic wavelengths. Meanwhile, the width of the resonances broaden when imperfections (defects) appear in the etalon, thus degrading the spectral resolution of the filter (e.g., Chabbal 1953; Meaburn 1976; Sloggett 1984; Hernandez 1988). Departure from collimated illumination (i.e., when the incident beam has a finite aperture) also widens the peaks and shifts them toward shorter wavelengths (e.g., Atherton et al. 1981; Sloggett 1984). Analytical expressions to determine the broadening of the spectral resolution are usually restricted to particular cases (e.g., the *limiting* finesse of Chabbal 1953). In addition, their derivation is sometimes unclear (e.g., the *aperture* finesse of Atherton et al. 1981) and the way in which different defects are added has been subject to debate (Sloggett 1984). We believe that this topic should be revisited to clarify the possible discrepancies and also to discuss the validity of the expressions given by different authors.

Concerning its imaging properties, Fabry–Pérots are used in both collimated (e.g., Bendlin et al. 1992; Martínez Pillet et al. 2011) and telecentric configurations (e.g., Kentischer et al. 1998; Solanki et al. 2015). In the first case, the etalon is located in a pupil plane. Consequently, different incidence angles in the etalon are mapped to different pixels of the detector. Therefore, in the case of a uniform object field, the image shows different peak intensities across the detector at monochromatic wavelengths due to the shift induced by the different incident angles on the etalon over the field of view (FOV). In the (image-space) telecentric configuration, the etalon is located at the focal plane while the exit pupil is located at infinity. In this setup (if perfect), each point of the etalon receives the same cone of rays from the pupil and the passband is kept constant along the FOV. Meanwhile, each point of the etalon sees the pupil as if it was not evenly illuminated. This effect is due to the variation on the incidence angle for rays coming from different parts of the pupil, which is known as *pupil apodization*. This produces

---

[1] Techniques for imaging reconstruction in spectrographs that employ slits are still at an early stage of development (e.g., Quintero Noda et al. 2015).

variations of the spatial point-spread function (PSF) of the system and of the spectral passband across the detector when defects are present in the etalon.

The image degradation introduced by the Fabry–Pérot in telecentric mode through pupil apodization was evaluated for the first time by Beckers (1998), who concluded that collimated illumination of the etalon is preferred over the telecentric configuration in diffraction-limited imaging telescopes. The PSF varies from one wavelength to another in the telecentric configuration, which gives raise to artificial line of sight (LOS) velocity signals that may not be corrected during data pre-processing. Spurious signals on the magnetic field can also appear. The magnitude of these effects will be discussed in the third part of this series of papers. Although his conclusions were valid, Beckers's (1998) calculations were not strictly correct because he considered variations in the magnitude of the electromagnetic field but omitted *phase errors*; i.e., fluctuations in the optical phase produced by the multiple reflections of light within the etalon. These fluctuations were incorporated by von der Lühe & Kentischer (2000), who concluded that image degradation effects appearing in telecentric configuration are even more pronounced than those predicted by Beckers (1998). They add that most wavefront degradation comes from pupil apodization instead of from phase fluctuations. Scharmer (2006) showed that phase variations can be partially compensated by refocusing the instrument because they depend quadratically with the pupil radial coordinate, in the same fashion as a defocus term.

The collimated configuration is not exempt of problems in terms of image degradation because the substrate surface roughness is amplified due to the high-reflectivity of the etalon surfaces (von der Lühe & Kentischer 2000). The amplitude and phase fluctuations in collimated configuration coming from these irregularities were studied by Scharmer (2006), who pointed out that the effects are less strong than predicted by von der Lühe & Kentischer (2000) but are still important, especially for high-reflecting etalons. In contrast to Beckers (1998), both these works find that the telecentric configuration is preferred over the collimated configuration if high-image quality is required. In our opinion, this comparison needs to be revisited. On the one hand, the von der Lühe & Kentischer (2000) results about the expected wavefront distortion in a collimated setup look too pessimistic. On the other hand, Scharmer's (2006) arguments about image degradation in collimated configurations invite to an in-depth study.

From our point of view several aspects are yet to be studied. First, some of the analytical approximations of the spectral performance of the etalon are not presented within the realm of a consistent theoretical framework and they differ from one author to another (Sloggett 1984). Furthermore, some of them have not been generalized to crystalline etalons (e.g., the *aperture finesse* defined by Atherton et al. 1981). Second, the effects of imperfect telecentrism (i.e., of having non-symmetric pupil apodization over the FOV when the exit pupil is not exactly at infinity, such as in real instruments) have not yet been thoroughly considered (to our knowledge). Third, disagreement between authors makes it unclear which configuration is to be preferred in terms of both image quality and spectral transmission. In particular, in an imperfect telecentric setup, both the PSF and the spectral profile can broaden and become asymmetric over the FOV (see Section 6). This means (among other things) that the PSF varies from pixel to pixel,

even if no defects are present in telecentric mode. This can be critical when referring to image quality. Moreover, a spectral shift is also produced over the FOV. Consequently, the passband does not remain constant and the advantage of using a telecentric setup is no longer obvious.

Etalons are sometimes made up of electro-optical and piezo-electrical crystals for tuning purposes, especially in space applications (Martínez Pillet et al. 2011; Solanki et al. 2015). The tuning is carried out through variations in the refraction index and thickness when applying a voltage. These crystals usually present birefringent properties and, because they are employed in polarimeters, can disturb the polarization properties of the incoming light and corrupt the polarimetric measurement. Anisotropic effects have only been taken into account through numerical experimentation (e.g., Doerr et al. 2008). They will be studied analytically in the second part of this series of papers for both the collimated and telecentric configuration, in terms of spectral and imaging performance.

This paper is structured as follows. We first summarize the relevant theory for analyzing the spectroscopic properties of Fabry–Pérot etalons (Sections 2 and 3). We then overview the most common optical configurations (Section 4), while emphasising the possible sources of the spectral profile degradation. We will then analyze the PSF deterioration in both perfect (Section 5) and imperfect (Section 6) telecentric configurations.

2. Basic Parameters and Nomenclature

A Fabry–Pérot etalon is simply a resonant optical cavity made up of two semi-reflective and semi-transparent surfaces that separate two different optical media of refractive indices n (the external) and n' (the internal). Note that single refractive indices implicitly indicate that the media are assumed to be isotropic. We assume that the media are homogeneous.[2] These are correct assumptions for air-gapped etalons (for example) but they are not for crystalline ones. Nevertheless, we keep the assumptions throughout this paper and defer the discussion of anisotropic etalons to the second paper in this series.

This optical cavity is also characterized by its geometrical thickness h and by the amplitude reflection and transmission coefficients r, r', t, and t' for the external (unprimed) and internal (primed) faces of each surface. As shown in Figure 1, a plane wave impinging the first (top) surface at an angle of incidence θ partially reflects on and refracts through both surfaces several times. The refraction angle is called θ'.

The fraction of energy reflected from and transmitted through the etalon is given by

$$R \equiv r^2 = r'^2, \tag{1}$$

$$T \equiv tt', \tag{2}$$

where we have assumed that $r = -r'$. R and T are called the reflectivity and transmittivity of the etalon. If there is no absorption, then

$$R + T = 1. \tag{3}$$

---

[2] An isotropic medium has the same properties and behavior no matter the direction of the light traveling through it because it is characterized by *scalar* dielectric permittivity, magnetic permeability, and electrical conductivity. If these physical quantities have no directional variations across the medium, then it is said to be homogeneous.
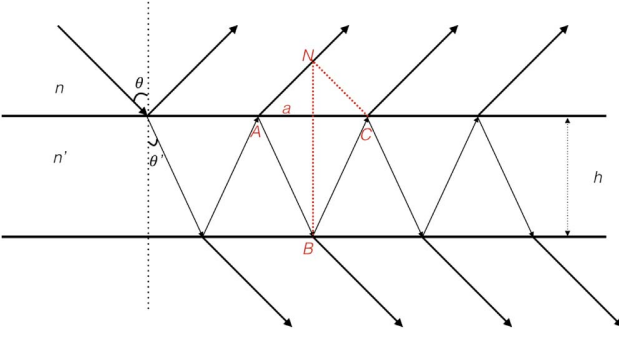
Figure 1. Transmission and reflection of a plane wave through an isotropic etalon.

If, on the contrary, the etalon is coated with a metal that absorbs light with an absorptivity A, then

$$R + T + A = 1. \tag{4}$$

3. The Transmission Profile for an Incident Plane Wave

Each of the transmitted and reflected rays in Figure 1 has a constant phase difference with its predecessor. Let us focus, for instance, in the second and third reflected rays. The optical path difference between them is

$$\Delta s = n'(\overline{AB} + \overline{BC}) - n\,\overline{AN}. \tag{5}$$

Since

$$\overline{AB} = \overline{BC} = \frac{h}{\cos\theta'}, \tag{6}$$

$$\frac{1}{2}\frac{\overline{AC}}{h} = \tan\theta', \tag{7}$$

and Snell's law,

$$n\sin\theta = n'\sin\theta', \tag{8}$$

one can finally obtain that

$$\Delta s = 2n'h\cos\theta'. \tag{9}$$

The corresponding phase difference between the two rays is

$$\delta = \frac{4\pi}{\lambda}n'h\cos\theta' + 2\phi, \tag{10}$$

where ϕ is the eventual phase shift introduced by the internal reflections. If the internal surfaces are not coated—as in crystalline etalons—, then ϕ can only be 0 or π. Meanwhile, if the reflecting surfaces are made of metallic films, then ϕ can take any value in the range $[0, \pi]$ depending on the incident angle. However, if θ' is close to zero, then ϕ may be considered to be constant. Furthermore, in general, h is very large compared to λ. In any case, ϕ can be neglected (Hecht 1998). According to Born & Wolf (1999) and others, the ratio between the transmitted, $I^{(t)}$, and the incident, $I^{(i)}$, intensities can be written as

$$g = \frac{I^{(t)}}{I^{(i)}} = \frac{\tau}{1 + F\sin^2(\delta/2)}, \tag{11}$$
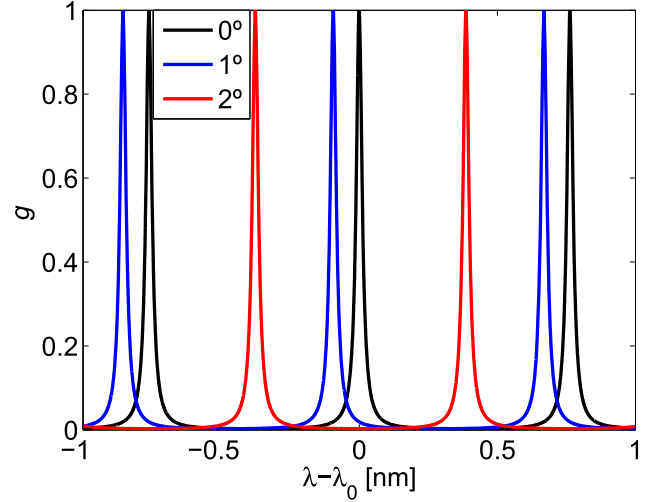
Figure 2. Transmission profile of an isotropic etalon as a function of wavelength distance to λ_0. An incident plane wave is assumed. Black, blue, and red lines correspond to $\theta = 0°$, $1°$, and $2°$, respectively.

where τ is the transmission (intensity) factor for normal incidence as given by

$$\tau = \left(1 - \frac{A}{1-R}\right)^2 \tag{12}$$

and parameter F is defined by

$$F \equiv \frac{4R}{(1-R)^2}. \tag{13}$$

One can now easily realize that Equation (11) provides a periodic function of δ, whose maxima are produced when $\delta_0 = 2m\pi$, with $m \in \mathbb{Z}$ or, equivalently, when

$$2n'h\cos\theta' = m\lambda_0. \tag{14}$$

m can be called the interferential order. A graphical representation of g as a function of wavelength can be seen in Figure 2. We have used $n' = 1,$[3] $h = 250$ μm, $A = 0$, $R = 0.9$, and $\lambda_0 = 617.234$ nm. For a given etalon with fixed refractive index and thickness, a different refraction (incidence) angle shifts the peaks of the transmission profile. Incident angles of $\theta = 0°$ (black line), $1°$ (blue line), and $2°$ (red line) have been used. A simple differentiation of Equation (14) readily shows that the peak shift is to the blue if θ' is increased and to the red if θ' is decreased.

3.1. Properties of the Transmission Profile

3.1.1. Transmission Peak Width and Order Separation

If we call w the (angular) FWHM of the peaks, then it is easy to see that half the maximum is reached at

$$\delta_w = 2m\pi \pm \frac{w}{2}, \tag{15}$$

or, according to Equation (11), when

$$\frac{1}{F} = \sin^2\frac{w}{4}, \tag{16}$$

---

[3] As for air at room temperature.

that is, when

$$w = \frac{4}{\sqrt{F}}, \qquad (17)$$

where we have assumed that $\sin(w/4) = w/4$. The FWHM in Equation (17) is in radians. If we want it in wavelength units, then it is easy to get

$$\Delta\lambda_w = \frac{w\lambda_0^2}{4\pi n'h\cos\theta'} = \frac{2\lambda_0}{\pi m\sqrt{F}}, \qquad (18)$$

by differentiating Equation (10) and using Equation (14).

Note that F in Equation (13) is an increasingly monotonic function of the reflectivity R. Therefore, Equation (18) tells us that the width of the transmission peaks basically depends on the reflectivity of the etalon. Note that $\Delta\lambda_w$ can slightly vary with the refraction angle (the bigger the angle, the broader the peak). This variation has small effects in solar applications because an angle of $1°$ represents a 2% modification of $\Delta\lambda_w$.

The *free spectral range* or separation between two successive peaks is equal to a shift

$$\Delta\delta_{\text{free}} = 2\pi. \qquad (19)$$

In wavelength units, analogously to Equation (18),

$$\Delta\lambda_{\text{free}} = \frac{\lambda_0^2}{2n'h\cos\theta'} = \frac{\lambda_0}{m}. \qquad (20)$$

Therefore, the free spectral range only depends on the optical thickness and on the refraction angle. The order separation without contamination of contiguous ones (a kind of cleanliness of the etalon transmission profile) is then given by the so-called *finesse*,

$$\mathcal{F}_{\text{r}} \equiv \frac{\Delta\delta_{\text{free}}}{w} = \frac{\pi\sqrt{F}}{2}, \qquad (21)$$

which is larger when the internal reflectivity on the etalon is larger. With this definition, the FWHM of the transmission peak can be rewritten as

$$\Delta\lambda_w = \frac{\lambda_0}{m\mathcal{F}_{\text{r}}}, \qquad (22)$$

or, equivalently,

$$\frac{\lambda_0}{\Delta\lambda_w} = m\mathcal{F}_{\text{r}}. \qquad (23)$$

The finesse is then inversely proportional to the FWHM of the transmission peaks: the larger the finesse, the thinner the peaks. The Fabry–Pérot resolving power is directly given by the product of the interferential order and the finesse. Since the width of real etalons can change due to other factors (see Section 4.1.1) and the concept of finesse remains useful, $\mathcal{F}_{\text{r}}$ in Equation (21) can be called the *reflectivity finesse*.

3.1.2. Tunability of the Etalon

The wavelength tuning procedure in real etalons implies a change in n', in h, or in θ. Equation (14) provides the necessary relationship between the three parameters and the wavelength of the transmission peak. If the selected tuning procedure is a tilt of the incidence angle, then one can approximately calculate

that an angle

$$\Delta\theta \simeq \sqrt{\frac{\lambda_0 n'}{h}} \qquad (24)$$

is necessary to tune the etalon from one transmission peak to the next (a whole free spectral range);[4] for example, with the values used for plotting Figure 2, $\Delta\theta \simeq 2°85$.

Since Equations (14), (18), and (20) depend on $\cos\theta'$, the transmission function is not the same across the FOV when illumination is out from normal incidence. Consequently, it is highly advisable to work with etalons that are as close as possible to normal incidence.

If we now keep fixed the incident angle, then a tuning equation can be derived from Equation (14) by taking logarithmic derivatives:

$$\frac{\Delta\lambda_0(V)}{\lambda_0} = \frac{\Delta n'(V)}{n'} + \frac{\Delta h(V)}{h}, \qquad (25)$$

where we have assumed that the tuning agent, the driver for changing the thickness or the refractive index of the etalon is a voltage. This is the case for piezoelectric or electro-optic etalons that can change either n', h or both by changing the feeding high voltage signal.

According to Álvarez-Herrero et al. (2006), the converse piezoelectric effect in Z-cut crystals[5] can be described by the linear relationship

$$\Delta h(V) = d_{33}V \qquad (26)$$

and the electro-optic change in the refractive index is given by (the unclamped Pockel's effect formula)

$$\Delta n'(V) = -\frac{n'^3 r_{13} V}{2h}. \qquad (27)$$

By combining Equations (25), (26), and (27), we get the final tuning relationship[6]

$$\Delta\lambda_0 = \left(d_{33} - \frac{n'^3 r_{13}}{2} \right) \frac{\lambda_0 V}{h}. \qquad (28)$$

3.1.3. Sensitivity to Variations in the Refractive Index and Etalon Thickness

There are three key parameters describing the etalon transmission profile, namely: the central wavelength, the peak FWHM, and the free spectral range. If the incident angle of the light beam is kept constant, then according to Equations (14), (18), (20), and (28), these three parameters depend on the refractive index n' and the thickness h. Impurities in the material or defects in polishing the surfaces can induce irregularities in any of them (or both) across the etalon clear aperture. These changes in the optical thickness can induce modifications in λ_0, $\Delta\lambda_w$, and $\Delta\lambda_{\text{free}}$. Consequently, an assessment of these possible changes is required.

---

[4] This equation can be obtained by using Equation (14) for m with $\theta = 0$ and for $m + 1$. For typical values of real etalons of interest in solar physics, $(1/m)^2$ turns out to be negligible (hence the approximation).

[5] Uniaxial crystals are certainly anisotropic and hence birefringent materials. We mention them here to illustrate a way of changing its (ordinary) refractive index.

[6] The actual values of the d_{33} and r_{13} coefficients depend on the specific sample device.

Error propagation in Equation (14) provides

$$\frac{\delta\lambda_0}{\lambda_0} = \frac{\delta n'}{n'} + \frac{\delta h}{h}. \qquad (29)$$

Error propagation in Equation (18) provides

$$\frac{\delta(\Delta\lambda_w)}{\Delta\lambda_w} = -\frac{\delta n'}{n'} - \frac{\delta h}{h}. \qquad (30)$$

A similar equation can be found for perturbations in the free spectral range:

$$\frac{\delta(\Delta\lambda_{\text{free}})}{\Delta\lambda_{\text{free}}} = -\frac{\delta n'}{n'} - \frac{\delta h}{h}. \qquad (31)$$

Therefore, a given percent error in h or n' is transmitted directly to λ_0, $\Delta\lambda_w$, and $\Delta\lambda_{\text{free}}$. Since typical thickness inhomogeneities in etalons are of the order of 1 nm, they amount a factor $4 \cdot 10^{-6}$ for thicknesses of 250 μm, approximately. This is perfectly negligible for $\Delta\lambda_w$ and $\Delta\lambda_{\text{free}}$. However, significant shifts of the order of the FWHM can be produced for the wavelength transmission peak. Perturbations in the refractive index are also much more important for the peak wavelength than for the peak width and free spectral range: a small percent or per thousand may be perfectly negligible for $\Delta\lambda_w$ and $\Delta\lambda_{\text{free}}$ but not for λ_0.

In summary, the expected impurities or inhomogeneities in our etalons have less of an effect on the shape of the transmission profile than on the peak wavelength. See Section 4 for a discussion on these defects for the two typical optical configurations in which etalons are mounted in astronomical instruments.

3.1.4. Transmission Peak as a Function of the Incident Angle

Let us consider a variation in δ due to a modification in the refraction angle (or the incidence angle, of course) for a given wavelength. In such a case, Equations (10) and (11) predict a maximum of the transmission profile for normal incidence. At given wavelengths, the transmitted intensity decreases with an increasing incidence angle. This is the cause of the so-called *pupil apodization*, which is discussed later in Section 4.2.

The monochromatic decrease in intensity is indeed induced by a shift in wavelength of the transmission peaks. Error propagation can now be written as

$$\frac{\delta\lambda_0}{\lambda_0} = \frac{\delta\cos\theta'}{\cos\theta'} = \sqrt{1 - \frac{\sin^2\theta}{n'^2}} - 1, \qquad (32)$$

where we have assumed shifts with respect to the peak (at $\theta = \theta' = 0$). If the incidence angle is small, then we can write the last equation in a more simple way:

$$\frac{\delta\lambda_0}{\lambda_0} \simeq -\frac{\theta^2}{2n'^2}. \qquad (33)$$

For our sample etalon in Figure 2, a maximum incidence angle of $0°.4$ translates to a maximum wavelength shift of, approximately, 15 pm, which is larger than the typical peak FWHM. Notice that the shift can be reduced by increasing the refraction index. For example, for Lithium Niobate, $n \simeq 2.3$ and $\delta\lambda_0 \simeq 2.8$ pm. Again, the effect of non-normal incident angle is negligible for the width of the transmission peaks and the free spectral range. Note that the right-hand side term of Equation (32) is $2.4 \cdot 10^{-6}$ and when multiplied by $\Delta\lambda_w \sim 10$
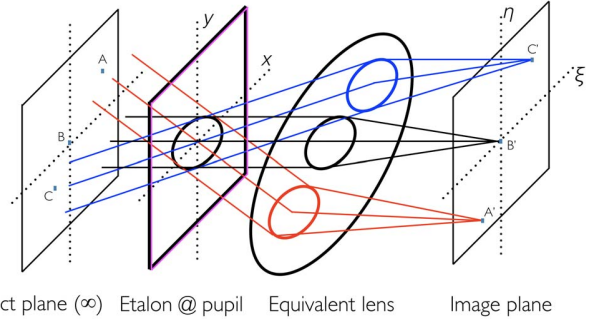

Figure 3. Layout of a collimated beam etalon configuration.

pm, it gives $\delta\Delta\lambda_w \sim 2.4 \cdot 10^{-4}$ pm. It is important to remark that, no matter the incidence angle, the right-hand sides in Equations (32) and (33) are always non-positive. This means that transmission peak shifts are always to the blue.

4. Two Optical Configurations

Fabry–Pérot etalons are used in solar physics in two typical optical configurations, namely: collimated and telecentric. In the first configuration, the etalon is located at (or very close to) a pupil plane. In the second configuration, the etalon is put very close to a focal plane. The properties and performance of the etalon are naturally different and are discussed in this section.

4.1. Collimated Configuration

Let us consider an optical configuration like the one sketched in Figure 3. The etalon is located on a pupil plane. In this location, the etalon is illuminated with parallel rays (plane waves) from each point in the object (assumed at infinity). The transmitted intensity at each image point is then given by Equation (11) multiplied by the surface of the pupil. This happens because all of the rays added at a given image point go through the etalon with the same incidence angle. As commented on in Section 3.1.4, we can deduce that in case of a uniform object field, images A' and C' will show a smaller peak intensity than B' at a monochromatic wavelength simply because the incidence angle (hence the refraction angle) is larger. This is an effect that could easily be corrected through a standard flat-field procedure. However, the sensors detect the flux of energy that passes through the entire transmission peak instead of the monochromatic intensity. Because the spectral width of the profile is almost insensitive to variations in the incidence angle (Section 3.1.4), there is no effect in the total flux of photons detected on the sensor over the FOV. The wavelength shift induced by the different incidence angle is of greater importance. The transmission functions at points A' and C' are blueshifted with respect to that at B'.

The results in Section 3.1.4 account for the effects of a non-zero angle between the etalon normal and the instrument optical axis. The sensitivity of the final image to inhomogeneities of the collimated etalon can be studied with the results from Section 3.1.3. Locally larger optical thicknesses imply redshifts and locally smaller optical thicknesses produce blueshifts. In this collimated configuration, the inhomogeneities are integrated and, hence, are spectrally blurred on the final image. These inhomogeneities broaden the effective transmission profile as a consequence of having different profiles shifted with respect to each other. This is discussed in

Figure 4. Typical defects of Fabry–Pérot etalons: (a) spherically shaped with a peak-to-peak excursion Δs_s; (b) irregularities following a Gaussian distribution with a variance Δs_g^2; (c) linear wedge with a peak-to-peak deviation Δs_p; and (d) sinusoidal defect of peak-to-peak amplitude Δs_a.

the following Section 4.1.1. The consequences on the spatial point-spread function of the instrument are considered in Section 5.1.

4.1.1. Effective Finesse

Regardless of quantitative effects, it is obvious that the highest quality etalons should be pursued. In other words, we typically aim at using the smoothest, flattest, and more accurately parallel etalons. However, the perfect etalon does not exist. Defects appear in real etalons that locally change the optical path through it. Most papers and books refer to air-gapped (or other fluid) etalons and they only discuss on inhomogeneities in the etalon width, h. However, crystalline etalons may also present irregularities in the refractive index, n'.[7] Since both h and n' always appear multiplied together, the relevant physical quantity is indeed the optical path $s \equiv n'h\cos\theta'$, which accounts for all possible incidence angles. The classical approach to these non-uniform etalons is to treat them as a set of individual etalons, each with a given optical thickness (e.g., Chabbal 1953). Although incoherent summation of the various etalon intensity distributions is not rigorously correct, diferences with the accurate coherent summation are not very large, according to Vaughan (1989). These differences were studied by Hernandez (1988), who showed that they are negligible for high-quality (highly reflective) etalons. The common approach (e.g., Atherton et al. 1981) is to ascribe different finesses to the various plate defects under consideration and add their inverses quadratically. This was first proposed by Meaburn (1976) under the assumption that all of the functions involved in the degradation of the intensity profile were Gaussian.

The most commonly employed expressions for the spherical, Gaussian, and departure from parallelism finesse defects (Figure 4) are probably those presented by Chabbal (1953). Analytical expressions for the sinusoidal defect (Figure 4(d)) have not been presented in the literature up to our knowledge, although this defect has already been studied by Sloggett (1984) and Hill (1963). The defect finesse formulas presented by Chabbal (1953) are restricted to the limit when the defect distribution is very broad compared to the original transmission profile (i.e., without including irregularities). This happens either when defects are very large or when the reflectivity is high and, therefore, the original spectral profile is very narrow. The latter case is of interest because achieving high finesses is usually intended and small variations in the optical path can degrade the profile severely. In this paper, we refer to Chabbal's (1953) expressions as *limiting* finesses because they restrict the maximum possible finesse of the etalon. However, these limiting expressions are usually employed as generic expressions (e.g., Atherton et al. 1981; Gary et al. 2006); i.e., as if they were valid for any magnitude of the defect.

---

[7] We restrict our analysis here to effects in one of the indices. Possible birefringence effects are deferred to a subsequent paper.

The most complete approach to describe the etalon plate defects is in our opinion the one by Sloggett (1984), who presented a general treatment applicable to any defect form or magnitude useful for etalons whose surface reflectivity is moderate to high. In particular, he heuristically suggested that the FWHM of a defect-broadened transmission profile, w, is approximately given by

$$w^2 = w_0^2 + \alpha^2\sigma_d^2, \tag{34}$$

where w_0 is the width of the profile corresponding to an etalon without defects (as given by Equation (17)), σ_d is the standard deviation of the probability density function associated to the perturbation or error in the phase δ introduced by the defects, and α is a coefficient that can be derived from numerical convolution of the transmission profile of a perfect etalon with the probability density function of the errors. This coefficient depends on the type and magnitude of the defect. Sloggett (1984) obtained by numerical methods that α converges to $2\sqrt{3} \simeq 3.46$ for all defects in the small magnitude regime ($\sigma_d/w_0 < 0.1$). This value of α agrees with the results found analytically by Steel (1986), who considered small perturbations of the incident wavefront caused by etalon defects. Note that for large defects compared to the original spectral profile ($\sigma_d \gg w_0$), the width of the degraded profile is equivalent to that of the defect distribution, w_d, and the value of α coincides with the factor that relates the FWHM of the distribution with its standard deviation ($w_d = \alpha\sigma_d$). The value of α in this limit must be consistent with the results of Chabbal (1953).

With this broadened profile, the reflective finesse no longer represents a spectral cleanliness of the etalon transmission profile. However, we can identify

$$\mathcal{F}_d \equiv \frac{2\pi}{\alpha\,\sigma_d} \tag{35}$$

as a *defect* finesse and speak of an *effective* finesse given by

$$\mathcal{F}_{\text{eff}} \equiv \left(\frac{1}{\mathcal{F}_r^2} + \frac{1}{\mathcal{F}_d^2}\right)^{-1/2}. \tag{36}$$

With this definition, we can continue using the finesse concept as an useful parameter for characterizing the etalon spectral cleanliness. Hence, by using this effective finesse in Equation (22) instead of the reflectivity finesse, the actual width of the etalon transmission peak becomes

$$\Delta\lambda_w = \frac{\lambda_0}{m\mathcal{F}_{\text{eff}}}. \tag{37}$$

Sloggett (1984) pointed out that defect finesse expressions obtained through Equation (35) could differ from the limiting finesses of Chabbal (1953) depending on the magnitude of the defect. Although he did not explicitly obtained finesse expressions for the different defects, we believe that they need to be presented to allow a comparison to be made with those of Chabbal (1953) and others. Here, we present compact expressions for four examples of the defect finesse assuming that defects are small ($\alpha = 2\sqrt{3}$). A complete discussion on the derivation of the defect finesses is carried out in Appendix A.

Consider a dish-like defect with a spherical or parabolic shape, such as the one shown in Figure 4(a), characterized by a
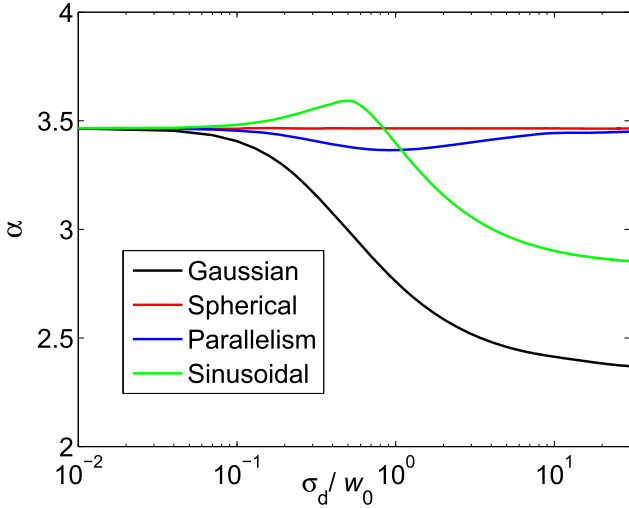
Figure 5. Value of the coefficient α for the Gaussian (black), spherical (red), parallelism (blue), and sinusoidal (green) defects against the standard deviation of probability density function associated to each defect normalized by the width of the profile of an etalon without defects, σ_d/w_0.

peak-to-peak excursion Δs_{s} in the optical path.[8] The defect finesse can be shown to be given by,

$$\mathcal{F}_{d_{\mathrm{s}}} = \frac{\lambda}{2\Delta s_{\mathrm{s}}}. \tag{38}$$

If we now focus on Figure 4(b), we have a microrough surface with deviations from s that follow a normalized Gaussian distribution with variance Δs_{g}^2. In this case, the defect finesse is

$$\mathcal{F}_{d_{\mathrm{g}}} = \frac{\lambda}{4\sqrt{3}\,\Delta s_{\mathrm{g}}} \simeq \frac{\lambda}{6.9\Delta s_{\mathrm{g}}}. \tag{39}$$

If the departure from parallelism is linear as in Figure 4(c), with a peak-to-peak excursion of Δs_{p}, then the defect finesse can be written as

$$\mathcal{F}_{d_{\mathrm{p}}} = \frac{\lambda}{\sqrt{3}\,\Delta s_{\mathrm{p}}} \simeq \frac{\lambda}{1.7\Delta s_{\mathrm{p}}}. \tag{40}$$

Finally, consider an etalon with an optical path roughness given by a sinusoid of amplitude Δs_{a} and zero offset. The corresponding defect finesse is

$$\mathcal{F}_{d_{\mathrm{a}}} = \frac{\lambda}{\sqrt{6}\,\Delta s_{\mathrm{a}}} \simeq \frac{\lambda}{2.5\Delta s_{\mathrm{a}}}. \tag{41}$$

Should the defects of a given etalon be described by the superposition of two or more of these distributions, then it is naturally understood that its inverse square finesse would result from summing up the square inverse finesses of each distribution.

As indicated previously, for $\sigma_d \gg w_0$, the value of α should give rise to consistent finesse expressions compared to the ones found by Chabbal (1953). Furthermore, these are (in principle) different from Equations (38)–(41). Figure 5 shows the value of α in the range $0.01 < \sigma_d/w_0 < 30$ obtained after numerical convolution of the four defect distributions that are considered here (see Appendix A) with the transmission profile g of an

etalon with reflectivity $R = 0.95$ and unity transmission factor.[9] We observe that α tends in all cases to $2\sqrt{3} \simeq 3.46$ for $\sigma_d/w_0 < 0.1$, as already shown by Sloggett (1984). In the limit $\sigma_d \gg w_0$, α tends to $2\sqrt{3}$ for the spherical and parallelism distributions, to $2\sqrt{2\ln 2} \simeq 2.35$ for the Gaussian distribution and to $2\sqrt{2} \simeq 2.83$ for the sinusoidal one. The limiting finesse $\mathcal{F}_d^{\mathrm{lim}}$ coincides then with Equations (38) and (40) for the spherical and the parallelism defects as the *limiting* value of α coincides with that of the small-defect regime. In contrast, for the Gaussian and sinusoidal distribution, the limiting finesse formulas differ from Equations (39) and (41). Their expressions are given by

$$\mathcal{F}_{d_{\mathrm{g}}}^{\mathrm{lim}} \simeq \frac{\lambda}{4.7\Delta s_{\mathrm{g}}}, \tag{42}$$

and

$$\mathcal{F}_{d_{\mathrm{a}}}^{\mathrm{lim}} \simeq \frac{\lambda}{2\Delta s_{\mathrm{a}}}. \tag{43}$$

The limiting value of α coincides in each case with the factor that relates the FWHM with the standard deviation of the defect distributions (Appendix A) and as expected agrees with the limiting finesse expression of of Chabbal (1953).

The defect finesse expressions that are presented here have only been restricted to two limits: small defects and large defects. In general, Equation (35) must be applied with the value of α that corresponds to the magnitude of the particular defect (Figure 5).

4.1.2. Transmission Profile Widths Across the Image

A further effect can produce a differential broadening of the transmission peaks of the etalon across the focal plane in a collimated configuration. Since any point in the final image is formed with rays that went through the etalon at higher incidence angle for greater radial distances from image center, the transmission peak broadening is dependent on this radial distance.

By differentiating Equation (18), one easily gets that the relative variation in the FWHM of the peak is

$$\frac{\delta\Delta\lambda_w}{\Delta\lambda_w} = \tan\theta'\,\delta\theta'. \tag{44}$$

With a typical value less than $0°\!.5$ for the maximum incidence angle in solar telescopes, the ratio is $8 \cdot 10^{-5}$. Therefore, we can safely disregard this effect for our very slow instruments.

4.1.3. Deviations from Perfect Collimation

Deviations from perfect collimation can be viewed as illuminating the etalon with a spherical wavefront of a finite numerical aperture. The consequence would be a broadening and a displacement of the profiles with respect to that of parallel illumination. Although aberrations may also be present in the incident wavefront, they will not be considered here. Following Sloggett's (1984) method, the broadening of the

---

[8] Sloggett (1984) refers to the peak-to-peak excursions as $2\Delta s$ instead of Δs.

[9] Note that Sloggett (1984) presented the value of α up to $5\sigma_d/w_0$ in his paper employing a Lorentzian function as transmission profile instead of g. We believe that this upper limit of σ_d/w_0 is insufficient to evaluate the tendency of α in the regime $\sigma_d \gg w_0$. Consequently, we have extended by a factor of six.
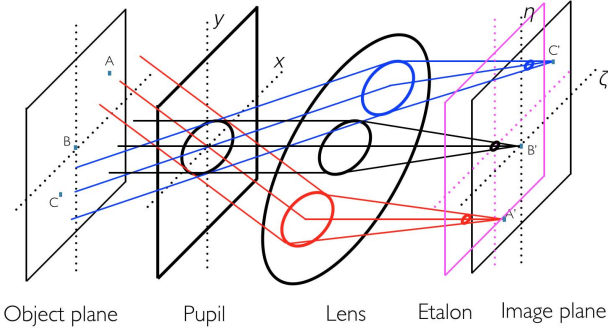
Figure 6. Layout of a telecentric beam etalon configuration where the entrance pupil is located at the focus of the lens (and the exit pupil is therefore at infinity). In this case, points A' and C' receive the same cone of rays as for point B'.

Figure 7. Rays coming from the pupil to the image plane. They go from the lens in Figure 6 to the etalon.

transmission profile due to the angular spread illumination of each point of the etalon can be managed with an *aperture finesse* (Appendix A) given by

$$\mathcal{F}_{d_{\mathrm{f}}} \equiv \frac{2\pi}{m\Omega}\frac{n'^2}{n^2} = \frac{2}{m\tan^2\theta_{\mathrm{m}}}\frac{n'^2}{n^2}, \qquad (45)$$

where Ω stands for the solid angle of the cone of rays traversing the etalon, and θ_{m} is the maximum incidence angle in the cone. This expression is compatible with that presented by Atherton et al. (1981), except for the factor n'^2/n^2. This disagreement is probably due to the fact that Atherton et al. (1981) considered an air-gapped etalon in their derivation and not the general (crystalline) case.

4.2. Telecentric Configuration

An alternative configuration can be used to keep the same passband across the FOV. In a (image-space) telecentric configuration (Figure 6) the etalon is located (almost) at the focal plane and the exit pupil is located at infinity (or, equivalently, the entrance pupil is at the front focal point of the system).

Each point of the etalon sees the same cone of rays coming from the pupil. Unlike the collimated case, all three points (i.e. A', B', and C') are evenly illuminated if the object field is flat and no wavelength shifts in the transmission peaks are expected from one point to another. However, the transmitted intensity is no longer g. Since these rays are coherent because they come from the same object point, the addition of intensities does not provide a solution and we should instead deal with electric field amplitudes.

4.2.1. Transmission Profile

The vector electric field of the ray transmitted by the etalon in Figure 1 is given by

$$\mathbf{E}^{(\mathrm{t})} = \frac{T e^{i\delta/2}}{1 - R e^{i\delta}}\mathbf{E}^{(\mathrm{i})}, \qquad (46)$$

where (t) and (i) refer again to the transmitted and incident quantities and R and T are given by Equations (1) and (3). This expression differs from that presented in most text books (e.g., Born & Wolf 1999) by the general phase factor $e^{i\delta/2}$, which is
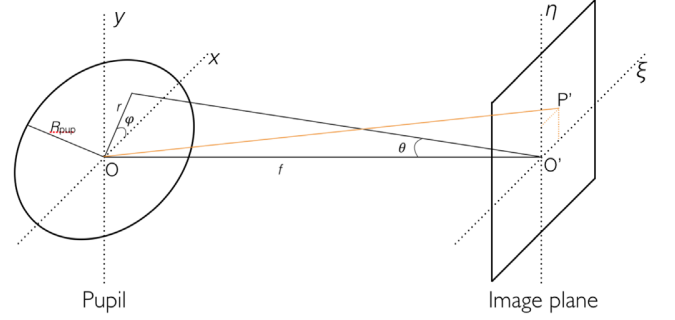
irrelevant in their discussion. However, it is at first important in our current analysis because it depends on the incidence angle.[10] The origin of the global phase is discussed in Appendix B.

With some simple algebra, Equation (46) can be cast as

$$\mathbf{E}^{(\mathrm{t})} = \frac{\sqrt{\tau}}{1 - R}\frac{e^{i\delta/2} - R\,e^{-i\delta/2}}{1 + F\sin^2(\delta/2)}\mathbf{E}^{(\mathrm{i})}, \qquad (47)$$

where τ is defined in Equation (12) and F in Equation (13). Consider now the geometry sketched in Figure 7. For a general optical system, the electric field at any point $P' = (\xi,\eta)$ is given by the sum of all electric fields across the pupil surface:

$$\widetilde{\mathbf{E}}^{(\mathrm{t})}(\xi,\eta) = \frac{1}{\pi R_{\mathrm{pup}}^2}\int\!\!\int_{\mathrm{pupil}}\mathbf{E}^{(\mathrm{t})}(x,y)\,e^{-ik(\alpha x + \beta y)}\,\mathrm{d}x\,\mathrm{d}y, \quad (48)$$

where $\alpha \equiv \xi/f$ and $\beta \equiv \eta/f$ are the cosine directors of OP' (notice that we restrict ourselves to small angles).[11] Therefore, the electric field in the image plane is proportional to the Fourier transform of that in the pupil plane. For our discussion about the telecentric configuration, we should concentrate in the electric field at point O': all the points in the focal plane receive the same cone of light.[12]

The axial symmetry of Figure 7 indicates that the pupil electric field only depends on r and we can thus write

$$\widetilde{\mathbf{E}}^{(\mathrm{t})}(0,0) = \frac{2}{R_{\mathrm{pup}}^2}\int_0^{R_{\mathrm{pup}}} r\,\mathbf{E}^{(\mathrm{t})}(r)\,dr. \qquad (49)$$

All points in the pupil at a distance r from its center have an associated incidence angle θ to the etalon. Therefore, each monochromatic ray out of the optical axis contributes less and less energy (Section 3.1.4) as θ increases. The bigger the distance to the pupil center, the smaller the energy. Hence, the pupil is seen from the etalon as if it were not evenly illuminated. This is the so-called *pupil apodization* effect, which was first discovered by Beckers (1998) and later discussed and elaborated by von der Lühe & Kentischer (2000) and Scharmer (2006). Moreover, the transmission peaks

---

[10] Neither von der Lühe & Kentischer (2000) nor Scharmer (2006) take this phase factor into account.
[11] We have normalized by the pupil surface to obtain quantities that can later be compared with the results for the collimated configuration.
[12] It is interesting to remark that there is no general convention on the (arbitrary) positiveness or negativeness of δ and, consequently, on the sign of the exponent of the direct Fourier transform. Other authors, such as Hecht (1998), use an opposite sign to the one used here.
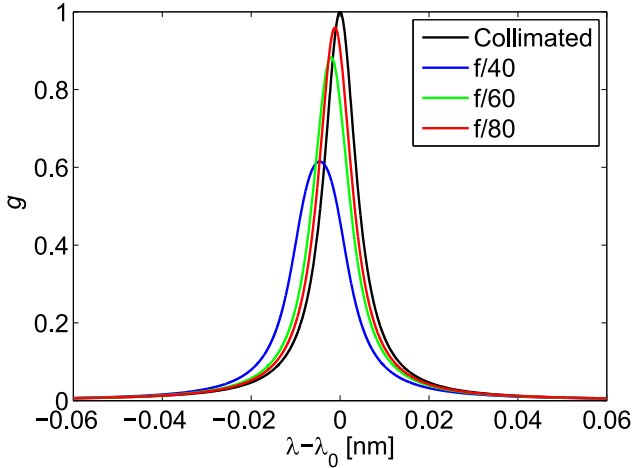
Figure 8. Transmission profiles as functions of the wavelength distance to 617.28 nm. A collimated configuration of the etalon is represented in black line. A telecentric configuration with $f/40$ (blue), $f/60$ (green) and $f/80$ (red) is also shown.

of the rays coming from the external parts of the pupil are shifted to the blue (Section 3.1.4) with respect to the central ray. Therefore, the integration of all of the rays should translate into a blueshifted and a broadened transmission peak, with a subsequent loss of spectral resolution as compared to the collimated case.

The average ratio between the transmitted and incident intensities in the telecentric configuration is then given by

$$\tilde{g} = \frac{\tilde{\mathbf{E}}^{(t)} \tilde{\mathbf{E}}^{(t)*}}{\mathbf{E}^{(i)} \mathbf{E}^{(i)*}}, \tag{50}$$

where the asterisk indicates the complex conjugate. Figure 8 shows a plot of the average transmission peak in a telecentric configuration with $f/40$, $f/60$ and $f/80$. As a reference, the same etalon but in a collimated configuration is used. A refractive index of $n' = 2.3$ has been used along with $\lambda_0 = 617.28$ nm, $h = 250\ \mu$m, $A = 0$, and $R = 0.92$. We will employ these parameters, corresponding to a commercial etalon, throughout the rest of this work. Table 1 gives the remaining key parameters for evaluating g and $\tilde{g}$ after Equations (11) and (50), respectively. As expected, the transmission profiles reduce their peak intensity and broaden when changing from the collimated configuration to telecentric configuration. The transmission profiles are also shifted bluewards with respect to the reference wavelength. These effects are more prominent for smaller f-numbers due to the increasing aperture of the incident cone of rays.

4.2.2. Effects on the Effective Finesse and on the Peak Wavelength

To circumvent the tedious (rigorous) calculation of Equation (49) after having substituted the electric field of Equation (47) into it, we can use the aperture finesse of Section 4.1.3 as an approximate measure of the transmission profile broadening. However, one should only include $\mathcal{F}_{d_f}$ in the effective finesse expression of Equation (36). To assess the validity of this approximation, we rewrite $\mathcal{F}_{d_f}$ in terms of the

Table 1
Etalon Parameters in Four Configurations, Namely: Collimated, and Telecentric, with $f/80$, $f/60$, and $f/40$

Parameters	Collimated	$f/80$	$f/60$	$f/40$
τ	1	0.96	0.88	0.60
$\Delta\lambda_0$ (pm)	0	-1.13	-2.02	-4.55
$\Delta\lambda_w$ (pm)	8.80	9.18	9.97	13.9
$\Delta\lambda_{\text{free}}$ (nm)	0.33	0.33	0.33	0.33
$\mathcal{F}_{\text{eff}}$	37.7	36.1	33.2	23.8

image-space f-number, $f\#$, as

$$\mathcal{F}_{d_f} = \frac{8(f\#)^2}{m} \frac{n'^2}{n^2}, \tag{51}$$

which gives $\mathcal{F}_{\text{eff}} = 36.5$, 34.2, 26.2 for $f/80$, $f/60$, $f/40$, respectively. These values are to be compared with the exact ones given in Table 1. As expected, the larger the $f\#$, the better the approximation.

We have seen that another consequence of receiving a cone of rays instead of a collimated beam is a blueshift of the spectral profile (Section 4.2). From the average change of phase compared to the collimated case, it can be shown (Appendix A) that the spectral shift of the profile, $\Delta\lambda_0$, depends on both the refraction index and the f-number through

$$\Delta\lambda_0 \simeq -\frac{\lambda_0}{16(f\#)^2} \frac{n^2}{n'^2}. \tag{52}$$

That is, the spectral shift decreases for larger f-numbers and refraction indices. For a collimated beam, $f\# \rightarrow \infty$, we have $\Delta\lambda_0 \rightarrow 0$ and $\mathcal{F}_a \rightarrow \infty$, as expected. Using this equation, the expected blueshifts are about -4.55 pm, -2.02 pm, and -1.14 for $f/40$, $f/60$, and $f/80$. These values fit extraordinarily well with those presented in Table 1.[13]

4.2.3. Plate-defect-induced Effects

Making an assessment of how sensitive the final image is to etalon inhomogeneities and to a non-zero angle between the instrument optical axis and the etalon optical axis is as easy as in Sections 3.1.3 and 3.1.4. Equations (30) and (31) are the same for all rays in the incoming cone of light because they are independent of the incident angle in a telecentric configuration. Then, the average transmitted intensity in Equation (50) will suffer exactly the same effect across the image; namely, that defects or errors in the optical thickness are only important for the wavelength tuning of the transmission peak. Modifications in the FWHM of peaks and the free spectral range can be neglected. Equation (32) is also valid for all of the rays in the cone. Hence, we should only take care of changes in the peak wavelength.

Since the defects of the etalon are directly mapped to the image in this telecentric configuration, the wavelength shifts have a direct influence in the derived LOS velocities with the instrument. To correct at first order for these LOS velocity shifts, one can measure them while taking flat-field exposures: if we determine the line position for every pixel with a flat

---

[13] Title (1970) found the same analytical expression for the blueshift of the spectral profile. However, the derivation that he followed is not rigorous because it is based on an analytical expression for the transmitted profile obtained by averaging Equation (11) over the cone of rays instead of adding electric field amplitudes.
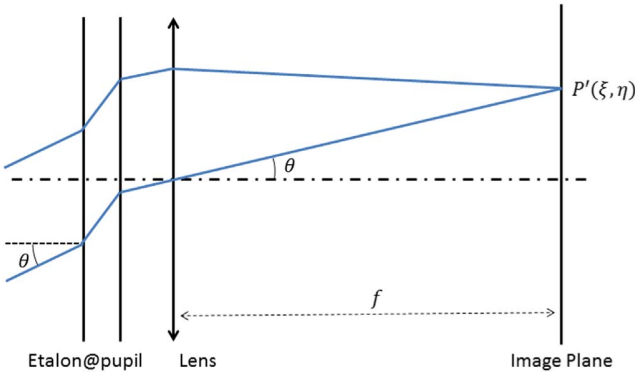
Figure 9. 2D layout of a collimated beam etalon configuration for two rays that impact on the etalon with an angle θ.

illumination, then we should only subtract the so-derived velocities from those evaluated independently. However, it is important to remark that the induced artificial LOS velocities cannot be corrected completely in telecentric mounts unless the PSF is fully characterized, both spatially and spectrally. This is probably one of the most important disadvantages of this configuration.

5. The PSF in the Two Configurations

In this section, we study the spectral and spatial PSF of the telecentric configuration compared to the collimated case.

Equations (47) and (48) are fully general for both configurations because they hold for monochromatic plane waves impinging the etalon. The electric field on the image plane is the Fourier transform of that illuminating the pupil. The difference between the two systems is whether or not $\mathbf{E}^{(t)}$ and the phase difference δ are constant across the pupil. That is, they are independent of the spatial coordinates (x, y) of the pupil plane in the collimated configuration whereas they are not in the telecentric configuration: $\mathbf{E}^{(t)}$ and δ do depend on x and y.

5.1. PSF in Collimated Configuration

Figure 9 displays the 2D layout of a collimated etalon configuration where two rays of incidence angle θ reach the etalon and later reach the image plane. Since the etalon is placed on the pupil, all rays striking on it with an angle θ will be projected on the same point $P'(\xi, \eta)$ of the image plane, no matter their incidence positions at the etalon. A relationship between P' and the incidence angle θ can easily be found if we assume that the stop is placed at the object nodal plane of the system (in a single lens paraxial system, this means that the stop is placed at the lens and the central ray is not deviated). If f stands for the focal length,

$$\cos \theta = \frac{f}{\sqrt{\xi^2 + \eta^2 + f^2}}. \quad (53)$$

The phase difference δ at P' can then be written as

$$\delta(\xi, \eta) = \frac{4\pi h}{\lambda} \sqrt{n'^2 - n^2 + \frac{n^2 f^2}{\xi^2 + \eta^2 + f^2}}. \quad (54)$$

It is important to remark that δ does not depend on the pupil plane coordinates (x, y). Therefore, for a perfect etalon with no

defects, Equation (48) simply turns into

$$\widetilde{\mathbf{E}}^{(t)}(\xi, \eta) = \frac{1}{\pi R_{\text{pup}}^2} \mathbf{E}_0^{(t)}(\xi, \eta) \int\int_{\text{pupil}} e^{-ik(\alpha x + \beta y)} dx dy, \quad (55)$$

where $E_0^{(t)}(\xi, \eta)$ is the electric field transmitted by the etalon that approaches P'. It should be noted that Equation (55) is proportional to the Fraunhofer integral of a circular aperture (Hecht 1998). Hence,[14]

$$\tilde{\mathbf{E}}^{(t)}(z; z_0) = \tilde{\mathbf{E}}_0^{(t)}(z_0) \frac{2J_1(z - z_0)}{z - z_0}, \quad (56)$$

where $J_1(z)$ is the first order Bessel function and the variable z is given by

$$z = \frac{2\pi}{\lambda} R_{\text{pup}} \frac{\sqrt{\xi^2 + \eta^2}}{f}. \quad (57)$$

Unlike the case of a clear circular aperture, space invariance has been lost with the collimated etalon and the response of the system depends on the position across the image. Thus, the PSF cannot be interpreted as a regular PSF because it varies from point to point. The instrument does not respond with the convolution of the object intensity distribution with the PSF. Rather, one has to multiply the object surface brightness with the *local* PSF and integrate. This local PSF can be expressed as

$$\mathcal{S}(z; z_0) = g(z_0) \left[\frac{2J_1(z - z_0)}{z - z_0} \right]^2, \quad (58)$$

where $g(z_0)$ is given by Equation (11) with the dependence on z_0 given through Equation (54). Then, the monochromatic, local PSF turns out to be the same as the PSF produced by a circular aperture except for a transmission factor. This result enables us to interpret the response of the etalon as that of a clear circular aperture (hence, through convolution with $\mathcal{S}_0 \equiv [2J_1(z)/z]^2$) but multiplied with the local transmission profile value. In other words, we have an *apodization* of the image. This implies that an etalon without defects in collimated configuration only affects the image quality by reducing the *monochromatic* intensity. As soon as we go radially out from the optical axis, $g(z_0)$ is shifted in wavelength (see Section 4.1) and, hence, it is reduced compared to the transmission factor (τ) at the given wavelength. Therefore, the most significant consequence that we can expect of image apodization is a radial decrease of the monochromatic signal-to-noise ratio (S/N) of the observations because the largest noise source is typically photon noise, which is proportional to the square root of the signal. Since g is a monotonically decreasing function of z, longer focal lengths can be beneficial for given etalons at the expenses of either reducing the FOV or increasing the size of the detector.

So far, we have discussed the monochromatic behavior of the etalons. The polychromatic response has to be addressed because our instruments always integrate a finite passband per each wavelength sample, which is done in Section 5.3.

For a real etalon with defects, Equation (55) is no longer valid. Either h, n', or both depend on the pupil plane coordinates because the defects are located at specific points

---

[14] Here we use z_0 as a parameter, which is denoted by the semicolon in front of it.
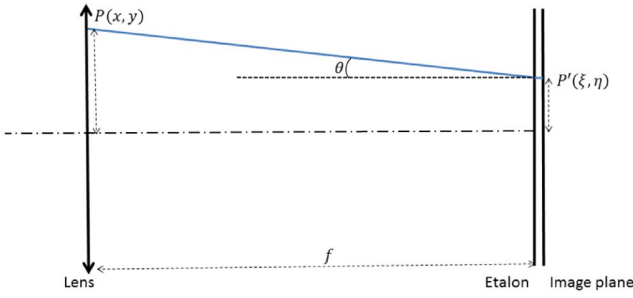
Figure 10. 2D Layout of a telecentric beam etalon configuration for a ray that comes from the pupil at $P(x, y)$ and is projected to the etalon at $P'(\xi, \eta)$.

(x, y). This dependence must be incorporated into Equation (54) and the PSF should be evaluated numerically. An approximation of the real PSF can be obtained through the convolution of $\mathcal{S}$ with a defect density distribution, in much the same way as we do to get the results of Section 4.1.1. Because $\mathcal{S}_0$ does not depend on δ, this convolution can only affect $g(z_0)$. We can then safely expect that the net effect of inhomogeneities are mostly seen in the spectral transmission but are not seen in the spatial shape of the PSF.[15]

The (unavoidable) presence of microroughness errors in the reflecting surfaces should translate into an increase of the energy contained in the wings of the PSF because they are high-frequency errors. This undesired excess of energy in the lobes of the PSF is commonly referred to as *stray light* and its consequence is a loss of contrast. In spectropolarimetry, stray light is a particularly delicate issue because it represents a contamination of the magnetic signal at a given feature by the signal originated in other structures located all around the feature.

Consider now an imperfectly collimated input beam. The phase shift depends in this case on the pupil coordinates as the incidence angle changes across the etalon. The net effect is essentially the same as locating the etalon in an imperfect telecentric configuration (Section 6). This is obvious because we only care about the irradiance distribution across the detector and thus the integrals that must be performed are the same as in the telecentric case, except for an irrelevant scale factor that accounts for the projection of the pupil on the etalon. The only difference is that etalon defects are still averaged out over the illuminated area, whereas in the telecentric mount the defects are directly mapped into the detector.

5.2. PSF in Telecentric Configuration

In the telecentric configuration, any point $P'(\xi, \eta)$ of the etalon sees a cone of rays, each coming from different parts of the pupil. Therefore, the phase shift δ now also depends on the

---

[15] Attention must be paid if the Strehl's ratio is used for evaluating the wavefront degradation in etalons because small variations in the optical path can lead to large variations in the transmission in $g(z_o)$. Thus, a decay in the monochromatic Strehl's ratio may come from a decay in the monochromatic transmission and not from degradation of the PSF. In our opinion, the Strehl's ratio should be employed only with the quasi-monochromatic PSF (Section 5.3). In any case, the PSFs normalization factors need to be chosen taking into account that the energy enclosed by the degraded and unaberrated PSFs must be the same.
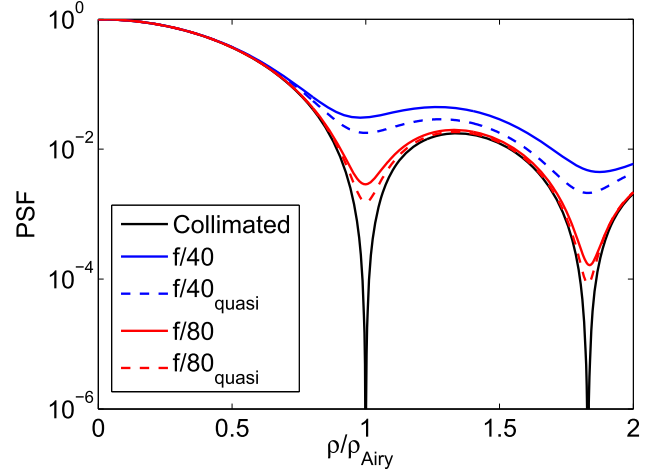
Figure 11. Normalized PSFs calculated in the telecentric configuration at $f/40$ and $f/80$ (blue and red lines, respectively) and in the collimated configuration (black) line for normal illumination of the pupil. The quasi-monochromatic PSFs of both f-numbers have also been represented (blue- and red-dashed lines, respectively).

pupil plane coordinates. From Figure 10,

$$\cos \theta = \frac{f}{\sqrt{(x - \xi)^2 + (y - \eta)^2 + f^2}}. \tag{59}$$

Hence, the explicit dependence on both the pupil and image plane coordinates is

$$\delta(x, y, \xi, \eta)$$
$$= \frac{4\pi h}{\lambda} \sqrt{n'^2 - n^2 + \frac{n^2 f^2}{(x - \xi)^2 + (y - \eta)^2 + f^2}}. \tag{60}$$

Likewise in the collimated etalon with defects case, $\mathbf{E}^{(t)}$ does depend here on the pupil plane coordinates and cannot be taken out from the integral in Equation (55). Therefore, the PSF must be calculated numerically.

Figure 11 shows the monochromatic PSFs as functions of the radial distance from the optical axis, $\rho \equiv (\xi^2 + \eta^2)^{1/2}$, normalized by the Airy disk radius of a clear, circular aperture, $\rho_{Airy} = 1.22 f \lambda_0 (2R_{pup})^{-1}$. Solid lines represent the monochromatic PSFs as evaluated at their respective peak wavelengths, $\lambda_t \equiv \lambda_0 + \Delta \lambda_0$, where $\Delta \lambda_0$ is given in Table 1. Dashed lines represent the quasi-monochromatic PSFs after integrating the finite etalon passband (see Section 5.3). Blue and red correspond to the $f/40$ and $f/80$ telecentric cases, respectively. For the sake of comparison, the PSFs are normalized to their maximum transmissions, which are also given in Table 1.

The differences between both collimated and telecentric configurations become more evident from the vicinity of the first minimum of the Airy pattern and are more prominent for the shorter $f\#$ beams.

Following Section 4.2, one could expect that the telecentric PSF becomes broadened when compared to the collimated case, whose width coincides with that for a clear, circular aperture: $\Delta \rho_{Airy} = 1.029 f \lambda_0 (2R_{pup})^{-1}$. However, this is actually only true at certain wavelengths. Figure 12 shows in solid lines the FWHM of the monochromatic PSF, $\Delta \rho$, normalized to $\Delta \rho_{Airy}$, against the wavelength shift from λ_0 for both $f/40$ (blue) and $f/80$ (red). We can observe that the PSF broadening is a wavelength-dependent effect, which was evaluated for the first time by Beckers (1998). The PSF narrows toward the blue
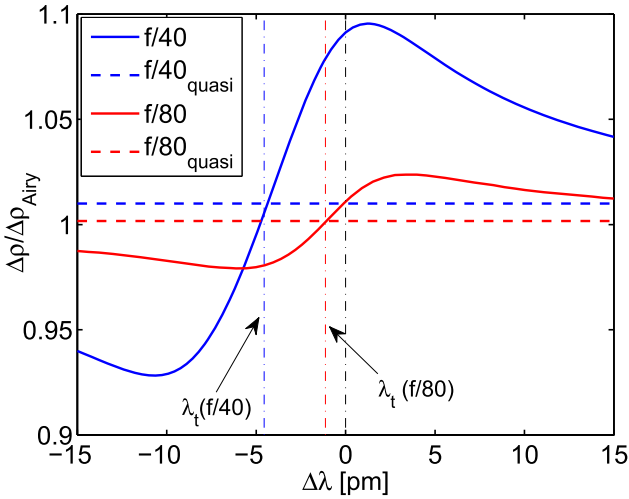
Figure 12. FWHM of the PSF in a perfect telecentric configuration normalized to the Airy disk FWHM as a function of the wavelength shift. f-numbers $f/40$ (blue line) and $f/80$ (red line) have been employed. The FWHM of the quasi-monochromatic PSFs for $f/40$ and $f/80$ (blue and red-dashed lines respectively) have also been included. Vertical, dashed–dotted lines mark the position of the maximum transmission wavelengths. In black, that of the collimated configuration.
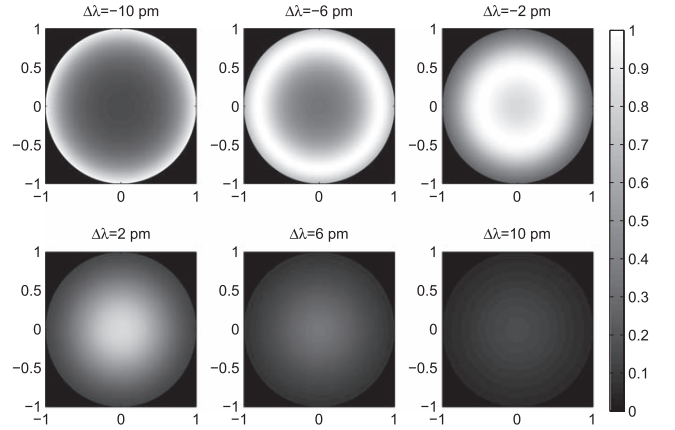
Figure 13. Pupil apodization in a telecentric mount illuminated with a $f/40$ beam for different shifts with respect to λ_0. From the upper left to the lower right: $\Delta\lambda = -10, -6, -2, 2, 6$ and 10 pm.

with respect to the FWHM at λ_t, while the opposite is the case for red wavelength displacements. This happens because pupil apodization (and phase errors) is a wavelength-dependent effect (Figure 13). Toward the red of λ_t, the center of the pupil is brighter than the edges. The effect is very similar to a Gaussian apodization of the pupil, which translates to a broadening of the central disk of the PSF. The effective size of the pupil decreases and also reduces the energy in the secondary rings (Mahajan 1991). Toward the blue of λ_t, a central obscuration appears and the brightness shifts with annular shape toward the edges. The practical effect of obscuring an optical system is to decrease the central disk of the PSF at the expenses of expanding the wings of the PSF (Mahajan 1991), thus contributing to stray-light effects. This argumentation is consistent with the results found by von der Lühe & Kentischer (2000).

The maximum and minimum FWHM of the PSFs differ in less than a 10% and 3% from $\Delta\rho_{\rm Airy}$ for the $f/40$ and $f/80$ beams, respectively. Also notice that the separation between the minimum and the maximum is of the order of the FWHM of the spectral profile (Table 1). For larger shifts, the pupil tends to be evenly illuminated and the PSF of a diffraction-limited system with the same pupil size is recovered. As

remarked by Beckers (1998), the wavelength dependence of the FWHM introduces artificial velocity signals in solar images with velocity structure. An evaluation of this effect in real instrumentation is presented in the third part of this series of papers, where we show that errors in the magnetic field can also appear.

In an ideal telecentric configuration, where all chief rays across the FOV are parallel to the optical axis, each point of the etalon receives the same cone of rays. Thus, all results obtained for normal illumination are also valid for any direction of the incident illumination of the pupil.

5.3. Quasi-monochromatic PSF

Real observations are polychromatic. Therefore, we should be interested in the quasi-monochromatic response of the system. Typically, in front of the quasi-monochromatic Fabry–Pérot etalon, instruments have an order-sorting pre-filter. Let $T(\lambda)$ be the transmission profile of the pre-filter (typically a window-shape function). If $O(\xi, \eta; \lambda)$ denotes the monochromatic brightness distribution of the object, then the image quasi-monochromatic intensity distribution centered at λ_0 can be expressed as

$$I(\xi, \eta; \lambda_0) = \int_{-\infty}^{+\infty} T(\lambda) \iint O(\xi, \eta; \lambda - \lambda_0) \cdot S(\xi - \xi_0, \eta - \eta_0, \lambda - \lambda_0) \, d\lambda \, d\xi_0 \, d\eta_0, \quad (61)$$

in the collimated configuration and

$$I(\xi, \eta; \lambda_0) = \int_{-\infty}^{+\infty} T(\lambda)[O(\xi, \eta; \lambda - \lambda_0) * S(\xi, \eta; \lambda - \lambda_0)] d\lambda, \quad (62)$$

in the telecentric configuration, where the symbol $*$ stands for convolution. Convolution in Equation (62) is carried out in the space domain. Therefore, only if the object brightness distribution is independent of wavelength (von der Lühe & Kentischer 2000),
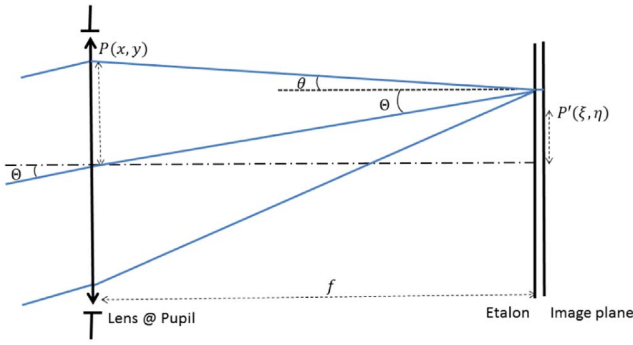
Figure 14. 2D Layout of a non-telecentric beam configuration (the lens and the pupil are located at the same position) for a collimated beam that illuminates the pupil with an incident angle Θ. The chief ray does not deviate, whereas the other rays reach the etalon with different angles θ.

Figure 15. Apodization of pupil as seen from the etalon for a telecentric beam with $f/60$ and at different angles of incidence of the chief ray in the vertical direction: $\Theta = 0°$, $0°\!1$, $0°\!2$, $0°\!3$, $0°\!4$ and $0°\!5$ from the upper left to the lower right. Coordinates have been normalized to the pupil radius.

Figure 16. PSF profiles of the a telecentric etalon with $f/80$ at λ_t and at different angles of incidence of the chief ray: $\Theta = 0°$ (black), $0°\!125$ (blue), $0°\!25$ (red), $0°\!375$ (green) and $0°\!5$ (magenta). Each profile is centered at $\rho_0 = f \sin \Theta$.

as in the case of the continuum, then O can go out from the integral and write

$$I(\xi, \eta; \lambda_0) = O(\xi, \eta;) * \int_{-\infty}^{+\infty} T(\lambda)S(\xi, \eta; \lambda - \lambda_0)\, d\lambda, \quad (63)$$

in the telecentric configuration. Hence, the right-hand side of the convolution can be identified as a *quasi-monochromatic* PSF, $\mathcal{S}_{\text{quasi}}$, which coincides with the integral in wavelength of the monochromatic S multiplied by $T(\lambda)$.

The quasi-monochromatic PSF is strictly valid only for the continuum wavelengths. Within the spectral lines, the spatial and spectral properties of light can be highly correlated and thus space invariance no longer holds. The response of the instrument depends on the object itself. However, one can reasonably expect that the integration in wavelength somehow reduces the purely monochromatic effects in the final images at other wavelength samples. This can only be checked numerically.[16]
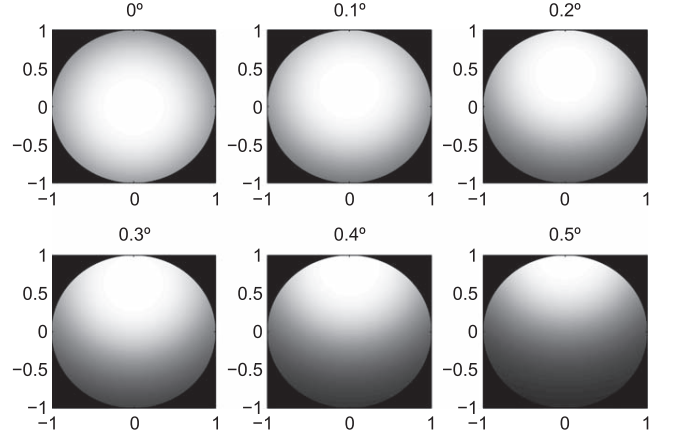
Along with the monochromatic PSFs, Figure 11 also shows $\mathcal{S}_{\text{quasi}}$ for the two telecentric cases in dashed lines. (The collimated $\mathcal{S}_{\text{quasi}}$ exactly coincides with the monochromatic one after normalization.) It can be seen that the quasi-monochromatic PSF performance is better than that of the monochromatic one, as best witnessed close to the minima. The reason for this is that the the position of the monochromatic PSF minima are very sensitive to wavelength variations in the vicinities of λ_0. The net effect is an improvement of the PSF when averaging spectrally the monochromatic PSFs (von der Lühe & Kentischer 2000).

Figure 12 also shows the quasi-monochromatic cases in dashed lines. The quasi-monochromatic PSF widths are larger than in the collimated configuration, although it can be seen that the effect of integrating the monochromatic PSFs virtually balances out their spectral variations.
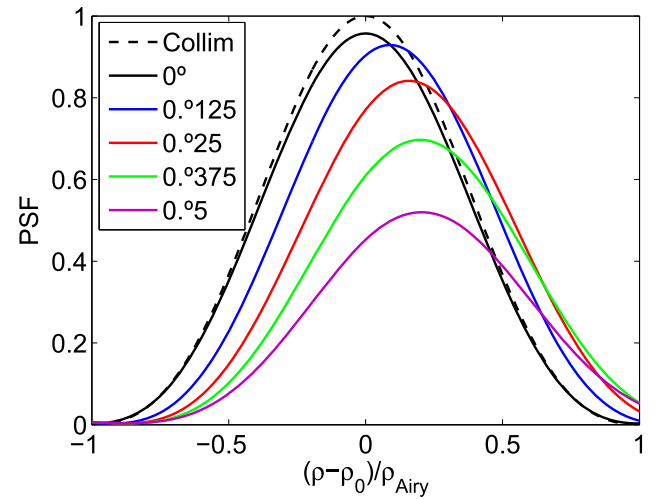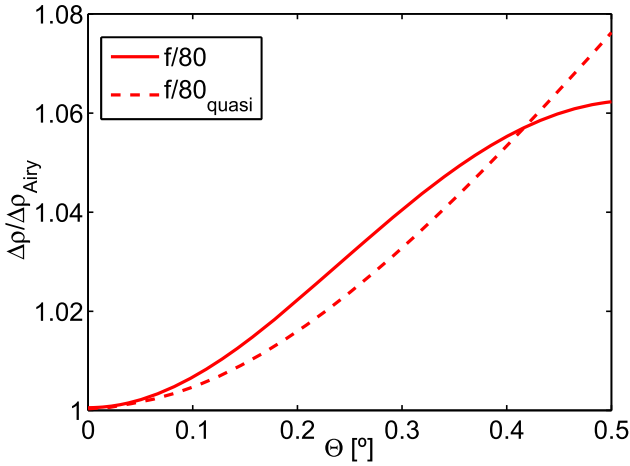
6. Deviations from Perfect Telecentrism

Real instruments cannot strictly follow the requirements for a perfect telecentric system. In an imperfect telecentric instrument, the entrance pupil is not exactly located at the focal plane of the instrument and the exit pupil is at an intermediate position between the lens and infinity. This situation is exemplified in Figure 14 where, without loss of generality, the pupil is assumed to be at the same location as the lens. The main consequence of this is that the chief ray cannot be normal to the etalon but is at an

incidence angle Θ, which varies across the image. Real instruments always have tolerances for such an incidence angle, which cannot be exactly zero as in the ideal case. With an oblique chief ray, the pupil apodization becomes asymmetric. Figure 15 displays the pupil illumination as seen from the etalon as a function of the chief ray angle of incidence. While the radial decrease in brightness is symmetric at $\Theta = 0$, it becomes more asymmetric as soon as Θ increases. This result certainly has an influence in the PSF that varies across the FOV.

6.1. PSF Shape over the FOV

Figure 16 shows the monochromatic PSF at the peak wavelength at normal incidence, λ_t, corresponding to a beam with $f/80$ for different angles of incidence of the chief ray against the radial coordinate of the image plane, ρ, centered at $\rho_0 = f \sin \Theta$ (corresponding to the maximum of the PSF of a collimated beam in a circular aperture with incident angle Θ) and normalized by the width of the Airy pattern, ρ_{Airy}. We can observe: (1) a spatial shift of the maximum with respect to the

---

[16] We refer the reader to the third paper of this series for a quantitative evaluation of this phenomenon.

Figure 17. FWHM of the PSF at λ_t normalized by the FWHM of the Airy disk across Θ for a $f/80$ beam (red-solid line). The FWHM of the quasi-monochromatic PSF (red-dashed line) and the FWHM of the PSF for a collimated beam have also been plotted (black-solid line).
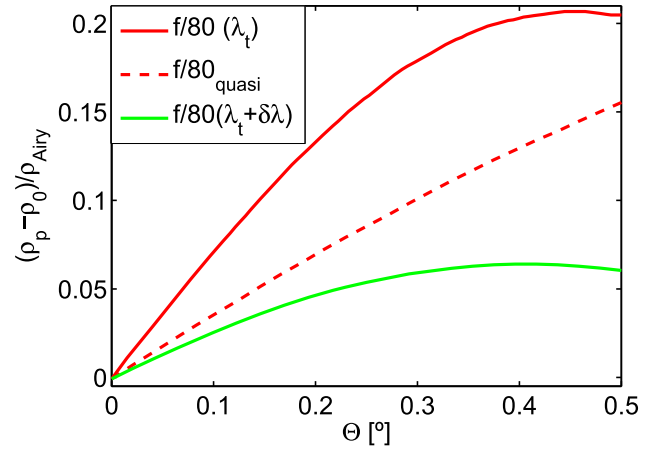

Figure 18. Spatial shift of the peak of the PSF at λ_t with respect to ρ_0 across Θ for a telecentric configuration with $f/80$ (red-solid line). The shift for the quasi-monochromatic PSF (red-dashed line), as well as at $\lambda + \delta\lambda$ (green-solid line) are also represented.

collimated case, (2) a broadening of the PSF, and (3) a decrease of the peak transmitted intensity across the FOV. It is also important to remark that perfect telecentrism is recovered at $\Theta = 0$ because Θ defines (in a certain sense) the degree of telecentrism. The fact that the PSF is not centered readily implies stray light from the surroundings. Note that $\sim 0.2\rho_{\text{Airy}}$ (the approximate peak of the PSF for $\Theta = 0°5$) is a third of a pixel in a critically sampled instrument. The broadening of the PSF drives the results in the same direction.

The change of the (normalized) FWHM against Θ is shown in Figure 17 for the monochromatic (λ_t) and quasi-monochromatic PSFs of an imperfect telecentric configuration illuminated with an $f/80$ beam. It is to be noticed that the PSF width grows monotonically with the chief ray incidence angle. The variation of width at $0°5$ is about 7% and 8% for the monochromatic and quasi-monochromatic curves, respectively. Figure 18 shows the spatial shift of the PSF peak, ρ_p, with respect to ρ_0 against Θ for λ_t, $\lambda_t + \delta\lambda$ ($\delta\lambda = 5$ pm) and for the quasi-monochromatic PSF. The etalon is illuminated with a $f/80$ beam in all cases. The spatial displacement is about 18% and 15% at $0°5$ for the monochromatic PSF at λ_t and for the quasi-monochromatic PSF, respectively. Interestingly, the dependence at $\lambda_t + \delta\lambda$ is different from that at λ_t, which indicates that the shift is wavelength dependent and that the PSFs overlap not only spatially but also spectrally over the image plane.

6.2. Behavior of the Spectral Profile over the FOV

The loss of symmetry in the cone of rays is also mapped into the transmission profiles of the etalon. These profiles will be shifted and deformed, as happens with the PSFs. Figure 19 shows the transmission profile as a function of the wavelength distance to λ_0 for $\Theta = 0°, 0°125, 0°25, 0°375$ and $0°5$. A beam with $f/60$ has been employed to clearly visualize the asymmetrization and loss of illumination with Θ. We can appreciate the blueshift across the FOV, as well as a decrease of the symmetry, a broadening of the profiles and a decrease of the peak transmitted intensity as Θ grows. Also note that at $\Theta = 0$ we recover the transmission profile for $f/60$ as presented in Figure 8.

Figure 20 shows the transmitted intensity with Θ evaluated at the wavelength of the peak transmission for normal illumination, λ_t. A beam with $f/80$ has been employed. The decay of
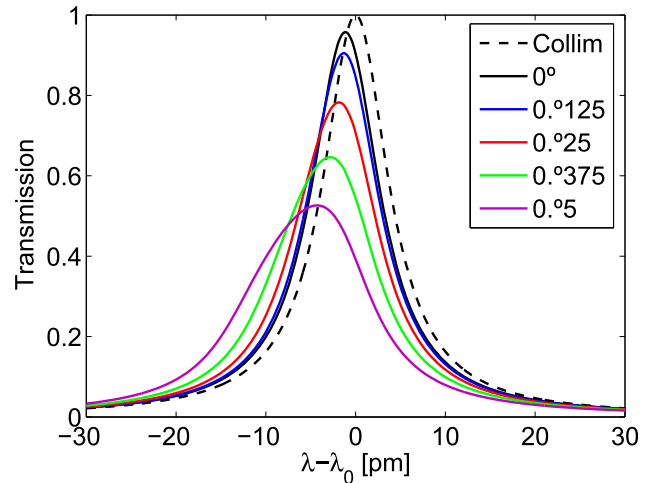
Figure 19. Spectral transmission function at $f/60$ for chief ray angles of incidence $\Theta = 0°$ (black), $0°125$ (blue), $0°25$ (red), $0°375$ (green), and $0°5$ (magenta).

transmission at λ_0 with the incident angle of the collimated case is also represented. The peak intensity goes from 0.96 and 1 at $0°$ to 0.52 and 0.49 at $0°5$ for the telecentric and collimated beams, respectively. It should be noticed that in the collimated case, the intensity decays faster with the incidence angle. We also show the total energy contained in the transmission profiles for both the telecentric and collimated beams with the chief ray incidence angle. We have normalized both to the total energy contained in the transmission profile of the collimated configuration (which remains constant over Θ). The total energy of the profile is calculated by integrating the spectral transmission factor, $\tilde{g}$. We can observe that the flux of the telecentric configuration is reduced by about 9% from the center of the image to its edges.

Although the telecentric configuration was devised to avoid the wavelength shift, $\Delta\lambda$, across the FOV (which is characteristic to the collimated configuration), a wavelength shift will appear in real instruments; as can be seen in Figure 19. Figure 21 shows the spectral displacement of the wavelength peak with Θ for the nominal wavelength, λ_0, for different f-numbers. It can be noted that the shift goes toward the blue for all angles and has a weaker dependence on Θ as the f-number decreases from infinity
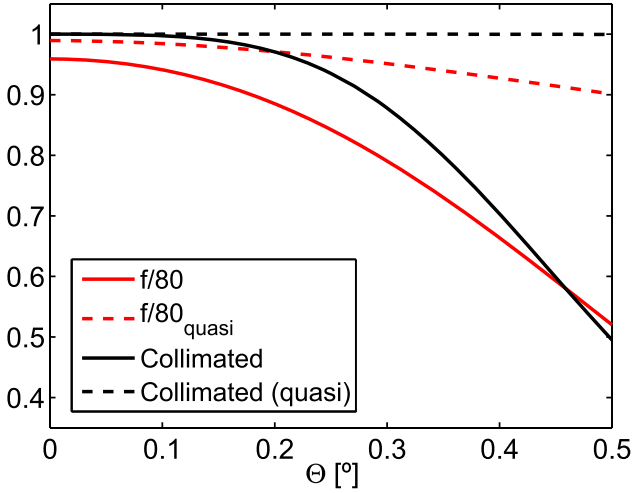
Figure 20. Transmitted intensity at λ_t for a telecentric configuration with $f/80$ across Θ (red-solid line) and for a collimated configuration (black-solid line). The total flux of energy transmitted normalized by the flux transmitted in the collimated configuration (black-dashed line) is also represented (red-dashed line).
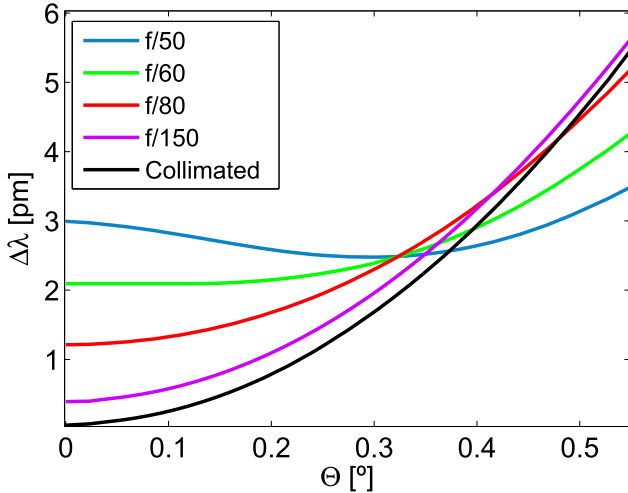
Figure 21. Spectral shift of the peak wavelength across Θ for f-numbers $f/50$ (blue), $f/60$ (green), $f/80$ (red), and $f/150$ (magenta). As reference, the spectral shift of the collimated configuration is also plotted (black line).

(collimated case) to $\simeq 60$. For $f\# < 60$, the shift is reduced as Θ increases until it reaches a minimum at a certain value (larger for smaller f-numbers) and then grows monotonically toward the blue. The weaker dependence with smaller f-numbers contrasts with other effects, such as the broadening and the asymmetrization of the PSF and of the spectral profile, where the effect is more prominent for smaller f-numbers. This indicates that, in general, a compromise must be reached between the spectral shift and the degradation of the PSF and of the spectral transmission with the f-number in our instruments.

To qualitatively understand why the wavelength shift decreases or increases over the FOV depending on both the f-number and the chief ray angle, let us take a look at Figure 14. If we set $\Theta = 0$ (normal illumination of the pupil), then the cone of rays becomes symmetric and the maximum incidence angle is the same at both sides of the optical axis. This effect is a wavelength displacement of the peak wavelength toward the blue of the nominal wavelength, λ_0. As Θ increases, the

maximum incidence angle decreases at one side of the optical axis and increases at the other side. This causes a sort of trade-off to increase or to decrease the shift with respect to normal illumination when averaging the electric field transmitted by the etalon over the pupil. This is of course $f\#$ dependent because the cone of rays reaching the etalon narrows when the f-number increases, and vice-versa.

7. Summary and Conclusions

We have discussed the properties of Fabry–Pérot etalons in the two optical configurations commonly employed in solar instruments, namely: collimated and telecentric. We have focused on their use as both tunable spectral filters and as imaging elements.

First, we have overviewed the general properties of Fabry–Pérot etalons, their tunability and their sensitivity to variations in the optical thickness. We have remarked that changes in the optical thickness particularly affect the peak wavelength but do not have as much of an effect on the shape of the transmission profile.

We have studied the degradation of the spectral profiles originated by both etalon defects and illumination with a beam of a certain aperture. We have followed the general treatment given by Sloggett ([1984](#)) and we have extended their results by presenting explicit formulas for the finesse defects of typical inhomogeneities (i.e., spherical, Gaussian, parallelism and sinusoidal). The expressions that we have found are valid for irregularities having a small effect in the transmission profile. We have also obtained formulas for the finesse defects in the opposite limit; i.e., when irregularities dominate. We have shown that these finesses agree with the limiting formulas of Chabbal ([1953](#)), which are commonly employed in the literature but are only valid for defects that produce a severe degradation of the profile. As expected, they differ from the small-defect case for the Gaussian and sinusoidal defects, whereas they coincide for the spherical and parallelism error. We have generalized the aperture finesse presented by Atherton et al. ([1981](#)) to the crystalline case and we have deduced an analytical expression for the blueshift of a telecentric etalon. The derived expressions show a good agreement with results obtained from numerical simulations of the spectral profile.

Regarding their imaging performance, we have shown that, in a collimated mount, the PSF is proportional to that of an ideal diffraction-limited instrument. The proportionality factor is given by the spectral profile of the etalon. This implies that convolution with the object cannot be applied because the PSF is not space invariant. A monochromatic decrease of the S/N is then expected from the center to the borders of the image. However, the decay of monochromatic transmission can be dramatic if variations of the optical thickness do not preserve the peak shift low compared to the width of the profile. In a perfect telecentric etalon the PSF remains the same from point to point but strongly depends on the wavelength over the transmission profile. This gives rise to artificial velocities and magnetic fields, which can only be calibrated in a first approximation.

We have argued that fluctuations of the optical path due to defects are averaged in collimated setups and only affect at first order to the transmission as we go off axis. Stray light is also expected if microroughness errors are present. However, the PSF shape remains equal and symmetric all over the FOV. In a telecentric setup, imperfections in the optical path produce a change on the PSF pixel-to-pixel and further contribute to artificial velocity and magnetic field signals. In the case that two or more etalons are combined to increase the effective free spectral range and/or to improve the resolution, the errors can

be amplified in both mounts and may also produce large local transmission variations in the telecentric configuration because of the different shifts of the spectral profiles due to different local thicknesses.

We have added in our discussion the effect of the quasi-monochromatic nature of the measurements due to the finite passband of the etalons. In general, the response of the instrument are found to depend on the object itself, in both the collimated and the telecentric configurations. Therefore, the quasi-monochromatic PSF cannot be employed as a regular one, except for observations of spectrally flat features (i.e., in the continuum). Purely monochromatic effects—such as the decay of intensity in collimated etalons and the artificial signals originated in telecentric ones—are expected to balance out in some way, although not entirely. Therefore, quantitative effects can only be evaluated numerically.

We have finally addressed the consequences of variations on the chief ray over the FOV in telecentric setups. We have shown that they can produce a severe asymmetrization, a broadening and a shift of both the peak transmission and the PSF. These effects are nonlinear with the angle and with the f-number, and are thus very sensitive to the optical tolerances of the instrument. A decrease of the transmitted flux of photons with larger incidence angles of the chief ray has also been demonstrated, apart from a reduction the monochromatic intensity. Except for the shift of the peak, these issues are not present in the collimated configuration and when combined they lead to artificial signals in the spectrum of the measured Stokes vector and to a degradation of the image. In addition, the widening and shift of the spectral profile in imperfect (real) telecentric mounts contradict the general conception of employing this configuration to keep the passband constant over the FOV.

The consequences of imperfect telecentrism can also be applied to imperfect collimated mounts, where the etalon is illuminated by a finite f-number beam with different incidence angles on the etalon. The only difference is that defects still average over the footprint of the beam on the etalon.

Appendix A
Derivation of the Small-defect Finesse Expressions

To model real etalons with typical defects, we call ϵ the error in δ induced by an optical path defect Δs. Thus,

$$\epsilon = \frac{4\pi\Delta s}{\lambda} = \frac{\Delta s}{s}\,\delta, \tag{64}$$

where δ is given by Equation (10), λ is the wavelength of the incident beam and $s \equiv n'h\cos\theta'$ is the optical path in one pass of the beam through the etalon. Let $D(\epsilon)$ be the probability density function for ϵ, so that $D(\epsilon_0)\,d\epsilon$ is the surface fraction of the etalon aperture, dS, for which the error in δ is in the range

$(\epsilon_0, \epsilon_0 + d\epsilon)$. That is:

$$dS = D(\epsilon)d\epsilon, \tag{65}$$

where

$$d\epsilon = \frac{4\pi}{\lambda}ds. \tag{66}$$

By definition, the error distribution function is just given then by

$$D(\epsilon) = \kappa\frac{dS}{d\epsilon}, \tag{67}$$

where κ is a normalization factor introduced for $D(\epsilon)$ to represent a probability density function in a strict sense, that is, to fulfill the property

$$\int_{-\infty}^{\infty} D(\epsilon)d\epsilon = 1. \tag{68}$$

Let us call μ_d and σ_d^2 the mean and variance of the distribution respectively. Assuming that the defects are small ($\alpha = 2\sqrt{3}$), Equation (35) can then be expressed as (Sloggett 1984)

$$\mathcal{F}_d = \frac{\pi}{\sigma_d\sqrt{3}}. \tag{69}$$

By relating the variance of the defect distribution with measurable parameters of the defect, such as departure from an ideal flat surface, we can obtain useful expressions for the defect finesse.

A.1. Spherical Defect

We will focus first on the spherical-shape defect shown in Figure 4(a). If we consider an etalon with circular or parabolic symmetry and define r as the radial coordinate (Figure 22(a)), then the optical path across the etalon surface is given by

$$s = ar^2 + s_0, \tag{70}$$

with a peak-to-peak excursion $\Delta s_s = aR^2$, where a is a proportionality factor, R is the radius of the etalon, and s_0 is the optical path at $r = 0$. The differential of the optical path can be expressed just as

$$ds = 2ardr. \tag{71}$$

Therefore, Equation (66), can be cast as

$$d\epsilon = \frac{8\pi}{\lambda}ardr. \tag{72}$$

On the other hand, taking advantage of the symmetry of the problem,

$$dS = 2\pi rdr. \tag{73}$$

Substituting this expression in Equation (67) we have that D_s is a rectangular distribution that, after normalization ($\kappa = 4a\lambda^{-1}\epsilon_{\max}^{-1}$), can be written as

$$D_s(\epsilon) = \begin{cases} \epsilon_{\max}^{-1} & \text{if } 0 < \epsilon \leqslant \epsilon_{\max}, \\ 0 & \text{otherwise} \end{cases} \tag{74}$$

where $\epsilon_{\max} = (4\pi/\lambda)\Delta s_s$. This distribution is also useful for uniformly distributed random defects and for aperture defects (Sloggett 1984). Its mean is just $\mu_{d_s} = \epsilon_{\max}/2$ and its variance
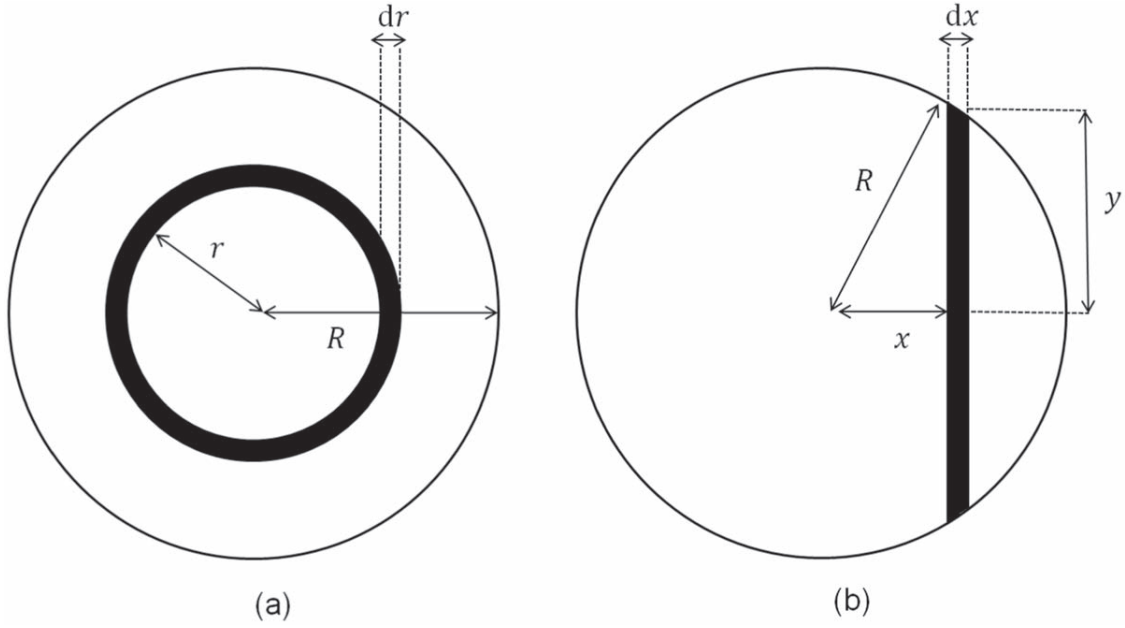
Figure 22. Coordinates employed for the calculation of the density distribution function of different defects: (a) coordinates used in the spherical defect; (b) coordinates used in both the parallelism and sinusoidal defect.

is given then by

$$\sigma_{d_s}^2 = \frac{1}{12}\epsilon_{\max}^2. \tag{75}$$

Consequently, substituting σ_{d_s} in Equation (69), we get that

$$\mathcal{F}_{d_s} = \frac{\lambda}{2\Delta s_s}. \tag{76}$$

Note that $\epsilon_{\max}$ also coincides with the FWHM of the defect distribution in this particular case. Therefore, the relation between σ_{d_s} and the FWHM is given by $w_{d_s} = 2\sqrt{3}\,\sigma_{d_s}$ and the limiting finesse is expected to coincide with that here deduced for small defects.

A.2. Gaussian Random Defect

If we now consider Figure 4(b), then we have a microrough surface with deviations from s that follow a normalized Gaussian distribution with variance Δs_g^2. In this case, the standard deviation of the distribution is obviously $\sigma_{d_g} = 4\pi\,\Delta s_g/\lambda$. Substituting this value in Equation (69),

$$\mathcal{F}_{d_g} = \frac{\lambda}{4\sqrt{3}\,\Delta s_g}. \tag{77}$$

Meanwhile, the FWHM of this distribution is related to the standard deviation as $w_{d_g} = 2\sqrt{2\ln 2}\,\sigma_{d_g}$. Therefore, the value of α will tend to $2\sqrt{2\ln 2}\,\sigma_{d_g}$ when defects dominate and the limiting finesse will differ from the finesse here deduced for small defects.

A.3. Parallelism Defect

For the parallelism defect shown in Figure 4(c), if we consider a circular etalon with radius R and define the X direction to be the direction of departure from parallelism (Figure 22(b)), the optical path depends on the x coordinate as

$$s = ax + s_0, \tag{78}$$

with a peak-to-peak deviation from parallelism $\Delta s_p = 2aR$, where a is a proportionality factor and s_0 is the optical path at $x = 0$. The differential of the optical path is simply

$$ds = a\,dx. \tag{79}$$

Therefore, using Equation (66)

$$d\epsilon = \frac{4\pi a}{\lambda}dx. \tag{80}$$

Meanwhile,

$$dS = 2y\,dx = 2(R^2 - x^2)^{1/2}dx, \tag{81}$$

and, substituting in Equation (64) we have that

$$x = \frac{\epsilon\lambda}{4\pi a}. \tag{82}$$

By replacing x in Equation (67) and restricting to $|\epsilon| \leqslant \epsilon_{\max}/2$, where $\epsilon_{\max} = (4\pi/\lambda)\Delta s_p$, we can express

$$D_p(\epsilon) = \kappa\frac{\lambda}{2\pi}\left[R^2 - \left(\frac{\lambda}{4\pi a}\right)^2\epsilon^2\right]^{1/2}. \tag{83}$$

The normalization constant is given in this case by $\kappa = (\pi a R^2)^{-1}$. We can cast this equation more elegantly as

$$D_p(\epsilon) = \begin{cases} 4/(\pi\epsilon_{\max})[1 - 4\epsilon^2/\epsilon_{\max}^2]^{1/2} & \text{if } |\epsilon| \leqslant \epsilon_{\max}/2 \\ 0 & \text{otherwise} \end{cases}, \tag{84}$$

Note that the mean is zero as it is symmetrical about $\epsilon = 0$. The variance is given by

$$\sigma_{d_p}^2 = \frac{\epsilon_{\max}^2}{16}. \tag{85}$$

Then, $\sigma_{d_p} = \pi \Delta s_p / \lambda$ and the defect finesse (Equation (69)) can be written as

$$\mathcal{F}_{d_p} = \frac{\lambda}{\sqrt{3}\, \Delta s_p}. \tag{86}$$

The FWHM of this distribution is given by $w_{d_p} = 2^{-1}\sqrt{3}\, \epsilon_{max} = 2\sqrt{3}\, \sigma_{d_p}$. As for the spherical defect, the limiting value of α is expected then to tend to $2\sqrt{3}$ for large defects.

A.4. Sinusoidal Defect

Consider finally an etalon with an optical path roughness given by a sinusoid of peak-to-peak amplitude Δs_a, as shown in Figure 4(d). If we consider a circular etalon with radius R and define the X direction to be the direction of the sinusoid, then the optical path has a dependence with the x coordinate

$$s = \frac{\Delta s_a}{2} \sin \omega x + s_0, \tag{87}$$

where Δs_a is peak-to-peak deviation amplitude of the sinusoid, ω is its (spatial) frequency of oscillation, and s_0 is the optical path at $x = 0$. The differential of the optical path is given by

$$ds = \frac{\Delta s_a}{2} \omega \cos \omega x\, dx. \tag{88}$$

Therefore, using Equation (66)

$$d\epsilon = \frac{2\pi\omega}{\lambda} \Delta s_a \sqrt{1 - 4(s - s_0)^2/\Delta s_a^2}\, dx, \tag{89}$$

and, according to Equation (64),

$$d\epsilon = \frac{2\pi\omega}{\lambda} \Delta s_a \sqrt{1 - (\epsilon\lambda)^2/(2\pi \Delta s_a)^2}\, dx. \tag{90}$$

Meanwhile, for a circular etalon

$$dS = 2dx = 2(R^2 - x^2)^{1/2}dx, \tag{91}$$

where x is related to ϵ by

$$x = \frac{1}{\omega}\left[\arcsin\left(\frac{2(s - s_0)}{\Delta s_a}\right) + 2\pi n\right]. \tag{92}$$

The term $2\pi n$, accounts for the multiplicity of the solutions, where $n = 0, \pm 1, \pm 2, \ldots, \pm N$, and

$$N = \frac{1}{2\pi}\left[\omega R - \arcsin\left(\frac{2(s - s_0)}{\Delta s_a}\right)\right]. \tag{93}$$

Then, in the range $|\epsilon| \leqslant \epsilon_{max}/2$, with $\epsilon_{max} = (4\pi/\lambda)\Delta s_a$,

$$D(\epsilon) \simeq \kappa \frac{\lambda\sqrt{R^2 - \omega^{-2}(\arcsin[2(s-s_0)/\Delta s_a] + 2\pi n)^2}}{\pi\omega\Delta s_a[1 - (\epsilon\lambda)^2/(2\pi\Delta s_a)^2]^{1/2}}. \tag{94}$$

If we approximate $R^2 \gg x^2$, which is valid for fast spatial modulations of the sinusoidal defect and for $n \ll N$

$$D(\epsilon) \simeq \kappa \frac{R\lambda}{\pi\omega\Delta s_a \sqrt{1 - (\epsilon\lambda)^2/(2\pi\Delta s_a)^2}}$$
$$= \kappa \frac{2R}{\omega\sqrt{\epsilon_{max}^2/4 - \epsilon^2}}, \tag{95}$$

where the normalization constant can be shown to be given by $\kappa = \omega(2R\pi)^{-1}$, then the probability density function can be cast as

$$D_a(\epsilon) = \begin{cases} \pi^{-1}[\epsilon_{max}^2/4 - \epsilon^2]^{-1/2} & \text{if } |\epsilon| \leqslant \epsilon_{max}/2 \\ 0 & \text{otherwise} \end{cases}, \tag{96}$$

Due to the symmetry of the distribution, $\mu_a = 0$ and

$$\sigma_{d_a}^2 = \frac{\epsilon_{max}^2}{8}. \tag{97}$$

Then, the finesse defect can be expressed as (Equation (69))

$$\mathcal{F}_{d_a} = \frac{\lambda}{\Delta s_a \sqrt{6}}. \tag{98}$$

The FWHM of this distribution, w_{d_a}, is just ϵ_{max}. Therefore, $w_{d_a} = 2\sqrt{2}\,\sigma \simeq 2.83\sigma_{d_a}$. The value of α will tend then to $2\sqrt{2}$ when defects dominate and the limiting finesse will differ from the one here deduced for small defects.

A.5. Aperture Finesse and Spectral Shift in Telecentric Configuration

Following the arguments of Sloggett (1984), we can also deduce an expression for the aperture finesse. Let us consider that the etalon with refraction index n' is at the focal plane of a lens of radius R. Each point of the etalon will receive rays coming from all parts of the lens. In this case, the phase error corresponding to each ray with incidence angle θ from a medium with refraction index n, compared to normal incidence and for $\theta \ll 1$, is given by

$$\epsilon = \frac{4\pi n' h}{\lambda}(1 - \cos\theta') \simeq \frac{n^2 m \pi \theta^2}{n'^2}, \tag{99}$$

where $m = 2n'h\lambda^{-1}$ is the interferential order for $\theta \simeq 0$. First, we shall calculate the density distribution of the incidence angle θ in the etalon, $D(\theta)$. Similarly to Equation (67)

$$D(\theta) = \kappa \frac{dS}{d\theta}. \tag{100}$$

Here dS represents the portion of the lens corresponding to the angles of the rays coming to the etalon with angles between (θ_0, $\theta_0 + d\theta$). Let r be the radial coordinate of the lens, then

$$dS = 2\pi r\, dr. \tag{101}$$

For small angles, $r \simeq \theta f$ and $dr \simeq \theta f^2 d\theta$, where f is the focal length of the system, thus

$$dS = 2\pi f^2 \theta d\theta, \tag{102}$$

and, for θ in the range $(0, \theta_m)$, where θ_m is the maximum incidence angle, the angular distribution is simply

$$D(\theta) = 2\pi\kappa f^2 \theta, \tag{103}$$

where $\kappa = (\pi f^2 \theta_m^2)^{-1}$ after normalization. To obtain $D(\epsilon)$ we can use the relation

$$D(\theta)d\theta = D(\epsilon)d\epsilon \tag{104}$$

and

$$\frac{d\theta}{d\epsilon} = \frac{n'^2}{2\pi n^2 m\theta}. \tag{105}$$

Then,

$$D_{\mathrm{f}}(\epsilon) = \begin{cases} n'^2(n^2m\pi\theta_{\mathrm{m}}^2)^{-1} & \text{if } 0 < \epsilon < \epsilon_{\max}, \\ 0 & \text{otherwise} \end{cases} \quad (106)$$

where $\epsilon_{\max} = n^2m\pi\theta_{\mathrm{m}}^2 n^{-2}$. Notice that the density distribution is a rectangular function, as for the spherical defect. Actually, we can rewrite Equation (106) as

$$D_{\mathrm{f}}(\epsilon) = \begin{cases} 1/(2\sqrt{3}\,\sigma_{d_{\mathrm{f}}}) & 0 < \epsilon < 2\sqrt{3}\,\sigma_{d_{\mathrm{f}}}, \\ 0 & \text{otherwise} \end{cases} \quad (107)$$

which only differs from Equation (74) by a constant that is not relevant because both distributions are normalized. The mean value of the distribution and its variance turn out to be

$$\mu_{d_{\mathrm{f}}} = \frac{\epsilon_{\max}}{2} = \frac{1}{2}\frac{n^2m\pi\theta_{\mathrm{m}}^2}{n'^2}, \quad (108)$$

$$\sigma_{d_{\mathrm{f}}}^2 = \frac{\epsilon_{\max}^2}{12} = \frac{1}{12}\left(\frac{n^2m\pi\theta_{\mathrm{m}}^2}{n'^2}\right)^2, \quad (109)$$

Using Equation (35) and $\Omega = \pi\theta_{\mathrm{m}}^2$, the aperture finesse can be deduced to be (Equation (69))

$$\mathcal{F}_{d_{\mathrm{f}}} = \frac{2\pi}{m\Omega}\frac{n'^2}{n^2}. \quad (110)$$

The FWHM of this distribution is therefore also given by $w_{d_{\mathrm{f}}} = 2\sqrt{3}\,\sigma_{d_{\mathrm{f}}}$. Since α tends for $2\sqrt{3}$ for both the small and large defect regime, the limiting finesse defect will coincide with this expression.

Since the mean value of this distribution is not zero (Equation (108)), the profile is expected to shift toward the blue. Because the density distribution is symmetrical about its mean, the retardance corresponding to the peak wavelength in telecentric configuration, λ_t, will be related to the retardance at the peak wavelength for collimated illumination by

$$\delta(\lambda_t) = \delta(\lambda_0) + \mu_{d_{\mathrm{f}}}(\lambda_0). \quad (111)$$

If we relate the maximum incidence angle with the f-number of the incident beam through $\theta_{\mathrm{m}} = (2f\#)^{-1}$, the transmission peak then depends on λ_0 as

$$\lambda_t = \frac{16(f\#)^2 n'^2\lambda_0}{16(f\#)^2 n'^2 + n^2}, \quad (112)$$

and the blueshift $\Delta\lambda_0 = \lambda_t - \lambda_0$ is then given by

$$\Delta\lambda_0 = -\frac{\lambda_0}{16(f\#)^2 + n^2}\frac{n^2}{n'^2}. \quad (113)$$

For large values of the f-number compared to the refraction index of the medium in which the etalon is immersed, we can simplify this expression to

$$\Delta\lambda_0 \simeq -\frac{\lambda_0}{16(f\#)^2}\frac{n^2}{n'^2}. \quad (114)$$

Appendix B
Transmitted Electric Field

If we denote by subindices 1, 2, … N the first, second and successive transmitted rays until the Nth ray in Figure 1, then their electric fields are given, following to the notation presented in Section 2, by

$$\begin{aligned}
\mathbf{E}_1^{(\mathrm{t})} &= tt'e^{i\delta/2}\mathbf{E}^{(\mathrm{i})}, \\
\mathbf{E}_2^{(\mathrm{t})} &= tt'r^2e^{i(\delta/2+\delta)}\mathbf{E}^{(\mathrm{i})}, \\
\mathbf{E}_3^{(\mathrm{t})} &= tt'r^4e^{i(\delta/2+2\delta)}\mathbf{E}^{(\mathrm{i})}, \\
&\vdots \\
\mathbf{E}_N^{(\mathrm{t})} &= tt'r^{2(N-1)}e^{i(\delta/2+(N-1)\delta)}\mathbf{E}^{(\mathrm{i})},
\end{aligned} \quad (115)$$

where a global phase $\delta/2$ has been included to take into account that the electric field is retarded in the first pass with respect one to the incident by the amount $2\pi\lambda^{-1}n'h\cos\theta'$. The transmitted electric field would be the superposition of each individual ray. Note that the transmitted rays follow a geometric sequence of common ratio $r^2e^{i\delta}$. As $r < 1$, the sum of all rays can be expressed as

$$\mathbf{E}^{(\mathrm{t})} = \frac{Te^{i\delta/2}}{1 - R\,e^{i\delta}}\,\mathbf{E}^{(\mathrm{i})}. \quad (116)$$

The global phase is usually neglected because it disappears when calculating the transmitted intensity by complex conjugating the electric field. However, this phase cannot be neglected for telecentric illumination of the etalon because it depends on the incidence angle and thus on the pupil coordinates.

ORCID iDs

F. J. Bailén ⓘ https://orcid.org/0000-0002-7318-3536
D. Orozco Suárez ⓘ https://orcid.org/0000-0001-8829-1938
J. C. del Toro Iniesta ⓘ https://orcid.org/0000-0002-3387-026X

References

Álvarez-Herrero, A., Belenguer, T., Pastor, C., et al. 2006, Proc. SPIE, 6265, 62652G
Atherton, P. D., Reay, N. K., Ring, J., & Hicks, T. R. 1981, OptEn, 20, 806
Beckers, J. M. 1998, A&AS, 129, 191
Bendlin, C., Volkmer, R., & Kneer, F. 1992, A&A, 257, 817
Bonaccini, D., Righini, A., Cavallini, F., & Ceppatelli, G. 1989, A&A, 217, 368
Born, M., & Wolf, E. 1999, Principles of Optics (Cambridge: Cambridge Univ. Press)
Cavallini, F. 2006, SoPh, 236, 415
Chabbal, R. J. 1953, J. Rech. CNRS, 24, 138
Doerr, H.-P., von der Lühe, O., II, & Kentischer, T. J. 2008, Proc. SPIE, 7014, 701417
Gary, G. A., West, E. A., Rees, D. E., et al. 2006, in ASP Conf. Ser. 358, Solar Polarization 4, ed. R. Casini & B. W. Lites (San Francisco, CA: ASP), 181
Hecht, E. 1998, Optics (4th ed.: Boston, MA: Addison Wesley Longman)
Hernandez, G. 1988, Fabry-Perot Interferometers (Cambridge: Cambridge Univ. Press)
Hill, R. M. 1963, AcOpt, 10, 141
Kentischer, T. J., Schmidt, W., Sigwarth, M., & Uexkuell, M. V. 1998, A&A, 340, 569
Mahajan, V. N. 1991, Tutorial Texts in Optical Engineering (Bellingham: SPIE)
Martínez Pillet, V., Del Toro Iniesta, J. C., Álvarez-Herrero, A., et al. 2011, SoPh, 268, 57
Meaburn, J. 1976, Astrophysics and Space Science Library, 56, 279
Puschmann, K. G., Denker, C., Balthasar, H., et al. 2013, OptEn, 52, 081606
Quintero Noda, C., Asensio Ramos, A., Orozco Suárez, D., & Ruiz Cobo, B. 2015, A&A, 579, A3
Scharmer, G. B. 2006, A&A, 447, 1111

Scharmer, G. B., Narayan, G., Hillberg, T., et al. 2008, ApJL, 689, L69
Sloggett, G. J. 1984, ApOpt, 23, 2427
Solanki, S. K., del Toro Iniesta, J. C., Woch, J., et al. 2015, in IAU Symp. 305, Polarimetry 305, ed. K. N. Nagendra et al. (Cambridge: Cambridge Univ. Press), 108
Steel, W. H. 1986, Interferometry (Cambridge: Cambridge Univ. Press)

Title, A. M. 1970, in IAU Symp. 41, New Techniques in Space Astronomy, ed. F. Labuhn & R. Lust (Dordrecht: Reidel), 325
van Noort, M. J., & Rouppe van der Voort, L. H. M. 2008, A&A, 489, 429
Vaughan, J. M. 1989, The Adam Hilger Series on Optics and Optoelectronics (Bristol: Hilger)
von der Lühe, O., & Kentischer, T. J. 2000, A&AS, 146, 499

Erratum

Eq. (61) should read

$$I(\xi, \eta; \lambda_0) = \int_0^\infty T(\lambda) g(\xi, \eta; \lambda - \lambda_0) \left[O(\xi, \eta; \lambda) * \mathcal{S}_0(\xi, \eta) \right] d\lambda, \qquad (4.1)$$

where $\mathcal{S}_0 \equiv [2J_1(z)/z)^2]$ and $*$ denotes the convolution operator. Meanwhile, the general image formation equation (without assuming spatial invariance of the PSF) would be given by

$$I(\xi, \eta; \lambda_0) = \int_0^\infty T(\lambda) \int_{-\infty}^\infty \int_{-\infty}^\infty \left[O(\xi_0, \eta_0; \lambda) \cdot \mathcal{S}(\xi_0, \eta_0; \xi, \eta; \lambda - \lambda_0) \right] d\xi_0 \, d\eta_0 \, d\lambda. \tag{4.2}$$

Paper II: The anisotropic case

On Fabry–Pérot Etalon-based Instruments. II. The Anisotropic (Birefringent) Case

F. J. Bailén , D. Orozco Suárez , and J. C. del Toro Iniesta
Instituto de Astrofísica de Andalucía (CSIC), Apdo. de Correos 3004, E-18080 Granada, Spain; fbailen@iaa.es, orozco@iaa.es, jti@iaa.es

Abstract

Crystalline etalons present several advantages with respect to other types of filtergraphs when employed in magnetographs, especially that they can be tuned by only applying electric fields. However, anisotropic crystalline etalons can also introduce undesired birefringent effects that corrupt the polarization of the incoming light. In particular, uniaxial Fabry–Pérots, such as LiNbO$_3$ etalons, are birefringent when illuminated with an oblique beam. The farther the incidence from the normal, the larger the induced retardance between the two orthogonal polarization states. The application of high voltages, as well as fabrication defects, can also change the direction of the optical axis of the crystal, introducing birefringence even at normal illumination. Here we obtain analytical expressions for the induced retardance and for the Mueller matrix of uniaxial etalons located in both collimated and telecentric configurations. We also evaluate the polarimetric behavior of Z-cut crystalline etalons with the incident angle, with the orientation of the optical axis, and with the f-number of the incident beam for the telecentric case. We study artificial signals produced in the output Stokes vector in the two configurations. Last, we discuss the polarimetric dependence of the imaging response of the etalon for both collimated and telecentric setups.

Key words: instrumentation: polarimeters – instrumentation: spectrographs – methods: analytical – polarization – techniques: polarimetric – techniques: spectroscopic

1. Introduction

Narrowband tunable filters are widely used in solar physics to carry out high-precision imaging in selected wavelength samples. In the particular case of Fabry–Pérot etalons, the sampling can be done by modifying the refraction index of the material, changing the width of the Fabry–Pérot cavity, or both. Naturally, temperature fluctuations and variations of the tilt angle of the etalon plates with respect to the incident light change their tunability as well.

The more common technology used in Fabry–Pérots in ground-based instruments is that of piezo-stabilized etalons (e.g., Kentischer et al. 1998; Puschmann et al. 2006; Scharmer et al. 2008). For space applications, however, they are very demanding in terms of total weight or mounting, to name a few. Solid etalons based on electro-optical and piezo-electric material crystals are way lighter and do not need the use of piezo-electric actuators, thus avoiding the introduction of mechanical vibrations in the system. Examples are LiNbO$_3$- or MgF$_2$-based etalons and liquid crystal etalons (e.g., Álvarez-Herrero et al. 2006; Gary et al. 2007), which can be tuned after modification of a feeding voltage signal. Crystals used in these Fabry–Pérot etalons are typically birefringent and therefore able to modify the polarization of light. The risk for uncertainties in the measured Stokes parameters, hence altering the polarimetric efficiencies of the system, is not null and should be assessed.

In liquid crystal etalons, the optical axis direction depends on the electric field applied, and therefore birefringence will change not only with the incident direction but also when tuning the etalon. To avoid this effect, lithium niobate or magnesium fluoride etalons can be used with given cut configurations that select their constant optical axis. Etalons with the optical axis parallel to the reflecting surfaces (Y-cut) are used sometimes (e.g., Netterfield et al. 1997), but the Z-cut configuration is often preferred (Martínez Pillet et al. 2011; Solanki et al. 2015), since the optical axis is perpendicular to

the reflecting surfaces of the etalon and, as a result, no polarization effects are expected for normal illumination. Although close to normal, typical instruments receive light from a finite aperture. Hence, spurious polarization effects cannot be neglected without an analysis. Moreover, local inhomogeneities of the crystals and other fabrication defects can modify the crystalline (birefringent) properties of the etalons.

Most efforts have been driven, so far, to study the propagation of the ordinary and extraordinary ray separately in some particular cases. One example is the work by Doerr et al. (2008), where spurious polarization effects due to oblique illumination in Fabry–Pérots have been studied numerically by considering the influence of thin film multilayer coatings in isotropic etalons. Another example can be found in Vogel & Berroth (2003), where experimental results on the polarization-dependent transmission in liquid (uniaxial) crystals are presented. On the other hand, Del Toro Iniesta & Martínez Pillet (2012) modeled the polarimetric response of uniaxial etalons as retarders to include their effect on the polarimetric efficiency of modern magnetographs, and Lites (1991) obtained an analytical expression for the Mueller matrix of a linear retarder (i.e., a crystalline Fabry–Pérot with very low reflectivity) taking into account multiple reflections on its surfaces. In Zhang et al. (2017) an accurate and efficient algorithm describing the electric field propagation in both isotropic and anisotropic etalons (and crystals in general) is presented. The study takes into consideration crosstalks between orthogonally polarized components and the effect of multilayer coatings, but no analytical expressions are obtained. A general theory of anisotropic etalons describing its polarimetric properties has not yet been presented to our knowledge.

This is the second in our series on Fabry–Pérot etalon-based instruments. After a comprehensive view of isotropic etalons (interferometers made with isotropic materials) and a discussion on the two most typical configurations for etalons in astronomical instruments, here we concentrate on the anisotropic case. We

carry out an analytical and numerical study of the polarimetric properties of uniaxial crystalline etalons (also applicable to liquid crystal etalons), to evaluate the effect of the birefringence introduced when the ray direction and the optical axis of the crystals are not parallel. We will neglect the effect of multilayer coatings for the sake of simplicity since their effect is expected to be many orders of magnitude smaller than that of the results presented here (Doerr et al. 2008; Zhang et al. 2017).

First, we study the induced birefringence in crystalline etalons (Section 2); second, we derive the Mueller matrix of the etalon (Section 3); and third, we focus on its polarimetric response (Section 4). Special emphasis is put into etalons in a telecentric configuration since misalignments appear in them in a natural way. We discuss the effects in the point-spread function (PSF) of the system (Section 5), and we analyze qualitatively the impact of birefringent etalons on solar instruments (Section 6). A thorough analysis on the consequences of using a Fabry–Pérot on real instruments is considered in the next work of this series of papers. Finally, we draw the main conclusions (Section 7).

2. Birefringence Induced in Crystalline Etalons

Crystalline uniaxial etalons present a given direction called *optical axis*, $\hat{\mathbf{e}}_3$, along which the two orthogonal components of the electric field stream with the same velocity. If the wavefront normal, $\hat{\mathbf{s}}$, is parallel to $\hat{\mathbf{e}}_3$, then the orthogonal components of the electric field travel with the same velocity, as it happens for normal illumination in Z-cut crystalline etalons. In such a situation, birefringence effects are not present. However, in any other direction, the propagation of the electric field components should be studied separately because they travel across a medium with different refraction indices.

For any given ray direction, $\hat{\mathbf{t}}$, the plane formed between $\hat{\mathbf{e}}_3$ and $\hat{\mathbf{t}}$ is called the *principal plane* of the medium.[1] Then, the electric field vector can be considered as the sum of two incoherent orthogonally polarized components:

$$\mathbf{E} = \mathbf{E}_o + \mathbf{E}_e, \tag{1}$$

where $\mathbf{E}_o$ and $\mathbf{E}_e$ are the so-called *ordinary* and *extraordinary* electric field components. The propagation of a light beam can be thought of as that of two linearly polarized beams, one having a velocity independent of direction, the ordinary beam, and the other with a velocity depending on direction, the extraordinary beam. The ordinary beam propagates like any beam through an isotropic medium. That is not the case for the extraordinary beam, whose energy does not propagate along the wavefront normal (but along the ray direction), unless this is parallel to the optical axis.

Figure 1 shows the splitting of an incoming ray with incidence angle θ when traveling through an etalon with its optical axis misaligned with respect to the surface normal. The ordinary and extraordinary rays propagate along different directions and, thus, traverse different optical paths at the exit.

The first measurable effect of the different propagations of both rays is a phase difference between the ordinary and the extraordinary beams because they split, and behave independently, except if $\hat{\mathbf{s}} \cdot \hat{\mathbf{e}}_3 = 1$. The difference in phase produced between every two successive extraordinary and ordinary
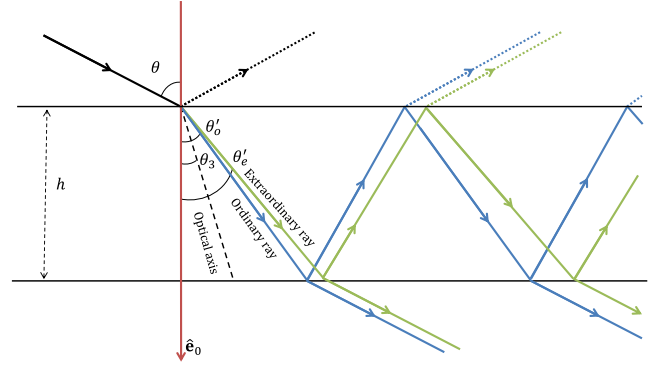
Figure 1. Layout of a ray with a certain incident angle θ entering an uniaxial etalon (black) whose optical axis is not parallel to the surface normal. (The convention for a Z-cut crystal calls Z that normal, but we reserve Z for the axis along the ray direction; see text for details.) The ray is split into two orthogonal rays, the ordinary (blue) and the extraordinary (green), each one refracted with different angles $\theta'_o \neq \theta'_e$ and thus having different optical paths and different phases when either transmitting or reflecting at the etalon surfaces.

beams due to its different geometrical paths through an etalon (Figure 1) is simply given by

$$\varphi \equiv \delta_e - \delta_o = \frac{4\pi h}{\lambda}(n_e \cos\theta'_e - n_o \cos\theta'_o), \tag{2}$$

where subindices o and e refer to the ordinary and extraordinary rays, respectively.[2]

Within an etalon, the wavefront direction vectors of the ordinary and extraordinary rays depend on the incident wavefront direction and on the refraction index for both the ordinary and extraordinary components. The geometrical paths along the ray and wavefront directions coincide for the ordinary ray but not for the extraordinary ray. Furthermore, the refraction index of the extraordinary beam depends on the direction $\hat{\mathbf{s}}$, so the propagation of the extraordinary component is more complex than that of the ordinary beam (Born & Wolf 1999):

$$\frac{1}{n_e^2(\gamma)} = \frac{1}{n_o^2}\cos^2\gamma + \frac{1}{n_3^2}\sin^2\gamma, \tag{3}$$

where γ is the angle between $\hat{\mathbf{s}}$ and $\hat{\mathbf{e}}_3$ and n_3 is the refraction index for an electric field vibrating along the optical axis of the etalon. Notice that $n_e = n_o$ if $\gamma = 0$.

The ordinary and extraordinary components propagate such that their transmitted electric field vectors can be given by Equation (45) of Paper I, each with their respective retardance:

$$\mathbf{E}_o^{(t)} = \frac{\sqrt{\tau_o}}{1-R}\frac{e^{i\delta_o/2} - Re^{-i\delta_o/2}}{1 + F\sin^2(\delta_o/2)}\mathbf{E}_o^{(i)}, \tag{4}$$

$$\mathbf{E}_e^{(t)} = \frac{\sqrt{\tau_e}}{1-R}\frac{(e^{i[\delta_o+\varphi]/2} - Re^{-i[\delta_o+\varphi]/2})}{1 + F\sin^2([\delta_o+\varphi]/2)}\mathbf{E}_e^{(i)}, \tag{5}$$

where τ_o and τ_e account for possible different values of the absorptance of the etalon for the ordinary and extraordinary

---

[1] The principal plane is also defined as that containing the optical axis, $\hat{\mathbf{e}}_3$, and the wavefront normal, $\hat{\mathbf{s}}$. Both definitions are equivalent since $\hat{\mathbf{t}}$ and $\hat{\mathbf{s}}$ are coplanar with $\hat{\mathbf{e}}_3$.

[2] We shall be using the basic nomenclature of Paper I for the sake of consistency. Hence, we refer the reader to that paper for the possible missing definitions.
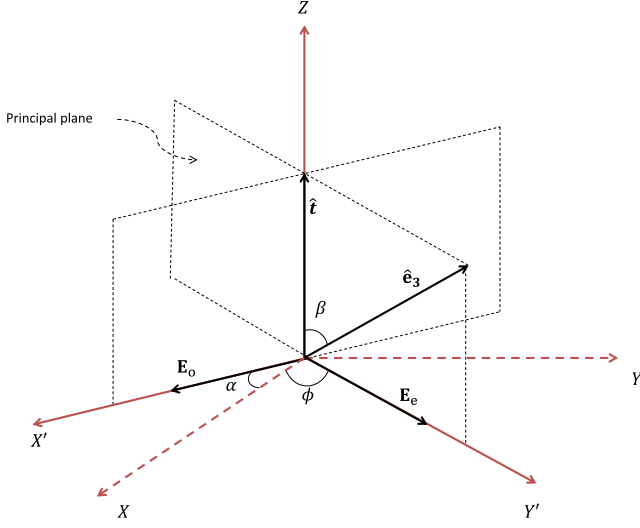
Figure 2. General reference frame *XYZ*, where the ray direction $\hat{\mathbf{t}}$ of the etalon coincides with *Z*. The ordinary electric field component, $\mathbf{E}_o$, is contained on a plane perpendicular to the principal plane and forms an angle α with *X* that depends on the $\hat{\mathbf{e}}_3$ direction. Spherical coordinates to describe the wavefront direction unitary vector $\hat{s}$ are also included: β is the polar angle (measured from *Z*), and ϕ is the azimuthal angle (measured from *X*).

rays. Note that even for $R = 0$ a retardance $\varphi/2$ is induced between the ordinary and extraordinary rays.

Without loss of generality, to describe the electromagnetic field components, we can choose a reference frame in which the *Z*-axis coincides with the ray direction, the Poynting vector direction (see Figure 2). This choice is kept for any incident ray. For the sake of simplicity, let us make the *X*-axis coincide with the direction of vibration of the ordinary electric field. The *Y*-axis is then parallel to the plane that contains the extraordinary electric field. In this reference frame, the transmitted electric field has only two orthogonal components, $\mathbf{E}_x^{(t)}$ and $\mathbf{E}_y^{(t)}$, whose propagation can be expressed in matrix form as

$$\begin{pmatrix} \mathbf{E}_x^{(t)} \\ \mathbf{E}_y^{(t)} \end{pmatrix} = \mathbf{H} \begin{pmatrix} \mathbf{E}_o^{(i)} \\ \mathbf{E}_e^{(i)} \end{pmatrix}, \tag{6}$$

where $\mathbf{H}$ is the so-called Jones matrix. Since the ordinary and extraordinary components are orthogonal and behave independently, $\mathbf{H}$ is diagonal in the chosen reference frame. Their components are given by the factor relating $\mathbf{E}^{(i)}$ and $\mathbf{E}^{(t)}$ in Equations (4) and (5). Usually, an arbitrary choice of the *X* and *Y* directions will not coincide with the plane containing $\mathbf{E}_o^{(i)}$ and $\mathbf{E}_e^{(i)}$, because the principal plane orientation depends on both the optical axis and ray directions. In that case, a rotation of the reference frame about *Z* is needed, as discussed in depth in Section 3.2.

Equation (6) is valid only for the propagation of $\mathbf{E}_o^{(i)}$ and $\mathbf{E}_e^{(i)}$ in a beam strictly collimated. As pointed out in Paper I, to obtain an expression valid for converging illumination, we have to integrate both the ordinary and extraordinary rays all over the aperture of the beam (the pupil in case of telecentric illumination) and get $\widetilde{\mathbf{E}}_o^{(t)}$ and $\widetilde{\mathbf{E}}_e^{(t)}$ (see Equation (48) of

Paper I). Then, it is easily seen that an equation like

$$\begin{pmatrix} \widetilde{\mathbf{E}}_x^{(t)} \\ \widetilde{\mathbf{E}}_y^{(t)} \end{pmatrix} = \widetilde{\mathbf{H}}' \begin{pmatrix} \mathbf{E}_o^{(i)} \\ \mathbf{E}_e^{(i)} \end{pmatrix} \tag{7}$$

can be written, where the linearity of the problem yields the new Jones matrix elements, $\widetilde{\mathbf{H}}'_{ij}$, as direct integrals of the old ones. Since the principal plane differs for each particular ray direction, a rotation of the Jones matrix needs also to be added, as thoroughly explained in Section 4.3.

3. Mueller Matrix for Crystalline Etalons

3.1. General Expression

Due to the birefringence induced by anisotropic crystalline etalons, uniaxial Fabry–Pérot filters show different responses for each of the incoming Stokes vector components. The more general way to study the polarization response of these etalons is by using the Mueller matrix formulation. According to Jefferies et al. (1989), the elements of the Mueller matrix, M_{ij}, are given by

$$M_{ij} = \frac{1}{2}\mathrm{Tr}[\sigma_i \mathbf{H} \sigma_j \mathbf{H}^\dagger], \tag{8}$$

where σ_i ($i = 0, 1, 2, 3$) are the identity and Pauli matrices with the sorting convention employed in Del Toro Iniesta (2003). In case $\mathbf{E}_x^{(t)}$ and $\mathbf{E}_y^{(t)}$ are parallel to $\mathbf{E}_o^{(i)}$ and $\mathbf{E}_e^{(i)}$, as described in the previous section, $\mathbf{H}$ is diagonal and the Mueller matrix can be expressed in the form

$$\mathbf{M} = \begin{pmatrix} a & b & 0 & 0 \\ b & a & 0 & 0 \\ 0 & 0 & c & -d \\ 0 & 0 & d & c \end{pmatrix}, \tag{9}$$

whose coefficients are given by

$$a = \frac{1}{2}(H_{11}H_{11}^* + H_{22}H_{22}^*),$$

$$b = \frac{1}{2}(H_{11}H_{11}^* - H_{22}H_{22}^*),$$

$$c = \frac{1}{2}(H_{22}H_{11}^* + H_{11}H_{22}^*),$$

$$d = \frac{i}{2}(H_{22}H_{11}^* - H_{11}H_{22}^*), \tag{10}$$

where $*$ refers to the complex conjugate. Using basic trigonometric equivalences and defining

$$\tau_{\mathrm{eff}} \equiv \sqrt{\tau_o \tau_e}, \tag{11}$$

$$\overline{\tau} \equiv \frac{\tau_o + \tau_e}{2}, \tag{12}$$

it can be deduced (Appendix B) that

$$a = \frac{\tau_{\mathrm{eff}}}{\zeta}\left[\frac{\overline{\tau}}{\tau_{\mathrm{eff}}} + \Gamma\right], \tag{13}$$

$$b = \frac{\tau_{\mathrm{eff}}}{\zeta}\Lambda, \tag{14}$$

$$c = \frac{\tau_{\mathrm{eff}}}{\zeta}\left[\Psi + \frac{\cos(\varphi/2)}{(1 - R)^2}\right], \tag{15}$$

$$d = \frac{\tau_{\text{eff}}}{\zeta}\left[\Omega - \frac{\sin(\varphi/2)}{(1-R)^2}\right], \qquad (16)$$

where

$$\zeta = \left[1 + F\sin^2\left(\frac{\delta_o}{2}\right)\right]\left[1 + F\sin^2\left(\frac{\delta_o + \varphi}{2}\right)\right], \qquad (17)$$

$$\Gamma = \frac{F}{2\tau_{\text{eff}}}\left[\tau_o\sin^2\left(\frac{\delta_o + \varphi}{2}\right) + \tau_e\sin^2\left(\frac{\delta_o}{2}\right)\right], \qquad (18)$$

$$\Lambda = \frac{F}{2\tau_{\text{eff}}}\left[\frac{\tau_o - \tau_e}{F} + \tau_o\sin^2\left(\frac{\delta_o + \varphi}{2}\right) - \tau_e\sin^2\left(\frac{\delta_o}{2}\right)\right], \qquad (19)$$

$$\Psi = \frac{F}{4}\left[R\cos\left(\frac{\varphi}{2}\right) - 2\cos\left(\delta_o + \frac{\varphi}{2}\right)\right], \qquad (20)$$

$$\Omega = -\frac{F}{4}R\sin\left(\frac{\varphi}{2}\right). \qquad (21)$$

Notably,

$$a + b = \frac{\tau_o}{1 + F\sin^2(\delta_o/2)} \qquad (22)$$

and

$$a - b = \frac{\tau_e}{1 + F\sin^2(\delta_e/2)}. \qquad (23)$$

That is, the transmission profiles (Equation (11) in Paper I) for the ordinary and extraordinary rays are recovered from the sum and subtraction of the two first elements of the Mueller matrix.

The Mueller matrix of a birefringent etalon is expressed as a function of the etalon parameters and the retardance induced between the ordinary and extraordinary rays. We can separate it into two matrices, one similar to that describing an ideal retarder, $\mathbf{M}_r$, and another one as a mirror due to the fringing effects, $\mathbf{M}_m$:

$$\mathbf{M} = \mathbf{M}_r + \mathbf{M}_m. \qquad (24)$$

If we define $\tau'_{\text{eff}} \equiv \tau_{\text{eff}}(1 - R)^{-2}$, we find that

$$\mathbf{M}_r = \frac{\tau'_{\text{eff}}}{\zeta}\begin{pmatrix} \bar{\tau}\tau'^{-1}_{\text{eff}} & 0 & 0 & 0 \\ 0 & \bar{\tau}\tau'^{-1}_{\text{eff}} & 0 & 0 \\ 0 & 0 & \cos(\varphi/2) & \sin(\varphi/2) \\ 0 & 0 & -\sin(\varphi/2) & \cos(\varphi/2) \end{pmatrix} \qquad (25)$$

and

$$\mathbf{M}_m = \frac{\tau_{\text{eff}}}{\zeta}\begin{pmatrix} \Gamma & \Lambda & 0 & 0 \\ \Lambda & \Gamma & 0 & 0 \\ 0 & 0 & \Psi & -\Omega \\ 0 & 0 & \Omega & \Psi \end{pmatrix}. \qquad (26)$$

The extraordinary direction in our numerical examples coincides with the fast axis, Y, since we set $n_e < n_o$.

It is also worth noticing that both matrices are multiplied by ζ^{-1}, which depends on both δ_0 and φ. Since these two quantities are wavelength and direction dependent, Equation (24) does not strictly correspond to the sum of a retarder and a mirror, except in the collimated, monochromatic case. In the limit when $R = 0$, since $F \equiv 4R(1 - R)^{-2}$ (Equation (13) of Paper I), the mirror matrix vanishes and the etalon Mueller matrix turns into that of an ideal retarder. On

the other hand, in the limit when $\varphi = 0$, i.e., in the limit of an isotropic etalon, it can be shown that $\mathbf{M}$ is reduced to the identity matrix except for a proportionality factor that corresponds to the transmission factor of an isotropic etalon (Equation (11) in Paper I).

Lites (1991) obtained a similar expression to Equation (24) but restricted to $R \ll 1$ and assuming both normal incidence on the etalon and that the optical axis is perpendicular to the surface normal. In that case the dependence on the wavelength and direction disappears and matrices in Equation (24) describe an ideal retarder and an ideal mirror. Our result is completely general since it is valid for any value of R and for any incident angle of the wavefront. Also notice that in Lites (1991) the plus and minus signs of d are interchanged due to the sign convention in the definition of the harmonic plane waves and, therefore, in σ_3.

Whenever $\varphi \neq 0$, the Mueller matrix becomes nondiagonal and spurious signals in the measured Stokes vector, known as *polarization crosstalk* in the solar physics jargon, are introduced. This is so because b and d introduce in Equation (9) crosstalk signals between I and Q and between U and V, respectively, if the Stokes parameters are measured after passing the light through the etalon. There are, however, some cases where these crosstalks are not relevant. For example, for totally polarized light in the Q direction, $I^{(i)} = Q^{(i)}$ and $U^{(i)} = V^{(i)} = 0$, and therefore

$$I^{(t)} = Q^{(t)} = (a + b)I^{(i)} = (a + b)Q^{(i)}. \qquad (27)$$

Hence, the transmission equation of an (ideal) isotropic etalon with the ordinary refractive index is recovered. This happens, for example, if the etalon is located after a linear polarizer with its optical axis parallel to the $+Q$ direction. In this case, artificial polarization signals do not appear.

So far, we have restricted to collimated illumination of the etalon with a convenient reference frame for expressing the Stokes vector. In telecentric configuration, the shape of the Mueller matrix, $\widetilde{\mathbf{M}}$, is the same in practice. The matrix elements, however, have a much more involved expression than in Equations (10) and (24) because they are now calculated from the integrated Jones matrix, $\widetilde{\mathbf{H}}$, across the pupil. This will be discussed in detail in Section 4.3.

3.2. Rotations of the Mueller Matrix

Since we here restrict to Z-cut crystals, propagation through the normal to the etalon reflecting surfaces does not produce any birefringence effect if the optical axis is perfectly aligned. For normal illumination, the choice of the $+Q$ direction is, then, irrelevant, since both the ordinary and extraordinary rays travel with the same velocity. For any other incident angle, a careful choice of the $+Q$ direction must be made, though. From Equation (6) it is natural to take the ordinary electric field direction ($+Q$ direction) as the X-axis. The geometry of the problem is depicted in Figure 2, where Z represents the ray direction. This direction does not necessarily coincide with the optical axis, $\hat{\mathbf{e}}_3$. Then, $\mathbf{E}_o$ vibrates in a plane perpendicular to the principal plane (see, e.g., Del Toro Iniesta 2003). A rotation of an angle α about Z is then mandatory for the Mueller matrix of the etalon to give proper account of birefringence. No further rotations are needed, though, since our reference frame is chosen such that Z coincides with the direction of observation.

The rotation angle α is given by

$$\cos \alpha = \mathbf{u}_x \cdot \mathbf{u}'_x, \tag{28}$$

where $\mathbf{u}_x = (1, 0, 0)$ is the unitary direction vector of X and $\mathbf{u}'_x$ is the unitary direction vector of X', which may be calculated from the normalized vectorial product of $\hat{\mathbf{t}} = (0, 0, 1)$ and $\hat{\mathbf{e}}_3 = (e_3^{(x)}, e_3^{(y)}, e_3^{(z)})$:

$$\mathbf{u}'_x = (e_3^{(y)}, -e_3^{(x)}, 0). \tag{29}$$

If we use polar, β, and azimuthal, ϕ, angles to describe $\hat{\mathbf{e}}_3$ (Figure 2), it is easy to find that

$$\cos \alpha = \sin \phi. \tag{30}$$

Thus,

$$\alpha = \pm(\phi - \pi/2). \tag{31}$$

This equation is valid whenever the angle between the ray direction and the optical axis, β, is different from zero. If $\beta = 0$, the wavefront normal and the optical axis are parallel, and we can set arbitrarily $\alpha = 0$ because of the rotational symmetry of the etalon about Z. It is important to remark that the polar and azimuthal angles are uncoupled in our description. That is, the retardance φ between the ordinary and extraordinary rays only depends on the angle β, whereas the rotation angle, α, only depends on ϕ.

The dual solution for α in Equation (31) reflects the intrinsic 180° ambiguity in polarimetry, as the situation described so far would be exactly the same for an ordinary electric field $-\mathbf{E}_o$. The usual convention is to employ positive signs for counter-clockwise rotations (right-handed) and negative signs for clockwise rotations. Consequently, if we set the XYZ directions as our reference frame, we should rotate the Mueller matrix of the etalon an angle $\alpha = \phi - \pi/2$ and vice versa. The Mueller matrix can then be cast as

$$\mathbf{M}_\alpha = \begin{pmatrix} a & bC_2 & bS_2 & 0 \\ bC_2 & aC_2^2 + cS_2^2 & (a-c)S_2C_2 & dS_2 \\ bS_2 & (a-c)S_2C_2 & aS_2^2 + cC_2^2 & -dC_2 \\ 0 & -dS_2 & dC_2 & c \end{pmatrix}, \tag{32}$$

where the coefficients C_2 and S_2 are given by $C_2 = \cos 2\alpha$, $S_2 = \sin 2\alpha$. This matrix gathers all the necessary information to describe the propagation of the Stokes components of any incident ray in the etalon.

4. Polarimetric Response of Birefringent Etalons

In any linear system, the polarimetric response is determined by its Mueller matrix coefficients, which are independent from the incident Stokes vector. We have shown that the Mueller matrix of crystalline etalons *only* depends on four independent coefficients and on the azimuthal orientation of the principal plane. The coefficients are related to optical parameters of the etalon (e.g., refraction indices and geometrical thickness), to the wavelength, and to the phase difference between the extraordinary and ordinary beams. The phase difference depends, at the same time, on the relative direction of the ray direction with respect to the optical axis. In this section we study the spectral behavior of these parameters in three different cases: (1) when collimated light illuminates the etalon with a certain angle with respect to the normal, (2) when the

illumination is normal to the etalon but the optical axis is misaligned, and (3) when the etalon is illuminated in telecentric configuration. We use the parameters of the SO/PHI Z-cut LiNbO₃ etalon: $n_o = 2.29$, $n_3 = 2.20$, $h = 251.63\ \mu\mathrm{m}$, $A = 0$, $R = 0.92$, and $\lambda_0 = 617.3356$ nm. We also assume that the etalon is immersed in air and that $\tau_o = \tau_e = 1$ for simplicity. The results can easily be extended to any etalon based on uniaxial crystals.

In LiNbO₃, the birefringence is typically smaller than 0.1 (e.g., Nikogosyan 2005) and can be neglected compared to n_o and n_e. Hence, a compact analytical expression for φ as a function of the incident angle and of the angle formed by the optical axis with Z can be found. Specifically, it can be shown (Born & Wolf 1999) that

$$n_e \cos \theta'_e - n_o \cos \theta_o{}' \simeq \frac{1}{\cos \theta'}(n_3 - n_o)\sin^2(\theta' - \theta_3), \tag{33}$$

where θ_3 is the angle between the optical axis and the surface normal and θ' is an arbitrary fictitious refracted angle that is given by

$$\theta' = \sin^{-1}\left(\frac{n \sin \theta}{n'}\right), \tag{34}$$

where n is the refraction index of the medium in which the etalon is immersed and n' can be taken as the average between n_3 and n_o:

$$n' \equiv \frac{n_3 + n_o}{2}. \tag{35}$$

Thus, we can rewrite Equation (2) as

$$\varphi \simeq \frac{4\pi h}{\lambda \cos \theta'}(n_3 - n_o)\sin^2(\theta' - \theta_3), \tag{36}$$

which directly depends on θ_3 and θ'. In the case θ' and θ_3 are close to zero, we can further approximate this expression as

$$\varphi \simeq \frac{8\pi h}{\lambda(2n'^2 - n^2\theta^2)}(n_3 - n_o)(n\theta - n'\theta_3)^2, \tag{37}$$

which is expressed as a function of the incident angle instead of the fictitious refracted angle. It is important to notice that when θ and θ_3 are zero, $\varphi = 0$ as predicted for normal illumination. Whenever either θ or θ_3 is different from zero, birefringent effects appear on the etalon. On the other hand, retardance increases with the width of the etalon, with the birefringence of the crystal, and with the inverse of the wavelength (it is therefore larger in the ultraviolet than in the infrared region). It is important to remark that Equation (36) is an approximate expression valid for materials with small birefringence. An exact formula of the retardance without restrictions in the magnitude of the birefringence was found by Veiras et al. (2010). The validity of Equation (36) in our numerical examples is discussed in Appendix D.

4.1. Effect of Oblique Illumination in Collimated Etalons

Consider a perfectly parallel and flat etalon with its optical axis aligned with the normal to the reflecting surfaces. Let us illuminate it with a collimated monochromatic beam with incidence angle θ. We assume that we have chosen a reference frame in which $\alpha = 0$, so the etalon Mueller matrix is given by Equation (9). Then, the etalon will behave as a wavelength-
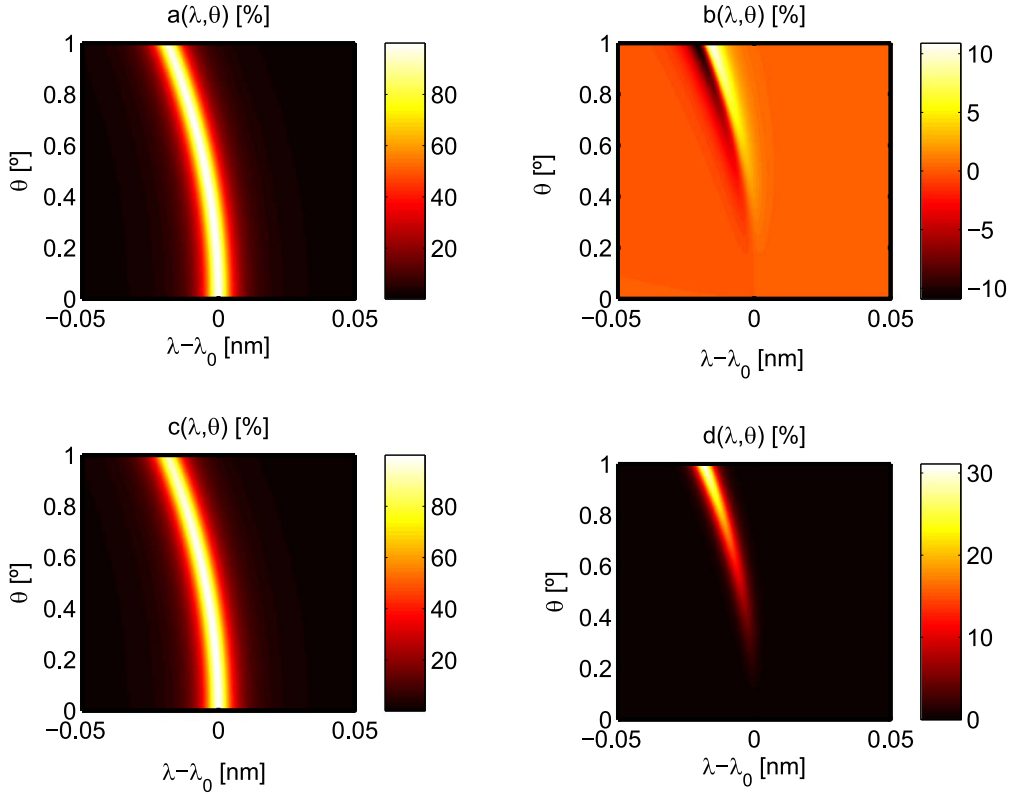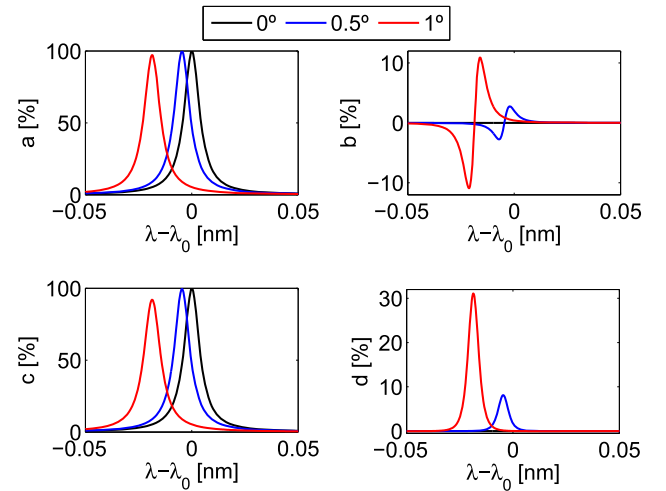
Figure 3. Variation of the a, b, c, and d coefficients of the Mueller matrix of the etalon as a function of wavelength and incident angle.

dependent retarder plus a mirror as described in Equation (24), modifying the polarization properties of the incoming Stokes vector. To see the effects, we represent the variation of the Mueller matrix coefficients as a function of the incident angle in Figure 3. We have restricted θ to vary from 0° to 1°, and we have limited the spectral range to the region $\lambda_0 \pm \delta\lambda$, where $\delta\lambda = 0.05$ nm, to cover the whole transmission profile centered at λ_0 (the location of the maximum transmission for normal incident illumination).

Notice that, at normal incidence, coefficients a and c are strictly the same and represent the *monochromatic* transmission profile of a perfect etalon, while b and d are just zero. That is, no crosstalks between Stokes parameters appear. As soon as b and d differ from zero, hence as soon as the incidence angle is larger than zero, crosstalks from I to Q, from Q to I, from U to V, and from V to U appear. In typical solar observations, the second and third contaminations are less important because the orders of magnitude of the Stokes profile signals usually are $\mathcal{O}(I) > \mathcal{O}(Q, U, V)$. To get a better insight on the relative effects of birefringence, we have plotted cuts of the images in Figure 4 at incidence angles of 0°, 0.°5, and 1°. Already apparent in Figure 3, there is a clear, nonlinear wavelength shift of the four parameters with increasing θ, as well as a decrease in the peaks of a and c. This is due to the wavelength splitting of the ordinary and extraordinary rays that can hardly be seen in these plots but will become apparent in the next section.

Parameters b and d are different from zero only when $\theta \neq 0$, as expected. Since they correspond to the off-diagonal elements of the etalon Mueller matrix, they introduce crosstalk signals in the transmitted Stokes vector. Remarkably, these spurious signals may be as much as 10% in Stokes Q (crosstalk from

Figure 4. a, b, c, and d coefficients of the Mueller matrix of the etalon as a function of wavelength for incident angles 0° (black solid line), 0.°5 (blue solid line), and 1° (red solid line).

Stokes I to Stokes Q and vice versa; see Figure 4) and up to 30% between Stokes U and Stokes V. All coefficients are positive, except for b, whose sign and magnitude depend on the separation of the ordinary and extraordinary peak wavelengths (Equation (10)). The exact antisymmetric shape with respect to the peak wavelength of the b coefficient heralds a wavelength splitting between the ordinary and extraordinary transmission profiles. Remember that these profiles coincide with $a + b$ and $a - b$, respectively, according to Equations (22) and (23). Both the sum and the subtraction of these coefficients have also been
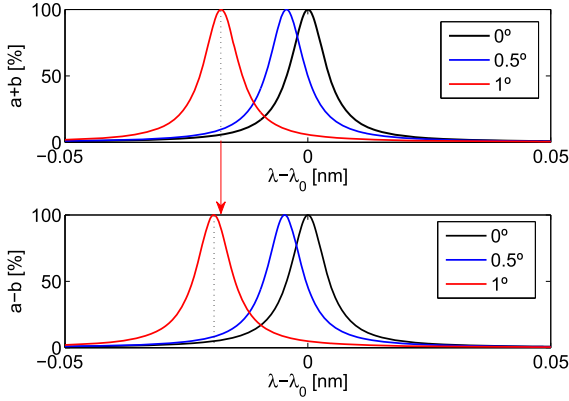
Figure 5. Spectral dependence of the transmission profile of the ordinary ray $(a + b)$ and of the extraordinary ray $(a - b)$ for different incidence angles $(\theta_3 = 0)$: $0°$ (black solid line), $0°5$ (blue solid line), and $1°$ (red solid line). The vertical solid lines pinpoint the peak location for the $1°$ case in both panels. Notice that the peaks are located at different wavelengths, as explained in the text.

plotted in order to check this property in Figure 5, where we can see that $a + b$ and $a - b$ profiles are symmetric and that both peak at different wavelengths.

So far, we have examined a flat wavelength spectrum (i.e., a continuum) of the incident light beam. However, when variations of the intensity with wavelength exist, as naturally occurs in solar absorption lines, an explicit dependence on the etalon Mueller matrix with wavelength appears. As a consequence, the crosstalk introduced between the Stokes parameters is wavelength dependent. Indeed, as we will see, the etalon can introduce asymmetries in the observed Stokes profiles, even when the input Stokes profiles are symmetric with respect to the central wavelength of the line. Figure 6 shows an example of what happens when we illuminate the etalon at different angles with synthetic Stokes I and Q profiles corresponding to the Fe I line at 617.3 nm. Again, we assume three different angles of incidence, $\theta = 0°$, $\theta = 0°5$, and $\theta = 1°$. The observed Stokes profiles have been determined by using the expressions

$$I^{(t)} = \frac{1}{N}(a * I^{(i)} + b * Q^{(i)}), \quad (38)$$

$$Q^{(t)} = \frac{1}{N}(a * Q^{(i)} + b * I^{(i)}), \quad (39)$$

where $*$ is the convolution operator and N is a constant introduced to normalize the observed profile to the continuum given by

$$N = \int_0^\infty a(\lambda)d\lambda. \quad (40)$$

As expected, the observed Stokes I and Q profiles are broader and shallower in the case of Stokes I and weaker in the case of Stokes Q than the synthetic ones, due to the limited spectral bandwidth of the etalon. Moreover, they are both blueshifted with respect to the λ_0, as expected (see Paper I). Remarkably, the crosstalk from Stokes I to Stokes Q, governed by the b coefficient of the etalon Mueller matrix, introduces a clear asymmetry in the observed Stokes Q profile. The asymmetries are evident when the incident angle θ is $1°$. These asymmetries are also present in Stokes I because of the crosstalk from Stokes Q to Stokes I, although in less amount

due to the larger values of the incident Stokes I component. In this case we have taken into account only linear polarized light, but the effects are larger when there is crosstalk between Stokes U and Stokes V, as one can deduce by just looking at Figure 4.

4.2. Effect of Local Domains in the Etalon

Either during the manufacturing process of etalons or when applying an intense electric field, local domains where the optical axis is not perpendicular to the etalon surfaces may appear. This implies that, even when illuminating the etalon with a collimated beam normal to the etalon surfaces, birefringent effects can arise. The magnitudes of these depend on the angles θ and θ_3, as well as on the relative orientation α of the plane containing the ordinary ray electric field with respect to the chosen X direction.

Let us suppose that we illuminate with a normal incident beam the etalon and that no other polarizing elements are present in our system. We can freely choose the X-axis of the etalon again to coincide with the vibration plane of $\mathbf{E}_o$. In this case, the Mueller matrix of the system is given again by Equation (9) and

$$\varphi = \frac{4\pi h}{\lambda}(n_3 - n_o)\sin^2\theta_3, \quad (41)$$

which, for small deviations, takes the form

$$\varphi \simeq \frac{4\pi h}{\lambda}(n_3 - n_o)\theta_3^2. \quad (42)$$

The nonzero elements of the Mueller matrix are plotted as a function of θ_3 in Figures 7 and 8. We can observe a similar effect to the one that appears when illuminating a perfect etalon with a collimated and oblique beam, except for the fact that, in this case, the spectral profile of the ordinary ray does not deviate and the splitting of the ordinary and extraordinary rays is more prominent. The spectral separation of the ordinary and extraordinary rays is clearly noticed in Figure 7 when approaching $1°$. The double peak in the spectral transmission is also visible in a and c in Figure 8. Crosstalk parameters b and d have a maximum absolute value of about 40% and 60%, respectively.

The birefringence is more noticeable when varying the optical axis angle than when changing the incident angle since the dependence with θ_3 is stronger than with θ in Equation (37). We have also represented the ordinary $(a + b)$ and extraordinary $(a - b)$ spectral transmission profiles in Figure 9 using Equations (22) and (23) for $\theta_3 = 0°$ and $1°$ to check both that the ordinary transmission ray does not shift to the blue, in contrast to the extraordinary ray, and that the ordinary and extraordinary profiles are symmetric.

4.3. Etalon Response in Telecentric Configuration

In a telecentric configuration, each point of the etalon is illuminated by an identical cone of rays coming from the pupil. This means, on the one hand, that each point of the etalon receives a set of rays, each one with different angles of incidence. On the other hand, the principal plane orientation changes with the direction of each particular incident ray. We must take care of both effects.

Consider an etalon within an optical system in a perfect telecentric configuration, where the chief ray is parallel to the optical axis over the whole field of view (FOV). In such an ideal
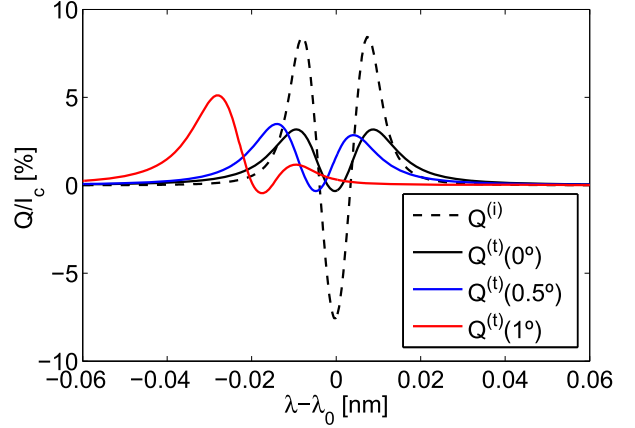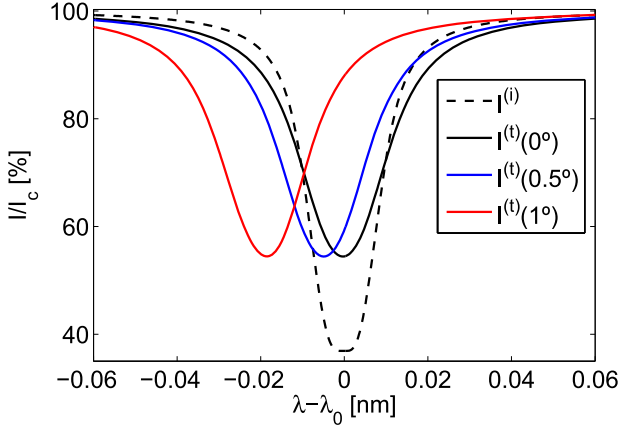
Figure 6. Reconstructed intensity profile of a synthetic Stokes profile (black dashed line) with the spectral response of the etalon at $\theta = 0$ (black solid line), $\theta = 0°5$ (blue solid line), and $\theta = 1°$ (red solid line).

configuration, the etalon receives the same cone of rays across the FOV, and the polarization response remains equal over the image. Without loss of generality, we can calculate the transmitted electric field at the center of the image and extend this result to all the points of the FOV. The only dependence of the electric field with the coordinates of the pupil (r, ϕ) is that of the ordinary and extraordinary retardances through the incidence angle $\theta(r)$:

$$\theta(r) = \arcsin\left(\frac{r}{\sqrt{r^2 + f^2}}\right). \tag{43}$$

Equation (6) neglects any corrections in the Mueller matrix when integrating over the azimuthal direction. Rotations of the principal plane over the cone of rays must be included, though. To do so, let us first rotate the Jones matrix an angle ϕ'. The components of the rotated Jones matrix, $\mathbf{H}'$, will be given by

$$\begin{aligned}
H'_{11} &= H_{11}\cos^2\phi' + H_{22}\sin^2\phi', \\
H'_{22} &= H_{11}\sin^2\phi' + H_{22}\cos^2\phi', \\
H'_{12} &= H'_{21} = (H_{11} - H_{22})\sin\phi'\cos\phi'.
\end{aligned} \tag{44}$$

The transmitted electric field shall then be calculated from the "integrated" Jones matrix $\widetilde{\mathbf{H}}'$, whose elements can be obtained from the Fraunhofer integral of the coefficients H'_{ij} (see Appendix A for further details). As explained in Paper I, the resulting integrals have no easy analytical integration and shall be evaluated numerically.

In an ideal telecentric configuration, the only dependence on the azimuthal angle is due to the rotation of the principal plane over the interval of integration. The Jones matrix elements of the telecentric configuration, $\widetilde{H}'_{ij}$, can then be cast as (Appendix A)

$$\begin{aligned}
\widetilde{H}'_{11} &= \widetilde{H}'_{22} = \frac{1}{2}(\widetilde{H}_{11} + \widetilde{H}_{22}), \\
\widetilde{H}'_{12} &= \widetilde{H}'_{21} = 0,
\end{aligned} \tag{45}$$

where

$$\widetilde{H}_{11} = \int_0^{R_p} r H_{11}(r)\,dr,$$

$$\widetilde{H}_{22} = \int_0^{R_p} r H_{22}(r)\,dr, \tag{46}$$

and R_p is the radius of the pupil. The diagonal elements of the rotated Jones matrix are therefore a linear combination of the elements of the nonrotated Jones matrix. Crosstalks between the ordinary and extraordinary components of the electric field are canceled out when integrating $\sin\phi\cos\phi$ over $(0, 2\pi)$. The Mueller matrix coefficients are then given by

$$\tilde{M}'_{ij} = \frac{1}{2}\mathrm{Tr}[\sigma_i \widetilde{\mathbf{H}}' \sigma_j \widetilde{\mathbf{H}}'^\dagger]. \tag{47}$$

Obviously, this matrix has again the form of Equation (9) with coefficients $\tilde{a}'$, $\tilde{b}'$, $\tilde{c}'$, $\tilde{d}'$:

$$\widetilde{\mathbf{M}}' = \begin{pmatrix} \tilde{a}' & \tilde{b}' & 0 & 0 \\ \tilde{b}' & \tilde{a}' & 0 & 0 \\ 0 & 0 & \tilde{c}' & -\tilde{d}' \\ 0 & 0 & \tilde{d}' & \tilde{c}' \end{pmatrix}, \tag{48}$$

where

$$\begin{aligned}
\tilde{a}' &= \frac{1}{2}(\widetilde{H}'_{11}\widetilde{H}'^*_{11} + \widetilde{H}'_{22}\widetilde{H}'^*_{22}), \\
\tilde{b}' &= \frac{1}{2}(\widetilde{H}'_{11}\widetilde{H}'^*_{11} - \widetilde{H}'_{22}\widetilde{H}'^*_{22}), \\
\tilde{c}' &= \frac{1}{2}(\widetilde{H}'_{22}\widetilde{H}'^*_{11} + \widetilde{H}'_{11}\widetilde{H}'^*_{22}), \\
\tilde{d}' &= \frac{i}{2}(\widetilde{H}'_{22}\widetilde{H}'^*_{11} - \widetilde{H}'_{11}\widetilde{H}'^*_{22}).
\end{aligned} \tag{49}$$

In this particular case, substituting Equation (45),

$$\begin{aligned}
\tilde{a}' = \tilde{c}' &= \frac{1}{4}(\widetilde{H}_{11}\widetilde{H}^*_{11} + \widetilde{H}_{22}\widetilde{H}^*_{22} + \widetilde{H}_{11}\widetilde{H}^*_{22} + \widetilde{H}_{22}\widetilde{H}^*_{11}), \\
\tilde{b}' = \tilde{d}' &= 0.
\end{aligned} \tag{50}$$

Therefore, the Mueller matrix is diagonal and no crosstalk appears between the different spectral profiles of the Stokes components if telecentricity is exact.

However, perfect telecentricity can only be reached ideally. In a normal scenario, there is a dependence with the azimuthal angle on the Jones matrix even if changes of orientation of the principal plane over the azimuthal angle ϕ were not considered, since the symmetry of the problem is broken. In an imperfect telecentric configuration, the chief ray direction deviates from normal incidence on the etalon over the FOV, and so does the
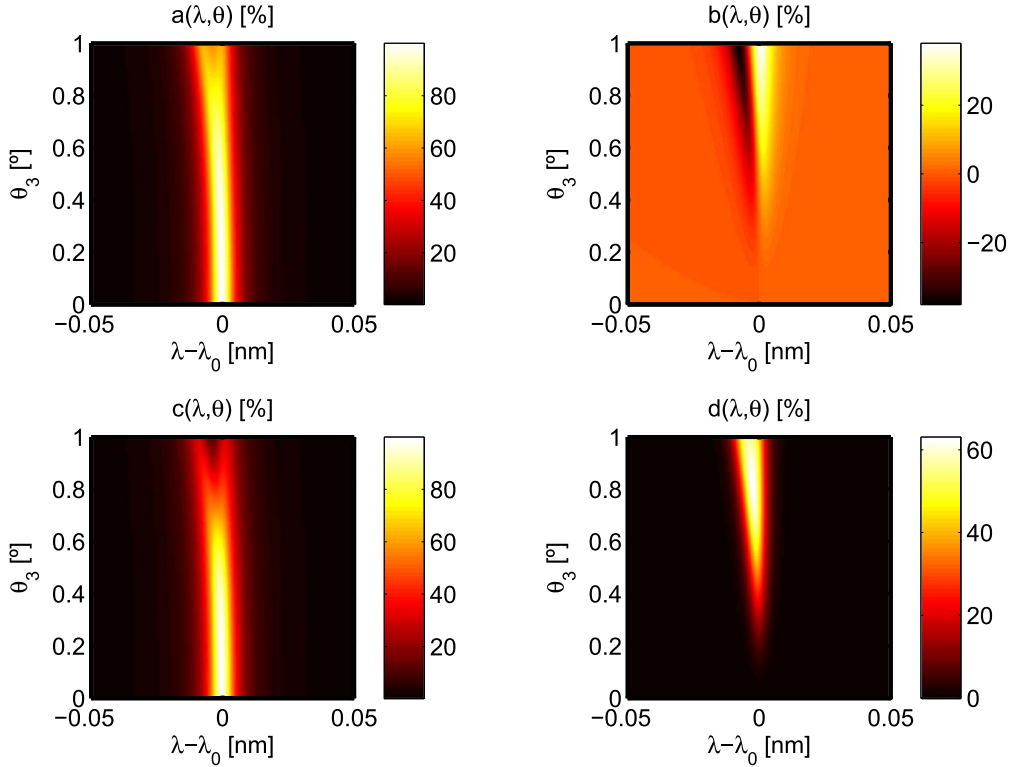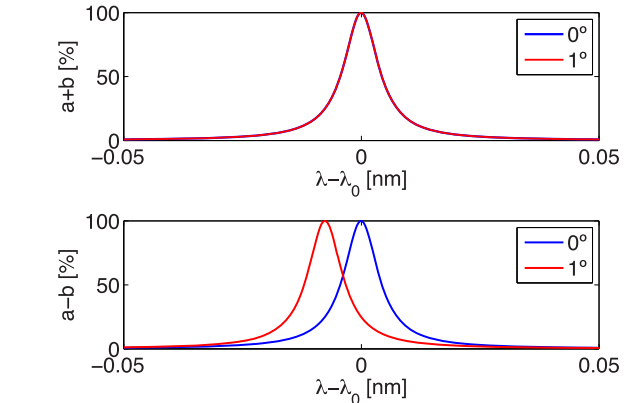
Figure 7. Variation of the a, b, c, and d coefficients of the Mueller matrix of the etalon as a function of the wavelength and of θ_3.
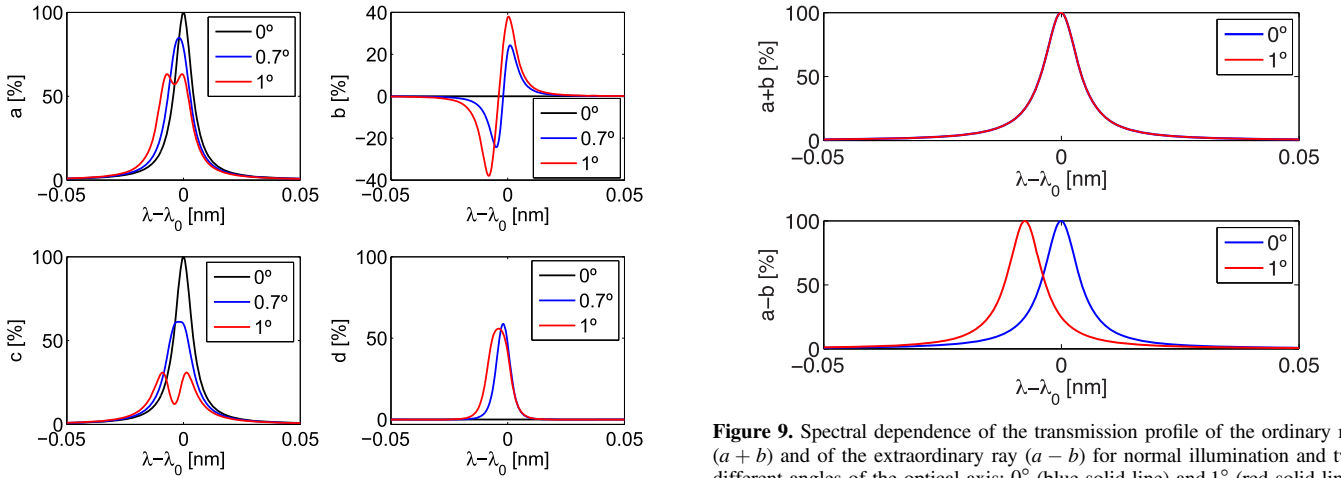
Figure 8. Variation of the a, b, c, and d coefficients of the Mueller matrix of the etalon as a function of the wavelength for $\theta_3 = 0°$ (black solid line), $0.7°$ (blue solid line), and $1°$ (red solid line).

Figure 9. Spectral dependence of the transmission profile of the ordinary ray $(a + b)$ and of the extraordinary ray $(a - b)$ for normal illumination and two different angles of the optical axis: $0°$ (blue solid line) and $1°$ (red solid line).

polarimetric response of the etalon, which is now expected to be spectrally asymmetric. Equations (45) and (48) cannot be applied. Actually a' is no longer equal to c', and b' and d' become different from zero. Furthermore, the Jones matrix off-diagonal elements are, in general, different from zero. The Mueller matrix elements should be calculated from Equation (47) with the coefficients H'_{ij} obtained following Appendix A.

Figure 10 represents the spectral response of the Mueller matrix elements as a function of λ for an optical system with $f/60$. Both a perfect telecentric configuration (chief ray at $0°$)

and an imperfect telecentrism in which the chief ray is deviated $0°.5$ have been considered. We only show the $\tilde{a}'$, $\tilde{b}'$, $\tilde{c}'$, and $\tilde{d}'$ components of the Mueller matrix since we have observed in our numerical experiments that other off-diagonal elements in the Jones matrix are several orders of magnitude below the diagonal terms. This implies that, in practice, $\widetilde{\mathbf{H}}'$ can be considered as diagonal and only the coefficients $\tilde{a}'$, $\tilde{b}'$, $\tilde{c}'$, and $\tilde{d}'$ need to be calculated.

The first thing to notice is that the profiles are blueshifted, as in the collimated configuration. We also see how $\tilde{a}'$ and $\tilde{c}'$ profiles for imperfect telecentrism are broader. Their peak values have decreased from about $\sim$90% at $0°$ to $\sim$40% at $0°.5$ due to the mentioned widening. These two effects are more
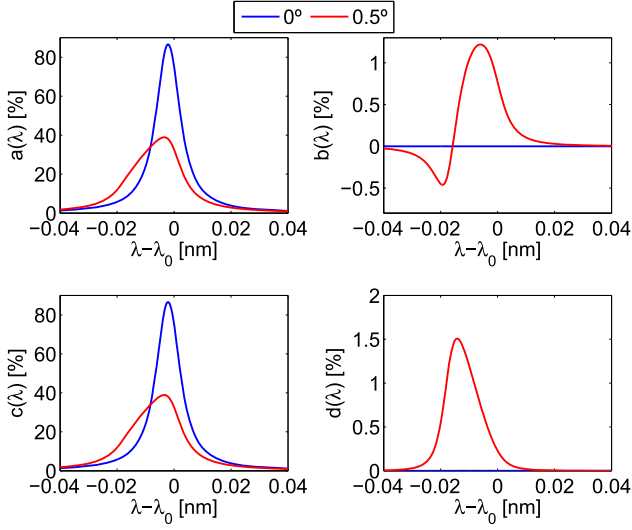
Figure 10. Variation of the $\tilde{a}'$, $\tilde{b}'$, $\tilde{c}'$, and $\tilde{d}'$ coefficients of the Mueller matrix of the etalon as a function of the wavelength for both perfect telecentrism (blue solid line) and imperfect telecentrism with a deviation of the chief ray of $0°.5$ (red solid line). A beam f-number of 60 has been employed.

important for shorter f-numbers because of the larger incidence angles (Paper I).

Remarkably, the four matrix elements have a clear asymmetric spectral dependence at $0°.5$. The maximum values of $\tilde{b}'$ and $\tilde{d}'$ are $\sim 1\%$ and $\sim 1.5\%$, respectively. These terms are responsible for the crosstalk among the Stokes parameters. Note that these large asymmetries in the spectral profile are not exclusive for birefringent etalons, since they also appeared in Paper I, where the isotropic case was studied. At $0°$ there is no crosstalk and $\tilde{a}'(\lambda) = \tilde{c}'(\lambda)$, as expected from Equation (50). Although not noticeable in this figure, the loss of symmetry in an imperfect telecentrism implies that $\tilde{a}'(\lambda) \neq \tilde{c}'(\lambda)$ at $0°.5$, as explained before.

Figure 11 shows the observed Stokes I and Q spectral profiles when illuminating the etalon with the same synthetic profile as in Section 4.1, and using a telecentric configuration with $f/60$ as well. We can see the displacement toward the blue produced by the effect of the different incidence angles. The profiles also broaden due to the effect of the convolution with the Mueller matrix of the etalon (Equations (38) and (39)) and become asymmetric. Moreover, an artificial continuous signal in the measured Q at $|\lambda - \lambda_0| > 0.03$ nm appears due to the crosstalk introduced from the continuous part of I. In order to estimate the induced artificial signals due to the birefringence of the etalon, we have also plotted $\Delta I = I^{(t)} - I_{nb}^{(t)}$ and $\Delta Q = Q^{(t)} - Q_{nb}^{(t)}$, where $I_{nb}^{(t)}$ and $Q_{nb}^{(t)}$ are the transmitted I and Q components of the Stokes vector for a non-birefringent etalon with refraction index n_o. The absolute maximum crosstalk goes from $\sim 0.2\%$ and $\sim 0.05\%$ at $0°$ to $\sim 0.65\%$ and $\sim 1.75\%$ at $0°.5$ in I and Q, respectively.

5. Imaging Response to Monochromatic Plane Waves

As discussed in Paper I, space invariance is not preserved in either the collimated or the (imperfect) telecentric case. We cannot speak, then, of a PSF that can be convolved with the object brightness distribution when studying the response of the etalon. Instead, we have to integrate the object with a *local* PSF. On the

other hand, since the object brightness usually varies with wavelength, the response of the Fabry–Pérot depends on the object itself. We need then to integrate spectrally the monochromatic response of the instrument (Equations (61) and (62) of Paper I). Moreover, orthogonal components of the electric field are, in general, modified in a different way when traversing through the etalon. We therefore expect the response to vary with the incident polarization as well.

The *local* PSF, $\mathcal{S}$, is defined as the ratio

$$\mathcal{S} = \frac{\widetilde{\mathbf{E}}^{(t)*}\widetilde{\mathbf{E}}^{(t)}}{\mathbf{E}^{(i)*}\mathbf{E}^{(i)}}, \tag{51}$$

where $\mathbf{E}^{(i)}$ is the electric field of the incident plane wave and $\widetilde{\mathbf{E}}^{(t)}$ is the image plane electric field, related to the incident ordinary and extraordinary rays by

$$\begin{aligned}
\widetilde{\mathbf{E}}_x^{(t)} &= \widetilde{\mathsf{H}}'_{11}\mathbf{E}_o^{(i)} + \widetilde{\mathsf{H}}'_{12}\mathbf{E}_e^{(i)}, \\
\widetilde{\mathbf{E}}_y^{(t)} &= \widetilde{\mathsf{H}}'_{21}\mathbf{E}_o^{(i)} + \widetilde{\mathsf{H}}'_{22}\mathbf{E}_e^{(i)}.
\end{aligned} \tag{52}$$

In a similar way to Section 4.3, coefficients $\widetilde{\mathsf{H}}'_{ij}$ are calculated from the Fraunhofer integrals (Appendix A) of the elements of the "rotated" Jones matrix, H'_{ij}, and depend on the image plane coordinates (ξ, η), on the chief ray coordinate in the image plane (ξ_0, η_0), and on the wavelength. We do not make these dependences explicit in the equations that follow for simplicity. Note that we do not restrict ourselves now to the center of the image, unlike in Section 4.3, since we are interested in not only the transmission profiles of the Stokes vector but also in the consequences of diffraction effects due to the limited aperture of the system.

Even if we neglect crossed terms in the Jones matrix, the response of the etalon is determined by the polarization of the incident light, since the diagonal terms of the Jones matrix are different. This statement is valid for both collimated and telecentric mounts. For isotropic media, since $\widetilde{\mathsf{H}}'_{12} = \widetilde{\mathsf{H}}'_{21} = 0$ and $\widetilde{\mathsf{H}}'_{11}\widetilde{\mathsf{H}}'^*_{11} = \widetilde{\mathsf{H}}'_{22}\widetilde{\mathsf{H}}'^*_{22}$, we recover the result for $\mathcal{S}$ presented in Paper I.

Equation (52) is written in terms of the ordinary and extraordinary electric field components. It may be more useful to find the relation of $\mathcal{S}$ with the incident Stokes parameters, though. This is as easy as obtaining the Mueller matrix through Equation (47) and noticing that $\widetilde{\mathbf{E}}^{(t)*}\widetilde{\mathbf{E}}^{(t)}$ represents the first component of the transmitted Stokes vector. Consequently, substituting in Equation (51),

$$\mathcal{S} = \tilde{\mathsf{M}}'_{11} + \tilde{\mathsf{M}}'_{12}\frac{Q^{(i)}}{I^{(i)}} + \tilde{\mathsf{M}}'_{13}\frac{U^{(i)}}{I^{(i)}} + \tilde{\mathsf{M}}'_{14}\frac{V^{(i)}}{I^{(i)}}. \tag{53}$$

Again, we can see that $\mathcal{S}$ depends in general on the polarization of the incident light. Although the expressions presented in this section are valid for both collimated and telecentric illumination, differences between both cases are obviously expected to arise, hence the need to study them separately.

5.1. Collimated Configuration

In the collimated configuration, there is a one-to-one mapping between the incidence angle of the rays on the etalon and their position on the image plane. As only the incidence angles are of interest, the location of the rays on the pupil is irrelevant, and the Fraunhofer integrals are proportional to that
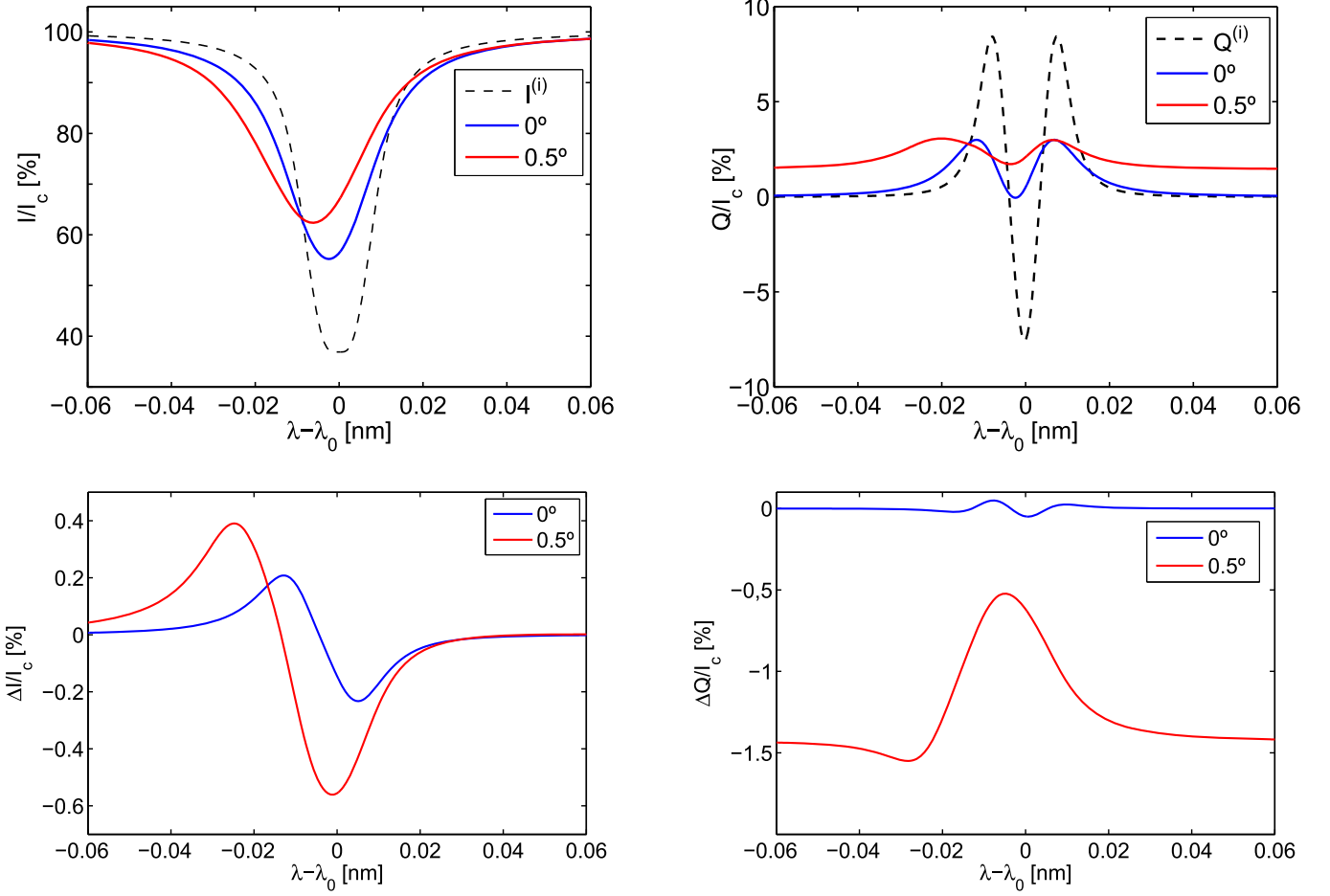
Figure 11. Observed Stokes I and Q profiles (left and right panels, respectively) when illuminating the etalon in telecentric configuration with $f/60$ with the orientation of the chief ray at $0°$ (blue solid line) and at $0°.5$ (red solid line). The black dashed line stands for the synthetic input Stokes I and Q profiles. The crosstalks induced in Stokes I and Stokes Q are shown in the bottom panels.

of a circular aperture with the same radius, similarly to the isotropic case. According to Appendix A, the Jones matrix terms are actually given by

$$\tilde{H}'_{11} = (H_{11}\cos^2\phi_0 + H_{22}\sin^2\phi_0)\frac{2J_1(z)}{z},$$

$$\tilde{H}'_{22} = (H_{11}\sin^2\phi_0 + H_{22}\cos^2\phi_0)\frac{2J_1(z)}{z},$$

$$\tilde{H}'_{12} = \tilde{H}'_{21} = (H_{11} - H_{22})\sin\phi_0\cos\phi_0\frac{2J_1(z)}{z}, \quad (54)$$

where the variables z and J_1 are defined in Paper I and ϕ_0 is the azimuthal orientation of the principal plane of the etalon with respect to the $+Q$ direction of the reference frame chosen to describe the Stokes vector (i.e., the azimuthal angle in Figure 2). Note that off-diagonal terms cannot be neglected unless $\phi_0 = 0$. Thus, $\mathcal{S}$ depends on the four Stokes parameters and varies over the image plane due to both the birefringence of the etalon and the reorientation of the principal plane with the incident ray direction. In fact, for the same radial position on the image plane, $\mathcal{S}$ changes because of the different orientations of the principal plane. A decrease of the intensity is also expected toward the edges of the image, as explained in Paper I.

We can only set $\phi_0 = 0$ for ray directions parallel to the optical axis. Assuming that the optical axis is perpendicular to the surfaces of the etalon, this occurs at normal illumination of the pupil. For this particular case, the Mueller matrix has the form of Equation (48), and, using Equations (53) and (54), an analytical expression for $\mathcal{S}$ can be found:

$$\mathcal{S} = \frac{1}{2}\left(\frac{2J_1(z)}{z}\right)^2\left[g_o + g_e + (g_o - g_e)\frac{Q^{(i)}}{I^{(i)}}\right], \quad (55)$$

where $g_o \equiv H_{11}H_{11}^*$ and $g_e \equiv H_{22}H_{22}^*$ are the transmission profiles of the ordinary and extraordinary rays for normal illumination of the etalon. This expression illustrates the polarimetric dependence of $\mathcal{S}$ for the collimated configuration and its proportionality to that of an ideal circular aperture. Notice that, since crossed terms in the Jones matrix are zero in this case, $\tilde{M}'_{13}$ and $\tilde{M}'_{14}$ are also null, and the dependence with Stokes components U and V disappears. For pupil incidence angles different from zero, expressions are much more involved and an analytical expression for S cannot easily be obtained.

5.2. Telecentric Configuration

For telecentric illumination of the etalon, the retardance is related to the pupil coordinates of the incident rays, unlike for the collimated case. The proportionality with the response of a

circular aperture disappears then, as occurred in the isotropic case, and the Jones matrix elements of Equation (52) must be evaluated numerically.

The response $\mathcal{S}$, as for the collimated case, depends on the polarization state of the incident light even for perfect telecentrism. This is because $\widetilde{H}'_{11} \neq \widetilde{H}'_{22}$ and $\tilde{H}'_{12} = \tilde{H}'_{21} \neq 0$ in general, as explained in Appendix A. Let us consider two simple cases, namely, $\mathbf{E}_e^{(i)} = 0$ and $\mathbf{E}_o^{(i)} = 0$. For the case $\mathbf{E}_e^{(i)} = 0$, according to Equation (52), the PSF follows the expression

$$\mathcal{S} = \tilde{H}'_{11}\tilde{H}'^*_{11} + \tilde{H}'_{21}\tilde{H}'^*_{21}. \tag{56}$$

For the case $\mathbf{E}_o^{(i)} = 0$, the PSF is described by

$$\mathcal{S} = \tilde{H}'_{22}\tilde{H}'^*_{22} + \tilde{H}'_{12}\tilde{H}'^*_{12}, \tag{57}$$

which is different from Equation (56) even if we ignore the crosstalk term (second term of the equations). Crosstalks can be neglected in practice for the telecentric configuration, as discussed in Section 4.3. Therefore, the third and fourth Mueller matrix terms of Equation (53) vanish, as for normal illumination in collimated etalons, and the response depends only on I and Q Stokes components (as well as on the birefringence of the etalon). Interestingly, the peak of $\mathcal{S}$ is just the transmission profile, $\tilde{a}'$ (Equation (50)), which is not affected by the incident polarization state of light.

Obviously, if the chief ray is not perpendicular to the etalon surfaces (imperfect telecentrism), the same arguments can be applied. Moreover, other effects explained in Paper I will appear. Essentially, $\mathcal{S}$ becomes asymmetric and varies from point to point. If telecentrism is perfect, although polarization dependent, $\mathcal{S}$ remains the same all over the FOV by definition.

To evaluate how $\mathcal{S}$ varies with the polarization of the incident light beam, we have calculated its width and its peak position for $Q = \pm 1$ states of polarization. We study their behavior with the degree of telecentrism by varying the chief ray angle, Θ, from $0°$ (ideal telecentrism) to $0°.5$. Figure 12 shows the results obtained for an $f/60$ beam. The X-axis of both top and bottom figures indicates the angle that the chief ray forms with the optical axis.

The top panel represents the shift of the PSF peak with respect to the position of the peak for the ideal diffraction-limited case (Airy disk) with Θ and for the two orthogonal polarizations. The results have been normalized by the radius of the collimated case. It can be seen clearly that the shift is different for orthogonal polarizations, meaning that $\mathcal{S}$ depends on the input beam polarization state. Deviations between orthogonal states would be larger for smaller f ratios.

The bottom panel shows the width of $\mathcal{S}$ normalized to that corresponding for the ideal diffraction-limited case. Notice that apart from an offset between the two curves, they depend slightly differently on Θ. The offset indicates that $\mathcal{S}$ is polarization dependent even for perfect telecentrism (i.e., when $\Theta = 0$), as explained before in the text.

6. Comments on the Birefringent Effects in Solar Instrumentation

The polarimetric effects described in earlier sections have an impact on the incident Stokes vector. Indeed, off-diagonal
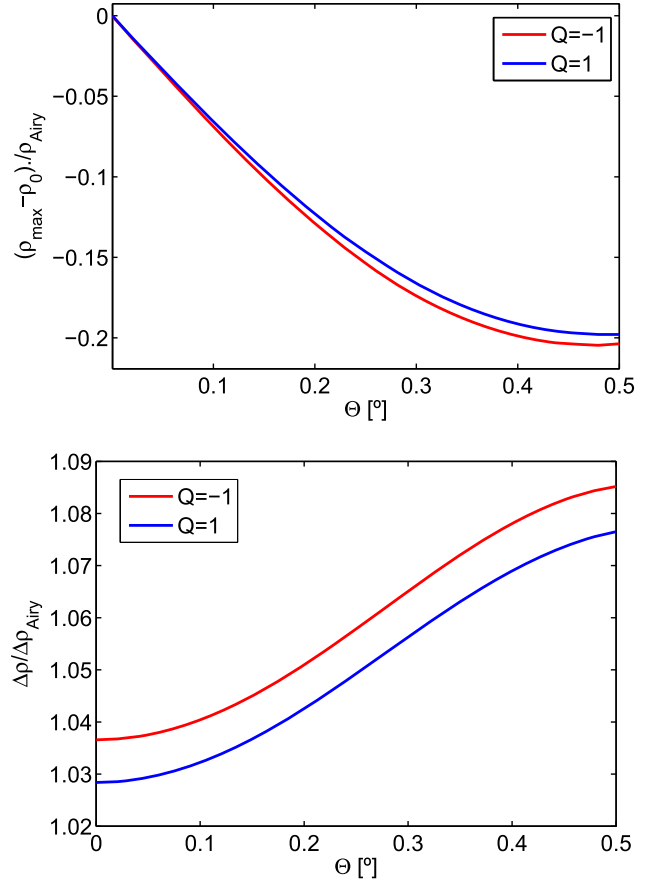
Figure 12. Spatial shift (top) of the peak of the PSF with respect to the Airy disk and FWHM of the PSF normalized to that of the Airy disk (bottom) as we move across the FOV in the image plane (X-axis). The plot includes the result for orthogonal polarization beams $Q = 1$ (blue) and $Q = -1$ (red). A telecentric beam with $f/60$ has been employed.

terms in the etalon Mueller matrix introduce crosstalks between the Stokes parameters that could deteriorate the measurements carried out by solar magnetographs. However, there are other factors that should also be considered for a proper evaluation of the spurious signals emerging in such instruments.

First, we need to take into account the combined response of the polarimeter and the etalon because both modify the polarization state of light. The final Mueller matrix of the instrument depends, then, on the relative position of the etalon with respect to the polarimeter. Usually, the Fabry–Pérot is located either between the modulator and the analyzer or behind it. When it is located after the analyzer, further crosstalks induced by the etalon are prevented. The reason for this is that the etalon is illuminated with linearly polarized light. If placed between the modulator and the analyzer, then the effect on the final Mueller matrix changes for each particular modulation of the signal.

Second, observations are not strictly monochromatic but quasi-monochromatic. Spectral integration of the Mueller coefficients decreases the magnitude of crosstalk terms, especially for b and $\tilde{b}'$ since they change their sign along the spectral profile (Figures 4 and 3).

Modulation of the signal and the quasi-monochromatic nature of the observations reduce the crosstalk induced by the

etalon Mueller matrix. These aspects will be addressed in the next work of this series of papers.

The calculations presented in previous sections represent a worst-case scenario. Let us consider two examples of instruments based on birefringent etalons: SO/PHI (Solanki et al. 2015) and IMaX (Martínez Pillet et al. 2011). The former is illuminated with a telecentric beam, whereas the second is mounted on a collimated configuration. For SO/PHI, the degree of telecentrism is kept below $0°.23$ in a $\sim f/60$ mount. In addition, its etalon is located after the analyzer. In the IMaX instrument, incidence angles are below $0°.44$, and the Fabry–Pérot is placed between the modulator and the analyzer. Deviations from normal illumination in SO/PHI and IMaX are lower than half the maximum angle employed in Figures 10 and 4. Moreover, deviations of the optical axis from the nominal one have only been observed to appear after the application in the laboratory of very intense electric fields and disappear after a certain interval of time. These deviations are distributed in small compact regions or *local domains* that cover a small fraction of the clear aperture. If these electric fields are not reached during operation, the harming effects can be considered negligible.

7. Summary and Conclusions

A general theory that considers the polarimetric response of anisotropic (uniaxial) crystalline etalons has been presented in this work. We have obtained an expression of the Mueller matrix that describes the polarimetric behavior of uniaxial crystalline etalons, and we have concluded that they can be described as a combination of an ideal mirror and a retarder, both strongly spectrally modulated. We have shown that the Mueller matrix of the etalon in a collimated configuration depends only on four elements that vary spectrally, with the direction of the incident rays and on the orientation of the optical axis. A careful choice of the reference frame depending on the orientation of the principal plane is also needed.

We have also deduced an analytical expression for the birefringence induced in uniaxial crystalline Fabry–Pérot etalons that takes into account both the direction of the incident rays and the orientation of the optical axis. By numerical experimentation, we have studied the effect of (1) oblique illumination in Z-cut etalons, (2) misalignments of the optical axis at normal illumination, and (3) locating the etalon in a telecentric configuration. We have considered the influence of illuminating with different f-numbers in the latter.

For the first case, we have evaluated the spectral dependence of the coefficients of the Mueller matrix with the angle of the incident light. We have shown that, with the parameters of a commercial etalon, the crosstalk between I and Q is about 10% at $1°$ and 30% between U and V. For the second case, we have shown that the same deviations of the optical axis introduce larger artificial signals between the Stokes parameters (40% and 60% between I and Q and U and V at $1°$). We have also evaluated the spectral transmission of a synthetic Stokes profile when traversing through the etalon for different incident angles. Asymmetries are induced in this case in the observed profiles due to the presence of crosstalk terms in the Mueller matrix, thus introducing spurious signals.

We have shown that in a perfect telecentric configuration the Mueller matrix is diagonal and no crosstalk appears between the different Stokes components. For an imperfect telecentric

beam, the Mueller matrix is not diagonal anymore, although it still keeps the *abcd* form in practice, and the spectral profiles of the Mueller matrix elements become asymmetric. We have studied the spectral profiles of the Mueller matrix coefficients and the degradation produced on a spectral artificial Stokes profile, and we have estimated the crosstalks produced in this configuration. Because of the birefringence of the etalon, artificial signals appear on the observed profile compared to the isotropic case, apart from the known broadening and blueshift effects.

A general method for obtaining the imaging response in crystalline Fabry–Pérots for both collimated and telecentric configurations has been developed. It has been shown that the response of the etalon is related in general to the polarization of the incident light, as well as to its birefringence. We have addressed the problem from two different points of view: by using the Jones formalism and by employing the Mueller matrix method. Both of them are equivalent. The advantage of the second is that it let us express the response directly as a function of the input Stokes parameters.

We have demonstrated that in a collimated setup the *local* PSF is modified with respect to the ideal PSF by a transmission factor that varies across the image plane both radially and azimuthally due to the correspondent rotations of the principal plane with the ray direction (Equation (54)). At the origin, the response is equal to the irradiance distribution of a circular unaberrated pupil modulated by a transmission factor that depends on the birefringence of the etalon and on the I and Q Stokes components that traverse through the etalon. In a perfect telecentric configuration the PSF also depends on the induced birefringence of the etalon and on the incident polarization state of light (namely, on I and Q again), although its peak transmission is polarization independent and its shape remains the same across the image plane. In imperfect telecentrism, an asymmetry and a variation of the response over the detector are also introduced. We have evaluated the spatial shift of the response for two orthogonal states of polarization with the degree of telecentrism, as well as its FWHM. We have shown that the local PSF peak and FWHM change differently with the chief ray angle for each polarization. The FWHM depends on the polarization of the incident light even for perfect telecentrism. The numerical results obtained are in agreement with our analytical argumentation.

Appendix A
Exact Expression of the Electric Field at the Focal Plane

The electric field of an electromagnetic wave at the focal plane of an optical instrument, $\widetilde{\mathbf{E}}^{(t)}(\xi, \eta; \xi_0, \eta_0; \lambda)$, is given by the Fraunhofer integral of the incident electric field at the pupil, $\mathbf{E}^{(i)}$. We have remarked on the dependence of the electric field with the coordinates of the focal plane (ξ, η), the chief ray position at the focal plane (ξ_0, η_0), and the wavelength, since

they are variables of interest for the calculation of the spectral transmission profile and of the monochromatic imaging response. We omit these explicit dependences from this point on.

If we choose radial coordinates (r, ϕ) to describe the pupil coordinates, we can write

$$\widetilde{\mathbf{E}}^{(t)} = \int_0^{R_p} \int_0^{2\pi} r\mathbf{E}^{(t)}(r, \phi, \lambda) e^{-ikr(\alpha\cos\phi + \beta\sin\phi)} \, \mathrm{d}r \, \mathrm{d}\phi, \quad (58)$$

where k is the wavelength vector of the incident wavefront, $\alpha \equiv (\xi - \xi_0)/f$ and $\beta \equiv (\eta - \eta_0)/f$ are the cosine directors (not to be confused with the angles of Figure 2), and R_p is the radius of the pupil.

Following the Jones formalism, we can also write

$$\widetilde{\mathbf{E}}^{(t)} \equiv \begin{pmatrix} \widetilde{\mathbf{E}}_x^{(t)} \\ \widetilde{\mathbf{E}}_y^{(t)} \end{pmatrix} = \widetilde{\mathbf{H}}' \begin{pmatrix} \mathbf{E}_o^{(i)} \\ \mathbf{E}_e^{(i)} \end{pmatrix}, \quad (59)$$

where the coefficients of $\widetilde{\mathbf{H}}'$ can be calculated from Equation (44) after integration:

$$\widetilde{H}'_{11} = \int_0^{R_p} \int_0^{2\pi} r[H_{11}(r, \phi, \lambda)\cos^2\phi' + H_{22}(r, \phi, \lambda)\sin^2\phi']$$
$$\times e^{-ikr(\alpha\cos\phi + \beta\sin\phi)} \, \mathrm{d}r \, \mathrm{d}\phi,$$

$$\widetilde{H}'_{22} = \int_0^{R_p} \int_0^{2\pi} r[H_{11}(r, \phi, \lambda)\sin^2\phi' + H_{22}(r, \phi, \lambda)\cos^2\phi']$$
$$\times e^{-ikr(\alpha\cos\phi + \beta\sin\phi)} \, \mathrm{d}r \, \mathrm{d}\phi,$$

$$\widetilde{H}'_{12} = \widetilde{H}'_{21} = \int_0^{R_p} \int_0^{2\pi} r[H_{11}(r, \phi, \lambda) - H_{22}(r, \phi, \lambda)]$$
$$\times \sin\phi' \cos\phi' e^{-ikr(\alpha\cos\phi + \beta\sin\phi)} \, \mathrm{d}r \, \mathrm{d}\phi,$$
$$(60)$$

where ϕ' is the azimuthal angle of the principal plane with respect to the $+Q$ direction of the reference frame chosen to describe the Stokes parameters (Figure 2). The coefficients of the Jones matrix $\mathbf{H}$ are given by Equations (4)–(6). Note that this expression considers the rotations of the principal plane of the etalon with the ray direction vector within the etalon. The dependence of the Jones matrix elements with the pupil coordinates is entirely given by that of retardances δ_o and δ_e through the incidence angles and changes with the optical configuration.

A1. Collimated Configuration

For collimated setups, the incidence angle is given by Equation (53) from Paper I:

$$\theta = \cos^{-1}\left(\frac{f}{\sqrt{\xi^2 + \eta^2 + f^2}}\right), \quad (61)$$

which does not depend on the pupil coordinates. Therefore, $H_{11} \neq H_{11}(r, \phi)$ and $H_{22} \neq H_{22}(r, \phi)$, and we can cast

Equation (60) as

$$\widetilde{H}'_{11} = (H_{11}\cos^2\phi_0 + H_{22}\sin^2\phi_0)$$
$$\times \int_0^{R_p} \int_0^{2\pi} re^{-ikr(\alpha\cos\phi + \beta\sin\phi)} \, \mathrm{d}r \, \mathrm{d}\phi$$
$$= (H_{11}\cos^2\phi_0 + H_{22}\sin^2\phi_0)\frac{2J_1(z)}{z},$$

$$\widetilde{H}'_{22} = (H_{11}\sin^2\phi_0 + H_{22}\cos^2\phi_0)$$
$$\times \int_0^{R_p} \int_0^{2\pi} re^{-ikr(\alpha\cos\phi + \beta\sin\phi)} \, \mathrm{d}r \, \mathrm{d}\phi$$
$$= (H_{11}\sin^2\phi_0 + H_{22}\cos^2\phi_0)\frac{2J_1(z)}{z},$$

$$\widetilde{H}'_{12} = \widetilde{H}'_{21} = (H_{11} - H_{22})\sin\phi_0\cos\phi_0$$
$$\times \int_0^{R_p} \int_0^{2\pi} re^{-ikr(\alpha\cos\phi + \beta\sin\phi)} \, \mathrm{d}r \, \mathrm{d}\phi$$
$$= (H_{11} - H_{22})\sin\phi_0\cos\phi_0\frac{2J_1(z)}{z}, \quad (62)$$

where we denote ϕ_0 instead of ϕ' to describe the azimuthal angle of the principal plane. This is to emphasize that ϕ_0 does not depend on the pupil coordinates and can be taken out of the integral, since the principal plane only changes in this case with the orientation of the incident rays, but not with their location on the pupil. The parameter z is given by

$$z = \frac{2\pi}{\lambda} R_{pup} \frac{\sqrt{\xi^2 + \eta^2}}{f}, \quad (63)$$

and J_1 is the first-order Bessel function. Whenever $\phi_0 = 0$ (as we can set for normal illumination of the pupil if $\theta_3 = 0$), the Jones matrix coefficients are greatly simplified:

$$\widetilde{H}'_{11} = H_{11}\frac{2J_1(z)}{z},$$
$$\widetilde{H}'_{22} = H_{22}\frac{2J_1(z)}{z},$$
$$\widetilde{H}'_{12} = \widetilde{H}'_{21} = 0. \quad (64)$$

A2. Telecentric Configuration

Unlike for the collimated configuration, a relation exists in telecentric setups between the incidence angle in the etalon and the coordinates of the pupil of the incident ray. This is described in Equation (59) of Paper I. Using radial coordinates, this expression can be rewritten as

$$\theta = \cos^{-1}\left(\frac{f}{\sqrt{(r\cos\phi - \xi)^2 + (r\sin\phi - \eta)^2 + f^2}}\right), \quad (65)$$

and no simplification of Equation (60) can be done in general. Only if we focus on the origin ($\xi = \eta = 0$) does the azimuthal dependence of $\widetilde{\mathbf{H}}'$ disappear, since

$$\theta = \cos^{-1}\left(\frac{f}{\sqrt{r^2 + f^2}}\right). \quad (66)$$

Note that in telecentric mounts each point of the image is illuminated by rays that have different orientations within the etalon. Therefore, appropriate rotations of the principal plane are needed over the integration domain. Since ϕ' is the azimuthal angle of the principal plane (Figure 2), its relation to the image plane azimuth ϕ can be found by geometrical considerations and depends on the ray coordinates on the pupil and chief ray position on the image plane:

$$\phi' = \tan^{-1}\left(\frac{\eta_0 - r\sin\phi}{\xi_0 - r\cos\phi}\right). \tag{67}$$

Now, none of the factors in Equation (60) can be taken out of the integral, and the expressions must be calculated numerically. We can only find an analytical expression for the Jones matrix elements at the center of the image plane, assuming that the optical axis is perpendicular and that $\xi_0 = \eta_0 = 0$. Then, $\phi' = \phi$, and we can simplify Equation (60) as

$$\tilde{H}'_{11} = \int_0^{R_p} r H_{11}(r)dr \int_0^{2\pi} \cos^2\phi \, d\phi$$
$$+ \int_0^{R_p} r H_{22}(r)dr \int_0^{2\pi} \sin^2\phi \, d\phi = \frac{1}{2}(\tilde{H}_{11} + \tilde{H}_{22}),$$
$$\tilde{H}'_{22} = \int_0^{R_p} r H_{11}(r)dr \int_0^{2\pi} \sin^2\phi \, d\phi$$
$$+ \int_0^{R_p} r H_{22}(r)dr \int_0^{2\pi} \cos^2\phi \, d\phi = \frac{1}{2}(\tilde{H}_{11} + \tilde{H}_{22}),$$
$$\tilde{H}'_{12} = \tilde{H}'_{21} = \int_0^{R_p} r[H_{11}(r) - H_{22}(r)] \, dr$$
$$\times \int_0^{2\pi} \sin\phi\cos\phi \, d\phi = 0, \tag{68}$$

where $\widetilde{H}_{11}$ and $\widetilde{H}_{22}$ were defined in Equation (46).

Appendix B
Mueller Matrix Coefficients Calculation

To calculate the coefficients a, b, c, and d of the Mueller matrix, we follow their definitions and use the nomenclature defined in Equations (17)–(21). We will employ the following definition of the Pauli matrices to be consistent with our sign convention (Del Toro Iniesta 2003):[3]

$$\sigma_0 = \begin{pmatrix} 1 & 0 \\ 0 & 1 \end{pmatrix}, \sigma_1 = \begin{pmatrix} 1 & 0 \\ 0 & -1 \end{pmatrix},$$
$$\sigma_2 = \begin{pmatrix} 0 & 1 \\ 1 & 0 \end{pmatrix}, \sigma_3 = \begin{pmatrix} 0 & i \\ -i & 0 \end{pmatrix}. \tag{69}$$

Now, according to Equation (8),

$$a = \frac{1}{\left[1 + F\sin^2\left(\frac{\delta_o}{2}\right)\right]\left[1 + F\sin^2\left(\frac{\delta_o + \varphi}{2}\right)\right]}$$
$$\times \left[\frac{\tau_o + \tau_e}{2} + \frac{F}{2}\tau_e\sin^2\left(\frac{\delta_o}{2}\right) + \frac{F}{2}\tau_o\sin^2\left(\frac{\delta_o + \varphi}{2}\right)\right]$$
$$= \frac{\tau_{\text{eff}}}{\zeta}\left(\frac{\bar{\tau}}{\tau_{\text{eff}}} + \Gamma\right). \tag{70}$$

---

³ Differences in the sign of the Pauli matrices lead to different conventions on the clockwise or anticlockwise rotation of the electric field polarization. For a more detailed discussion, please visit Appendix A of Jefferies et al. (1989).

Similarly,

$$b = \frac{1}{\left[1 + F\sin^2\left(\frac{\delta_o}{2}\right)\right]\left[1 + F\sin^2\left(\frac{\delta_o + \varphi}{2}\right)\right]}$$
$$\times \left[\frac{\tau_o - \tau_e}{2} + \frac{F}{2}\tau_o\sin^2\left(\frac{\delta_o + \varphi}{2}\right) - \frac{F}{2}\tau_e\sin^2\left(\frac{\delta_o}{2}\right)\right]$$
$$= \frac{\tau_{\text{eff}}}{\zeta}\Lambda. \tag{71}$$

For c and d we shall first calculate $H_{22}H_{11}^*$ and $H_{11}H_{22}^*$:

$$H_{22}H_{11}^* = \frac{\tau_{\text{eff}}}{\zeta(1-R)^2}[e^{i\varphi/2} + R^2 e^{-i\varphi/2}$$
$$- 2R\cos(\delta_o + \varphi/2)], \tag{72}$$

$$H_{11}H_{22}^* = \frac{\tau_{\text{eff}}}{\zeta(1-R)^2}[e^{-i\varphi/2} + R^2 e^{i\varphi/2}$$
$$- 2R\cos(\delta_o + \varphi/2)]. \tag{73}$$

Therefore, we can express c and d as

$$c = \frac{\tau_{\text{eff}}}{\zeta}\left[\frac{\cos(\varphi/2)}{(1-R)^2} + \frac{F}{4}R\cos(\varphi/2)\right.$$
$$\left. - \frac{F}{2}\cos(\delta_o + \varphi/2)\right] = \frac{\tau_{\text{eff}}}{\zeta}\left[\frac{\cos(\varphi/2)}{(1-R)^2} + \Psi\right], \tag{74}$$

$$d = \frac{\tau_{\text{eff}}}{\zeta}\left[\frac{-\sin(\varphi/2)}{(1-R)^2} - \frac{F}{4}R\sin(\varphi/2)\right]$$
$$= \frac{\tau_{\text{eff}}}{\zeta}\left[\frac{-\sin(\varphi/2)}{(1-R)^2} + \Omega\right]. \tag{75}$$

Appendix C
Electro-optic and Piezo-electric Effects in Z-cut Lithium Niobate Etalons

In Z-cut lithium niobate etalons, tuning of the transmitted wavelength is made by applying an electric field along the Z-cut direction. LiNbO₃ is an electro-optical material that presents changes in the refractive index by application of an external electric field through the Pockels effect. Changes in the width of the etalon also occur due to piezo-electric effects. Both have an influence on the birefringence of the crystal. In this appendix, we obtain a more general expression than Equation (36) for the birefringence that also takes into account the presence of external fields.

The Pockels effect depends not only on the particular optical axis of the crystal but also on the direction of the incoming light and on the direction of the electric field. At an atomic level an electric field applied to certain crystals causes a redistribution of bond charges and possibly a slight deformation of the crystal lattice. In general, these alterations are not isotropic, that is, the changes vary with direction in the crystal and, therefore, the permeability tensor is no longer diagonal in the presence of an external electric field (e.g., Kasap et al. 2012).

Consequently, even if the applied external field direction coincides with the optical axis (Z in this case), there is no guarantee that for normal illumination no birefringence will

appear. This will depend on the crystal symmetry class, which determines the form of the electro-optical tensor and not only on the direction of the incoming light and on the direction of the optical axis. For example, an uniaxial Z-cut crystal like KDP (KH_2PO_4) or lithium niobate ($LiNbO_3$) might become biaxial when applying an external field along the Z-axis. In the case of KDP, the field along Z rotates the principal axes by $45°$ about Z and changes the principal indices n_1 and n_2. The particular effect of applying an electric field for lithium niobate needs to be studied for our specific application.

C1. Pockels Effect

The Pockels effect consists of a linear change in the impermeability tensor due to the linear electro-optic effect when an electric field is applied. The impermeability tensor is defined as $\eta \equiv \epsilon_0 \epsilon^{-1}$, where ϵ_0 is the vacuum permittivity and ϵ is the permittivity tensor. This tensor is diagonal in the principal coordinates with elements $\eta_{11} = 1/n_1^2$, $\eta_{22} = 1/n_2^2$, and $\eta_{33} = 1/n_3^2$. The change in the impermeability tensor can be expressed as

$$\Delta \eta_i = \sum_j r_{ij} E_j, \quad (76)$$

where r_{ij} are the components of the electro-optical tensor and E_j are the components of the electric field. Subindices i and j take the values $i = 1, …, 6$ and $j = 1, 2, 3$. The new impermeability tensor, $\bar{\eta}$, is no longer diagonal in the principal dielectric axes system:

$$\bar{\eta} = \begin{pmatrix} 1/n_1^2 + \Delta \eta_1 & \Delta \eta_6 & \Delta \eta_5 \\ \Delta \eta_6 & 1/n_2^2 + \Delta \eta_2 & \Delta \eta_4 \\ \Delta \eta_5 & \Delta \eta_4 & 1/n_3^2 + \Delta \eta_3 \end{pmatrix}. \quad (77)$$

The presence of cross terms indicates that the principal dielectric axis system is changed. Determining the new principal axes and the new refraction indices requires that the impermeability tensor is diagonalized, thus determining its eigenvalues and eigenvectors. Lithium niobate is a trigonal 3 m point group crystal (Nikogosyan 2005), and therefore its electro-optical tensor is given by (Bass et al. 1995)

$$r = \begin{pmatrix} 0 & -r_{22} & r_{13} \\ 0 & r_{22} & r_{13} \\ 0 & 0 & r_{33} \\ 0 & r_{51} & 0 \\ r_{51} & 0 & 0 \\ -r_{22} & 0 & 0 \end{pmatrix}, \quad (78)$$

where r_{22}, r_{13}, r_{33}, and r_{51} depend on both the material and the specific sample. We can take the values $r_{22} \simeq 6.8$, $r_{13} \simeq 9.6$, $r_{33} \simeq 30.9$, and $r_{51} \simeq 32.6$ (all in pm V^{-1}) at $\lambda = 632.8$ nm as reference for $LiNbO_3$ (Nikogosyan 2005). If we apply an electric field along the optical axis ($j = 3$),

$$\Delta \eta_1 = \Delta \eta_2 = r_{13} V/h,$$
$$\Delta \eta_3 = r_{33} V/h,$$
$$\Delta \eta_4 = \Delta \eta_5 = \Delta \eta_6 = 0, \quad (79)$$

where V is the associated potential difference associated with the applied electric field. In this case, the impermeability tensor

is symmetric and the new refraction indices, $\bar{n}_1$, $\bar{n}_2$, $\bar{n}_3$, are given by

$$\bar{n}_1 = \bar{n}_2 \equiv \bar{n}_o(V) = \frac{n_o}{\sqrt{1 + r_{13}Vn_o^2/h}} \simeq n_o - \frac{r_{13}n_o^3 V}{2h}, \quad (80)$$

$$\bar{n}_3(V) = \frac{n_3}{\sqrt{1 + r_{33}Vn_3^2/h}} \simeq n_3 - \frac{r_{33}n_3^3 V}{2h}. \quad (81)$$

Note that Equation (80) coincides with the known unclamped Pockels effect formula for $LiNbO_3$ (Equation (27) of Paper I). This leads us to an explicitly modified relation between the n_e and n_o that takes into account both the incidence angle of the incoming light and the applied voltage employed to tune the etalon:

$$\frac{1}{n_e^2(\theta, V)} = \frac{1}{\bar{n}_o^2(V)} \cos^2 \theta + \frac{1}{\bar{n}_3^2(V)} \sin^2 \theta. \quad (82)$$

Very interestingly, since the impermeability tensor is diagonal and $\bar{n}_1 = n_2'$ for a Z-cut $LiNbO_3$ when an electric field in the direction of the optical axis is applied, the crystal remains uniaxial and there is no birefringence induced at normal illumination, no matter the intensity of the electric field. For $\theta \neq 0$ the birefringence is both angle and voltage dependent.

C2. Piezo-electric Effect

There is a second important effect that happens in $LiNbO_3$ when applying an electric field: the piezo-electric effect. It consists of a change of shape due to the application of an electric field and can be described by a linear relationship between the acting voltage and the change of width of the etalon. If the electric field is applied along the optical axis direction, the change of width is described (Weis & Gaylord 1985) by

$$\Delta h = d_{33}V, \quad (83)$$

where $d_{33} \simeq 26$ pm V^{-1} (Nikogosyan 2005). We can check whether the piezo-electric and electro-optical coefficients obtained from Nikogosyan (2005) agree with the measured voltage tuning sensitivity found in Martínez Pillet et al. (2011): 0.0335 pm V^{-1} for the IMaX instrument aboard Sunrise. The estimated value is given by

$$\frac{\Delta \lambda}{V} = \left(d_{33} - \frac{n_o^3 r_{13}}{2}\right)\frac{\lambda_0}{h} \simeq -0.078 \text{ pm V}^{-1}, \quad (84)$$

which is twice as large as the experimental value. This departure from the measured value can be due to the fact that the electro-optical coefficients depend on the specific sample of lithium niobate material and on the wavelength. However, although these results differ considerably, we can use these piezo-electric and electro-optical coefficients to get a quantitative estimation of the order of magnitude of the birefringence φ. Using Equations (36), (80), (81), and (83), it is
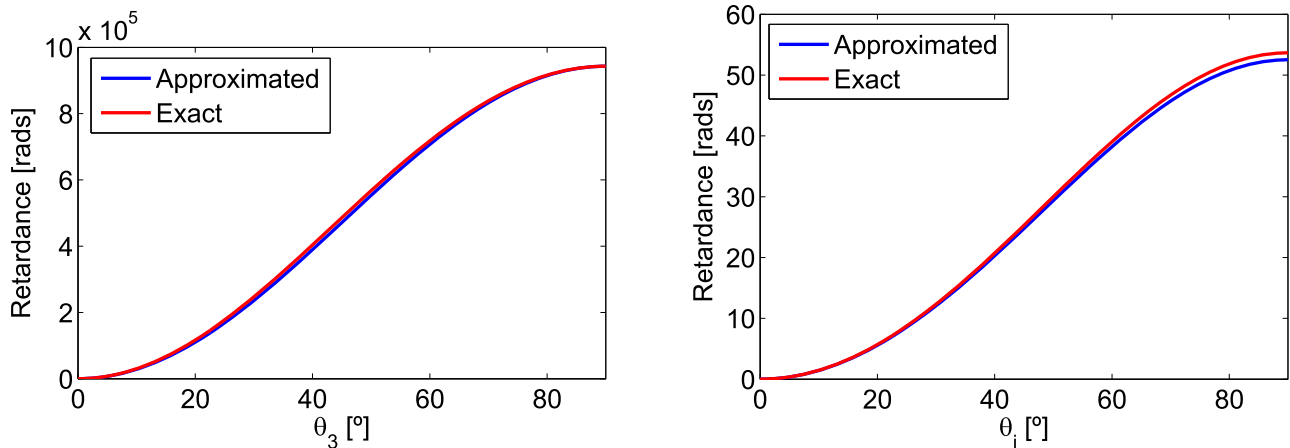
Figure 13. Retardance calculated by the approximated Equation (36) (blue solid line) and the exact expression found by Veiras (red solid line) as a function of the polar angle of the optical axis at normal illumination (left) and as a function of the incidence angle for an optical axis perpendicular to the etalon reflective surfaces (right).

straightforward to show that

$$
\varphi'(V) \simeq \frac{4\pi(h + d_{33}V)}{\lambda \cos\theta'}\left[n_o - n_3 + \frac{V(r_{13}n_o^3 - r_{33}n_3^3)}{2(h + d_{33}V)}\right] \\
\times \sin^2(\theta' - \theta_3).
$$

(85)

Notice that θ' will also depend on V as n depends on the ordinary and extraordinary indices (Equation (35)). The maximum relative variation of $\varphi(V)$ with respect to $\varphi(V = 0)$ happens at the limits of the recommended range of voltages, ± 3000 V, of a commercial CSIRO etalon (Martínez Pillet et al. 2011) and turns out to be $\simeq 1.4\%$ if we use the above experimental electro-optical and piezo-electric coefficients (Nikogosyan 2005) and $n_o = 2.29$, $n_e = 2.20$, $R = 0.92$, $A = 0$, $\lambda = 617.3$ nm. This variation is very small compared to the birefringence produced by other effects and has been neglected in this work.

Appendix D
Exact Expressions for the Retardance in Uniaxial Media

A completely general calculation of phase shifts between orthogonal components of the electric field in uniaxial media was found by Veiras et al. (2010) taking into account the orientation of the optical axis for any plane wave with an arbitrary incident direction. Their results are not restricted to small birefringence media, in contrast to Equation (36). They also consider the orientation of the plane of incidence. The expressions of Veiras et al. (2010) and ours should be completely equivalent in the small birefringence regime. Figure 13 shows a comparison between the Veiras et al. (2010) expressions and Equation (36) in two particular cases, namely, for normal illumination with a variable polar angle of the optical axis and for an optical axis perfectly perpendicular to the interphase with a variable incidence angle. We have employed the same parameters of the lithium niobate etalon used throughout this work. We can observe that differences between the exact and approximated expressions are almost negligible with θ_3 for normal illumination (left) and can only be

appreciated well for incidence angles higher than $50°$ and for $\theta_3 = 0$ (right).

ORCID iDs

F. J. Bailén ⓘ https://orcid.org/0000-0002-7318-3536
D. Orozco Suárez ⓘ https://orcid.org/0000-0001-8829-1938
J. C. del Toro Iniesta ⓘ https://orcid.org/0000-0002-3387-026X

References

Álvarez-Herrero, A., Belenguer, T., Pastor, C., et al. 2006, Proc. SPIE, 6265, 62652G
Bailén, F. J., Orozco Suárez, D., & Del Toro Iniesta, J. C. 2019, ApJS, 241, 9, (Paper I)
Bass, M., Stryland, E., Williams, D. R., et al. 1995, Handbook of Optics, Vol. II: Devices (2nd ed.; New York: McGraw-Hill)
Born, M., & Wolf, E. (ed.) 1999, Principles of Optics (Cambridge: Cambridge Univ. Press)
Del Toro Iniesta, J. C. 2003, Introduction to Spectropolarimetry (Camabridge: Cambridge Univ. Press)
Del Toro Iniesta, J. C., & Martínez Pillet, V. 2012, ApJS, 201, 22
Doerr, H.-P., von der Lühe, O., II, & Kentischer, T. J. 2008, Proc. SPIE, 7014, 701417
Gary, G. A., West, E. A., Rees, D., et al. 2007, A&A, 461, 707
Jefferies, J., Lites, B. W., & Skumanich, A. 1989, ApJ, 343, 920
Kasap, S., Ruda, H., & Boucher, Y. 2012, Cambridge Illustrated Handbook of Optoelectronics and Photonics (Cambridge: Cambridge Univ. Press)
Kentischer, T. J., Schmidt, W., Sigwarth, M., & Uexkuell, M. V. 1998, A&A, 340, 569
Lites, B. W. 1991, Solar Polarimetry, 166
Martínez Pillet, V., Del Toro Iniesta, J. C., Álvarez-Herrero, A., et al. 2011, SoPh, 268, 57
Netterfield, R. P., Freund, C. H., Seckold, J. A., et al. 1997, ApOpt, 36, 4556
Nikogosyan, D. 2005, in Nonlinear Optical Crystals: A Complete Survey, ed. D. Nikogosyan (Berlin: Springer), 427
Puschmann, K. G., Kneer, F., Seelemann, T., & Wittmann, A. D. 2006, A&A, 451, 1151
Scharmer, G. B., Narayan, G., Hillberg, T., et al. 2008, ApJL, 689, L69
Solanki, S. K., del Toro Iniesta, J. C., Woch, J., et al. 2015, in IAU Symp 305, Polarimetry, ed. K. N. Nagendra et al. (Cambridge: Cambridge Univ. Press), 108
Veiras, F. E., Perez, L. I., & Garea, M. T. 2010, ApOpt, 49, 2769
Vogel, W., & Berroth, M. 2003, Proc. SPIE, 4944, 293
Weis, R. S., & Gaylord, T. K. 1985, ApPhA, 37, 191
Zhang, S., Hellmann, C., & Wyrowski, F. 2017, ApOpt, 56, 4566

Paper III: Instrument applications

On Fabry–Pérot Etalon-based Instruments. III. Instrument Applications

F. J. Bailén , D. Orozco Suárez , and J. C. del Toro Iniesta
Instituto de Astrofísica de Andalucía (CSIC), Apdo. de Correos 3004, E-18080 Granada, Spain; fbailen@iaa.es, orozco@iaa.es, jti@iaa.es
Received 2019 October 28; revised 2019 November 29; accepted 2019 November 29; published 2020 January 16

Abstract

The spectral, imaging, and polarimetric behavior of Fabry–Pérot etalons have an influence on imaging vector magnetograph instruments based on these devices. The impact depends on the optical configuration (collimated or telecentric), on the relative position of the etalon with respect to the polarimeter, on the type of etalon (air-gapped or crystalline), and even on the polarimetric technique to be used (single-beam or dual-beam). In this paper, we evaluate the artificial line-of-sight velocities and magnetic field strengths that arise in etalon-based instruments, attending to the factors mentioned. We differentiate between signals that are implicit to telecentric mounts due to the wavelength dependence of the point-spread function and those emerging in both collimated and telecentric setups from the polarimetric response of birefringent etalons. For the anisotropic case, we consider two possible locations of the etalon—between the modulator and the analyzer or after it—and we include the effect on different channels when dual-beam polarimetry is employed. We also evaluate the impact of the loss of symmetry produced in telecentric mounts due to imperfections in the illumination and/or to a tilt of the etalon relative to the incident beam.

Unified Astronomy Thesaurus concepts: Polarimeters (1277); Spectrometers (1554); Spectropolarimetry (1973); Polarimetry (1278); Spectroscopy (1558); Solar instruments (1499)

1. Introduction

Some solar magnetographs are based on the combination of a polarimeter with a tunable bidimensional filter, typically a Fabry–Pérot etalon. The final goal of these instruments is to precisely infer the solar magnetic field and plasma velocities from the spectrum and state of polarization of light. Hence, it is mandatory to have control over the polarimetric influence of all optical elements on the polarization measurement process. Usually, the whole system is calibrated in such a way that the Mueller matrix of the instrument contains information on the modulator, the analyzer, and the remaining elements in the optical setup. This way, it is not necessary to pay much attention to the polarimetric behavior of the particular optical elements. However, etalons used as monochromators have an impact on the measurement of the Stokes vector even if they are perfectly isotropic. Their influence into real observations is such that it cannot be calibrated using standard techniques (i.e., with flat illumination) and depends on the manner they are illuminated: collimated or telecentric. For a detailed discussion on the imaging performance of etalons in collimated and telecentric configurations, we refer the reader to the following works: Beckers (1998), von der Lühe & Kentischer (2000), Scharmer (2006), Righini et al. (2010) and Bailén et al. (2019a), the first in our series of papers.

In particular, etalons mounted in a telecentric configuration (ideally) keep the same transmission profile across the field of view (FoV), at the expense of leading to artificial signals in the measured Stokes vector, due to asymmetries induced in the point-spread function (PSF) over the spectral profile (Beckers 1998). Moreover, irregularities on the etalon and deviations from perfect telecentric illumination further degrade the measurements.[1] For

---

[1] We use the term "perfect telecentrism" when referring to telecentric illumination in which the chief ray impinges the etalon perpendicularly to its reflecting surfaces. We consider that any deviation from such a situation is an imperfection because it degrades the spectral transmission and the PSF of the instrument. Thus, we refer to those cases as "imperfect telecentrism," even if the deviation is only caused by a tilt of the etalon while keeping the telecentrism over the FoV.

example, strictly speaking, no PSF can be defined for the system since translational invariance is lost and the spatial response of the etalon is different for each point over the FoV (see Bailén et al. 2019a, hereafter Paper I). Instead, we can only speak of a *local* PSF to stick to known and simple concepts.

Departures of the chief ray from normal incidence produce an asymmetrization of the spectral transmission profile and of the spatial shape of the local PSF of the instrument. It also introduces a widening of the transmission profile and of the local PSF, as well as a shift of their peaks (Paper I). Defects associated with deviations of the flatness of the reflecting surfaces can also modify the local PSF and the spectral transmission pixel to pixel.

In collimated setups, the effects associated with fluctuations of the optical path due to roughness errors average over the area of the etalon that is illuminated. In addition, the PSF dependence on wavelength over the passband is nonexistent, but other problems can arise. For instance, we can no longer speak of PSF, much like in the imperfect telecentric case, because of the loss of space invariance associated with a transmission factor that appears in the PSF and which depends on the image plane coordinates (Paper I). Moreover, the monochromatic transmission can be reduced drastically if defects on the etalon are not kept low enough.

In both collimated and telecentric configurations, the response of the instrument depends on the object itself. Hence, the inferred Stokes vector can be altered simply because of the polychromatic nature of the observations, no matter which configuration is employed. This is of special importance for telecentric mounts, because of the strong spectral dependence their PSFs suffer from. Naturally, changes of the cavity errors during the spectral scan can also have an impact on the measurement of the Stokes vector for both mounts. Such a change on the defects distribution has been confirmed recently in piezo-stabilized etalons (Greco et al. 2019).

Examples of instruments based on etalons illuminated with a telecentric beam include the Italian Panoramic Monochromator

at THEMIS (Bonaccini et al. 1989, and references therein), the TESOS spectrometer at the VTT (Kentischer et al. 1998), the CRisp Imaging SpectroPolarimeter instrument at the Swedish 1 m Solar Telescope (Scharmer et al. 2008; van Noort & Rouppe van der Voort 2008), the PHI instrument on board the Solar Orbiter mission (Solanki et al. 2015), and the Visible Tunable Filter at the upcoming DKIST (Schmidt et al. 2016). Solar instruments equipped with etalons mounted in a collimated setup include the Interferometric Bidimensional Spectrometer at the Dunn Solar Telescope of the Sacramento Peak Observatory (Cavallini 1998), the GFPI at GREGOR (Puschmann et al. 2013), and the IMaX instrument aboard SUNRISE (Martínez Pillet et al. 2011).

Among the instruments mentioned, IMaX and PHI use Fabry–Péróts based on lithium niobate crystals to allow for spectral scanning without the need to use piezo-actuators. The birefringent properties of this crystal also contribute to modify the incident Stokes vector. In particular, the polarimetric behavior depends on the etalon geometry, wavelength, angle of the incident wavefront, birefringence of the crystal, and on the orientation of the optical axis angle of the crystal with respect to the wavefront normal in the way described by Bailén et al. (2019b; hereafter Paper II). Of course, birefringence can also appear locally within the etalon due to local surface defects created during the polishing and to the polarization-dependent response of the coating of the etalon (Doerr et al. 2008).

Fortunately, the etalon is never positioned at the beginning of the optical setup when doing full polarimetric measurements. Rather, it is usually illuminated by a polarimetric modulated intensity signal if the etalon is located before the analyzer or just with linearly polarized light when it is at the very end of the optical path, following the analyzer. The influence of the etalon in the polarimetric behavior of polarimeters has been addressed already (Del Toro Iniesta & Martínez Pillet 2012). These authors considered the effect of typical optical elements and included a birefringent Fabry–Pérot, concluding that the optimum polarimetric efficiencies can still be reached no matter the retardance introduced by the etalon. However, they did not take into account either the real Mueller matrix of the etalon nor the influence of the optical configuration; rather, they just represented the etalon as an additional retarder plus a mirror within the optical path.

In a more realistic situation, the birefringent effects brought about by the etalon depend on the optical setup, i.e., on how the etalon is illuminated within the optical path. In collimated setups, the coefficients of the Mueller matrix of the etalon are reduced to four independent terms that vary with the parameters mentioned above (Paper II). The spectral dependence of the coefficients is particularly strong and plays an important role in quasi-monochromatic observations. Moreover, the Mueller matrix shape changes with the principal plane orientation, which is determined by the plane formed by the wavefront vector and the optical axis of the crystal. This implies that the impact of the birefringence of the etalon is different for each direction of the wavefront—and thus for each pixel. In perfect telecentric mounts, off-diagonal terms on the Mueller matrix are null and the effect of the birefringence is translated only into the transmission profile (Paper II). In real instruments in which illumination differs from perfect telecentrism and/or local deviations of the optical axis appear during the process of manufacturing (*local domains*), the Mueller matrix no longer remains diagonal and the effect on the

polarimetric measurements is more pronounced since cross-talks between different Stokes components can appear, just like in the collimated case.

This paper is a continuation of the work presented in Bailén et al. (2019a, 2019b), where we reviewed the spectral, imaging, and birefringent properties of Fabry–Pérot etalons when located in solar magnetographs. Here we evaluate the influence of etalons in the process of measuring physical solar quantities from the observations, i.e., we assess their imprints in the inferred line-of-sight (LoS) velocities and the magnetic field strengths from solar vector magnetographs. We begin with an evaluation of artificial signals in isotropic telecentric mounts for both perfect and imperfect illumination of the etalon (Section 2). Next, we study the effects of birefringence on the measurements (Section 3). We consider two possible locations of the etalon: after the polarimeter and between the modulator and the analyzer. We also differentiate between collimated and telecentric setups and we include the effects of imperfect illumination of the etalon.

2. Artificial Signals in Isotropic Telecentric Mounts

Beckers (1998) was the first to predict that the spectral dependence of the PSF implicit to etalons in telecentric configuration gives rise to artificial signals in the LoS velocities. He also warned that these signals are expected to arise in images with velocity structure. The origin of the spurious LoS velocities comes from the fact that observations are not purely monochromatic, but rather quasi-monochromatic (Equation (61) of Paper I). The wavelength dependence induces asymmetries in the observed profile even if the original is completely symmetric. Obviously, magnetic field measurements are also influenced by these asymmetries, although they are not mentioned by Beckers (1998); what is more important, the induced signals cannot be mitigated unless the PSF is completely characterized. The latter is almost impossible in practice.

A proper evaluation of these false signals requires a careful comparison between a reference case where the spectral PSF is assumed to be invariant in wavelength and a real observation in which the PSF varies over the spectral bandwidth. Of course, the modulation scheme of the instrument and the position of the etalon in the optical train must be considered as well, especially for etalons that are anisotropic. In this section we will address only the case of etalons that are isotropic (see Section 3 for a discussion on the impact of birefringent etalons). To evaluate the spurious signals, we have compared the expected LoS velocities and magnetic field strength when taking into account the spectral dependence originated in the telecentric case (Paper I) with the results obtained with an *ideal* wavelength-independent reference PSF. The ideal PSF we have chosen is simply the monochromatic telecentric PSF at its peak transmission wavelength, modulated spectrally by the transmission profile that corresponds to the same telecentric configuration. This PSF of reference does not show any spatial variation across the passband of the etalon. Rather, it shows only a modulation of intensity, like in a collimated case, and, hence, it does not introduce spurious signals when measuring the Stokes vector.

For the test, we assume a polarimeter consisting of a pair of liquid crystal variable retarders (LCVRs) as modulator and a linear polarizer as analyzer, similarly to the PHI and IMaX instruments. Application of different voltages to each of the

Table 1
Optimum Retardances Used for the LCVRs in the IMaX and PHI Instruments

	PM1	PM2	PM3	PM4
$\delta_1[°]$	225	225	315	315
$\delta_2[°]$	234.736	125.264	54.736	305.264

LCVRs translates into different retardances—and consequently, in a modulation of the signal recorded by the instrument cameras. A linear combination of four different modulations is enough to obtain the four Stokes parameters. Furthermore, a proper choice of the retardances optimizes the polarimetric efficiencies in the sense of minimizing error propagation in the measurement of the Stokes vector (Del Toro Iniesta & Collados 2000). Table 1 shows the retardances for both LCVRs, δ_1 and δ_2, and for the four modulations in sequential order (from PM1 to PM4) employed to obtain an optimum modulation scheme in the mentioned instruments. In imaging instruments, this process is done at each of the wavelengths of interest. Once the Stokes parameters have been determined, it is possible, using different diagnostic techniques, to infer the LoS velocity and the vector magnetic field of the plasma.

We have simulated the effect of a telecentric etalon in the inferred LoS velocities and magnetic field strength on a set of synthetic spectral images of the four Stokes parameters obtained through magnetohydrodynamical (MHD) simulations (Vögler et al. 2005). The spatial sampling of the synthetic data is 0″0287 and the size of our image is 256×256 pixels^2. The spectral range goes from -40 to 40 pm in steps of 1 pm and is centered about the 525.02 nm Fe I line observed by IMaX.[2] We have modulated the Stokes vector monochromatically with the set of retardances presented in Table 1 assuming the etalon is placed after the analyzer. This choice of the etalon position is irrelevant, however, because it is considered to be isotropic. Figure 1(a) shows the simulated Stokes I parameter at the continuum (top), as well as the LoS velocity structure (middle) and the magnetic field strength (bottom) corresponding to the input data. A solar pore with an intense magnetic field can be appreciated, covering an area of approximately 100×100 pixels^2.

The different *observed* intensity maps at each wavelength of the spectral range are obtained over the range ±20 pm with respect to the center of the line by tuning the transmission profile of the etalon over the target spectral line and applying Equation (62) of Paper I. The PSF considered corresponds to a perfect telecentric $f/40$ isotropic etalon with $n = 2.3$, $h = 250\,\mu m$, $R = 0.92$, and $A = 0$.[3] Next, we have obtained the Stokes parameters at each wavelength with the proper demodulation matrix (Del Toro Iniesta & Martínez Pillet 2012). Finally, we have compared the corresponding LoS velocities and magnetic field strengths with the ones obtained with the reference PSF mentioned above.

For the sake of simplicity, the LoS velocities and magnetic field strength signals have been calculated using the center of gravity (CoG) method (Semel 1967). Figure 1(b) shows the spurious signals obtained for the LoS velocities (left) and magnetic fields strength (right) in the telecentric case when compared to the reference case, labeled as *ideal*, defined above.
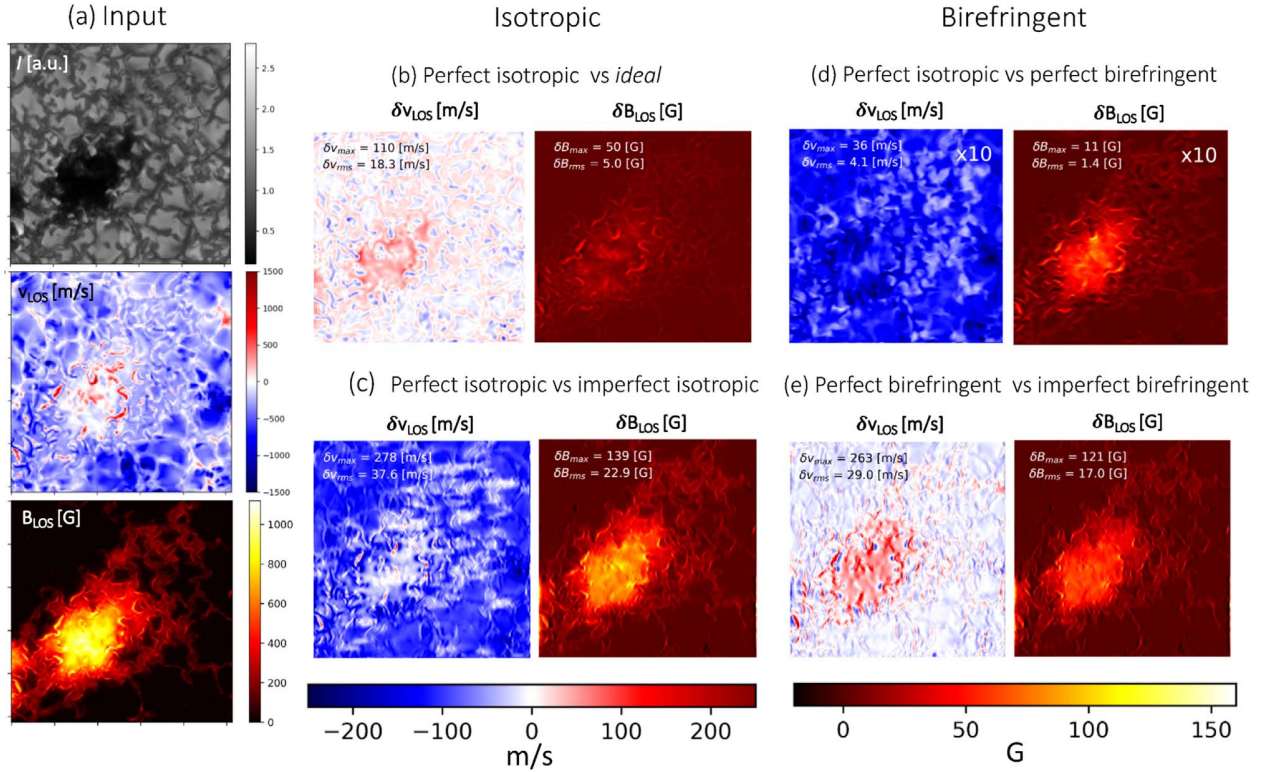
We have focused on "perfect telecentrism," that is, to normal incidence of the chief ray on the etalon surfaces for the whole FoV. It can be seen that the difference between signals reach values up to $\sim110\,m\,s^{-1}$ for the LoS velocity, δv_{LOS}, and as much as ~50 Gauss for the field strength, δB_{LOS}, both in absolute value. The artificial LoS velocity map shows considerable small-scale fluctuations associated with the presence of granules, intergranular lanes, and a pore. Of course, this is because the Stokes parameters have changed after passing through the etalon. Although not shown, it is pertinent to observe that the artificial signals obtained for Stokes V are always below $\sim5\%$ in the wing of the 525.02 nm Fe I line, where the Stokes V reaches a maximum. The rms and maximum values of the spurious signals can be found in Table 2.

In the case that the cone of rays is inclined at a small angle with respect to the normal of the etalon, the loss of symmetry with respect to the normal causes both the spectral transmission of the etalon and the spatial PSF to become asymmetric (Paper I). Such an effect happens locally in imperfect telecentric mounts, where the chief ray deviates gradually from the center of the image plane to its borders. It also occurs when the etalon is tilted to suppress ghost images on the focal plane originated by multiple reflections. Since the effects are equivalent, we will refer hereafter to these two cases indistinctly as "imperfect telecentrism." The induced asymmetries are expected to further introduce false LoS velocities and magnetic field signals. Naturally, asymmetries in the instrumental profile can also arise from an unsymmetrical spatial distribution of cavity errors (e.g., Reardon & Cavallini 2008). Figure 1(c) shows the map of artificial LoS velocities (left) and magnetic signals (right) that appear in an imperfect isotropic telecentric configuration with a chief ray angle of 0°5. As reference, a perfect isotropic telecentric etalon has been considered. Differences between the perfect and imperfect telecentric mounts are as large as ~140 G in δB_{LOS}, $\sim280\,m\,s^{-1}$ in δv_{LOS} and $\sim18\%$ in V (Table 2). Such high signals are caused by a large shift and a significant asymmetrization of the observed spectral profile. The PSF is shifted and loses its spatial symmetry (see Paper I), thus displacing the profiles and introducing an offset in the velocities ($\sim80\,m\,s^{-1}$). The rms value of the artificial velocities is probably better suited for comparison purposes with perfect telecentrism. In this case, the rms velocity is $\sim37.5\,m\,s^{-1}$, whereas for the velocities in Figure 1(b) it is approximately half this value, $\sim18\,m\,s^{-1}$. Note that typical tolerances in real instruments usually keep deviations below 0°5. Moreover, this value corresponds to a maximum deviation and mostly effects to the borders of the image while here we have assumed that the whole image suffers from such a deviation.

So far, we have focused on a telecentric configuration with an $f/40$ aperture. Such wide apertures are not common in solar instruments. Rather, the f-numbers are typically larger than $f/100$, especially for ground-based telescopes. Examples include the beams illuminating the etalons of THEMIS ($f/192$), TESOS ($f/125$ and $f/265$), and of the Visible Tunable Filter ($f/200$). In addition, deviations from perfect telecentrism in these instruments are not as large as the one assumed here. However, tilt of the etalon to suppress ghost images is common and it affects the relative inclination of the cone of rays over the whole FoV. Fortunately, tilts applied are typically far below 0°5. PHI is an exception since its etalon is illuminated by an $f/56$ or by an $f/63$ beam depending on the configuration. In addition, tolerances in this instrument allow for a maximum deviation of the chief ray over the FoV of 0°23. Nonetheless,

---

[2] Although we will concentrate our tests in this spectral line, the results are of the same order for other lines, such as the Fe I 617.3 nm observed by PHI.
[3] The reader is referred to Paper I for the missing definitions.

Figure 1. (a) Synthetic input maps from MHD simulations: Stokes *I* (top), LOS velocities (middle), and LOS magnetic field (bottom). Panels (b) to (e) present a comparison of observed LOS velocities (left) and magnetic fields (right) by a telecentric etalon for different situations, considering both the isotropic ((b) and (c)) and the birefringent cases ((d) and (e)). Panel (b) shows the residual signal after subtracting the one obtained when employing the reference wavelength independent PSF, labeled as *ideal*, and the signals that appear using the isotropic PSF that considers the wavelength dependence. Panel (c) illustrates the difference between the "perfect" isotropic telecentric configuration, where the chief ray is perpendicular to the etalon surfaces, with respect to an "imperfect" isotropic telecentric configuration in which the chief ray has an incidence angle on the etalon of $0°.5$. Panel (d) shows the difference between the signals arising for a perfect birefringent and an isotropic mount. Panel (e) is the same as (c), but considering a birefringent etalon.

the impact on the measurements is more benign than those shown in Sections 2, 3.1.2, and 3.2.2, because of the larger aperture and the better telecentrism.

Figure 2 shows the maximum and rms values of the spurious signals obtained for a perfect telecentric configuration with *f*-numbers 40, 60, 80, 100, and 120. Fitting of the data to a curve of the type $a_0 + a_1(f\#)^{-1} + a_2(f\#)^{-2}$ is also displayed for each subfigure, where a_0, a_1, and a_2 are the adjusted coefficients. We observe that artificial signals decay roughly in a quadratic way with the inverse of the $f\#$. Consequently, we can safely disregard the mentioned effects in etalons illuminated by the slow beams associated with ground-based instruments. For PHI, undesired signals are still expected to be seen, although less than half the values presented here for an $f/40$ telecentric configuration. The use of such a "fast" beam and such a large deviation of the chief ray in our simulations simply serves to illustrate more clearly the possible artificial signals that can appear in telecentric mounts. In any case, a careful assessment is required for the future generation of space instruments, which will probably require "small" *f*-numbers ($<f/60$) for compactness purposes.

3. Effects of Etalon Birefringence on the Polarimetric Modulation

In Paper II, we showed that the Mueller matrix of a birefringent etalon is a combination of both a retarder and a mirror modulated by a wavelength-dependent gain factor.

Thus, any deviation from normal illumination has an impact on the optimum polarimetric efficiencies and on the measured Stokes parameters. The presence of the etalon can be evaluated easily if the polarimetric response of the etalon is included in the Mueller matrix of the polarimeter. A distinction between the next two cases is mandatory: either (1) the etalon is located after the analyzer (Figure 3(a)) or (2) the etalon is placed at an intermediate position between the modulator and the analyzer (Figure 3(b)). The second configuration is common in dual-beam polarimeters, such as IMaX, whereas the first is used in single-beam instruments, like PHI. Both use also a birefringent etalon made of lithium niobate.

The illumination of the etalon (collimated or telecentric) is also important in the analysis since it changes the functional shape of the Mueller matrix coefficients. We will consider each case separately in the next sections assuming the same polarimeter as in the previous section.

3.1. Etalon Located after the Analyzer

3.1.1. Collimated Configuration

The Mueller matrix of a polarimeter formed by a pair of LCVRs and an analyzer is given by $\mathbf{M}_{\mathrm{pol}} = \mathbf{L}\mathbf{R}_2\mathbf{R}_1$, where $\mathbf{L}$, $\mathbf{R}_2$, and $\mathbf{R}_1$ correspond to the Mueller matrices of a linear polarizer with its transmission axis at $0°$, a retarder with fast axis at $45°$, and a retarder with fast axis at $0°$ (all angles measured with respect to the $+Q$ direction). The Mueller

Table 2
Summary of Results of the Artificial Signals Found in Telecentric ($f/40$) and Collimated Configuration

Configuration	$\delta v_{\rm rms}$ (m s^{-1})	$\delta v_{\rm max}$ (m s^{-1})	$\delta B_{\rm rms}$ (G)	$\delta B_{\rm max}$ (G)	$\delta V_{\rm rms}$ (%)	$\delta V_{\rm max}$ (%)
Isotropic perfect telecentric vs. isotropic monochromatic telecentric	18.3	110	5.0	50	0.4	4.9
Isotropic imperfect telecentric vs. isotropic perfect telecentric	37.6	278	22.9	139	2.2	18
Birefringent perfect telecentric vs. isotropic perfect telecentric	4.1	36	1.4	11	0.09	0.8
Birefringent perfect telecentric (channel 1 vs. channel 2)	...	...	...	...	...	0.006
Birefringent imperfect telecentric vs. birefringent perfect telecentric	29.0	263	17.0	121	2.3	20
Birefringent collimated before analyzer (channel 1 vs. channel 2)	...	...	...	...	...	0.3
Birefringent collimated before analyzer vs. birefringent collimated after analyzer	3	15	0.07	0.7	0.03	0.45
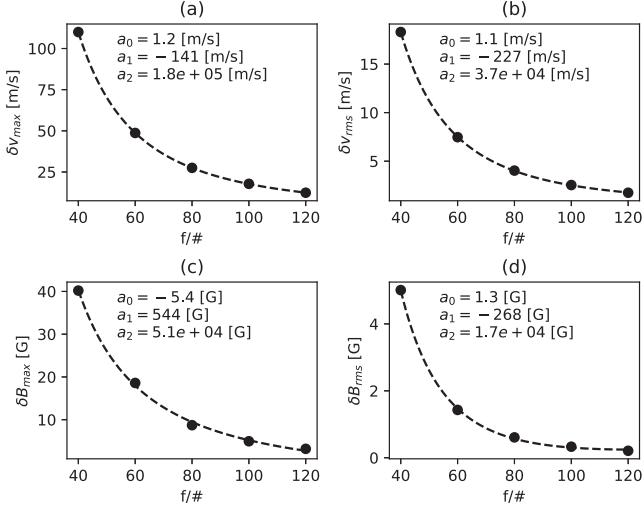
Figure 2. Maximum and rms value calculated from the maps of artificial LoS velocities ((a) and (b), respectively) and magnetic field ((c) and (d), respectively) arising in a telecentric setup vs. the f-number of the beam. Values obtained directly from simulations are displayed as dots, whereas the corresponding fitting is shown as a dashed line.

matrix of the polarimeter can be cast in such a case as

$$\mathbf{M}_{\rm pol} = \frac{1}{2}\begin{pmatrix} 1 & \cos\delta_2 & \sin\delta_1\sin\delta_2 & -\cos\delta_1\sin\delta_2 \\ 1 & \cos\delta_2 & \sin\delta_1\sin\delta_2 & -\cos\delta_1\sin\delta_2 \\ 0 & 0 & 0 & 0 \\ 0 & 0 & 0 & 0 \end{pmatrix}, \quad (1)$$

where δ_1 and δ_2 are the retardances associated to the LCVRs at $0°$ and $45°$, respectively. If we assume that the etalon is in a collimated configuration and is placed after the analyzer (Figure 3(a)), then the Mueller matrix of the system is given by $\mathbf{M}_{\rm tot} = \mathbf{M}_{\rm et}\,\mathbf{M}_{\rm pol}$, where $\mathbf{M}_{\rm et}$ is the Mueller matrix of the etalon. The Mueller matrix $\mathbf{M}_{\rm et}$ can be cast as (Equation (32) in Paper II)

$$\mathbf{M}_{\rm et} = \begin{pmatrix} a & bC_2 & bS_2 & 0 \\ bC_2 & aC_2^2 + cS_2^2 & (a-c)S_2C_2 & dS_2 \\ bS_2 & (a-c)S_2C_2 & aS_2^2 + cC_2^2 & -dC_2 \\ 0 & -dS_2 & dC_2 & c \end{pmatrix}, \quad (2)$$

where a, b, c, and d are defined in Equation (10) from Paper II and depend on the etalon geometry, wavelength, angle of the incident wavefront, birefringence of the crystal, and on the orientation of the optical axis angle of the crystal. Coefficients $C_2 \equiv \cos 2\alpha$ and $S_2 \equiv \sin 2\alpha$ arise from a rotation of an angle α about Z that is introduced to take into account the orientation

of the etalon principal plane.[4] The multiplication of $\mathbf{M}_{\rm et}$ by $\mathbf{M}_{\rm pol}$ yields

$$\mathbf{M}_{\rm tot} = \frac{1}{2}\begin{pmatrix} \Lambda & \Lambda\cos\delta_2 & \Lambda\sin\delta_1\sin\delta_2 & -\Lambda\cos\delta_1\sin\delta_2 \\ \Xi & \Xi\cos\delta_2 & \Xi\sin\delta_1\sin\delta_2 & -\Xi\cos\delta_1\sin\delta_2 \\ \Pi & \Pi\cos\delta_2 & \Pi\sin\delta_1\sin\delta_2 & -\Pi\cos\delta_1\sin\delta_2 \\ \Sigma & \Sigma\cos\delta_2 & \Sigma\sin\delta_1\sin\delta_2 & -\Sigma\cos\delta_1\sin\delta_2 \end{pmatrix}, \quad (3)$$

where

$$\begin{aligned} \Lambda &= a + bC_2, \\ \Xi &= bC_2 + aC_2^2 + cS_2^2, \\ \Pi &= bS_2 + (a-c)C_2S_2, \\ \Sigma &= -dS_2. \end{aligned} \quad (4)$$

The instrument modulation matrix is then given by

$$\mathbf{O} = g^{(+)}(\lambda)\begin{pmatrix} 1 & \cos\delta_2^{(1)} & \sin\delta_1^{(1)}\sin\delta_2^{(1)} & -\cos\delta_1^{(1)}\sin\delta_2^{(1)} \\ 1 & \cos\delta_2^{(2)} & \sin\delta_1^{(2)}\sin\delta_2^{(2)} & -\cos\delta_1^{(2)}\sin\delta_2^{(2)} \\ 1 & \cos\delta_2^{(3)} & \sin\delta_1^{(3)}\sin\delta_2^{(3)} & -\cos\delta_1^{(3)}\sin\delta_2^{(3)} \\ 1 & \cos\delta_2^{(4)} & \sin\delta_1^{(4)}\sin\delta_2^{(4)} & -\cos\delta_1^{(4)}\sin\delta_2^{(4)} \end{pmatrix}, \quad (5)$$

where

$$g^{(+)}(\lambda) = \frac{a(\lambda) + b(\lambda)\cos 2\alpha}{2}. \quad (6)$$

The superscript in δ_1 and δ_2 enumerates the sequential order of the modulation, i.e., $\delta^{(1)}$ corresponds to the retardance for modulation PM1 in Table 1, $\delta_1^{(2)}$ refers to modulation PM2, etc. The superscript $(+)$ has been introduced to emphasize that the etalon is illuminated with linear polarization along the $+Q$ direction.

The modulation scheme is the same as that of a polarimeter in which the presence of the etalon is neglected, except for a gain factor that depends on both the wavelength and on the direction of the wavefront normal. This factor also varies across the etalon whether the illumination is not homogeneous or the optical axis is deviated from the Z direction, which occurs in local domains, i.e., in regions that suffer from local imperfections that change the crystal optical axis. In any case, the gain factor is absorbed in what is known as "flat fielding" of the instrument, a correction factor that takes into account inhomogeneities in the distribution of intensity on the detector because of local changes in the transmission. Therefore, the

---

[4] The principal plane is the one formed by the wavefront vector with the optical axis. Its orientation must be taken into account in the analysis because it determines the propagation properties of orthogonal electric fields.
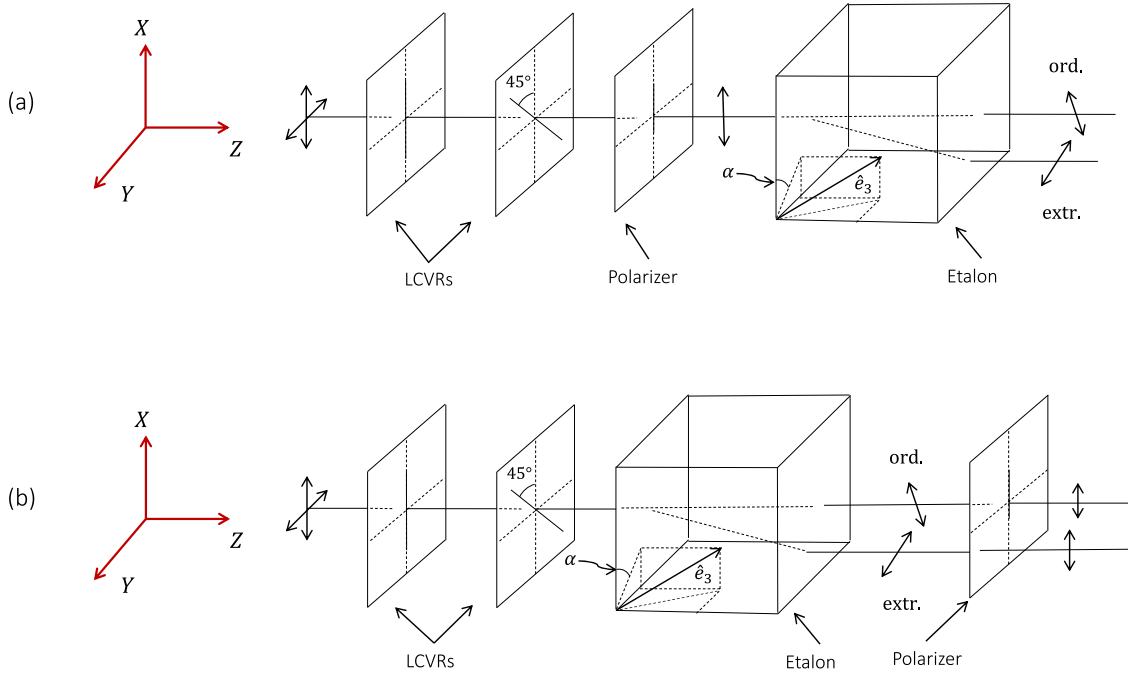
Figure 3. Layout of the transmission of the electric field components of the incident light: (a) when the etalon is located after the analyzer (left), and (b) when the etalon is located between the LCVRs and the analyzer (right).

modulation scheme of Table 1 remains optimal at each particular monochromatic wavelength even when considering the birefringence of the etalon. Also note that the PSF in this configuration is the same as that of an ideal circular aperture modulated by the transmission factor $g^{(+)}(\lambda)$. Hence, the measured Stokes parameters are expected to be insensitive to birefringence whenever the etalon is positioned after the polarimeter and illuminated by a collimated beam.

3.1.2. Telecentric Configuration

Let us assume now that the etalon is illuminated, not with collimated light, but with a telecentric beam. In this configuration, Equation (2) does not hold and we need to use Equation (48) from Paper II. Therefore, the Mueller matrix of the etalon, $\tilde{\mathbf{M}}_{et}$, is now given by

$$\tilde{\mathbf{M}}_{et} = \begin{pmatrix} \tilde{a}' & \tilde{b}' & 0 & 0 \\ \tilde{b}' & \tilde{a}' & 0 & 0 \\ 0 & 0 & \tilde{c}' & -\tilde{d}' \\ 0 & 0 & \tilde{d}' & \tilde{c}' \end{pmatrix}, \tag{7}$$

where coefficients $\tilde{a}'$, $\tilde{b}'$, $\tilde{c}'$, and $\tilde{d}'$ are defined in Equation (49) of Paper II.[5] These coefficients vary in a different manner when compared to the collimated case with the wavelength, etalon geometry, birefringence, etc. The modulation matrix remains the same as in Equation (5), except for the gain factor, which is given in this case by

$$\tilde{g}^{(+)}(\lambda) = \frac{\tilde{a}'(\lambda) + \tilde{b}'(\lambda)}{2}. \tag{8}$$

Hence, the modulation scheme of Table 1 remains optimal monochromatically in a telecentric birefringent configuration,

as for collimated setups. However, the PSF is different compared to that of the isotropic telecentric configuration. In particular, an asymmetry on the spatial shape of the "birefringent" PSF is induced along two perpendicular directions even for perfect telecentrism, i.e., it becomes elliptic. This is shown in the Appendix. Differences between the isotropic and the birefringent PSFs can be interpreted as spurious signals in the measured Stokes parameters that must be added to those presented in previous sections. Figure 1(d) shows the artificial LoS velocities (left) and magnetic field strength (right) when comparing the telecentric isotropic case against the telecentric birefringent case. Note that the maps have been multiplied by a factor $\times 10$ to maintain the same color scale in all subfigures from (b) to (e). This means that signals are about an order of magnitude lower than the ones obtained in the other cases. In particular, the maximum difference at the wing of the line in V is $\sim 0.8\%$, and about 10 G and 35 m s^{-1} in the LoS magnetic field and velocities (Table 2).[6]

Obviously, deviations of the chief ray angle from normal illumination can also contribute to the emergence of artificial signals, as in the isotropic case. Figure 1(e) shows the difference between the observed LoS velocities and magnetic field strength compared to the perfect birefringent telecentric case. Differences in the magnetic field are as much as 120 G and 260 m s^{-1} for the LOS velocities (Table 2). The maximum value of the artificial V at the wing of the line is about 20%. Note that the results are comparable to those obtained for the isotropic case in Figure 1(c), which indicates that the impact on the measurements due to the anisotropy of the etalon is small compared to the effect of the wavelength dependence of the

---

[5] Note that tildes are employed to allude to the telecentric configuration. This notation is consistent with that of Paper II.

[6] We have employed ordinary and extraordinary refraction indices n_o=2.3 and $n_e = 2.2$, corresponding to lithium niobate, for the simulations of the birefringent Fabry–Pérot. The remaining parameters of the etalon are the same as in previous sections, and are consistent with the simulations presented in Paper II.

PSF intrinsic to these mounts, whether the Fabry–Pérot is birefringent or not.

3.2. Etalon Located between the Modulator and the Analyzer

3.2.1. Collimated Configuration

In dual-beam instruments, the etalon is never placed after the polarimeter. Instead, it is located between the modulator and the analyzer (Figure 3(b)) in order to avoid the use of two etalons, i.e., one for each orthogonal beam in which light is split. A good example of a dual-beam instrument is IMaX, which employs a beam splitter as an analyzer to record orthogonal polarizations, $\pm Q$, in two different cameras. In this type of configuration, etalon anisotropies are expected to have a stronger impact on the measured Stokes vector than when located after the polarizer—and thus illuminated with linear polarization. In particular, the optimum modulation scheme presented in Table 1 can no longer be optimal (Del Toro Iniesta & Martínez Pillet 2012), and the measured Stokes vector can differ for orthogonal channels only because of the birefringence of the etalon.

Assuming that the etalon is in a collimated configuration and following the notation of Section 3.1, the Mueller matrix is given by $\mathbf{M}_{pol} = \mathbf{L}\mathbf{F}$, where we have defined $\mathbf{F}$ as $\mathbf{M}_{et}\mathbf{R}_2\mathbf{R}_1$. Given that only the coefficients of the first two rows and columns of $\mathbf{L}$ are different from zero, we only need to calculate the coefficients of the first two rows of $\mathbf{F}$ in order to derive the modulation matrix of the instrument:

$$
\begin{aligned}
F_{11} &= a, \\
F_{12} &= bC_2 \cos \delta_2, \\
F_{13} &= b \sin \delta_2 (C_2 \sin \delta_1 - S_2 \cos \delta_1), \\
F_{14} &= b(S_2 \sin \delta_1 - C_2 \sin \delta_2 \cos \delta_1), \\
F_{21} &= bC_2, \\
F_{22} &= (aC_2^2 + cS_2^2) \cos \delta_2 + dS_2 \sin \delta_2, \\
F_{23} &= (aC_2^2 + cS_2^2) \sin \delta_2 \sin \delta_1 + (a - c)S_2 C_2 \cos \delta_1 \\
&\quad - dS_2 \sin \delta_1 \cos \delta_2, \\
F_{24} &= -(aC_2^2 + cS_2^2) \sin \delta_2 \cos \delta_1 + (a - c)S_2 C_2 \sin \delta_1 \\
&\quad + dS_2 \cos \delta_1 \cos \delta_2.
\end{aligned}
$$
(9)

When dual-beam techniques are employed, we must differentiate between the Mueller matrices corresponding to the $\pm Q$ channels. For the $+Q$ channel:

$$
\mathbf{M}_{pol}^{(+)} = \frac{1}{2} \begin{pmatrix} F_{11} + F_{21} & F_{12} + F_{22} & F_{13} + F_{23} & F_{14} + F_{24} \\ F_{11} + F_{21} & F_{12} + F_{22} & F_{13} + F_{23} & F_{14} + F_{24} \\ 0 & 0 & 0 & 0 \\ 0 & 0 & 0 & 0 \end{pmatrix}.
$$
(10)

For the $-Q$ channel, the Mueller matrix is just

$$
\mathbf{M}_{pol}^{(-)} = \frac{1}{2} \begin{pmatrix} F_{11} - F_{21} & F_{12} - F_{22} & F_{13} - F_{23} & F_{14} - F_{24} \\ F_{21} - F_{11} & F_{22} - F_{12} & F_{23} - F_{13} & F_{24} - F_{14} \\ 0 & 0 & 0 & 0 \\ 0 & 0 & 0 & 0 \end{pmatrix}.
$$
(11)

Each row of the modulation matrix ($\mathbf{O}$) corresponds to the first row of Equations (10) or (11) evaluated for the particular retardances of the LCVRs of the modulation scheme. Note that,
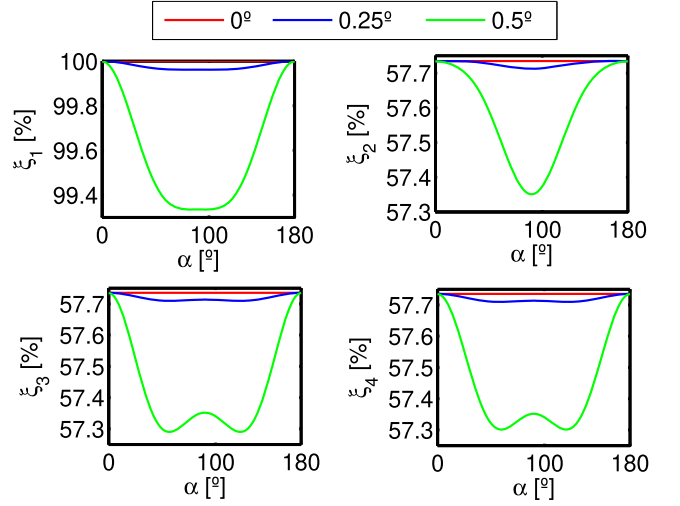

Figure 4. Components of the efficiency vector as a function of the orientation of principal plane of the etalon, using the modulation scheme of Table 1 for illumination of the etalon with incident angles $\theta_i = 0°$ (red solid line), $\theta_i = 0°.25$ (blue solid line), and $\theta_i = 0°.5$ (green solid line). The wavelengths at which the transmission profile peaks, λ_p, have been employed at each incident angle. The etalon is located between the modulators and the analyzer in this configuration.

in this case, the optimum modulation scheme depends on coefficients a, b, c, and d; on the channel ($\pm Q$), and on the orientation of the principal plane of light. Hence, it differs in general from the one showed in Table 1 and varies over the FoV for each monochromatic wavelength.

Figure 4 shows the dependence of the efficiency vector (Collados 1999) for the $+Q$ channel as a function of the orientation of the principal plane, α, when using the modulation scheme of Table 1. Results are shown for incident angles $\theta = 0°$, $0°.25$, and $0°.5$ at the corresponding peak wavelengths of the transmission profile $\lambda_p = \lambda_0 + \Delta\lambda_1$, $\lambda_0 + \Delta\lambda_2$, and $\lambda_0 + \Delta\lambda_3$, where $\Delta\lambda_1 = 0$ pm, $\Delta\lambda_2 = -1.18$ pm, and $\Delta\lambda_3 = -4.54$ pm. It can be observed that the efficiency decreases from the optimum value whenever $\alpha \neq 0°$, $180°$. The maximum variation is $\sim 0.6\%$ for the first component of the efficiency vector and $\sim 0.4\%$ for the other components.

Demodulation with such a nonoptimum scheme in a collimated etalon can introduce further artificial signals in the measured Stokes parameters than just those presented above. Moreover, the spurious signals are different for the two orthogonal beams. Figure 5 shows the map with the difference between the measured Stokes V at its wing on the $\pm$, Q channels for a collimated etalon with maximum incidence angle $0°.5$ (which corresponds to the outermost parts of the FoV). In IMaX, the maximum incidence angle is $0°.44$. Differences are below $\sim 0.3\%$ in our simulations, so we can safely disregard this effect in that instrument.

We have also compared the measured LoS velocities and magnetic field strengths for a collimated configuration that uses a dual beam with respect to another where the etalon is placed after the analyzer. For the dual-beam configuration, the Stokes parameters have been obtained by averaging the signals recorded at each channel. The rms difference in magnetic field strength is below 0.7 Gauss. Velocities differ less than 15 m s^{-1}, and the maximum artificial signal in V is $\sim 0.45\%$.
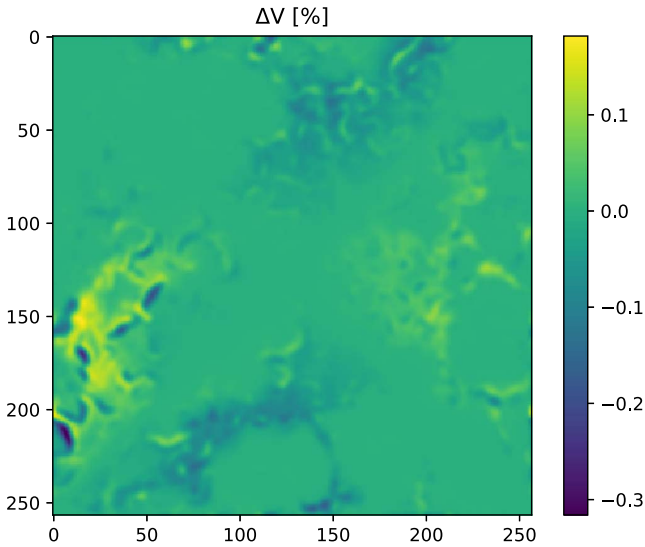
Figure 5. Difference between the measured circular polarization in each channel at the wing of the Fe I 525 line for an anisotropic (uniaxial) collimated etalon placed between the LCVRs and the analyzer.

3.2.2. Telecentric Configuration

When the etalon is mounted on a telecentric configuration, its Mueller matrix becomes particularly symmetric, as shown in Equation (7). In fact, the Mueller matrix of the etalon commutes with that of the analyzer due to their symmetry. It is equivalent, then, to place the Fabry–Pérot either before or after the analyzer; the only difference being that dual-beam techniques can be used only if placed before the analyzer. In that case, the modulation matrix for the $+Q$ channel is given by Equation (5), except for the gain factor, which is determined by Equation (8), as explained in Section 3.1.2. The gain factor corresponding to the modulation matrix of the $-Q$ channel is the same except for a minus sign that changes $\tilde{a}' + \tilde{b}'$ by $\tilde{a}' - \tilde{b}'$.

Although monochromatic polarimetric efficiencies remain optimal, the measured Stokes parameters in each channel are expected to be somewhat different because the PSFs change slightly for orthogonal polarizations (Paper II). This effect induces cross-talk signals in the measured Stokes parameters. We have obtained that the maximum difference between both channels is ∼0.006% in V at the wing of the line. This additional contribution to the spurious signals is insignificant compared to the previous ones and it naturally disappears in isotropic etalons.

4. Summary and Conclusions

An evaluation of the artificial LoS velocities and magnetic field strength signals that arise in magnetographs based on Fabry–Pérot etalons has been performed. We have distinguished between telecentric and collimated illumination of both crystalline and isotropic etalons. We have also considered different locations of the etalon within the optical path, in particular, instruments where the etalon is placed after the polarimeter and those in which it is positioned in an intermediate location between the modulator and the analyzer to allow for dual-beam polarimetry. Our analysis has consisted in simulating the impact of an etalon-based instrument similar to IMaX and PHI on the maps of the Stokes components along the 525.02 nm Fe I Zeeman sensitive line.

Regarding isotropic etalons, collimated setups are (ideally) exempt from the emergence of spurious signal since no spectral variation of the PSF appears in this configuration. However, in telecentric mounts, such signals are originated by a severe dependence of the PSF shape with the wavelength across the transmission profile. For the particular case of a telecentric $f/40$ isotropic etalon, spurious velocities obtained through the CoG method are as large as $110\,\mathrm{m\,s^{-1}}$, whereas the magnetic field and Stokes V reach values up to 50 G and 5%, respectively. In telecentric mounts affected by a departure of the chief ray of $0°\!\!.5$, signals can be as high as $280\,\mathrm{m\,s^{-1}}$ for the LoS velocities and 140 G for the magnetic field strength when compared to the perfect telecentric configuration. A shift in the map of velocities also arises in this case because of an asymmetrization of the transmission profile and of the PSF. Apart from the shift, the map of artificial velocities shows structures with a corresponding rms value twice as large as for the perfect configuration ($\sim$37.5 m s^{-1}).

In relation to birefringent etalons, we have showed that the ideal modulation scheme derived by Del Toro Iniesta & Martínez Pillet (2012) still remains optimal for both telecentric and collimated setups regardless of the birefringence exhibited by the Fabry–Pérot, as long as the etalon is placed after the polarimeter. Significant differences arise when comparing the telecentric and collimated setups, though. In particular, for the telecentric birefringent configuration, we have shown that:

1. Placing the etalon between the modulator and the analyzer has the same impact as locating it after the polarimeter since its Mueller matrix commutes with that of the analyzer.
2. The PSF differs from the isotropic case and becomes elliptic. Compared to the nonbirefringent telecentric case, artificial signals in the velocities and magnetic field for an $f/40$ beam show values up to $40\,\mathrm{m\,s^{-1}}$ and 9.5 G, respectively. The Stokes V is 0.8%, at most, in the wings of the profile. These artificial signals are an order of magnitude smaller than the ones simply caused by the wavelength dependence of the PSF.
3. Cross-talks between orthogonal channels appear when using dual-beam techniques, but are negligible ($\sim$0.006% in the wing of V).

On the other hand, for collimated anisotropic mounts, we have proved that:

1. The measurement of the Stokes parameters is insensitive to birefringence whenever the etalon is positioned after the analyzer.
2. The Mueller matrix of the polarimeter is modified when the etalon is situated before the analyzer. Hence, the optimum efficiencies and the measurement of the Stokes vector are affected. In particular:
   (a) The efficiencies depend on the incident wavefront direction and on the wavelength. When the optimum modulation scheme is employed, monochromatic efficiencies decrease, although the reduction is only 0.6% at most for a $0°\!\!.5$ incidence.
   (b) The measured Stokes vector is different from the one corresponding to an etalon located after the polarimeter. Again, the differences are not dramatic; they remain under $15\,\mathrm{m\,s^{-1}}$ for the velocity, 0.7 G for the

magnetic field and 0.45% for Stokes V compared to a collimated setup in which the etalon is placed after the analyzer.

(c) Signals recorded by orthogonal channels in dual-beam instruments are also different due to the presence of the etalon, but these are kept below 0.3% at V Stokes wing.

We have also shown that the expected spurious signals in telecentric configurations mounted in ground-based instruments are virtually insignificant because of the very slow apertures employed in such telescopes ($\gg f/40$). In particular, we expect a decrease of the spurious signals with $\sim (f\#)^{-2}$. Attention must be paid to etalons aboard space instruments, though, because size constraints usually lead to apertures much faster than the ones typical of ground-based instruments.

A careful assessment on the spatial distribution and magnitude of defects in the optical thickness of the etalon is also mandatory to evaluate possible additional spurious signals regardless of the configuration employed. As explained in Paper I, microroughness errors increase the energy contained in the wings of the PSF (*stray light*) with the subsequent loss of contrast. This is particularly true in collimated mounts and translates into further contamination of the magnetic field signals. In telecentric setups, such errors modify the PSF pixel-to-pixel, which also cause additional artificial signals. Cavity errors are of special relevance when two or more etalons are employed to improve either the spectral resolution or the free spectral range (or both) since defects are amplified in both collimated and telecentric mounts—and, hence, the corresponding artificial signals. In addition, the Mueller matrix of the polarimeter is also modified with respect to the one presented here for each configuration when several birefringent etalons are used. Therefore, instruments using more than one Fabry–Pérot require a detailed analysis to take into account the possible sources of contamination addressed in this paper and the ones emerging from the magnification of cavity errors.

Appendix
PSF in Orthogonal Directions: Birefringent Case

Anisotropies in the etalon cause an asymmetry of the PSF on orthogonal directions even if telecentrism is perfect (and, hence, the Jones matrix terms only depend on the radial coordinates of the pupil). Let us consider that the etalon is illuminated with Stokes components $I = Q$ and $U = V = 0$. According to Paper II, the PSF is then given by $\mathcal{S} = \tilde{a}' + \tilde{b}' = \tilde{H}'_{11}\tilde{H}'^{*}_{11}$. For a perfect telecentric configuration, it was shown in Paper II that the first Jones coefficient is given by

$$\tilde{H}'_{11} = \int_0^{R_p} \int_0^{2\pi} r [H_{11}(r, \lambda)\cos^2\phi + H_{22}(r, \lambda)\sin^2\phi] e^{-ikr(\alpha\cos\phi+\beta\sin\phi)} \, dr d\phi. \quad (12)$$

Since H_{11} and H_{22} only depend on the radial coordinate of the pupil, we can cast this integral as

$$\tilde{H}'_{11} = \int_0^{R_p} r H_{11}(r, \lambda) \int_0^{2\pi} \cos^2\phi \, e^{-ikr(\alpha\cos\phi+\beta\sin\phi)} \, dr d\phi + \int_0^{R_p} r H_{22}(r, \lambda) \int_0^{2\pi} \sin^2\phi \, e^{-ikr(\alpha\cos\phi+\beta\sin\phi)} \, dr d\phi. \quad (13)$$

Let us take into account two orthogonal directions in the image plane. For example, the direction along ξ and the direction along η. The Jones term for each case is just

$$\tilde{H}'_{11}(\xi, \eta = 0) = \int_0^{R_p} r H_{11}(r, \lambda) \int_0^{2\pi} \cos^2\phi \, e^{-ikr\alpha\cos\phi} \, dr d\phi + \int_0^{R_p} r H_{22}(r, \lambda) \int_0^{2\pi} \sin^2\phi \, e^{-ikr\alpha\cos\phi} \, dr d\phi, \quad (14)$$

$$\tilde{H}'_{11}(\xi = 0, \eta) = \int_0^{R_p} r H_{11}(r, \lambda) \int_0^{2\pi} \cos^2\phi \, e^{-ikr\beta\sin\phi} \, dr d\phi + \int_0^{R_p} r H_{22}(r, \lambda) \int_0^{2\pi} \sin^2\phi \, e^{-ikr\beta\sin\phi} \, dr d\phi. \quad (15)$$

The two integrals differ from the exponent of the complex exponential. It turns out that

$$\int_0^{2\pi} \cos^2\phi \, e^{-ikr\alpha\cos\phi} \, dr d\phi = \int_0^{2\pi} \sin^2\phi \, e^{-ikr\beta\sin\phi} \, dr d\phi, \quad (16)$$

and

$$\int_0^{2\pi} \sin^2\phi \, e^{-ikr\alpha\cos\phi} \, dr d\phi = \int_0^{2\pi} \cos^2\phi \, e^{-ikr\beta\sin\phi} \, dr d\phi. \quad (17)$$

Similarly, for the second diagonal element of the Jones matrix

$$\tilde{H}'_{22} = \int_0^{R_p} r H_{22}(r, \lambda) \int_0^{2\pi} \cos^2\phi \, e^{-ikr(\alpha\cos\phi+\beta\sin\phi)} \, dr d\phi + \int_0^{R_p} r H_{11}(r, \lambda) \int_0^{2\pi} \sin^2\phi \, e^{-ikr(\alpha\cos\phi+\beta\sin\phi)} \, dr d\phi. \quad (18)$$

Hence,

$$\tilde{H}'_{22}(\xi, \eta = 0) = \int_0^{R_p} r H_{22}(r, \lambda) \int_0^{2\pi} \cos^2\phi \, e^{-ikr\alpha\cos\phi} dr d\phi + \int_0^{R_p} r H_{11}(r, \lambda) \int_0^{2\pi} \sin^2\phi \, e^{-ikr\alpha\cos\phi} \, dr d\phi, \quad (19)$$

$$\tilde{H}'_{22}(\xi = 0, \eta) = \int_0^{R_p} r H_{22}(r, \lambda) \int_0^{2\pi} \cos^2\phi \, e^{-ikr\beta\sin\phi} dr d\phi + \int_0^{R_p} r H_{11}(r, \lambda) \int_0^{2\pi} \sin^2\phi. \quad (20)$$

Using Equations (16) and (17), we can see that

$$\tilde{H}'_{11}(\xi, \eta = 0) = \tilde{H}'_{22}(\xi = 0, \eta),$$
$$\tilde{H}'_{11}(\xi = 0, \eta) = \tilde{H}'_{22}(\xi, \eta = 0). \quad (21)$$

That is, if $\mathcal{S} = \tilde{a}' + \tilde{b}'$, then $\tilde{a}'(\xi, \eta = 0) = \tilde{a}'(\xi = 0, \eta)$, but $\tilde{b}'(\xi, \eta = 0) = -\tilde{b}'(\xi = 0, \eta)$. Therefore, $\mathcal{S}(\xi, \eta = 0) \neq \mathcal{S}(\xi = 0, \eta)$. In consequence, the PSF varies for orthogonal directions in birefringent etalons and the symmetry of the PSF

is no longer preserved. In practice, the loss of spatial symmetry has a low impact on the measurements because $\tilde{b}$ is much smaller than $\tilde{a}$ (Paper II), as shown in Section 3.1.2.

ORCID iDs

F. J. Bailén ● https://orcid.org/0000-0002-7318-3536
D. Orozco Suárez ● https://orcid.org/0000-0001-8829-1938
J. C. del Toro Iniesta ● https://orcid.org/0000-0002-3387-026X

References

Bailén, F. J., Orozco Suárez, D., & del Toro Iniesta, J. C. 2019a, ApJS, 241, 9
Bailén, F. J., Orozco Suárez, D., & del Toro Iniesta, J. C. 2019b, ApJS, 242, 21
Beckers, J. M. 1998, A&AS, 129, 191
Bonaccini, D., Righini, A., Cavallini, F., & Ceppatelli, G. 1989, A&A, 217, 368
Cavallini, F. 1998, MmSAI, 69, 627
Collados, M. 1999, in ASP Conf. Ser. 184, Third Advances in Solar Physics Euroconference: Magnetic Fields and Oscillations, ed. B. Schmieder, A. Hofmann, & J. Staude (San Francisco, CA: ASP), 3
Del Toro Iniesta, J. C., & Collados, M. 2000, ApOpt, 39, 1637
Del Toro Iniesta, J. C., & Martínez Pillet, V. 2012, ApJS, 201, 22
Doerr, H.-P., von der Lühe, O., II, & Kentischer, T. J. 2008, Proc. SPIE, 7014, 701417
Greco, V., Sordini, A., Cauzzi, G., et al. 2019, A&A, 626, A43
Kentischer, T. J., Schmidt, W., Sigwarth, M., & Uexkuell, M. V. 1998, A&A, 340, 569
Martínez Pillet, V., Del Toro Iniesta, J. C., Álvarez-Herrero, A., et al. 2011, SoPh, 268, 57
Puschmann, K. G., Denker, C., Balthasar, H., et al. 2013, OptEn, 52, 081606
Reardon, K. P., & Cavallini, F. 2008, A&A, 481, 897
Righini, A., Cavallini, F., & Reardon, K. P. 2010, A&A, 515, A85
Scharmer, G. B. 2006, A&A, 447, 1111
Scharmer, G. B., Narayan, G., Hillberg, T., et al. 2008, ApJL, 689, L69
Schmidt, W., Schubert, M., Ellwarth, M., et al. 2016, Proc. SPIE, 9908, 99084N
Semel, M. 1967, AnAp, 30, 513
Solanki, S. K., del Toro Iniesta, J. C., Woch, J., et al. 2015, in Proc. IAU Symp. 305, Polarimetry, ed. K. N. Nagendra et al. (Cambridge: Cambridge Univ. Press), 108
van Noort, M. J., & Rouppe van der Voort, L. H. M. 2008, A&A, 489, 429
Vögler, A., Shelyag, S., Schüssler, M., et al. 2005, A&A, 429, 335
von der Lühe, O., & Kentischer, T. J. 2000, A&AS, 146, 499

Paper IV: Analytical formulation of telecentric etalons

On Fabry–Pérot Etalon-based Instruments. IV. Analytical Formulation of Telecentric Etalons

F. J. Bailén , D. Orozco Suárez , and J. C. del Toro Iniesta
Instituto de Astrofísica de Andalucía (CSIC), Apdo. de Correos 3004, E-18080 Granada, Spain; fbailen@iaa.es, orozco@iaa.es, jti@iaa.es
Received 2021 January 20; revised 2021 March 29; accepted 2021 April 13; published 2021 May 6

Abstract

Fabry–Pérot etalons illuminated with collimated beams have been analytically characterized in detail since their invention. Meanwhile, most of the features of etalons located in telecentric planes have been studied only numerically, despite the wide use of this configuration in astrophysical instrumentation for decades. In this work we present analytical expressions for the transmitted electric field and its derivatives that are valid for etalons placed in slow telecentric beams, like the ones commonly employed in solar instruments. We use the derivatives to infer the sensitivity of the electric field to variations in the optical thickness for different reflectivities and apertures of the incident beam, and we compare them to the collimated case. This allows us to estimate the wavefront degradation produced by roughness errors on the surfaces of the Fabry–Pérot etalons and to establish the maximum allowed rms value of the cavity irregularities across the footprint of the incident beam on the etalons that ensures diffraction-limited performance. We also evaluate the wavefront degradation intrinsic to these mounts, which is produced only by the finite aperture of the beam and that must be added to the one produced by defects. Finally, we discuss the differences in performance of telecentric and collimated etalon-based instruments and we generalize our formulation to anisotropic etalons.

Unified Astronomy Thesaurus concepts: Spectropolarimetry (1973); Solar instruments (1499); Fabry-Perot interferometers (524); Astronomical instrumentation (799)

1. Introduction

Fabry–Pérot interferometers (etalons) are frequently included in solar magnetographs to carry out the wavelength scanning of spectral lines that are sensitive to magnetic fields. Despite the common use of this technology, there is no consensus among the solar community on their optimum configuration within the instrument in terms of both image quality and spectral performance. So far, two setups have been employed: collimated and telecentric. In a collimated mount, the etalon is located on a pupil plane, thus receiving a collimated beam from each point of the observed object field (at infinity). This mount offers a better spectral resolution than the telecentric one at the expense of shifting the transmission profile across the field of view (FOV). In addition, incident beams always illuminate the same area of the etalon no matter their direction. This means that individual local defects on the etalon are averaged across the illuminated clear aperture and have a common influence on both the transmitted wavefront and the transmission profile over the whole FOV. In telecentric setups the etalon is very close to a focal plane, whereas the entrance pupil is imaged into infinity. Then, the footprint of the incident beam is much smaller than in the collimated case and local defects are directly mapped onto the final image, thus producing point-to-point variations of both the transmission profile and the imaging performance.

Defects can be caused by deviations of the homogeneity in the cavity (in the case of crystalline etalons) and/or geometry of the etalon plates with respect to the ideal considerations from which the classical model of a Fabry–Pérot etalon is derived (e.g., Born & Wolf 1999). Usually, defects originate mainly due to departures departure of the reflecting plates from flatness and parallelism, or from imperfections in the coating, which may result in deviations from flatness or the introduction of equivalent defects through phase errors. The impact of such irregularities on the transmission profile has been studied in

numerous works (e.g., Hill 1963; Ramsay 1969; Sloggett 1984; Hernandez 1988). An extensive discussion on the influence of defects in the intensity of the transmitted light was carried out by Bailén et al. (2019a), hereinafter Paper I. Defects produce variations in the phase of the transmitted electric field as well. These variations can be understood as errors in the transmitted wavefront and can cause a degradation of the imaging performance of the instrument. The first works that addressed the influence of defects on the imaging performance of an etalon are the ones of Ramsay (1969) and Steel (1986). The degradation of the transmitted wavefront was also studied later by von der Lühe & Kentischer (2000). The results presented in these works refer to strictly monochromatic wavefronts in collimated etalons and represent a worst-case scenario, though. Scharmer (2006) considered a more realistic approach that included quasi-monochromatic effects that occur because of the limited resolution of the instruments. von der Lühe & Kentischer (2000) and Scharmer (2006) suggest a large degradation of the image quality in collimated etalons and recommend the telecentric configuration to achieve diffraction-limited performance. Their results are restricted, however, to collimated etalons only. A qualitative discussion on the impact of defects on image quality for telecentric etalons and a computational method to evaluate their influence on the point-spread function (PSF) was presented later in Righini et al. (2010), but an analytical study similar to the ones presented by von der Lühe & Kentischer (2000) and Scharmer (2006) for telecentric etalons has not been published yet, to our knowledge. From our point of view, such an approach would give a valuable insight on the imaging performance of this configuration that would allow a proper comparison with collimated setups, especially when taking into account high-frequency errors that can affect the transmitted wavefront even if the footprint of the incident beam on an etalon is small.

There are other sources of image degradation apart from physical defects of the etalon. In particular, imperfections on the illumination of the Fabry–Pérot etalon can reduce the image quality of the instrument, as evaluated in Paper I. On the other hand, telecentric setups always suffer from a characteristic wavelength-dependent apodization of the pupil as seen from the etalon. This effect has an impact on the measured maps of the magnetic field and radial plasma velocities and depends greatly on the *f*-number of the incident beam. The influence of pupil apodization on these mounts was studied for the first time by Beckers (1998) and recently by Bailén et al. (2020), hereinafter Paper III. The choice of the optimum setup (collimated or telecentric) in a given instrument depends, then, not only on the particular map of defects of the etalon, but also on the optical parameters, tolerances of the instrument, and quality of the etalon, as explained by Righini et al. (2010).

This work is the fourth in our series of papers. We derive an analytical expression for the electric field transmitted in telecentric etalons and we investigate the sensitivity of the transmission profile and of the transmitted phase of the electric field to variations of geometry and illumination by taking advantage of the analytical derivatives of the electric field. To our knowledge, this is the first time the electric field equation is solved analytically for a telecentric configuration. Such a solution has many practical advantages, apart from wavefront sensitivity analyses, that are not explored here. One of them would be its possible application in the calibration procedure of telecentric instruments, especially for space-borne magneto-graphs, whose computational capabilities are very limited.

We start with the derivation of the analytical expression of the transmitted electric field and its derivatives for telecentric setups (Section 2). We continue with an analysis of the impact of defects on the transmitted wavefront (Section 3.1), as well as the one coming from the intrinsic pupil apodization expected in these mounts (Section 3.2). We discuss the advantages and drawbacks of each configuration in terms of imaging performance (Section 3.3) and, finally, we generalize our formulation to birefringent etalons in Section 4. Section 5 summarizes the main results of the paper and draws some conclusions.

2. Analytical Expressions

In a telecentric configuration the etalon is located at, or very close to, an intermediate image plane of the instrument, whereas the entrance pupil is set to coincide with the object focal plane (see Figure 6 in Paper I). This allows for a homogeneous illumination across the etalon, provided that the observed object is uniform. The spectral transmission in this setup broadens and differs from the one corresponding to the collimated case (Equation (11) in Paper I) as a result of the finite aperture of the incident beams, but the central wavelength of the passband is kept constant over the FOV (ideally), unlike in collimated mounts. The transmitted intensity cannot be approximated in this configuration like the average transmission corresponding to collimated beams reaching the etalon with different incidence angles. Instead, coherent superposition of electric fields must be carried out to account for the phase mismatches of rays that propagate along different directions.

In Paper I we showed that, for a monochromatic plane wave that impinges the etalon, the transmitted electric field, $\mathbf{E}^{(t)}$, is related to the incident electric field, $\mathbf{E}^{(i)}$, by

$$\mathbf{E}^{(t)} = \frac{\sqrt{\tau}}{1-R} \frac{e^{i\delta/2} - R\, e^{-i\delta/2}}{1 + F \sin^2(\delta/2)} \mathbf{E}^{(i)}, \qquad (1)$$

where τ is the (intensity) transmission factor of the etalon at normal incidence, δ is the phase difference between two successively transmitted rays, and F is a factor that depends exclusively on the reflectivity of the Fabry–Pérot surfaces. These three factors are related to several parameters of the etalon, like the surface reflectivity, R, absorption, A, refraction index, n', and thickness, h, but also to the angle of refraction of the beam, θ'. The dependencies are given through the following expressions:

$$\tau = \left(1 - \frac{A}{1-R}\right)^2, \qquad (2)$$

$$F = \frac{4R}{(1-R)^2}, \qquad (3)$$

and

$$\delta \simeq \frac{4\pi}{\lambda} n' h \cos\theta'. \qquad (4)$$

In an ideal telecentric configuration in which the chief ray is perpendicular to the etalon across the whole FOV, the transmitted electric field of each individual ray depends only on the radial coordinates of the pupil, r, whereas the total transmitted electric field (after integration over the pupil), $\tilde{\mathbf{E}}^{(t)}$, is given by Equation (49) of Paper I. We can normalize the radial coordinate to the pupil radius of the instrument, R_{pup}, and rewrite this equation simply as

$$\tilde{\mathbf{E}}^{(t)} = 2 \int_0^1 \varrho\, \mathbf{E}^{(t)}(\varrho)\, d\varrho, \qquad (5)$$

where $\varrho \equiv r R_{\mathrm{pup}}^{-1}$. So far we have presented the electric field of the individual rays as a function of δ, which changes with the refraction angle, θ'. The latter depends, in turn, on the incident angle, θ. It is convenient to start using Snell's law in order to change the dependence with δ in Equation (1) to r. Since

$$\cos\theta' = \sqrt{1 - \left(\frac{\sin^2\theta}{n'^2}\right)}, \qquad (6)$$

and θ is very small for our cases of interest ($f\# \gg 1$), its sine can be approximated by its tangent (see Figure 7 in Paper I) to give

$$\cos\theta' \simeq \sqrt{1 - \frac{\varrho^2}{4n'^2(f\#)^2}} \simeq 1 - \frac{\varrho^2}{8n'^2(f\#)^2}, \qquad (7)$$

where $f\#$ is the *f*-number of the incident beam on the etalon. If we now call

$$a \equiv \frac{2\pi}{\lambda} n' h, \qquad (8)$$

and

$$b \equiv \frac{1}{8n'^2(f\#)^2}, \qquad (9)$$

we can write

$$\frac{\delta}{2} = a(1 - b\varrho^2). \tag{10}$$

Then, Equation (1) can be cast as

$$\mathbf{E}^{(t)} = \frac{\sqrt{\tau}}{1 - R}\left[\frac{(1 - R)\cos(a[1 - b\varrho^2])}{1 + F\sin^2(a[1 - b\varrho^2])} + i\frac{(1 + R)\sin(a[1 - b\varrho^2])}{1 + F\sin^2(a[1 - b\varrho^2])}\right]\mathbf{E}^{(i)}. \tag{11}$$

Now we can write Equation (5) as

$$\tilde{\mathbf{E}}^{(t)} = 2\sqrt{\tau}\left\{\int_0^1 \frac{\varrho\cos(a[1 - b\varrho^2])}{1 + F\sin^2(a[1 - b\varrho^2])}\,d\varrho \right. \\ \left. + i\frac{1 + R}{1 - R}\int_0^1 \frac{\varrho\sin(a[1 - b\varrho^2])}{1 + F\sin^2(a[1 - b\varrho^2])}\,d\varrho\right\}\mathbf{E}^{(i)}. \tag{12}$$

This equation has analytical integration. Indeed,

$$\int_0^1 \frac{\varrho\cos(a[1 - b\varrho^2])}{1 + F\sin^2(a[1 - b\varrho^2])}\,d\varrho \\ = \frac{1}{\alpha_1}[\arctan(\gamma_1) - \arctan(\gamma_2)], \tag{13}$$

and

$$\int_0^1 \frac{\varrho\sin(a[1 - b\varrho^2])}{1 + F\sin^2(a[1 - b\varrho^2])}\,d\varrho \\ = \frac{1}{\alpha_2}\left[\ln\left(\frac{(1 + \gamma_3)^2 + \gamma_4^2}{(1 - \gamma_3)^2 + \gamma_4^2}\right) - \ln\left(\frac{(1 + \gamma_3)^2 + \gamma_5^2}{(1 - \gamma_3)^2 + \gamma_5^2}\right)\right], \tag{14}$$

where we have defined

$$\alpha_1 \equiv 2ab\sqrt{F},$$
$$\alpha_2 \equiv 2\alpha_1\sqrt{F + 1},$$
$$\gamma_1 \equiv \sqrt{F}\sin a,$$
$$\gamma_2 \equiv \sqrt{F}\sin(a[1 - b]),$$
$$\gamma_3 \equiv \sqrt{\frac{F}{F + 1}},$$
$$\gamma_4 \equiv \frac{\tan\left(\frac{a}{2}[1 - b]\right)}{\sqrt{F + 1}},$$
$$\gamma_5 \equiv \frac{\tan(a/2)}{\sqrt{F + 1}}. \tag{15}$$

Equations (13)–(15) are tedious and, unfortunately, there is no easy way to simplify them further. The reason for this is that they cannot be either expanded into power series or neglected as a result of a large sensitivity of the transmitted electric field to small changes in any of the parameters. Note, however, that apart from a transmission factor $\sqrt{\tau}$, the final expression depends only on three coefficients: R (or, equivalently, F), a, and b. This means that the electric field transmitted by the etalon is determined uniquely by the absorptivity and reflectivity of the etalon and by the quantities $n'h\lambda^{-1}$ and $n'f\#$. Note that the refraction index acts only as an amplification factor of both the thickness and the f-number in the equations. Crystalline etalons can benefit, then, from much faster apertures (and, hence, from much smaller etalon and instrument
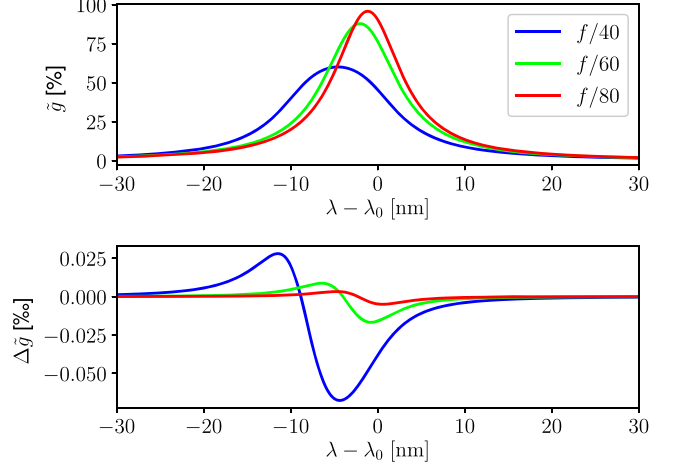
Figure 1. Top: transmission profiles (expressed in %) of an etalon in telecentric beams with f-numbers $f/40$ (blue), $f/60$ (green), and $f/80$ (red). Bottom: difference between the transmission profile calculated numerically and the one obtained with the analytical expressions (expressed in ‰).

dimensions) while keeping the same spectral and imaging properties, which makes them appropriate in instruments with stringent size requirements and, in particular, in balloon- or space-borne telescopes (e.g., Martínez Pillet et al. 2011; Solanki et al. 2020).

Once we have an analytical solution for the transmitted electric field, we can calculate other physical quantities of interest, like the transmission profile of the etalon. Transmission, $\tilde{g}$, is defined as the average ratio between the transmitted and incident intensities in the telecentric configuration and is given simply by

$$\tilde{g} = \frac{\tilde{\mathbf{E}}^{(t)}\tilde{\mathbf{E}}^{(t)*}}{\mathbf{E}^{(i)}\mathbf{E}^{(i)*}} = \frac{\text{Re}\{\tilde{\mathbf{E}}^{(t)}\}^2 + \text{Im}\{\tilde{\mathbf{E}}^{(t)}\}^2}{\mathbf{E}^{(i)}\mathbf{E}^{(i)*}}, \tag{16}$$

where the asterisk indicates the complex conjugate. Figure 1 shows the transmission profile for three incident telecentric beams with $f/40$, $f/60$, and $f/80$ on a crystalline etalon with $n = 2.3$, $h = 250$ μm, $R = 0.92$, and $A = 0$. We will keep the same parameters for the numerical examples hereinafter. Note that the transmission is broadened and shifted to the blue with respect to that of an equivalent collimated configuration tuned at $\lambda_0 = 617.3$ nm, as described in detail in Paper I. The profiles have been calculated with Equations (12)–(16). The differences between these profiles and the ones calculated by numerical integration of Equation (5) are also shown (in ‰). Numerical integration has been carried out without expanding $\cos\theta'$ into a power series and both the absolute and relative tolerance for the integration method have been adjusted to be several orders of magnitude stricter than the maximum difference found for each profile. Hence, the tiny differences that appear are basically due to the small angle approximation used to obtain the analytical solution.

The results shown for a crystalline etalon in Figure 1 and henceforth also correspond to an air-gapped Fabry–Pérot etalon with the same reflectivity and absorptivity, but a cavity 2.3 times larger (575 μm) and f-numbers 2.3 times greater. Table 1 shows the equivalence between the f-numbers employed in the numerical examples presented hereinafter for a crystalline etalon and those corresponding to an air-gapped etalon with $h = 575$ μm. Note that the range of apertures used in our

Table 1
Apertures Employed for the Crystalline Etalon and the Ones Corresponding to
Its Equivalent Air-gapped Etalon

Type of Etalon	*f*-numbers			
Crystalline	$f/40$	$f/60$	$f/80$	$f/100$
Air	$f/92$	$f/138$	$f/184$	$f/230$

numerical examples is compatible with the *f*-numbers commonly employed in ground-based instruments that use air-gapped Fabry–Pérot etalons.

Having access to the analytical expression of the transmitted electric field has numerous advantages. For instance, we can calculate the analytical derivatives with respect to a and b to evaluate the sensitivity to variations of any of the etalon parameters. We are going to focus here on the derivative with respect to a, because we are interested on the variations on the electric field that arise from changes in thickness across the aperture. The derivative of the transmission profile with respect to a can be cast simply as

$$
\frac{\partial \tilde{g}}{\partial a} = \frac{2}{\mathbf{E}^{(i)}\mathbf{E}^{(i)*}}
$$
$$
\times \left(\mathrm{Re}\{\tilde{\mathbf{E}}^{(t)}\} \frac{\partial}{\partial a} \mathrm{Re}\{\tilde{\mathbf{E}}^{(t)}\} + \mathrm{Im}\{\tilde{\mathbf{E}}^{(t)}\} \frac{\partial}{\partial a} \mathrm{Im}\{\tilde{\mathbf{E}}^{(t)}\} \right). \quad (17)
$$

The derivatives of the real and imaginary parts of the electric field are given by

$$
\frac{\partial \mathrm{Re}\{\tilde{\mathbf{E}}^{(t)}\}}{\partial a} = \frac{2\sqrt{\tau}}{\alpha_1} \left[\frac{\alpha_1'}{\alpha_1}(\arctan\gamma_2 - \arctan\gamma_1) + \frac{\gamma_1'}{1+\gamma_1^2} - \frac{\gamma_2'}{1+\gamma_2^2} \right], \quad (18)
$$

$$
\frac{\partial \mathrm{Im}\{\tilde{\mathbf{E}}^{(t)}\}}{\partial a} = \frac{2\sqrt{\tau}}{\alpha_2} \frac{1+R}{1-R} \left[\frac{\alpha_2'}{\alpha_2} \left\{ \ln\left(\frac{(1+\gamma_3)^2 + \gamma_5^2}{(1-\gamma_3)^2 + \gamma_5^2}\right) - \ln\left(\frac{(1+\gamma_3)^2 + \gamma_4^2}{(1-\gamma_3)^2 + \gamma_4^2}\right) \right\} \right.
$$
$$
\left. + \frac{8\gamma_3\gamma_5\gamma_5'}{[(1+\gamma_3)^2 + \gamma_5^2][(1-\gamma_3)^2 + \gamma_5^2]} - \frac{8\gamma_3\gamma_4\gamma_4'}{[(1+\gamma_3)^2 + \gamma_4^2][(1-\gamma_3)^2 + \gamma_4^2]} \right], \quad (19)
$$

where the prime denotes the partial derivative with respect to a:

$$
\begin{aligned}
\alpha_1' &= 2b\sqrt{F}, \\
\alpha_2' &= 4b\sqrt{F(F+1)}, \\
\gamma_1' &= \sqrt{F}\cos a, \\
\gamma_2' &= \sqrt{F}(1-b)\cos(a[1-b]), \\
\gamma_4' &= \frac{1-b}{2\sqrt{F+1}}\sec^2\left(\frac{a}{2}[1-b]\right), \\
\gamma_5' &= \frac{1}{2\sqrt{F+1}}\sec^2\left(\frac{a}{2}\right).
\end{aligned} \quad (20)
$$

Figure 2 shows $\partial\tilde{g}/\partial a$ over the transmission profile for both a collimated and three telecentric configurations with different *f*-numbers illuminating the crystalline etalon. Apart from the blueshift that also appears in Figure 1, the amplitudes of the telecentric profiles decrease with increasing apertures because the spectral resolution of the etalon worsens with smaller
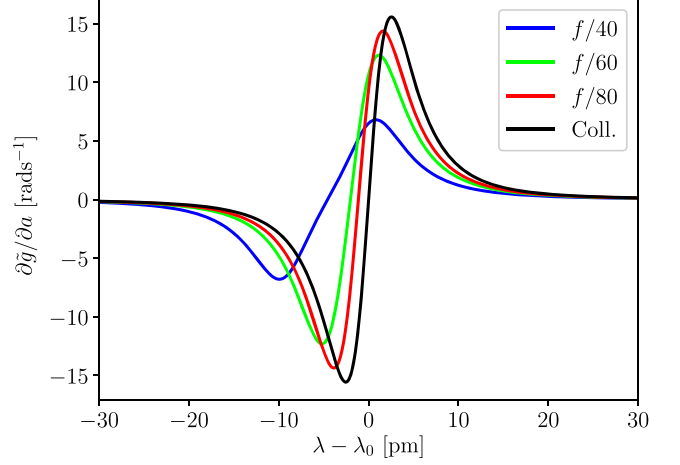
Figure 2. Spectral dependence of the derivative of the transmission profile with respect to a corresponding to a telecentric $f/60$ mount (green) and to a collimated configuration (red).

f-numbers, which translates into a less steep profile. Each curve is also shifted by the same amount as its transmission peak does.

The derivatives of Figure 2 have an antisymmetric shape and change of sign at the peak transmission wavelength. Hence, the effect of a change in a is mostly seen as a shift in $\tilde{g}$ and has a negligible impact on its width, as already evaluated in Paper I for the collimated configuration. Then, inhomogeneities in the etalon cavity and/or errors on the plates' flatness across the footprint of the incident beam produce only different shifts of the transmission profiles point to point. The average effect of the local shifts of the transmission across the footprint of the beam is a broadening of the passband and a reduction of the transmission peak.

Note that $\partial\tilde{g}/\partial a$ encodes the sensitivity of the transmission profile to variations of wavelength and optical thickness, but not to changes of the focal length, which are contained in the partial derivative with respect to b (Equation (9)). Fluctuations in the refraction index have an impact on both a and b. The derivatives of $\tilde{g}$ with respect to b can easily be calculated by substituting the quantities with primes in Equations (18) and (19) with their corresponding partial derivatives with respect to b. Figure 3 shows the derivative of the transmission profile with respect to b for different *f*-numbers. The profiles exhibit a similar behavior, except for a change of sign, to those of Figure 2, but are not completely antisymmetric since increasing b has the effect of both shifting the profile and broadening it. The derivatives with respect to b are three orders of magnitude larger, too. However, $a \sim n'h\lambda^{-1}$ is typically about 10^3–10^4
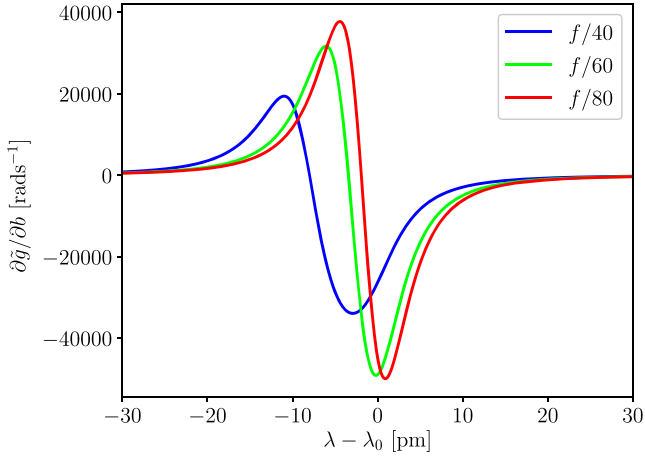
Figure 3. Spectral dependence of the derivative of the transmission profile with respect to b corresponding to telecentric beams with $f/40$ (blue), $f/60$ (green), and $f/80$ (red).

Figure 4. Top: dependence of the phase of the transmitted field with wavelength across the transmission profile for an $f/60$ telecentric (green) and a collimated (red) configuration. Bottom: corresponding derivatives of the phase with respect to a across the transmission profile.

rads in the etalons employed in solar instruments, whereas $b \sim (n'f\#)^{-2}$ is of the order of 10^{-4}–10^{-6} rads. In our numerical example, a is approximately nine orders of magnitude larger than b, which means that a small perturbation of the former has much more importance on δ (Equation (10)) and, hence, on the transmission profile.

3. Phase Error Amplification and Image Quality

3.1. Errors Introduced by Defects

The transmission profile derived in Section 2 corresponds to an ideal homogeneous and isotropic etalon whose reflecting surfaces are perfectly parallel to each other. In a real case, the etalon presents irregularities and/or inhomogeneities that disturb the transmitted electric field and degrade not only the spectral resolution, but also the imaging performance of the instrument. Righini et al. (2010) qualitatively discuss the image quality degradation produced in telecentric etalons and provide a method to evaluate the impact when a particular map of the defects is measured. However, a quantitative evaluation of the impact produced by defects on the wavefront in telecentric etalons has not been presented so far, to our knowledge.
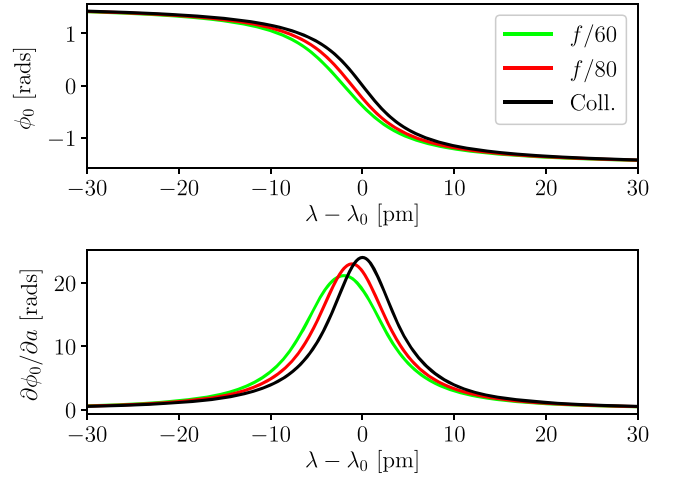
Here we will follow Scharmer (2006) to estimate the wavefront error introduced by defects of the etalon in a telecentric mount. This is as simple as calculating the perturbation produced in the optical phase by such irregularities and/or inhomogeneities. We will consider here the sensitivity of the phase to variations of the parameter a, Δa. For simplicity, we neglect any variations on b produced by changes of the f-number and/or the refraction index, as justified in Section 2. The distorted phase, ϕ, can be approximated at first order, then, as

$$\phi \approx \phi_0 + \frac{\partial \phi_0}{\partial a} \Delta a, \qquad (21)$$

where ϕ_0 is the unperturbed ideal phase given by

$$\phi_0 = \arctan\left(\frac{\mathrm{Im}\{\tilde{\mathbf{E}}^{(\mathrm{t})}\}}{\mathrm{Re}\{\tilde{\mathbf{E}}^{(\mathrm{t})}\}}\right), \qquad (22)$$

which can be evaluated simply using Equations (12), (13), and (14). The derivative of the phase can be calculated

analytically through the derivatives of the real and imaginary parts of the electric field as

$$\frac{\partial \phi_0}{\partial a} = \frac{1}{1 + \tan^2 \phi_0} \frac{1}{\mathrm{Re}\{\tilde{\mathbf{E}}^{(\mathrm{t})}\}}$$
$$\times \left[\frac{\partial}{\partial a} \mathrm{Im}\{\tilde{\mathbf{E}}^{(\mathrm{t})}\} - \tan \phi_0 \frac{\partial}{\partial a} \mathrm{Re}\{\tilde{\mathbf{E}}^{(\mathrm{t})}\} \right], \qquad (23)$$

where the derivatives of the electric field are given by Equations (18) and (19). The final expression is cumbersome and will not be presented here, but approaches, for very large f-numbers, to

$$\lim_{f\#\to\infty} \frac{\partial \phi_0}{\partial a} = \frac{1 + R}{1 - R} \frac{\sec^2 a}{1 + \left(\frac{1+R}{1-R}\right)^2 \tan^2 a}, \qquad (24)$$

which corresponds, as it should be, to the derivative of the phase of the transmitted electric field in an ideal collimated configuration. Note that this equation differs from the one given by Scharmer (2006) in terms of δ because of the inclusion in our work of a global phase, usually unimportant, on the transmitted electric field (see Paper I for further details).

Figure 4 shows the dependence of the phase over the transmission profile for two telecentric beams and for the collimated configuration (top), as well as the corresponding derivatives with respect to a (bottom). The shape and magnitude of the derivatives is quite similar for the collimated and telecentric cases, and so will be the sensitivity of the phase to errors in the optical thickness. Note that the peaks of the derivative in the telecentric cases are shifted to the blue with respect to λ_0, in the same way that their transmission profile does. Moreover, the derivative reaches higher peaks as the f-number is increased. The reason for this is that the the spectral resolution is improved as the f-number increases, which translates into a sharper profile of the phase around the transmission peak.

Again, the results for the collimated mount do not coincide exactly with the phase error amplification function given by
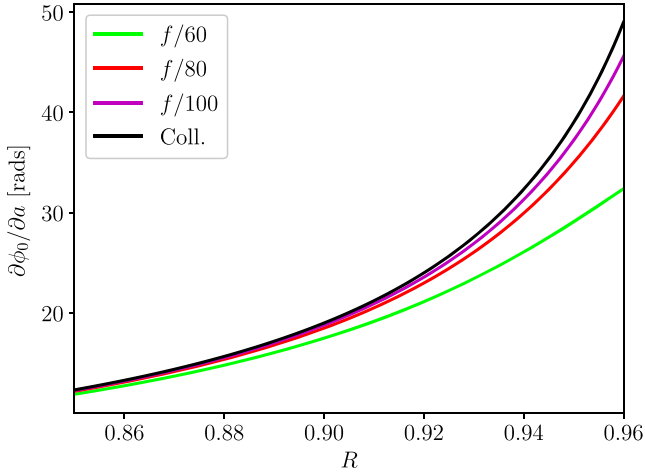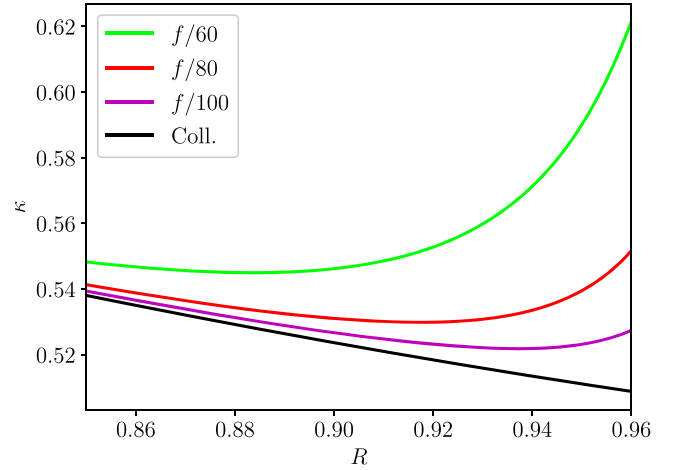
Figure 5. Derivative of the phase with respect to parameter a, at the peak transmission wavelength, as a function of the reflectivity of the etalon surfaces for an $f/60$ (green), an $f/80$ (red), and an $f/100$ (magenta) telecentric beam, as well as for the collimated case (black).

Figure 6. Factor κ as a function of the reflectivity for different telecentric beams: $f/60$ (green), $f/80$ (red), and $f/100$ (magenta). The collimated case is also shown (black).

Scharmer ([2006](#)) because of the omission in his work of a global phase.[1] In particular, his expression tends to negative values at wavelengths far from the maximum transmission, whereas ours is always positive. The maximum of the derivative for the collimated configuration is also different: $(1 + R)(1 - R)^{-1}$ in our case, to be compared with the value of $2R(1 - R)^{-1}$ found by Scharmer ([2006](#)). According to our results, the degradation of the wavefront for the collimated mount at the peak transmission is expected to be, then, a bit more optimistic than the one calculated by Scharmer ([2006](#)), especially for low to moderate reflectivities.

Apart from the aperture of the beam, reflectivity also plays an important role in the degradation of the wavefront. In particular, the closer the reflectivity to unity, the sharper the electric field module and phase profiles. Hence, the derivatives across the transmission profile also increase with larger reflectivities. Figure [5](#) shows the maximum of the derivative of the phase with respect to a as a function of the reflectivity. The derivative has been evaluated for different apertures of the beam. The collimated case is also shown for comparison purposes. Note that the larger the f-number, the higher the value of the derivative and the more important the impact of the reflectivity on the sensitivity to defects. Once again, the reason for this is that the transmission and phase profiles also get steeper when approaching collimated illumination.

As expected from Figure [4](#), the maximum wavefront degradation is at the peak of the transmission profile. Hence, the results shown in Figure [5](#) represent a worst-case scenario if used to evaluate the optical quality of the etalon. Scharmer ([2006](#)) suggested that the effect of the finite width of the passband of the etalon can be estimated by multiplying the monochromatic wavefront error produced at the peak transmission by a factor $1/2$. The choice of this factor is not entirely justified, though. A more appropriate approach would consist of calculating the quasi-monochromatic ("effective") wavefront degradation after integrating the derivative of the phase with

respect to a across the transmission profile as

$$\left(\frac{\partial \phi_0}{\partial a}\right)_{\text{eff}} = \frac{\int \frac{\partial \phi_0}{\partial a}(\lambda)\tilde{g}(\lambda)d\lambda}{\int \tilde{g}(\lambda)d\lambda}. \tag{25}$$
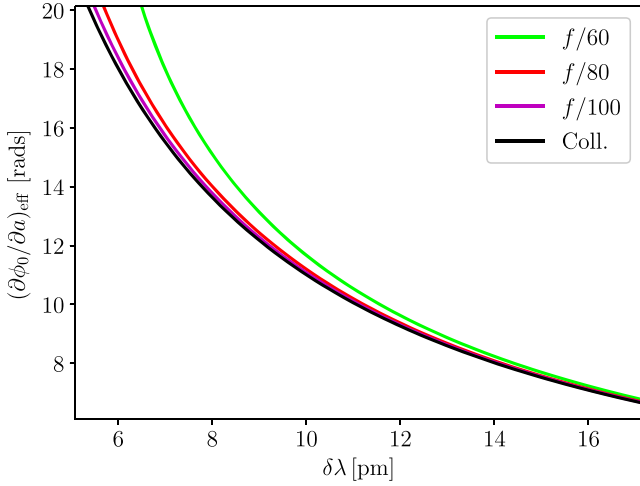
Of course, we can always relate the quasi-monochromatic derivative of the phase to the monochromatic derivative at the maximum of the transmission profile through a factor κ as

$$\left(\frac{\partial \phi_0}{\partial a}\right)_{\text{eff}} = \kappa\left(\frac{\partial \phi_0}{\partial a}\right)_{\text{peak}}, \tag{26}$$

where κ depends, in general, on the parameters of the etalon and on its illumination. Figure [6](#) shows the dependence of the factor κ against the reflectivity for telecentric configurations with different f-numbers, as well as for the collimated case. Our results show that κ is very close to $1/2$, as estimated qualitatively by Scharmer ([2006](#)). This is particularly true for collimated mounts and for telecentric setups with "large" f-numbers ($f\# \geqslant 80$), almost independently of the reflectivity of the etalon. For mounts illuminated with faster beams, κ shows a stronger dependence with the reflectivity and amounts to ~ 0.60 for an $f/60$ beam and $R = 0.96$.

In the light of these results, the derivative of the phase clearly seems to depend greatly on the spectral resolution of the Fabry–Pérot etalon, which is given by the combined effect of the plates' reflectivity, the f-number of the incident beam, and the distribution of defects across the footprint of the beam illuminating the etalon. For a more general comparison among the two mounts it can be then appropriate to express the derivative of the phase in terms of the spectral resolution. According to Steel ([1986](#)), the derivative of the phase at the maximum of the transmission profile in the collimated configuration, $(1 + R)(1 - R)^{-1}$, can be related to the finesse of the etalon, $\mathcal{F}$, through the expression

$$\left(\frac{1 + R}{1 - R}\right)^2 = 1 + \left(\frac{2}{\pi}\mathcal{F}\right)^2. \tag{27}$$

---

[1] The phase error amplification function described by Scharmer ([2006](#)) is calculated as the derivative of the phase with respect to δ, instead of to a. It is necessary, then, to include a factor 2 in his expressions for comparison purposes.

Figure 7. Quasi-monochromatic (effective) derivative of the phase with respect to a against the spectral resolution, $\delta\lambda$, for an $f/60$ (green), an $f/80$ (red), and an $f/100$ (magenta) telecentric beam, as well as for the collimated case (black)

Hence, we can write the absolute value of the derivative in terms of the spectral resolution, $\delta\lambda$, as

$$\left| \frac{\partial \phi_0}{\partial a} \right|_{\text{peak}} = \sqrt{1 + \left(\frac{\lambda_0^2}{\pi n h \delta\lambda} \right)^2} \qquad (28)$$

This equation is strictly valid for the collimated configuration. However, we have found through numerical experimentation that the expression fits very well for the telecentric configuration as long as we substitute $\delta\lambda$ by its corresponding spectral resolution. This means that the maximum of the derivative depends only on the spectral resolution, no matter if the etalon is illuminated with telecentric or collimated light. Since the value of κ found in Figure 6 is greater for the telecentric configuration than for the collimated case, the effective quasi-monochromatic derivative is actually expected to be slightly larger in a telecentric mount than in a collimated setup exhibiting the same spectral resolution. This is demonstrated in Figure 7, which shows the effective wavefront degradation calculated after integrating the response along the transmission profile as a function of the spectral resolution for telecentric setups with different f-numbers and for the collimated configuration. Note that the smaller the $\delta\lambda$ and the f-number, the larger the derivative of the phase when compared to the collimated case.

Let us imagine now that the thickness of the etalon varies across the footprint of the incident beam following a certain distribution with an rms value $\langle\Delta h\rangle$. Using Equation (21), the rms of the effective wavefront error induced by the etalon, $\langle\Delta\phi\rangle_{\text{eff}}$, is simply given by

$$\langle\Delta\phi\rangle_{\text{eff}} = \left| \frac{\partial \phi_0}{\partial a} \right|_{\text{eff}} \frac{2\pi n'}{\lambda} \langle\Delta h\rangle, \qquad (29)$$

from which the Strehl ratio, S, can be estimated as (Mahajan 1981)

$$S = \exp\left(-\langle\Delta\phi\rangle_{\text{eff}}^2\right). \qquad (30)$$

According to the Maréchal criterion, diffraction-limited performance of the etalon is achieved when the rms of the

wavefront degradation stays below $\lambda/14$ or, equivalently, when the Strehl ratio is larger than 0.8. Using Equation (26), the condition for the rms of the error thickness to ensure diffraction-limited optical quality, $\langle\Delta h\rangle_{\text{diff}}$, can be written, then, simply as

$$\langle\Delta h\rangle_{\text{diff}} < \frac{\lambda}{14\kappa n' \left| \frac{\partial \phi_0}{\partial a} \right|_{\text{peak}}}. \qquad (31)$$

Expressions for the maximum allowed cavity errors can be found in an analogous way by setting the peak-to-valley wavefront degradation below $\lambda/4$ (the Rayleigh criterion) or, equivalently, by multiplying the right side of the equations presented here by a factor of 3.5. For a value of the reflectivity of 0.90, the rms of the irregularities on the thickness must be better than $\sim \lambda/300$ or ~ 2 nm at $\lambda = 617$ nm for both a collimated and an $f/60$ configuration. If the reflectivity is increased up to 0.95, the flatness shall be $\sim \lambda/630$ in the collimated case and $\sim \lambda/550$ in the telecentric configuration to accomplish diffraction-limited performance. The flatness requirement over the footprint of the telecentric setup converges with increasing f-number to that of the collimated mount even for large reflectivities. If we set the spectral resolution to be the same in the two setups, the collimated configuration overtakes the telecentric one. For instance, for a moderate resolution of 10 pm, the requirement on the rms of the thickness error is $\sim \lambda/350$, to be compared with the slightly stricter $\sim \lambda/375$ value for the $f/60$ case. If $\delta\lambda = 7$ pm, then the maximum allowed rms decreases to $\sim \lambda/500$ and $\sim \lambda/580$, respectively. A similar expression to Equation (31) can be found for the requirement in homogeneity on the refraction index. If we ignore perturbations introduced by b, the maximum allowed rms of the refraction index variations across the footprint can be shown to be of the order of $\sim 5 \times 10^{-4}\%$ to fulfill the diffraction limit requirement.

These requirements on the roughness and on the refractive index homogeneity apply to the area illuminated by the incident beam on the etalon. In collimated mounts, where the etalon is at a pupil plane, the whole clear aperture of the etalon is always illuminated no matter the observed point on the object field. In telecentric setups, the footprint of the incident beam is much smaller because of the very close location of the etalon with respect to the image plane. On the other hand, the rms value of thickness errors tend to increase with the aperture, especially if they are caused by one of the large-scale defects mentioned in Paper I (departure of parallelism, spherical defect, sinusoidal defect, etc.). The incident wavefront is usually expected, then, to be much less distorted by defects in telecentric mounts than in collimated setups even though the sensitivity to errors in the thickness is very similar in both configurations. In fact, errors on the wavefront due to cavity defects have been barely discussed in the literature so far when studying the telecentric configuration because their scale has been usually assumed to be large compared to the very small footprint of the incident beam on such etalons. However, etalons are affected not only by large-scale defects, but also by high-frequency microroughness or polishing errors of the surfaces, which are usually distributed almost uniformly over the etalon area (e.g., Reardon & Cavallini 2008). If these defects dominate over other sources of error, the choice of the

optimum configuration will depend on their scale relative to the footprint. Telecentric setups minimize wavefront errors if the thickness map varies spatially in a scale larger than (or comparable to) the size of the footprint on the etalon, but if these variations are of a very high frequency, then they could have an important impact on the wavefront. In this case the superiority of telecentric mounts over the collimated configuration in terms of wavefront degradation is not so clear and could be surpassed by the other drawbacks that are present in these setups.

3.2. Degradation of Image Quality Intrinsic to Telecentric Mounts

Telecentric beams introduce wavefront errors through the mere fact that pupil illumination is no longer homogeneous as seen from the etalon (*pupil apodization,* Beckers 1998). In Paper I we argued that apodization of the pupil is responsible for a transfer of energy between the central part of the PSF and its wings, thus degrading the image with respect to a perfect unaberrated optical system. This is a wavelength-dependent effect that introduces artificial features in the observed image, as evaluated in Paper III, and would occur even in a perfect etalon with no defects.

To estimate the impact of pupil apodization on the wavefront, we can deal with the integration of rays with different incidence angles on the etalon as if it were a "defect" on the illumination compared to a collimated beam. The rms value of the density distribution of such an error is given by Equation (109) of Paper I. Then, we can use an approach similar to the one followed in Section 3.1 to calculate the perturbation produced by this aperture defect on the transmitted wavefront. The rms value of the phase error at the maximum of the transmission profile, $\langle \Delta \phi \rangle_{\text{peak}}$, is then simply given by

$$\langle \Delta \phi \rangle_{\text{peak}} = \frac{1 + R}{1 - R} \frac{\pi h}{\lambda n'(f\#)^2 8\sqrt{3}}. \quad (32)$$

In order to estimate the total (monochromatic) degradation of the wavefront produced by a telecentric etalon, this expression should be added quadratically to the perturbation introduced in Equation (21), which accounts for the impact of irregularities.

Observe also that a careful choice of the reflectivity is mandatory in telecentric instruments even when defects are ignored, especially for compact instruments with low *f*-numbers. Beams faster than $f/60$ (or $\sim f/140$ in an air-gapped etalon) are almost prohibitive in terms of monochromatic imaging performance even for moderate reflectivities of the order of ~ 0.9. In particular, the minimum *f*-number that achieves a wavefront degradation smaller than $\lambda/14$, when no defects are present, is $\sim f/40$ for $R = 0.90$ and $\sim f/60$ for $R = 0.95$.

The above results represent a worst-case scenario because image quality has been evaluated monochromatically at the peak of the transmission profile. Once again, we can use Equation (26) to take into account the finite passband of the etalon. This relaxes the diffraction-limiting requirement on the incident beam aperture considerably. In fact, the limiting *f*-number that keeps the rms error better than $\lambda/14$ is $\sim f/30$ and $\sim f/40$ for $R = 0.90$ and $R = 0.95$, respectively. Moreover, much of this degradation can be eliminated by a simple refocus of the etalon (Scharmer 2006). There are compelling reasons to illuminate the etalon with much slower beams, though. As

already mentioned, pupil apodization introduces other undesired effects, apart from phase errors, which can be greatly reduced when increasing the *f*-number (Paper III). Unfortunately, the larger the *f*-number, the less compact the instrument and the bigger the etalon. Hence, a compromise must be found between artificial signals and the aperture of the incident beam to minimize the effects of pupil apodization while containing the size of the instrument and etalon within realistic and affordable limits. To select the optimum aperture of the incident beam on the etalon, we recommend a careful assessment on the impact of the finite aperture of the incident beam taking into account a complete consideration on the polychromatic nature of the observations in the way described in Paper III.

3.3. Discussion on the Imaging Performance of the Two Configurations

The location of the etalon in a telecentric configuration within the optical path can be chosen carefully to minimize the footprint of the incident beam (and, hence, the impact of high-frequency errors in the wavefront). Yet, wavefront errors produced in this setup are still expected to be smaller than in a collimated configuration.

Unfortunately, if the telecentric configuration is chosen to reduce the impact of defects in the wavefront, then there is also a risk of having different spatial PSFs and transmission profiles across the FOV due to the local variations of the optical thickness over the aperture. This is especially true if two or more etalons are used in tandem to improve the free spectral range and the resolving power of the instrument, each one with a different cavity map. In such a case, the transmission profile is not only shifted, but it becomes asymmetric and its peak is reduced due to the detuning of the individual transmission profiles of each etalon that take place point to point. These effects induce artificial signals in the spectrum of the observed Stokes vector that can be larger than the required polarimetric sensitivity of the instrument locally. To reduce the impact on the Stokes profiles, differential shifts of the spectral profiles must be kept as low as possible by minimizing cavity errors. First order corrections of the measured data are also possible if a careful reduction technique is followed. An example of a flat-fielding procedure that successfully mitigates the effect of the loss of invariance on the spectral profile can be found in de la Cruz Rodríguez et al. (2017).

Telecentric etalons present other problems that must be considered as well, like artifacts introduced by the strong spectral dependence of their PSF or by deviations from perfect telecentrism (Papers I and III). The latter can arise simply when tilting one of the etalons to move inner etalon ghost images away from the detector. To reduce both effects, the *f*-number of the incident beam should be as large as possible. If two Fabry–Pérot etalons are employed, it is also highly advisable, first, to combine low- and high-finesse etalons and, second, to apply the minimum necessary tilt only (or mostly) to the etalon with lowest resolution (Scharmer 2006).

The collimated configuration is not immune to problems either, especially when more than one etalon is employed. Differential shifts of the individual transmission profiles over the FOV can also appear in pairs of collimated etalons when one of them is tilted to avoid ghost images on the detector. The shifts of the individual transmissions across the FOV causes field-dependent asymmetries on the total transmission profile

that have the same impact as the ones described above for the telecentric configuration. Moreover, although the overamplification of errors by the presence of a second etalon exists in both configurations, collimated dual-etalon setups run a higher risk of decreasing the optical quality of the instrument below requirements due to the much larger footprint of their beam, unless cavity errors are kept small enough (0.5–1 nm rms over the full clear aperture, typically).

A proper choice on the optimum configuration needs, then, careful considerations on the impact of cavity defects and of tilts of the etalon, if any, on the measured signals based on the expected thickness maps of the etalons to be employed. Also important are the implications associated with each configuration on the required dimensions, quality, and costs of the etalons (and of the instrument itself). In particular, the diameter of the etalon in a collimated configuration, $\varnothing_{\mathrm{coll}}$, assuming a square $F \times F$ FOV, can be related to the entrance pupil diameter of the telescope, $\varnothing_{\mathrm{pup}}$, and to the maximum allowed spectral shift of the transmission profile across the FOV, $\Delta\lambda$, using the Lagrange invariant and Equation (33) of Paper I, as

$$\varnothing_{\mathrm{coll}} = \frac{F\varnothing_{\mathrm{pup}}}{2n'\sqrt{\frac{\Delta\lambda}{\lambda}}}, \tag{33}$$

which can be rewritten in terms of the spectral resolving power of the etalon, $\mathcal{R}$, and $\epsilon \equiv \Delta\lambda/\delta\lambda$, with $\delta\lambda$ being the spectral resolution of the Fabry–Pérot etalon at the wavelength of interest:

$$\varnothing_{\mathrm{coll}} = \frac{F\varnothing_{\mathrm{pup}}}{2n'}\sqrt{\frac{\mathcal{R}}{\epsilon}}. \tag{34}$$

For the telecentric configuration, making use of the Lagrange invariant again, the diameter of the etalon, $\varnothing_{\mathrm{tel}}$, is given simply as

$$\varnothing_{\mathrm{tel}} = \sqrt{2}F\varnothing_{\mathrm{pup}}f\#, \tag{35}$$

where $f\#$ is the f-number of the incident beam on the etalon. The ratio of the sizes corresponding to both configurations depend therefore only on the resolving power, the f-number, the refraction index, and ϵ, like

$$\frac{\varnothing_{\mathrm{coll}}}{\varnothing_{\mathrm{tel}}} = \sqrt{\frac{\mathcal{R}}{8\epsilon}}\frac{1}{n'f\#}. \tag{36}$$

Figure 8 shows the ratio $\varnothing_{\mathrm{coll}}/\varnothing_{\mathrm{tel}}$, parameterized with the value of ϵ, as a function of $\mathcal{R}$ for the case $n'f\# = 150$. Note that the ratio is below or only slightly above unity for resolving powers up to ~150,000, unless the requirement on the maximum tolerable shift across the FOV is set as tight as $\Delta\lambda = 0.25\delta\lambda$. The allowed shift on the collimated configuration differs from one instrument to another, but is usually of the order of $\epsilon = 0.75$. This choice of ϵ guarantees that a maximum of only one wavelength sample is lost at the corner of the FOV when a critical sampling is assumed (i.e., when the spectral sampling is $0.5\delta\lambda$). For this value of ϵ the ratio is larger than unity only when resolving powers above 150,000 are required. It is important to remark that large-scale errors in the telecentric configuration also cause significant wavelength shifts of the spectral profile across the FOV. For example, a parabolic 4 nm peak-to-valley error (~$\lambda/150$) would cause a shift comparable to the FWHM of the transmission profile ($\epsilon = 1$) for a resolving power of 150,000.
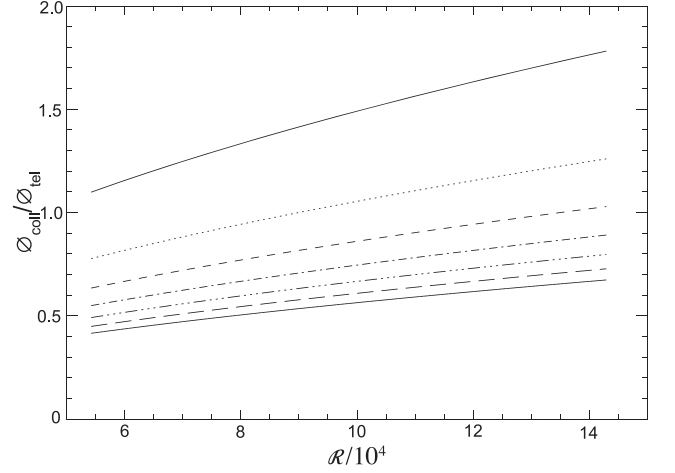
Figure 8. Size ratio of the etalons as a function of the resolving power. Different lines correspond to various values of ϵ. From top to bottom, $\epsilon = 0.25$, 0.5, 0.75, 1, 1.25, 1.5, 1.75.

The next generation of 4 m ground-based telescopes will require etalons with diameters of the order of 150–200 mm or more, no matter the chosen configuration. Such large etalons need to be carefully designed, exploring the contribution of cavity errors on different spatial scales to the instrument performance and to the optical quality achieved by the overall system. Meanwhile, future space-borne telescopes, with much smaller apertures and dimensions, can benefit from the use of collimated mounts for two reasons: first, this setup avoids the problems related with the use of the fast beams that would be required if a telecentric configuration were employed in such compact instruments and, second, the etalons to be employed in this case are much smaller than those needed in ground-based instruments due to the reduced telescope aperture, making it easier to manufacture them with qualities high enough to ensure diffraction-limited performance.

4. Analytical Expressions for Birefringent Etalons

Electro-optical etalons, like the ones employed in the Imaging Magnetograph eXperiment (Martínez Pillet et al. 2011) and Polarimetric and Helioseismic Imager (Solanki et al. 2020), are filled with an anisotropic material that shows birefringent properties. Let us consider a birefringent etalon within a perfect telecentric configuration, where the chief ray is parallel to the optical axis over the whole FOV. The transmission profile is, then, given by Equation (50) of Bailén et al. (2019b), hereinafter Paper II. This expression depends on the Jones matrix terms, which, in turn, depend on the retardances of the ordinary and extraordinary beams, δ_{o} and $\delta_{\mathrm{e}} \equiv \delta_{\mathrm{o}} + \varphi$, where φ is given by Equation (36) of Paper II. For small incidence angles, we can approximate δ_{o} and δ_{e} as

$$\frac{\delta_{\mathrm{o}}}{2} = a(1 - b_{\mathrm{o}}\varrho^2), \tag{37}$$

$$\frac{\delta_{\mathrm{e}}}{2} = a(1 - b_{\mathrm{e}}\varrho^2), \tag{38}$$

where a coincides with Equation (8), b_{o} is just Equation (9) with $n' = n_{\mathrm{o}}$, and b_{e} is given by

$$b_{\mathrm{e}} = b_{\mathrm{o}} - c, \tag{39}$$

where we have defined c as

$$c \equiv \frac{n_3 - n_o}{n_o(n_3 + n_o)^2} \frac{1}{(f\#)^2}. \tag{40}$$

Integration of the electric fields for the ordinary and extraordinary rays yields Equations (13) and (14) with the only difference that b must be substituted with b_o or b_e correspondingly. Then, an analytical expression for the Mueller matrix of telecentric etalons can be found simply using Equations (45)–(48) of Paper II. Although the resulting analytical equations are quite laborious and will not be shown here, this method offers an efficient way of calculating the Mueller matrix of etalons in telecentric setups without the need of performing numerical integration, which facilitates calibration and postprocessing tasks on space instruments based on anisotropic etalons, whose computational resources are limited.

5. Summary and Conclusions

We have analytically solved the equation that governs the transmitted electric field of isotropic telecentric etalons. The found solution is valid for large f-numbers ($f\# \gg 1$) typical of solar instruments and is determined only by the reflectivity, absorptivity, and two coefficients that are proportional to $n'h\lambda^{-1}$ and $(n'f\#)^{-2}$, respectively, where n' is the refraction index of the etalon, h its thickness, and λ the wavelength of interest. The fact that n' appears only as a proportionality factor of h and of the f-number shows that there is a unique equivalence between the solution corresponding to a crystalline etalon and an air-gapped Fabry–Pérot etalon whose thickness and f-number is n' times larger. Then, our results obtained for a crystalline etalon with $n' = 2.3$ and $h = 250$ μm illuminated with telecentric beams ranging from $f/40$ to $f/100$ are completely general also for an air-gapped etalon with $n' = 1$ and $h = 575$ μm placed in beams with apertures that go from $f/92$ to $f/230$, typical of ground-based solar instruments. This means that crystalline etalons can be placed in much faster telecentric instruments compared to their air-gapped counterparts, with obvious advantages in the instrument and etalon dimensions.

From the analytical expression of the electric field, we have obtained its derivatives and we have evaluated the sensitivity of the transmission profile and of the phase of the electric field to variations in the etalon parameters. We have shown that the transmission is barely affected by changes in the incident f-number, but depends strongly on the thickness, refraction index and wavelength. Similarly to collimated etalons, the transmission profile is mostly shifted by disturbances on the optical cavity, whereas small changes in the f-number produce both a shift and a change of width on the profile. At the maximum of the transmission, the phase of the transmitted electric field is also affected by changes in the optical thickness, but in a lesser extent than in collimated instruments for etalons with the same reflectivity. This is due to the lower resolution of the transmission profile in telecentric setups, which translates into a smoother spectral dependence of the phase. The lower the reflectivity and the larger the f-number, the more similar the impact to the collimated case. We have found also that the monochromatic response of the phase at the transmission peak is the same in both configurations as long as they show the same spectral resolution.

To account for the limited resolution of the etalon, we have estimated the quasi-monochromatic sensitivity of the phase by integrating its derivative over the transmission profile. We have compared it with the sensitivity at the maximum of the transmission profile through a proportionality factor that depends slightly on the reflectivity and on the aperture of the beam. We have shown numerically that this factor approaches to $\sim 1/2$ for the collimated configuration, as predicted by Scharmer (2006). For the telecentric case the factor is larger than $1/2$ and increases with decreasing f-number, although it approaches $1/2$ for low to moderate reflectivities. This means also that, for a given spectral resolution, the effective (quasi-monochromatic) transmitted phase of the etalon is more sensitive to cavity errors in a telecentric configuration than in collimated setups.

A simple expression to evaluate the wavefront degradation produced by roughness errors on the etalon surfaces has been presented, too. Such an expression suggests that the choice of the reflectivity—or, more specifically, of the spectral resolution —plays a very important role in the magnitude of the distortion of the wavefront, setting a limit to the maximum allowed rms value of the irregularities on the optical thickness over the footprint, as already observed for the collimated configuration by Scharmer (2006). Cavity errors of etalons mounted in telecentric setups are expected to produce a smaller wavefront degradation than when mounted in a collimated configuration, unless the etalon is mostly affected by thickness errors and/or inhomogeneities of a very high frequency that vary in spatial scales smaller than the footprint of the incident beam. We have derived also an expression to infer the image degradation that appears in telecentric mounts only because of the finite aperture of the incident beam. Such a degradation has a strong dependence with the reflectivity and with the f-number and appears even if no defects are present in the etalon. This effect compensates somehow the lower sensitivity of telecentric etalons to defects, although it can be mostly corrected with a refocus of the detector, in the same way the parabolic error is calibrated in collimated mounts.

We have included a discussion on the differences in optical and spectral performance of the telecentric and collimated configurations that accounts for other important effects. We have presented expressions for the required diameter of the etalon in each configuration, too. Telecentric etalons are safer in terms of wavefront distortion, but can introduce artificial signals in the measured magnetic field and line-of-sight plasma velocities, as well as point-to-point variations (and even asymmetries) of the PSF and of the spectral transmission, especially when several etalons are located in tandem. Meanwhile, collimated setups with two or more etalons take the risk of overamplifying the wavefront errors in excess and also introducing field-dependent asymmetries in the transmission if one of the etalons is tilted with respect to the other. The magnitude of these effects must be assessed together with other considerations on the dimensions and cost of the instrument and of the etalon to choose the optimum configuration for each particular instrument.

Finally, we have extended our formulation to the case in which the etalon is anisotropic. In particular, we have introduced a simple modification of the solution valid for the isotropic case that allows for the direct calculation of a transmitted electric field corresponding to the ordinary and extraordinary rays. The electric fields can be employed, then, to analytically calculate the Mueller matrices of telecentric etalons

in the way described in Paper II without the need for integrating the equations numerically.

ORCID iDs

F. J. Bailén ⓘ https://orcid.org/0000-0002-7318-3536
D. Orozco Suárez ⓘ https://orcid.org/0000-0001-8829-1938
J. C. del Toro Iniesta ⓘ https://orcid.org/0000-0002-3387-026X

References

Bailén, F. J., Orozco Suárez, D., & del Toro Iniesta, J. C. 2019a, ApJS, 241, 9
Bailén, F. J., Orozco Suárez, D., & del Toro Iniesta, J. C. 2019b, ApJS, 242, 21
Bailén, F. J., Orozco Suárez, D., & del Toro Iniesta, J. C. 2020, ApJS, 246, 17
Beckers, J. M. 1998, A&AS, 129, 191
Born, M., & Wolf, E. 1999, Principles of Optics, 986 (Cambridge: Cambridge Univ. Press), 986
de la Cruz Rodríguez, J., Löfdahl, M. G., Sütterlin, P., et al. 2017, CRISPRED: CRISP imaging spectropolarimeter data reduction pipeline, Astrophysics Source Code Library, ascl:1708.003
Hernandez, G. 1988, Fabry-Perot Interferometers, 360 (Cambridge: Cambridge Univ. Press), 360
Hill, R. M. 1963, AcOpt, 10, 141
Mahajan, V. N. 1981, JOSA, 71, 1561
Martínez Pillet, V., Del Toro Iniesta, J. C., Álvarez-Herrero, A., et al. 2011, SoPh, 268, 57
Ramsay, J. V. 1969, ApOpt, 8, 569
Reardon, K. P., & Cavallini, F. 2008, A&A, 481, 897
Righini, A., Cavallini, F., & Reardon, K. P. 2010, A&A, 515, A85
Scharmer, G. B. 2006, A&A, 447, 1111
Sloggett, G. J. 1984, ApOpt, 23, 2427
Solanki, S. K., del Toro Iniesta, J. C., Woch, J., et al. 2020, A&A, 642, A11
Steel, W. H. 1986, Interferometry (2nd ed.; Cambridge: Cambridge Univ. Press)
von der Lühe, O., & Kentischer, T. J. 2000, A&AS, 146, 499

Conclusions

We have presented an overview on the behavior of collimated and telecentric etalon-based instruments from a spectral, imaging, and polarimetric perspective.

With respect to the spectral characteristics of these instruments, we have focused on reviewing the deterioration of the transmission profile produced by cavity errors, by the finite f-number in telecentric etalons and by imperfections on the illumination in such mounts. We have presented a general approach that address the impact of the most common defects on the finesse no matter their magnitude through the method proposed by Sloggett (1984). We have derived compact analytical expressions for errors that have a small and large impact on the transmission and that are completely valid for solid etalons.

Concerning the imaging properties, we have studied the spatial shape of the PSF in collimated and telecentric mounts both at monochromatic wavelengths and including the finite passband of the etalon. In particular, we have shown that:

1. In an ideal collimated configuration, the spatial shape of the PSF is simply that of a circular aperture, whereas the transmission profile acts only as a proportionality factor that apodizes the image to its edges. Hence, the monochromatic response is simply given by the convolution of the object and the diffraction-limited PSF modulated by the transmission factor. Meanwhile, in a perfect telecentric etalon the spectral and spatial parts of the PSF are strongly correlated and cannot te separated.

2. In real collimated setups, (spatial) stray light coming from high frequency defects, and its subsequent decrease on the image contrast, is the main source of degradation expected, but the response is still the same across the FoV. In the telecentric configuration the response varies point to point due to local thickness errors and inhomogeneities.

3. Small misalignments of a few tenths of degree among the incident cone of rays and the etalon, coming from either departures of perfect telecentrism over the FoV or by a tilt of the etalon to get rid of ghost images on the detector, induce a noticeable asymmetrization, broadening, and shift of both the peak transmission and the PSF in telecentric mounts. A degradation of the (quasi-monochromatic) SNR is also expected. These effects depend non linearly with the relative tilt and with the f-number.

4. The quasi-monochromatic response of the etalon is correlated with the observed object in the two setups when considering the small but finite width of the spectral transmission of the etalon. Therefore, the quasi-monochromatic PSF cannot be employed as a regular one, except for observations of spectrally flat features (i.e., in the continuum).

Regarding the polarimetric response, we have derived a general expression of the Mueller matrix that describes the polarimetric behavior of uniaxial crystalline etalons no matter the birefringence induced. We have found also a compact formula to evaluate the birefringence of solid etalons that accounts for the orientation of the incident beam and that of the optical axis. We have demonstrated that:

1. The Mueller matrix of anisotropic uniaxial etalons has two contributions: one corresponding to a mirror and another one given by the polarimetric response of a retarder, both strongly modulated across the transmission profile.

2. In collimated mounts, the Mueller matrix depends only on four elements. These terms exhibit large variations across the transmission profile, but also with the incidence angle and the direction of the optical axis. Different orientations of the principal plane can be addressed through a proper rotation of the Mueller matrix.

3. In an ideal telecentric configuration, no off-diagonal terms are expected on the Mueller matrix. Imperfections in the telecentrism induce cross-talk terms on the Mueller matrix, as well as an spectral asymmetry on the coefficients. Again, the Mueller matrix is completely characterized by four terms that change along the bandpass.

4. The PSF depends on the state of polarization of the incident Stokes vector. In particular:

   a) In the collimated configuration, the spatial shape PSF coincides with that of the isotropic case, but the proportionality factor now changes with the orientation of the principal plane, which rotates over the image, and is modulated by the incident Stokes vector.

   b) In (perfect) telecentric mounts, the dependence of the PSF with the Stokes vector is seen directly to its spatial shape, which changes with the incident polarization. In a real (imperfect) telecentric configuration, the same applies, but the PSF becomes asymmetric, too.

We have carried out an assessment of the spurious signals on a simulated instrument taking into account the effects mentioned above. We have shown that the magnitude of the spurious signals arising from the wavelength dependence of the PSF in a telecentric configuration goes with the inverse square of the f-number. Our numerical results suggest that the corresponding artificial LoS magnetic field and plasma velocities can be prohibitively large even for instruments with moderate resolving powers, especially if the f-number is not sufficiently large ($\gtrsim f/40$ for a resolving power of $\sim 60,000$ and an etalon with a large refrative index of 2.3). In an imperfect telecentric configuration the situation is even more pessimistic because of the asymmetrization of the transmission profile and of the PSF. In this case, more pronounced signals are expected accompanied by a shift of the plasma velocities. In relation to the effects produced by the birefringence of the etalon, the impact depends on the specific location of the etalon within the optical train:

1. If located after the analyzer of the polarimeter:

   a) The optimal efficiencies are reached with the ideal modulation scheme introduced by Del Toro Iniesta & Martínez Pillet (2012), no matter the chosen configuration.

   b) No artificial signals appear in the collimated configuration, regardless the birefringence of the etalon.

   c) The azimuthal symmetry of the telecentric PSF is lost and it becomes elliptic. Nevertheless, the contamination of the LoS velocities and magnetic field is an order of magnitude below the one produced by pupil apodization effects in our numerical experiments.

2. If placed between the modulator and the analyzer:

   a) In collimated setups, the presence of the etalon changes the Mueller matrix of the polarimeter and produces an spectral and field-dependent modulation of polarimetric efficiencies. The maximum change on the efficiency is expected to be below $1\,\%$ in a typical instrument, though.

   b) In the telecentric configuration, the polarimetric response remains the same as if situated after the analyzer. The reason for this is that its Mueller matrix commutes with that of the analyzer.

c) In dual-beam instruments, the etalon modifies the measured Stokes vector from one channel to the other, but the changes in the signal are expected to be completely negligible in telecentric mounts and below 1% at the wing of V in collimated setups.

Finally, we have found an analytical solution for the transmitted electric field of isotropic Fabry-Pérots illuminated with a telecentric beam. Our solution holds for f-numbers much greater than unity, like the ones used in solar instruments. We have found that the refractive index, n', simply amplifies the thickness and the f-number. The main implication of this result is that the electric field remains exactly the same for a solid etalon illuminated with an f-number n' times smaller than the one corresponding to an air-gapped Fabry-Pérot as long as its thickness is reduced by the same factor. Therefore, lithium niobate etalons, with a large index of refraction of ~ 2.3, benefit from an important reduction on the instrument size and on its diameter while preserving the same spectral and imaging properties as air-gapped etalons. We have generalized the analytical solution to the propagation of the ordinary and extraordinary rays in uniaxial etalons. This way, the Mueller matrix of the etalon can be evaluated analytically, too.

The analytical solution has given us access to its derivatives, from which we have inferred the sensitivity of the transmission and of the electric field phase to changes on the thickness, refractive index and f-number. From such a study:

1. We have proven that the electric field is very sensitive to small variations on the two former parameters but is barely affected by errors on the incident aperture.

2. We have shown that the transmitted phase is less sensitive to errors in the thickness and refractive index than in collimated instruments. The differences are emphasized as the reflectivity is increased and the f-number is reduced.

3. We have derived a formula that translates to wavefront errors the physical defects of the etalon across the small, but finite, footprint of the incident beam. Such an expression is consistent with the one found by Scharmer (2006) for the collimated configuration in the limit of f/∞ and suggests that:

   a) Wavefront degradation is amplified in a non-linear way by the spectral resolution. Therefore, the larger the resolving power of

the instrument, the tighter the requirements on the magnitude of the defects across the footprint to achieve diffraction limited performance.

b) The transmitted phase shows the same sensitivity to defects at the maximum of the transmission peak for the two mounts, but the quasi-monochromatic response is more important for telecentric setups and increases with lower f-numbers, especially when the resolution approaches to the limit imposed by the aperture finesse.

c) The deformation of the wavefront is expected to be less pronounced for telecentric etalons simply because errors tend to scale with the footprint size. However, if the magnitude of microroughness errors is comparable to that of large-scale defects and they are of higher frequency than the one corresponding to the footprint size, the induced wavefront degradation must still be evaluated. This is especially true when "large" footprints of ~ 1 mm or more, typical of telecentric instruments, illuminate the etalon.

4. We have dealt with the finite f-number of the incident beam as if it were a defect and we have obtained the corresponding wavefront degradation. We have found that the f-number limits the maximum achievable optical quality of the instrument even for ideal etalons. The dependence of the expression obtained with the aperture of the pupil shows a radial trend when evaluated at the wavelength of the transmission peak consistent with the one found by Scharmer (2006). This contribution to the wavefront deformation can be partly compensated by a refocus, but it cannot be eliminated completely when considering the finite pass-band of the etalon.

Bibliography

Álvarez-Herrero, A., Belenguer, T., Pastor, C., et al. 2006, Proc. SPIE, 6265, 62652G. doi:10.1117/12.671966

Alvarez-Herrero, A., García Parejo, P., Laguna, H., et al. 2015, Proc. SPIE, 9613, 96130I. doi:10.1117/12.2188591

Atherton, P. D., Reay, N. K., Ring, J., & Hicks, T. R. 1981, Optical Engineering, 20, 806

Bailén, F. J., Orozco Suárez, D., & del Toro Iniesta, J. C. 2019, ApJS, 241, 9. doi:10.3847/1538-4365/aafdb3

Bailén, F. J., Orozco Suárez, D., & del Toro Iniesta, J. C. 2019, ApJS, 242, 21. doi:10.3847/1538-4365/ab1c57

Bailén, F. J., Orozco Suárez, D., & del Toro Iniesta, J. C. 2020, ApJS, 246, 17 doi:10.3847/1538-4365/ab5db4

Bailén, F. J., Orozco Suárez, D., & del Toro Iniesta, J. C. 2021, ApJS, 254, 18 doi:10.3847/1538-4365/abf8bc

Barthol, P., Gandorfer, A., Solanki, S. K., et al. 2011, Sol. Phys., 268, 1. doi:10.1007/s11207-010-9662-9

Beck, C., Schmidt, W., Kentischer, T., et al. 2005, A&A, 437, 1159. doi:10.1051/0004-6361:20052662

Beck, C., Bellot Rubio, L. R., Kentischer, T. J., et al. 2010, A&A, 520, A115. doi:10.1051/0004-6361/200913441

Beckers, J. M. 1998, A&AS, 129, 191

Bendlin C., Volkmer R., Kneer F., 1992, A&A 257, 817

Bonaccini, D., Righini, A., Cavallini, F., & Ceppatelli, G. 1989, A&A, 217, 368

Born, M., & Wolf, E. 1999, Principles of Optics, by Max Born and Emil Wolf, pp. 986. ISBN 0521642221. Cambridge, UK: Cambridge University Press, October 1999., 986

Cavallini, F. 1998, Memorie della Societa Astronomica Italiana, 69, 627.

Cavallini, F. 2006, Sol. Phys., 236, 415. doi:10.1007/s11207-006-0103-8

Chabbal, R. J., Recherche des Meilleures Conditions d'Utilisation d'un Spectromètre Fabry-Perot, J. Rech. CNRS 24, 138 (1953)

Collados, M. 1999, Third Advances in Solar Physics Euroconference: Magnetic Fields and Oscillations, 184, 3

de la Cruz Rodríguez, J., Löfdahl, M. G., Sütterlin, P., et al. 2015, A&A, 573, A40. doi:10.1051/0004-6361/201424319

Del Toro Iniesta, J. C. 2003, Introduction to Spectropolarimetry, by Jose Carlos del Toro Iniesta, pp. 244. ISBN 0521818273. Cambridge, UK: Cambridge University Press, April 2003., 244. doi:10.1017/CBO9780511536250

Del Toro Iniesta, J. C., & Martínez Pillet, V. 2012, ApJS, 201, 22. doi:10.1088/0067-0049/201/2/22

Del Toro Iniesta, J. C. & Ruiz Cobo, B. 2016, Living Reviews in Solar Physics, 13, 4. doi:10.1007/s41116-016-0005-2

Doerr, H.-P., von der Lühe, O., II, & Kentischer, T. J. 2008, Proc. SPIE, 7014, 701417

Ejlli, A., Della Valle, F., & Zavattini, G. 2018, Applied Physics B: Lasers and Optics, 124, 22. doi:10.1007/s00340-018-6891-3

Gary, G. A., West, E. A., Rees, D. E., et al. 2006, Astronomical Society of the Pacific Conference Series, 358, 181

Gonsalves, R. A. 1982, Optical Engineering, 21, 829. doi:10.1117/12.7972989

Greco, V. & Cavallini, F. 2013, Optical Engineering, 52, 063001. doi:10.1117/1.OE.52.6.063001

Greco, V., Sordini, A., Cauzzi, G., et al. 2019, A&A, 626, A43. doi:10.1051/0004-6361/201935302

Hecht, E. 1998, Optics, 4th Edition, Addison Wesley Longman Inc, 1998,

Hernandez, G. 1988, Fabry-Perot Interferometers, by G. Hernandez, pp. 360. ISBN 052136812X. Cambridge, UK: Cambridge University Press, August 1988., 360

Hill, R. M. 1963, Optica Acta, 10, 141

Iglesias, F. A. & Feller, A. 2019, Optical Engineering, 58, 082417. doi:10.1117/1.OE.58.8.082417

Jefferies, J., Lites, B. W., & Skumanich, A. 1989, ApJ, 343, 920. doi:10.1086/167762

Kentischer, T. J., Schmidt, W., Sigwarth, M., & Uexkuell, M. V. 1998, A&A, 340, 569

Lites, B. W. 1991, Solar Polarimetry, 166

Lites, B. W., Elmore, D. F., Streander, K. V., et al. 2001, Proc. SPIE, 4498, 73. doi:10.1117/12.450047

Mahajan, V. N. 1991, Tutorial Texts in Optical Engineering, Bellingham: SPIE (The International Society for Optical Engineering), 1991,

Martínez Pillet, V., Collados, M., Bellot Rubio, L. R., et al. 1999, Astronomische Gesellschaft Abstract Series

Martínez Pillet, V., Del Toro Iniesta, J. C., Álvarez-Herrero, A., et al. 2011, Sol. Phys., 268, 57. doi:10.1007/s11207-010-9644-y

Meaburn, J. 1976, Astrophysics and Space Science Library, 56, 279

Molodij, G. & Rayrole, J. 2003, EAS Publications Series, 9, 89

Müller, D., St. Cyr, O. C., Zouganelis, I., et al. 2020, A&A, 642, A1. doi:10.1051/0004-6361/202038467

Netterfield, R. P., Freund, C. H., Seckold, J. A., et al. 1997, ApOpt, 36, 4556.

Debi Prasad, C. & Gosain, S. 2002, Experimental Astronomy, 13, 153.
doi:10.1023/A:1025564731907

Paxman, R. G., Schulz, T. J., & Fienup, J. R. 1992, Journal of the Optical
Society of America A, 9, 1072. doi:10.1364/JOSAA.9.001072

Puschmann, K. G., Denker, C., Balthasar, H., et al. 2013, Optical Engi-
neering, 52, 081606. doi:10.1117/1.OE.52.8.081606

Puschmann, K. G., Kneer, F., Seelemann, T., & Wittmann, A. D. 2006,
A&A, 451, 1151

Ramsay, J. V. 1969, ApOpt, 8, 569. doi:10.1364/AO.8.000569

Reardon, K. P. & Cavallini, F. 2008, A&A, 481, 897. doi:10.1051/0004-
6361:20078473

Righini, A., Cavallini, F., & Reardon, K. P. 2010, A&A, 515, A85.
doi:10.1051/0004-6361/200913302

Rimmele, T. R., Warner, M., Keil, S. L., et al. 2020, Sol. Phys., 295, 172.
doi:10.1007/s11207-020-01736-7

Scharmer, G. B. 2006, A&A, 447, 1111 doi:10.1051/0004-6361:20052981

Scharmer, G. B., Narayan, G., Hillberg, T., et al. 2008, ApJL, 689, L69

Scherrer, P. H., Bogart, R. S., Bush, R. I., et al. 1995, Sol. Phys., 162, 129.
doi:10.1007/BF00733429

Scherrer, P. H., Schou, J., Bush, R. I., et al. 2012, Sol. Phys., 275, 207.
doi:10.1007/s11207-011-9834-2

Schmidt, W., Schubert, M., Ellwarth, M., et al. 2016, Proc. SPIE, 99084N.
doi:10.1117/12.2232518

Semel, M. 1967, Annales d'Astrophysique, 30, 513

Sigwarth, M., Baumgartner, J., Bell, A., et al. 2016, Proc. SPIE, 9908,
99084F. doi:10.1117/12.2232271

Sloggett, G. J. 1984, ApOpt, 23, 2427

Socas-Navarro, H., Elmore, D., Pietarila, A., et al. 2006, Sol. Phys., 235,
55. doi:10.1007/s11207-006-0020-x

Solanki, S. K., del Toro Iniesta, J. C., Woch, J., et al. 2020, A&A, 642, A11. doi:10.1051/0004-6361/201935325

Steel, W. H. 1986, Interferometry.. W. H. Steel. Cambridge University Press.

Title, A. M. 1970, Fabry-Perot Interferometers as Narrow-band Optical filters, Part one: Theoretical Considerations. Harvard College Observatory.

Tritschler, A., Schmidt, W., Langhans, K., et al. 2002, Sol. Phys., 211, 17. doi:10.1023/A:1022459132089

Tritschler, A., Sankarasubramanian, K., Rimmele, T., et al. 2007, American Astronomical Society Meeting Abstracts #210

Quintero Noda, C., Asensio Ramos, A., Orozco Suárez, D., & Ruiz Cobo, B. 2015, A&A, 579, A3

Vaughan, J. M. 1989, The Adam Hilger Series on Optics and Optoelectronics, Bristol: Hilger, 1989

van Noort, M., Rouppe van der Voort, L., & Löfdahl, M. G. 2005, Sol. Phys., 228, 191. doi:10.1007/s11207-005-5782-z

van Noort, M. J., & Rouppe van der Voort, L. H. M. 2008, A&A, 489, 429

van Noort, M. 2017, A&A, 608, A76. doi:10.1051/0004-6361/201731339

Vogel, W., & Berroth, M. 2003, Proc. SPIE, 4944, 293

Vögler, A., Shelyag, S., Schüssler, M., et al. 2005, A&A, 429, 335. doi:10.1051/0004-6361:20041507

von der Lühe, O. 1993, A&A, 268, 374

von der Lühe, O., & Kentischer, T. J. 2000, A&AS, 146, 499. doi:10.1051/aas:2000283

Zhang, S., Hellmann, C. & Wyrowski, F. 2017, ApOpt, 56, 4566.